

Research & Development
2013

Mechanical Engineering Letters, Szent István University

Annual Technical-Scientific Journal of the Mechanical Engineering Faculty,
Szent István University, Gödöllő, Hungary

Editor-in-Chief:
Dr. István SZABÓ

Editor:
Dr. Gábor KALÁCSKA

Executive Editorial Board:

Dr. István BARÓTFI	Dr. István HUSTI
Dr. János BEKE	Dr. Sándor MOLNÁR
Dr. István FARKAS	Dr. Péter SZENDRŐ
Dr. László FENYVESI	Dr. Zoltán VARGA

International Advisory Board:

Dr. Patrick DE BAETS (B)
Dr. Radu COTETIU (Ro)
Dr. Manuel GÁMEZ (Es)
Dr. Klaus GOTTSCHALK (D)
Dr. Yurii F. LACHUGA (Ru)
Dr. Elmar SCHLICH (D)
Dr. Nicolae UNGUREANU (Ro)

Cover design:
Dr. László ZSIDAI

HU ISSN 2060-3789

All Rights Reserved. No part of this publication may be reproduced, stored in a retrieval system or transmitted in any form or by any means, electronic, mechanical, photocopying, recording, scanning or otherwise without the written permission of Faculty.

Páter K. u. 1., Gödöllő, H-2103 Hungary
dekan@gek.szie.hu, www.gek.szie.hu,

This research program is supported by TÁMOP-4.2.1.B-11/2/KMR-2011-003
(Improvement of Research and Education Standard of Szent István University)

Volume 10 (2013)

**Selected Collection from the Research
Results of Year 2012 -2013 and
from Synergy 2013 International Conference
organized by the Faculty of Mechanical Engineering,
Szent István University**

Contents

1. Institute for Mechanics and Machinery (Professor Dr. István SZABÓ, Director of the Institute)	9
István OLDAL, Ferenc SAFRANYIK: Discrete element model of particle outflow	10
László BENSE: Discussion of the jean pain's method	18
Attila LÁGYMÁNYOSI, István SZABÓ, László BENSE: Surface description with LASER light	23
2. Institute for Mathematics and Informatics (Professor Dr. Sándor MOLNÁR, Director of the Institute)	30
Márk MOLNÁR, Sándor MOLNÁR, József MOLNÁR: Depletable Resources in Economic Models	32
Sándor MOLNÁR: On the properties of linear time varying systems	42
Richárd KICSINY: Real-time state observers for solar heating systems	60
3. Institute for Process Engineering (Professor Dr. János BEKE, Director of the Institute)	67
László TÓTH, Norbert SCHREMPF, János BEKE: De-icing of road surfaces (Bridges) with heat	68
László MÁTHÉ, Péter KISS, Lajos LAIB, György PILLINGER, Gábor MAGDICS: Run-Off-Road Vehicle Speed Analysis from Terrain Tracks	81
László TÓTH, János BEKE, Péter SEMBERY: Utilisation possibilities of environmental energy carriers	91
4. Institute for Environmental Engineering Systems (Professor Dr. István FARKAS, Director of the Institute)	101
Piroska VÍG, István FARKAS: Effect of volumetric flow rate on energy production of vacuum tube solar collector	102

Ivett KOCSÁNY, István SERES, István FARKAS: Spectral sensitivity of photovoltaic modules	111
Zoltán DODOG: Thermal performance of different exterior building boundaries	120
5. Institute for Mechanical Engineering Technology (Professor Dr. Gábor KALÁCSKA, Director of the Institute)	129
László ZSIDAI, Zoltán SZAKÁL: Development of tribology model systems for research of PA6 and PEEK polymer composites	130
Tamás PATAKI, Attila KÁRI-HORVÁTH, Zoltán SZAKÁL: Drawing process of carbon nanotube „y” junctions	140
Viktor ERDÉLYI, László JÁNOSI: Development of orientation strategy and guidance tool for visually impaired people	145
6. Invited Papers from „Synergy” International Conference 2013	151
H.-P. SCHWARZ, Ph. RÜGER, A. KICHERER, R. TÖPFER: Development of an autonomous driven robotic platform used for ht-phenotyping in viticulture	153
Z. GERGELY J. BEKE: A micro-controller-based algorithm for fast and robust edge detection in white paprika sorting process	161
L. TÓTH, N. SCHREMPF, J. BEKE: The situation of application of wind power plant in the world and in Hungary	170
F. SZIDAROVSKY, S. MOLNÁR, M. MOLNÁR, Cs. FOGARASSY: Modeling conflicting interests in a water distribution problem with game theory	180
L. MAGÓ: Cost and shift hours demand of transportation tasks in the field root vegetable production technology	192
T. RIEGLER, C. RECHBERGER, F. HANDLER, H. PRANKL: Characterizing quality of tillage by means of stereo vision	199
R. TÓTH, M. DARÓCZI: Simulation of grain harvesting	209
K. KOTROCZ, Gy. KERÉNYI: Investigation of soil-rigid wheel contact under three different circumstances using discrete element method	215

K. TAMÁS, J. RÁDICS, István J. JÓRI: Developing a precise soil model by DEM	223
P.V. R. KOVÁCS, S. BESZÉDES, L. LUDÁNYI, C. HODÚR, G. KESZTHELYI-SZABÓ: Energetic investigation of microwave treatment	233
I. M. DAL FABBRO, C. DE ALMEIDA, J. GAZZOLA: Elastic behavior of sunflower (<i>Heliantus annuus</i>) seeds under constrained compression	241
T. ANTAL, B. KERÉKES, L. SIKOLYA: Physical properties of freeze dried vegetables by different thermal and chemical pre-treatments	250
Gy. CSIMA, E. VOZÁRY: Effect of measure settings on creep-recovery test results of candy gums	260
T. BAROSS, L. JÁNOSI, Á. KREJCZINGER: Development of a compensator element for the ITER core CXRS diagnostics	269
L. JÁNOSI, V. ERDÉLYI, E. SÁRKÖZY: Development of process control for small scale biodiesel production plant	277

Institute for Mechanics and Machinery



Professor Dr. István SZABÓ,
Director of the Institute

Dear Reader,

The Institute of Mechanics and Machinery has been known for integrating fundamental engineering disciplines in the fields of classical mechanics, design, computer aided technologies, and machine constructions. Today it consists of three scientific and educational units:

- – Department of Mechanics and Technical Drawing
- – Department of Machinery
- – Department of Agricultural and Food-industrial Machines

IMM has got two external departments : Department of Biotechnics hosted by Oncotherm Ltd., and Department of Farm Machinery set up by the National Institute of Agricultural Engineering.

The Institute is also housing the Computer Aided Engineering Center, a research facility to cover wide range of IT technologies that are linked to mechanical engineering procedures.

Courses provided by our staff covers a wide range from basic engineering areas (e.g. computer aided drawing, statics, strength of materials etc.) to more specialized domains at all levels of studies.

In recent years, the Institute's research capacity has been increased and many advanced research and development projects have been undertaken in collaboration with local industries and internationally renowned organizations.

Activities are concentrated around the following key areas of engineering fields:

- Biomechanics
- Applied engineering numerical methods
- Computer based modeling and analyses
- Advanced methods in engineering design
- Energy purpose biomass production
- System Engineering and machinery management

I am convinced that selected papers published in the following pages may give some impression of the scientific activity and the researchers' interest at the Institute for Mechanics and Machinery.

Dr. Istvan Szabó
Director

Discrete element model of particle outflow

István OLDAL, Ferenc. SAFRANYIK
Department of Mechanics and Technical Drawing,
Institute for Mechanics and Machinery

Abstract

The outflow properties of silos depend on the properties of the stored granular material and on the silo design. Several empirical and analytical model are used to determinate the discharge rate of silos. Any analytical model is unable to predict the discharge rate in case of mass flow with acceptable accuracy. The aim of our work is to create a numerical model, which can determine the discharge rate of wheat in a case of funnel flow and also in case of mass flow.

Keywords

silo, DEM, discharge, flow patterns, discharge rate

1. Introduction

Granular materials have great importance in almost every field of the industry. The transportation and handling of agricultural products, comestibles, compounds, chemicals and minerals have special needs that have to be taken into account as well as the design of the connected apparatuses. Silos are used by food industry, agriculture, mining and pharmaceutical industries for storing granular materials. The solution of the upcoming problems regarding the discharge of silos (design of the connecting apparatuses, stop of mass flow, etc.) can result serious cost decrease during the design of a new or re-design of an existing silo.

The fundamental conditions of applicability of silos are the possibility of the discharging and the knowledge of the discharge rate (in view of design of the connecting apparatuses). It can be that the material flow is stopped because of stable arching. Arching means the formation of a material layer in the granular material which is capable to bear the load arising from the material above. The appearance of arches holds up the flow of granular material (e. g. the discharge of silo) and results overload on the silo walls (Keppler, 2009). During designing of silos we have to take into consideration the properties of stored granular materials, therefore we can avoid the stop of discharge. Because of their special mechanical behavior the discharge of granular materials differs from the discharge of liquids. In case of fluids, the flowing velocity changes with fluid level, in case of granular materials, the velocity and the discharge rate are constant (independent of the filling level of silo).

The outflow properties of silos depend on the properties of the stored material and on the silo design. For this reason this has long been a subject of interest to both researchers and process engineers (Langston et al., 1995). The geometry and the surface conditions of the bin and the properties of the stored material define the flow pattern. In general the silos are classified in two different types: mass flow and funnel flow (Janssen, 1895).

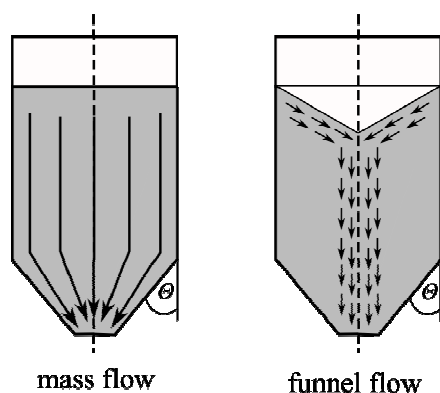


Figure 1. Flow patterns

In a mass flow silo all of the granular material moves when the silo is discharged, the material that enters the silo first is discharged first (this is a “first in, first out” behavior). In a funnel flow design the movement of the material is confined to the vertical region in the center of the silo, the material that enters first is discharged last (Janssen 1895). In case of a funnel flow silo stagnant zones are near the silo walls, where the particles flow slowly or there are stagnant. In extreme cases the silo may not empty completely under the force of gravity.

One of the first studies of granular flow in silos was based on a continuum model by Janssen (1895). His results showed that the pressure on the bottom of the bin is independent of the filling level. Therefore Janssen’s theory (1895) predicts that the discharge rate is independent for the filling level. Significant efforts have been made since Janssen’s work to determine the discharge rate of a silo using experiments. Thus several theories were forming to determinate the discharge rate of silos:

- For cohesionless granular materials:
 - Hagen model (Hagen, 1852),
 - Beverloo model (Beverloo, 1961),
 - Johanson model (Johanson, 1965),
 - Zanker model (Zanker, 1975),
 - Gjavec-Keller model (Gjavec and Keller, 1984),
 - British Standard (British Standard, 1991),
 - Oldal model (Oldal et al., 2012).

- For cohesive granular materials:
 - Janssen model (Janssen, 1895),
 - Carleton model (Carleton, 1972).

From the above Beverloo’s empirical and Oldal’s analytical model can be used in particular circumstances. The difference between other models and measurements is too significant, consequently the other models are unable to determine the discharge rate with acceptable accuracy (see Fig. 2).

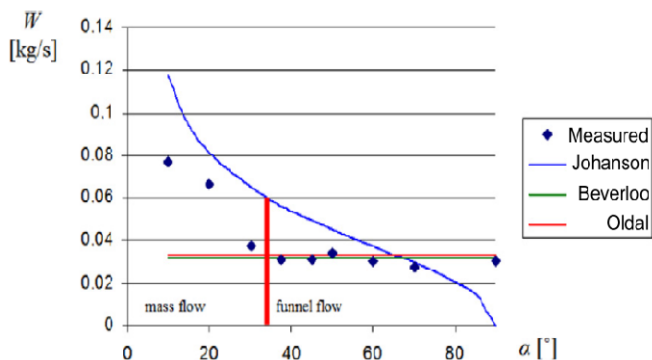


Figure 2. Measured and predicted discharge rate (Oldal et al., 2012)

2. Material and method

In this paper a new numerical model for modeling the silo discharge is proposed. This model was made by Discrete Element Method. We used this method because none of the analytical models are able to describe the process in non-stationary case but a DEM model is suitable for describe the whole discharge process, still in case of emptying bin. The Discrete Element Method (DEM) is a numerical technique for modeling the static and dynamic mechanical properties of the granular materials. The method is based on the simulation of the motion of granular materials as separate particles and involves the movement of all particles and detection their collision with other particles and with their environment (Cundall, 1979). DEM is commonly used in many fields of engineering such as in the pharmaceutical, mining, food industries or agriculture. In agriculture this is commonly used to define the behavior and motion of granular materials in dryers or in silos and hoppers, such as flow patterns, segregations, and discharge rate. The method is continually developed and the experimental studies are also now gone on. Relying on previous models we established a new numerical model of silo discharge.

Our work is based on laboratory outflow experiments and simulations. We were making simulations and outflow measurements with wheat. To validate the numerical model, we were creating model silos. The mass of the discharged wheat was measured by three load cells. The measurements were repeated five

times in case of every model silo. The goal of the measurements was the determination of the amount of outflowing wheat as a function in time. The mass change functions were determined by also the simulations and these were compared with the measurement results. The aim of the experiments was the validation of DEM model. The aim of our work is to create a numerical model, which can determine the discharge rate of wheat in a case of funnel flow and also in case of mass flow and to validate that the micromechanical parameters of wheat which validated for mixed flow dryer (Keppler et al., 2012)0 are suitable for modeling silo discharge.

DEM has been used by different authors to study the outflow properties of silos such as pressure distribution (Goda and Ebert, 2005, Gonzalez et al., 2012), flow patterns (Ketterhagen et al., 2007, Gonzalez et al., 2012), flow velocity (Gonzalez et al., 2012), and segregation processes (Ketterhagen et al., 2007).

All simulations were undertaken using EDEM Academic 2.4 (2012) discrete element software. To modeling the outflow of wheat was used the Hertz-Mindlin no slip contact model with the following micromechanical parameters for the description of the interaction between particles (Keppler et al., 2012):

Table 1. Micromechanical parameters of wheat

Material	ν [-]	G [MPa]	ρ [kg·m ⁻³]	C_{rw} [-]	C_{rs} [-]	μ_{0w} [-]	μ_{0s} [-]	μ_{rw} [m]	μ_{rs} [m]
Wheat	0,4	$3,58 \cdot 10^8$	1430	0,5	0,6	0,3	0,25	0,01	0,01
Steel	0,3	$8 \cdot 10^{10}$	7500	0,6	-	0,25	-	0,01	0,01

The particle model has been created as the clump of three spheres, having radiuses 1,5 mm and 1,25 mm respectively. The distance between the centers of the spheres on the edges was 1,5 mm (see Fig. 3).

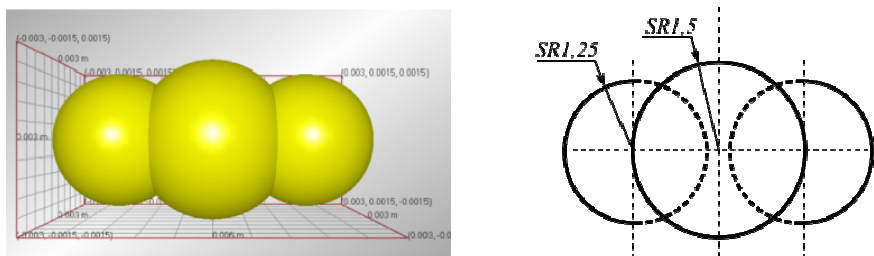


Figure 3. Particle model of wheat (Keppler et al., 2012)

We used in present wok two geometrical models. The geometrical model was a cylinder with a diameter of 200 mm and conical bin with outlet diameter of 60 mm and the cone half angle 30°. The second geometrical model was a same

cylinder but the cone half angle of the bin 60° . In all cases a virtual volume was created, which was the same shape and in the same position with the geometrical models.

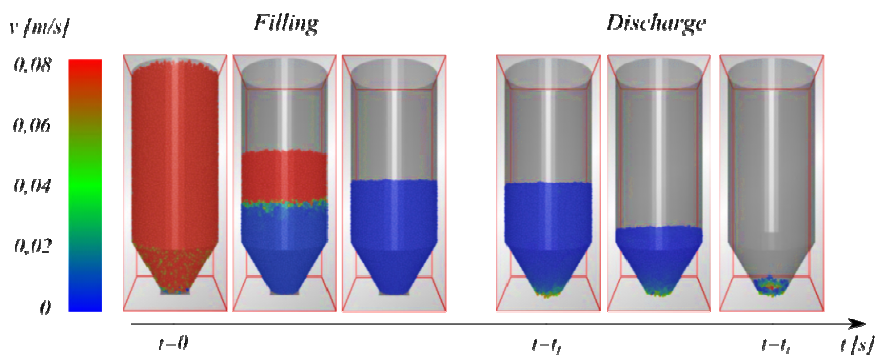


Figure 4. Steps of the simulation process

In the simulation process the first step was the generation of all of the particles, these were generated randomly in the virtual volume. The generated particles were allowed to fall under gravity; this step was the filling of silo. During the filling process the outlet of the silo was closed. The next step was the emptying of the silo. When the particles reach a static state then the outlet of the silo was opened and all of the particles were discharged. To the end of the filling process the bulk reaches a static state (his energy of motion is about zero). On the Fig. 4 the particles were painted according to their vertical velocity. Vertical velocity of the blue particles is minimal and the vertical velocity of red particles is maximal.

3. Results and discussion

Based on the results of experiments the mass of the discharged material in function of time can see on Fig. 5/a. As we expected the mass-change functions are linear in all cases. This means, that the discharge rate is constant, since this is the slope of the linear. Consequently the discharge rate is independent of the filling level of silo.

Similarly to the experiments we determined the mass-change functions based on the simulation results. In case of all simulation the mass-change functions are also linear. This means that the new numerical model is suitable for right modeling this physical phenomenon (see Fig. 5/b).

The average discharge rates of simulations were compared with measurements results. The difference between the numerical model and measurements are by both bins less than 5% (see Fig. 6). So the discharge of wheat can be on a suitable manner modeled.

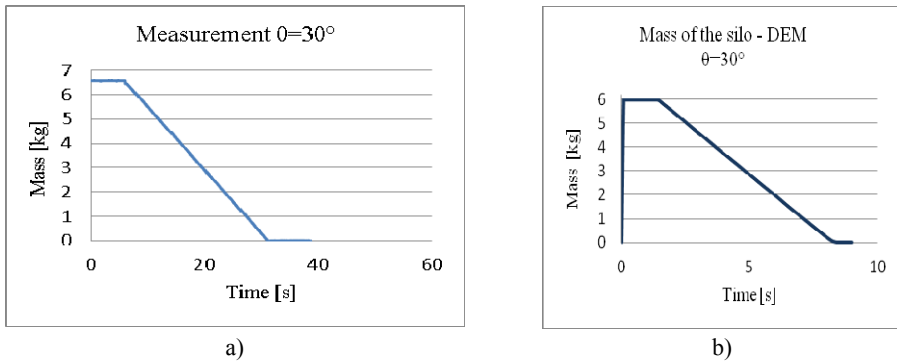


Figure 5. Mass-time functions

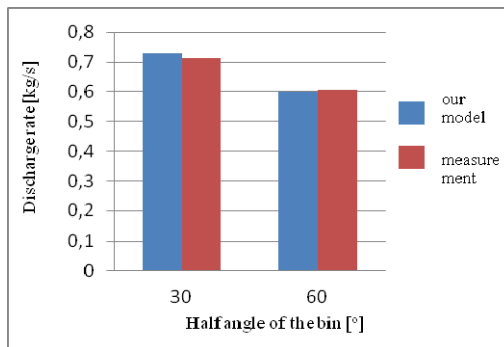


Figure 6. Average discharge rates

On Fig. 5. can be seen the section of the silo during the discharge process. The particles were painted according to their vertical velocity. Vertical velocity of the blue particles is minimal and the vertical velocity of red particles is maximal. As we expected the flow mode is mass flow in case of 30° bin half angle (see Fig. 7/a) and in case of 60° bin half angle (see Fig. 7/b) is funnel flow.

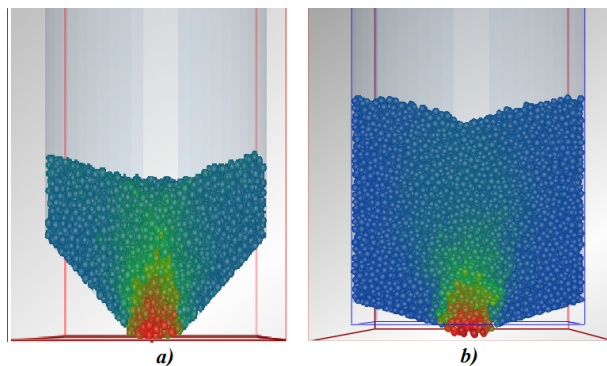


Figure 7. Flow patterns in simulation

Conclusions

A new numerical model for silo discharge of wheat was created which is suitable for description the outflow process with an adequate accuracy. In case of all simulation and all measurements the mass-change functions are linear. This means that our new numerical model is suitable for right modeling this physical phenomenon. Based on the results of the simulations the flow mode is in accordance with the expected: we got in case of a bin with a half angle 30° mass flow and in case of a bin with a half angle 60° funnel flow. The discharge rate is in good agreement with reality (the difference is less than 5%) in case of both bins. With the numerical model the whole discharge process can be described. None of the analytical models are able to describe the process in non-stationary case. With the numerical model the whole discharge process can be described, still in case of an emptying bin. None of the analytical models are able to describe the process in this non-stationary case. The particle model and the micromechanical parameters of wheat which are validated for a mixed flow dryer are suitable for modeling also the silo discharge.

Nomenclatures

C_r	coefficient of restitution	-
G	shear modulus	MPa
W	discharge rate	kg/s
<i>Greek letters</i>		
ρ_h	density of the bulk material	kg/m ³
ν	Poisson's ratio	-
μ_0	coefficient of static friction	-
μ_r	coefficient of rolling friction	m
θ	half angle of bin	°

Acknowledgement

Financial support from TÁMOP 4.2.1.B-11/2/KMR-2011-0003 and the Bolyai Scholarship of the Hungarian Academy of Sciences is gratefully acknowledged by Istvan Oldal Ph.D.

References

- [1] Beverloo, R. (1961), The flow of granular solids through orifices, Chemical Engineering Science 15 (262), pp. 260-269.
- [2] British Standard Summaries (1991), BS5502: Part 74: 1991. Building and Structures for Agriculture. Design and Construction of Bins & Silos for Combinable Crops.

- [3] Carleton, A.,J. (1972), The effect of Fluid-Drag Forces on the Discharge of Free Flowing Solids from Hoppers. *Powder Technology*, Volume 6, pp. 91-96.
- [4] Cundall, P; Strack, O. (1979), A discrete numerical model for granular assemblies. *Geotechnique*, Volume 29, Issue 1, pp. 47-65.
- [5] Gjacev, L., V., Keller, H. (1984), Grundlagen einer Theorie zum Schüttgutaussfluss aus Bunkern und einige Ergebnisse ihrer experimentellen Überprüfung. *Wissenschaftliche Zeitschrift der Hochschule für Architektur und Bauwesen Weimar*, Vol. 30. pp. 269-272.
- [6] Goda, T.,J., Ebert, F. (2005), Three-dimensional discrete element simulations in hoppers and silos. *Powder Technology* 158, pp. 58-68.
- [7] Gonzalez-Montanello, C., Ramírez, A., Fuentes, J.,M., Ayuga, F. (2012), Numerical effects derived from en masse filling of agricultural silos in DEM simulations,. *Computers and Electronics in Agriculture* 81, pp. 113-123.
- [8] Hagen, E. (1852), Druck und Bewegung des trockenen Sandes. Bericht über die zur Bekanntmachung geeigneten Verhandlungen der Königlich Preußischen Akademie der Wissenschaften zu Berlin 1852, pp. 35-42.
- [9] Janssen, H.,A (1895), Versuche über Getreidedruck in Silozellen, *Zeitschrift des Vereines der Deutschen Inegniuere* 39, pp. 97-123.
- [10] Johanson, J.,R, (1965), Method of calculating rate of discharge from hoppers and bins, *SME of AIME, Transactions* 232, pp. 69-80.
- [11] Keppler, I. (2009), Arching in silos, a new model, *Bulletin of the Szent István University, Gödöllő* 1, pp. 331-342.
- [12] Keppler, I., Kocsis, L., Oldal, I., Farkas, I., Csatar, A. (2012), Grain velocity distribution in a mixed flow dryer, *Advanced Powder Technology* 23, pp. 824-832.
- [13] Ketterhagen, W.,R., Curtis, J.,S., Wassgren, C.,R., Kong, A., Narayan, P.,J., Hancock, B.,C. (2007), Granular segregation in discharging cylindrical hoppers: A discrete element and experimental study, *Chemical Engineering Science* 62, pp. 6423-6439.
- [14] Langston, P.,A., Tüzün, U., Heyes, D.,M. (1995), Discrete element simulation of granular flow in 2D and 3D hoppers: dependence of discharge rate and wall stress on particle interactions, *Chemical Engineering Science* 50 (6), pp. 967-987.
- [15] Oldal, I., Keppler, I., Csizmadia, B., Fenyvesi, L. (2012), Outflow properties of silos: The effect of arching, *Advanced Powder Technology* 23, pp. 290-297.
- [16] Zanker, A. (1975), Estimating the flow of solids through openings. *Process Engineering* (July), pp. 66-67.

Discussion of the Jean Pain's method

László BENSE

Department of Agricultural and Food-industrial Machines,
Institute for Mechanics and Machinery

Abstract

Jean Pain described an integrated method of biomass utilization in the 70s. The method is based on the simultaneous heat utilization of forestry waste compost stacks and the utilization of deponia gas. The method was working, but it did not spread because it needs significant work effort. The increasing demand for renewable energy utilization is the cause why the Jean Pain method has to be examined again. Especially because increasing number of environmentalists claim that this method is the only real possibility for biomass utilization. These organizations do not support the firing of biomass and they have doubts about energetic purpose biomass utilization as well. In my work I analyze the generalization of the method.

Keywords

renewable energy sources, biomass, Jean Pain's method

1. Introduction, the origin of Jean Pain's method

Jean Pain was not an agronomist or a researcher. In a period of his life he was a forest guard at a dry countryside. The forest fires progressively destroyed the landscape. As an outsider Jean Pain did not understand why weather has such a negative impact on those mediterranean woods which survived centuries of fires. He found out that burning of underwood causes the destruction of trees. In the feudal times the rural population could collect the waste bushes and wood. If the underwood is rare, the fire does not cause significant damage in the forest. After the 2nd World War the foresters were responsible for cleaning the woods. Jean Pain encountered with the exploited wood, and he had to utilize it somehow.



Figure 1. The initial idea

He knew that the underwood is part of the ecological system, which cannot be regularly removed from the forest. He found that it is optimal if the waste returns back to the forest after composting. He made significant experiments with bush compost: he used it like a soil, for biogas production and for producing hot water with heat exchangers.

2. Extension of the Jean Pain's method

Jean Pain did everything to handle his experiments as a standardized method. He heated his house with the waste heat of the compost and produced electricity with a gas aggregate.

He drove his van with his own produced uncleaned biogas.

The Jean Pain Association was formed in Belgium. It worked on the method with governmental subsidy for a while.

At this time at the Londerzeel estate hot seed beds and glass houses were heated with compost. The students of Gent Technical University measured the produced heat amount of a compost pile. They have found that the water produced energy amount is bigger than the difference between raw and fermented composted heat amount.

This contradicts to the first law of thermodynamics, so the results were not published.

In the public mind, it is stated, that bigger amount of heat can be derived from a pile of compost than its heating value.

As the amount of animals is decreasing in the world, with it the value of organic manure is decreasing too. It seems that firing of biomass is wasting of natural nutriment.

With composting heat energy can be gained whilst the waste becomes valuable material, and biogas can be gained as well.

Nowadays this process is applied as well to produced biomass and it is believed that it is the only CO₂ free utilization method of it. The Jean Pain method is generalized.

3. Discussion of the Jean Pain's method

Jean Pain proved with his experiments that his method is working at self-sufficient farms. In a city a big pile of compost, a gas collector and a heat exchanger tube is not easy to handle, the situation is not realistic. The system is sustainable, but it might be that we are not on the good route of environmental friendly solutions.

First of all: biomass degradation goes with CO₂ disengage. So does composting as well. The firing of biomass (from energy plantations); composting and biogas development are similar if we think about how long the CO₂ was tied.

The amount and content of glasshouse gases can be adjusted with changing of the raw material. The most important factor is the nitrogen proportion. In case of nitrogen surplus ammonia appears; in case of relative nitrogen shortage the multiplication of microorganisms is starting slowly. The unnecessary carbon quits as CO₂. The optimal C/N proportion would be 35:1, at bush compost it is between 200 and 300, which is unsuitable for producing compost.

At composting the biodegradation is made by aerob microorganisms. At the beginning of the degradation 1 m³ oxygen is used up in 2 hours. This means that the pile must be loose, which can be reached with structured material or with often mixing. The heat exchanger in the pile obstructs the mixing, so artificial ventilation has to be installed. According to Jean Pain, the inner temperature of the pile can stay above 60°C until 18 months, even in cold winter weather. But we must state that, the termophilic stage is 6-8 weeks, after it the prism is cooling, the pile even might freeze (See Fig. 2.).

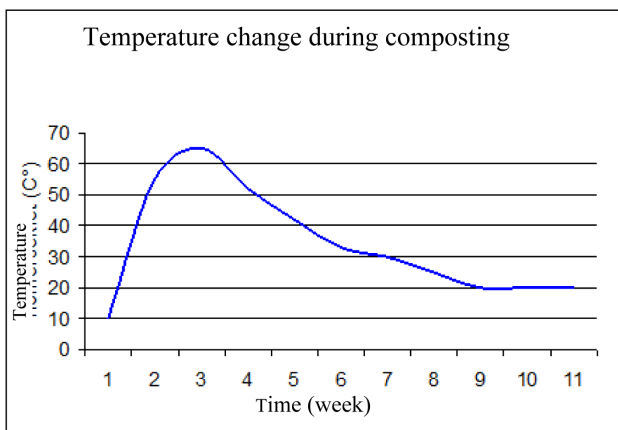


Figure 2. Inner temperature of compost pile

Sterilization on high temperature is an important effect. For this until 3-6 days the prism must be held on 55-65°C. If we take away heat from the compost then microorganisms, seeds and mushroom spores are not perishing, so the end product can only used with care as manure.

In reality Pain unfolded the pile in every 90 days and removed the heat exchanger. The half raw compost was used for covering the soil, because he knew that the organic material in the soil fires the stabilized compost as well. Under the mulch layer a rich structured soil is formed. The method can be used for decultivating of destroyed ecological systems.

The golden rule of economic biomass applies to every big quantity, but small value material: it should be utilized at the place of production, in its produced form with minimal work effort. In this case the last two demands do not injure. The translation costs were meant to compensate the cogenerated utilization of

deponia gas and waste heat. This can be an acceptable compromise, but the removal of the heat exchanger (Fig.3) makes the machinery almost impossible.



Figure 3. Installing a heat exchanger in a compost furnace

The method applies high work effort. At the before mentioned Londerzeel estate the load change was eased. The tubes of the heat exchangers were built in the concrete base. The soaked wood can be loaded form a tip cart. The heat transfer efficiency is wrong: to heat a 100m² house 15-20 m³ bush compost is needed instead of 10 m³. With developing the heat exchanger positioning 4-5 m³ could be enough. Because of the low temperature compost heating could be used only for ground and wall heating.

Conclusions

The case of biomass utilization should not be seen in black and white (as no other things as well). The conditions have to be taken into consideration and on the basis of them the optimal process can be chosen. Jean Pain's method is even good in the case of produced biomass to provide farms with energy. In the case of farms raw material can be collected and there is enough place for compost furnaces. Farms can utilize ripe compost as well, which is an additional cost in case of residential utilization. The method is also good for those communal companies who collect residential green waste. Glass houses and industrial buildings can be heated with compost heat and with deponia gas waste deliverer machines can be operated. The ripe compost can be sold as manure. For residential and plant usage biomass firing must be taken into consideration, but produced biomass should be used for that purpose, not waste material. This way the whole removal of biomass can be avoided, the price of biomass can be kept and biomass utilization will not influence the price food.

Acknowledgements

This research program is supported by TAMOP-4.2.1.B-11/2/KMR-2011-0003 (Improvement of Research and Education Standard of Szent István University).

References

- [1] Ida And Jean Pain: The methods of Jean Pain (Another kind of garden). 7th edition. Villecrose, France, 1980. National Library No. 10424.
- [2] <http://www.onpeutlefaire.com/ilslontfait/ilof-jean-pain-broussaille.php>
- [3] <http://www.eautarcie.com/hu/07d.html>
- [4] <http://alternativenergiak.hupont.hu/8/komposztkazan#ixzz2X8eM1lpi>
- [5] Czupy I, Vágvölgyi A: Mezőgazdasági (növénytermesztés, állattartás, erdészeti) hulladékok kezelése és hasznosítása. http://www.tankonyvtar.hu/hu/tartalom/tamop425/0021_Mezogazdasag_hulladekai/adatok.html
- [6] Bense L, Nagy I: Szántóföldi favágók. *Agrofórum*, 2012. 4: 138-141. ISSN 1788-5884.
- [7] Bense L, Fenyvesi L, Pazsiczki I, Szabó I, Szendrő P: Investigation of the dependence of dynamics of biogas production at maize silage as an additive row material. *Mechanical Engineering Letters*, 2012. vol. 7:47-52. HU ISSN 2060-3789. CD-ROM ISSN 2060-3797.
- [8] Bense L: Az energianád hasznosítási lehetőségei, és európai termesztésének technológiája. „Kistélepülések komplex energetikai fejlesztését támogató program létrehozása” című projekt. Szakmai nap, Gödöllő, 2011. 12. 16.
- [9] Bense L, Percze A: Égetnivaló energianád. *Haszon Agrár Magazin*, 2010, 10: 31-33. ISSN 1788-5922.

Surface description with LASER light

Attila LÁGYMÁNYOSI¹, István SZABÓ¹, László BENSE²

¹Department of Machinery, Institute for Mechanics and Machinery

²Department of Agricultural and Food-industrial Machines,

Institute for Mechanics and Machinery

Abstract

In this article a 3D imagery based evaluation method is presented which provides with an opportunity to measure the above mentioned tyre, chopped materials and soil surfaces with a relatively low calculation- intensive method compared to other, conventional 3D imagery techniques. Basic implements of the measurement are a digital camera as a recorder and some different laser light source with which was selected upon the aims this study. For data processing LabView and Matlab software were used.

Keywords

image processing, 3D surface analysis, Computer-Aided Engineering

1. Introduction

Both in industrial and agricultural areas one can find many instances where certain features of an object are determined by surface geometrical measurements. Typically, in these cases a sort of surface terminal layer is evaluated. For example at the examination of objects exposed to abrasion like tyre tread. In agriculture the surface scragginess is evaluated in case of soil surface, distribution of clods or describing chopped materials.

These evaluations are mainly based on measuring geometrical parameters. Beside several other possibilities, the solutions provided by image processing are also used to measure them.

3D imagery based geometrical measurements are a special group of image processing. It provides with good solution for measuring and describing tyres, chopped materials and soil surfaces. Due to the large amount of data provided by the 3D imagery numerous mathematical operations are required during the processing. These measuring methods are often time-consuming, so accelerating techniques are under development. A possible solution for that is to use such algorithms which filter out from the data set of the 3D image only the absolutely necessary data. After that the measuring algorithm uses purely the pre-filtered data.

In case only the necessary data are recorded during the 3D imaging originally then the 3D image needs not be created as total so the speed of the evaluation processes can be further increased.

In this article a 3D imagery based evaluation method is presented which provides with an opportunity to measure the above mentioned tyre, chopped materials and soil surfaces with a relatively low calculation- intensive method compared to other, conventional 3D imagery techniques. Basic implements of the measurement are a digital camera as a recorder and some different laser light source with which was selected upon the aims this study. For data processing LabView and Matlab software were used.

2. The applied system and materials

The applied equipments

Throughout the experiments was used two industrial digital cameras type were Basler SCA640 and SCA 1390. The main technical parameters were: color video format 70fps and 17 fps with Ethernet connection. The applied computer was a PC with the following features: I7 quad processor, 6Gb memory, graphical subsystem with 1Gb memory. The connection between the scanner cameras and computer was 4channel high speed gigabit Ethernet interface. The used software for imaging and postprocessing was Matlab, LabView and the Ms_Excel.

The 3 investigated object were the car tires, soil with inhomogenous surface and woodchips like as a chopped material.

The investigated materials

The examined material were some mixed soil, woodchips and car tires:



Figure 1. Examples to investigated materials: soils, woodchip and tires

The applied methods

During the imaging experiment the special line LASER lighting was applied. Besides the “scanner’s” cameras get any additional light from the background lighting which was a minimal influence on setup period. After the background lighting was turn of while the scanning was. Surface was always normalised to ensure that its unevenness only relates to size irregularities of respective elements. In that cases the scanning method will not produce a complete model of the subject. This is the main feature for the applied method. The tire imaging was used by rotated object. The soil imaging was used with moving laser line. The woodchips imaging was made with the moving sampling holder box.

With the soil and woodchips samples used for recording were placed in boxes where multiple layers of cover was ensured. In that cases were thoroughly mixed the sample materials and placed in the boxes with their surface. All sample groups were re-recorded 3 times.

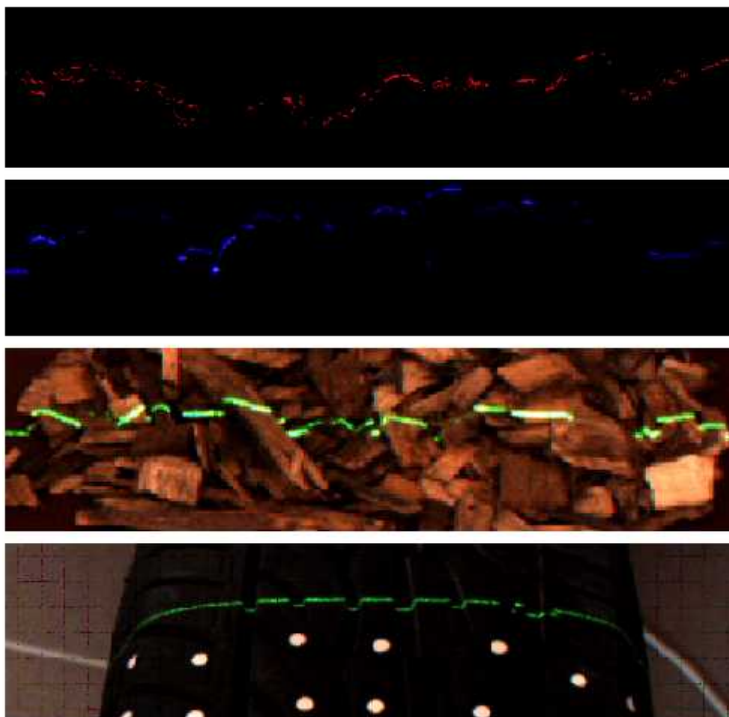


Figure 2. Some example of image recording with the different object, used 3 types of LASER light source

The figure 2. present the different situation with lighted background and the full dark background measuring methods. To the postprocessing work the full black background was applied, because in these cases the data point more easier come out from the background picture points.

Figure 3. is basically a representation of the points on the surface of the object sample. Examining like a 2D slice matrix of the 3D matrix allows us to get a cross-section of the scanned material set. These measured data represent a cross section is perpendicular to the surface of the set, we get a cross cut image of the original object surfaces. Thus the visible range of dots is given by the cross cuts of parallel planes perpendicular to the plane of the surface. The recorded data in case of soil surface and the woodchip presented same dispersion of the images, only the physical sizes were different. From this it can be observed that a given set can be characterised only by a given probability distribution as individual element size can be assessed only statistically.

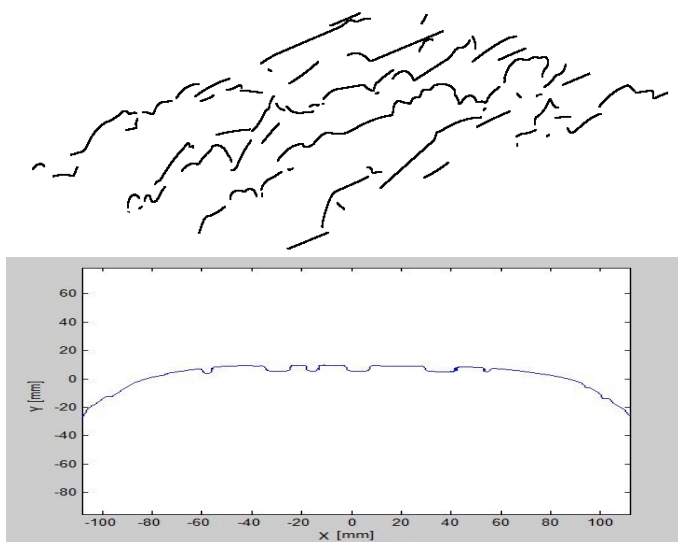


Figure 3. The recorded cross section point of woodchip surface and tire (recorded data)

3. Measurements and results

From this method to it can be observed that a given set can be characterised only by a given probability distribution as individual element size can be assessed only statistically in case of soil surface and woodchips investigation. In the case of tire investigation this method completely useful to describe and to determine the profile.

An example of the statistically description

Figure 4 shows the distribution of measured points for the three size classes after sampling and averaging. From the figure it can be observed that in the smallest size class the number of dots at a certain depth surpass 2500 and that more than 90% of the dots are located between the values of 7 and 16 mm's. In the case of the next size class the occurrence is spread to the range of 5-19 mm's and the

most frequent values are under 2000 elements. For the largest size class the maximal individual element number stays under 500 and has the widest spread.

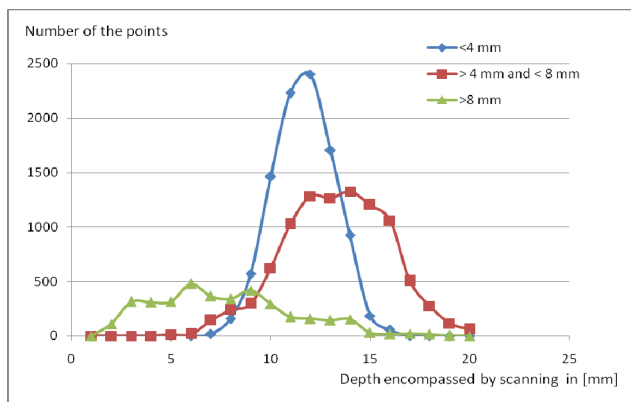


Figure 4. Number of points averaged for the woodchips size classes (a chosen example)

Thus, after examining the range of the spread of the dots characterising the cross cuts the following values are obtained:

- <4 mm –class: 10 mm
- >4 mm és <8 mm –class: 15 mm
- >8 mm class: 19 mm.

An example of the tire profile description

In this example a cross cut image of the original set. ‘X’ and ‘Y’ axes scale are in [mm]-scale and x = 0 is the geometrical center.

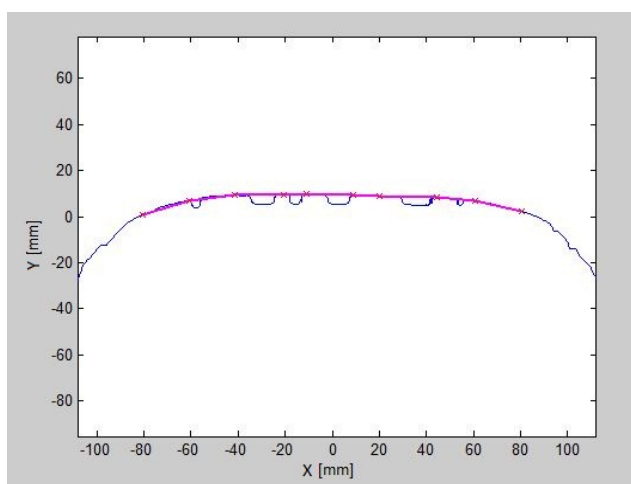


Figure 5. The recorded tire profile and the calculated and fitted curve

With an algorithm found the local maximum values from an interval. The interval size was 20 mm, because this is the upper limit for the largest groove in the surface. The program was then used to fit a curve to the local maximum points. This curve is a fifth degree polynomial, it's the simplest curve that gives a sufficiently good fit.

The program was used afterwards to determine the location of the center of the profile, the half of the depth of the middle groove and moved the polynomial to that point. The points above the curve were useful, the points under the curve were useless. The useful points are where the tire connects with the ground.

In the other case when for the better perception was modified the scale from 1:1 to 8:1 in the 'Y' axes got back better figures.

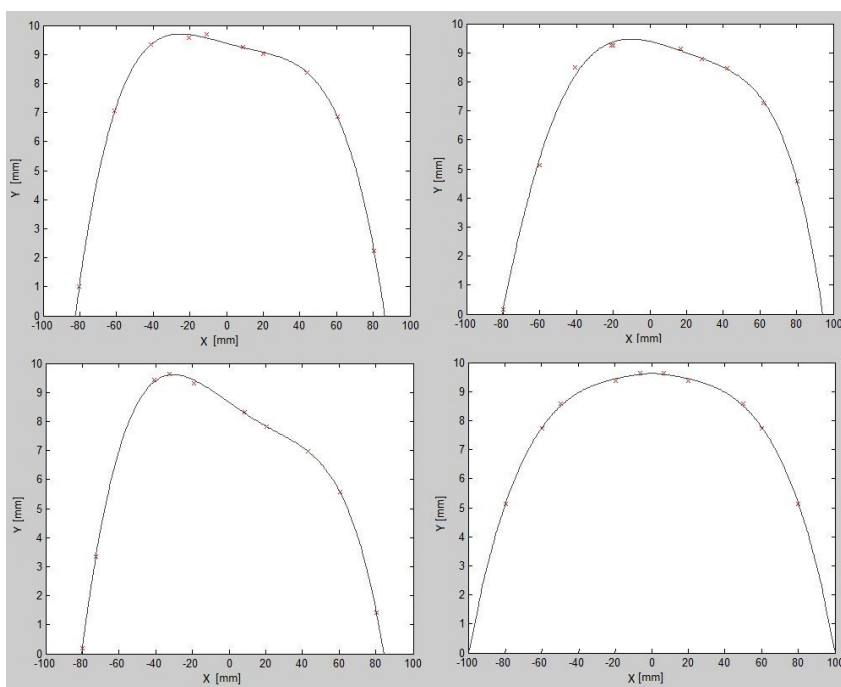


Figure 6. The abrasion on the different tires, with enlarged representation

The above figures well demonstrate the effect of abrasion. The figures show the fitted polynomials for the respective tires. It is well demonstrated that Profile C shows the worst condition and Profile D is from a new tire.

Conclusions

Summarising the results, we can state that the images of woodchips and soil surface description the recorded imaging procedure can provide a valuable

starting point to draw conclusions on the size of surface scragginess in the examined material set. This relationship can be demonstrated. The ongoing research is expected to provide applicability in a broader size spectrum by further refining and modifying the applied methodology. The applied method provide an image processing procedure, without 3D imaging as this would result in a real-time industrial applicability by making evaluation faster and simpler.

In the case of tire description the developed mathematical model the abrasion of the tire can be examined in detail and can be used to indicate abnormal abrasion. The ongoing research is expected to provide applicability in a broader size spectrum by further refining and modifying the applied methodology. The applied method provide an image generation to 2D, without 3D imaging as this would result in a real-time industrial applicability by making evaluation faster and simpler.

Acknowledgements

This paper was sponsored by TÁMOP-4.2.1.B-11/2/KMR-2011-0003 project

References

- [1] Bernardini, F. and Rushmeier, H.E. (2002): The 3D Model Acquisition Pipeline, *Comput. Graph. Forum* 21 (2): 149–172. DOI:10.1111/1467-8659.00574
- [2] Bense L, Szendrő P, Vincze Gy (2006): Theoretical Questions of Burning-Purpose Use of Wood-Chips Congeries. *Hungarian Agricultural Engineering*, 2006, 19. 20-22.
- [3] Szalay D. K. (2011): A terepi és laboratóriumi spektroradiometria szerepe a légi hiperspektrális technológiában. XVI Fiatal Műszakiak Tudományos Ülészaka, Kolozsvár, Románia 2011.03.24-25. 305-308 pp.

Institute for Mathematics and Informatics



Professor Dr. Sándor MOLNÁR
Director of the Institute

Dear Reader,

The Institute for Mathematics and Informatics consists of the following three departments: the Department of Mathematics (dept. head: Prof. Dr. Zoltán Varga, the Department of Informatics (dept. head: Prof. Dr. Sándor Molnár) and the External Department of Applied Informatics (dept. head: Prof. Dr. András Edelmayer) which is located at the Computer and Automation Research Institute of the Hungarian Academy of Sciences (MTA SZTAKI). Our research activities in the last year (2012) were as follows.

Department of Mathematics

In the years 2012-13, the second and third years of an on-going four-year research project on “Dynamic modelling of stage-structured multi-species population systems”, funded by the Hungarian Scientific Research Fund (OTKA), have been successfully closed, boosting with 20 published scientific articles mostly in leading international journals, coauthored in international cooperation, with a cumulated impact factor 27,5. A PhD thesis entitled „Energetically-based control of a solar heating system” has been successfully defended, and in related topics papers with a total impact factor 6.5 have been published. Further papers have been published in the fields of epidemic models with delay, Fourier analysis, game theory, demographic background of pay-as-you-go pension systems and didactics of mathematics.

Department of Informatics

The Department has focused its research efforts primarily on linear systems theory. Energy and environment modeling remains a field of interest, sustainability in macroeconomic models is one of the new topics under investigation. Besides a new PhD thesis being prepared on the application of artificial neural networks in geostatistical processes, the other relevant focus of activities is applied research in the fields of embedded measurement, control and communication systems, signal processing, detecting and control algorithms.

External Department of Applied Informatics

The Department focuses on control and systems theory and its applications, especially fault detection, distributed networking, advanced filtering. Another direction of research is vehicle control, fleet management in real life traffic situations, and intelligent metering in power systems.

Depletable Resources in Economic Models

Márk MOLNÁR², Sándor MOLNÁR¹, József MOLNÁR²

¹Department of Informatics, Institute of Mathematics and Informatics

²Institute of Economics, Szent István University

Abstract

After giving a brief overview of economic modeling of exhaustible resources we present a possible approach of modeling depletable resources and economic growth. We highlight the importance of energy efficiency and energy saving measures while providing background for economic growth through the extension of the Solow-model.

Keywords

energy efficiency, economic modeling, sustainability, depletable resources

1. Introduction

The first step towards the comprehension of the role of natural resources in economic issues – and indirectly sustainability – was taken by Malthus in 1798 whose main concern was about the growing population of Britain and the finite supply of land. In 1865 Jevons provided some insights on sustainability while studying the finite coal supplies and the growing energy need of Britain. A major step in this line was the research of Hotelling (1932) who has provided the foundations of the economic analysis of finite resources.

In 1972 Meadows considered the sustainability of our civilization given the physical limits of the planet's resources to provide inputs to production and dealing with the waste products thereof. The general concern raised by Meadows was that we can run out of resources, and this inspired economists like Dasgupta and Heal ("The Optimal Depletion of Exhaustible Resources" 1974), Solow (1974), and Stiglitz („Growth with Exhaustible Natural Resources: Efficient and Optimal Growth Paths", 1974) to develop new ideas and models on economic growth when a depletable natural resource, together with human-made capital, is a significant input to aggregate production. Their additions to the theory of nonrenewable resources was not followed intensively in the next decade but their significance in growth theories is everlasting.

In the following we outline a possible approach which underlines the importance of efficiency improvements in the economy.

2. Production function extended with energy use

We define the production function with the usual denotation as follows

$$Y = F(K, E, L) = K^\alpha E^\beta L^\gamma \quad (1)$$

where K denotes capital used, E the utilised (non-renewable) resources (e.g. fossile energy, etc), and L for labour used in production. It is assumed that the sum of factor productivity is $\alpha + \beta + \gamma = 1 \Rightarrow \gamma = 1 - (\alpha + \beta)$: $\alpha, \beta, \gamma > 0$, we have constant returns to scale. The production function is thus assumed to be a Cobb-Douglas function. Resource used is interpreted as the complete economy's primary energy demand, but it can be easily extended to the complete natural resource demand.

Further assumptions concern the dynamics of the respective factor inputs:

$$\begin{aligned} \dot{E} &= \varepsilon E \\ \dot{K} &= sF(K, E, L) - \delta K = sY - \delta K, \quad s, \varepsilon, n, \delta > 0 \\ \dot{L} &= nL \end{aligned} \quad (1b)$$

Energy utilisation and labour use (population is assumed to move together with labour) follows an exponential process, where ε and n are respectively growth rate of energy use and population, s denotes the rate of saving and δ the rate of amortisation. Following the mainstream, we use the labour intensive form of the production function, which we denote with $f(k, e)$ and derive as follows:

$$f(k, e) = \frac{F(K, E, L)}{L} = \frac{K^\alpha E^\beta L^\gamma}{L} = \frac{K^\alpha E^\beta L^{(1-(\alpha+\beta))}}{L} = \frac{K^\alpha}{L^\alpha} \frac{E^\beta}{L^\beta} = k^\alpha e^\beta, \quad (2)$$

where k and e denotes capital and energy use per worker:

$$k = \frac{K}{L}, \quad \text{and} \quad e = \frac{E}{L} \quad (3)$$

Let's now examine the time derived form of the labour intensive indicators. We can easily formulate, that

$$\dot{k} = \frac{\partial \frac{K}{L}}{\partial t} = \frac{\dot{K}L - \dot{L}K}{L^2} = \frac{sF(K, E, L) - \delta K}{L} - \frac{\dot{L}K}{LL} = sf(k, e) - (n + \delta)k, \quad (4)$$

using also (1) and (3). Energy use per capita is derived as follows:

$$\dot{e} = \frac{\partial \frac{E}{L}}{\partial t} = \frac{\dot{E}L - \dot{L}E}{L^2} = \varepsilon \frac{E}{L} - n \frac{E}{L} = (\varepsilon - n)e. \quad (5)$$

The above equation simply states that growth in per capita energy consumption is the difference of energy consumption growth of the society and

population growth. Let's now examine the time derived form of the production function, the dynamics of production:

$$\frac{\partial f(k, e)}{\partial t} = \alpha k^{\alpha-1} e^{\beta} \dot{k} + \beta e^{\beta-1} k^{\alpha} \dot{e} = \alpha \frac{k^{\alpha} e^{\beta}}{k} \dot{k} + \beta e^{\beta} k^{\alpha} \frac{\dot{e}}{e} = \alpha \frac{\dot{k}}{k} f(k, e) + \beta (e - n) f(k, e)$$

Utilising the RHS of (4) and (5) it is visible, that

$$\begin{aligned} \frac{\partial f(k, e)}{\partial t} &= (\alpha \left(\frac{sf(k, e) - (n + \delta)k}{k} \right) + \beta(\varepsilon - n)) f(k, e) \\ \frac{\partial \ln f(k, e)}{\partial t} &= (\alpha \left(\frac{sf(k, e) - (n + \delta)k}{k} \right) + \beta(\varepsilon - n)) \end{aligned} \quad (6)$$

Thus, we can deduce the following, energy consumption increases per capita production in our model economy. Output grows proportionally with the difference of energy growth and population growth, thus population growth does not automatically mean output growth (for example because larger share of the resources have to be allocated to self sustenance). The model economy can be put on a growth path only if energy use or resource use is continuously increased (efficiency improvement is not introduced in our model yet). We can deduce in a similar manner that the increasing population will imply an increasing energy demand which can not be met by production and which intuitively will be constrained by our natural resources. Similarly interesting question is if negative population growth can effect per capita production. Total production can be positively or negatively influenced depending on how elastic is our production function with respect to labour use. A target of research can be to analyse if modern society's decreasing population is in connection with per capita (energy) consumption maximalisation.

Introducing energy efficiency in the model

To analyse the problem of sustainability in depth we extend our model with (energy) efficiency, applying this as a multiplier on energy consumption. We consider this more important than labour intensive growth as from the beginning of the industrial revolution the economic development is based on automation and machinery thus our production is characterised increasingly with our energy consumption and labour is not a primary constraint. Labour intensity of production is decreasing even further with advanced computerised methods, production control, CAD and CAE, etc. As an example, in the past a design of a machine element took at least 100 engineer hours while nowadays a workstation can do this process with testing in a couple of hours without the need to produce a test copy.

Thus we introduce labour and energy (or resource) efficiency on the macro level, denoting these respectively with η_L and η_E . Energy efficiency can also be interpreted as the proportion of depletable/renewable energy used: the higher this ratio the more efficient an economy is, or the less non-renewable is required to produce a unit of output. This notation allows for a sufficient flexibility in

interpreting our results. Let's write the production function in the following form:

$$Y = K^\alpha (\eta_E E)^\beta (\eta_L L)^\gamma$$

$$\alpha + \beta + \gamma = 1 \Rightarrow \gamma = 1 - (\alpha + \beta) \quad (7)$$

It is to be noted that η -s are not thermodynamical efficiencies but simple multipliers indicating factor efficiency in an economically sound measure¹. Additionally the following assumptions are made:

$$\dot{\eta}_L = h_L \eta_L$$

$$\dot{\eta}_E = h_E \eta_E \quad (8)$$

showing that factor efficiencies change and improve (a logical postulate). We use the simplifying assumption that technological development improves labour efficiency and energy efficiency with constant rates, respectively (h_L , h_E). We assume that the amount of resources (energy sources, etc.) is finite, $E_0 = E_t$ in all t time periods. Notice that this does not mean the depletion of our energy reserves as this amount is available in each period but implies a constraint as an upper limit of energy use for the time being. Trivial solutions for the differential equations on labour and efficiencies are as follows:

$$L_t = L_0 e^{nt}$$

$$\eta_{L_t} = \eta_{L_0} e^{h_L t}$$

$$\eta_{E_t} = \eta_{E_0} e^{h_E t} \quad (9)$$

Log-linearising the production functions time derivative gives the following:

$$Y \rightarrow \ln Y$$

$$\frac{\partial \ln Y}{\partial t} = \alpha \frac{\partial \ln K}{\partial t} + \beta \left(\frac{\partial \ln \eta_E}{\partial t} + \frac{\partial \ln E}{\partial t} \right) + (1 - (\alpha + \beta)) \left(\frac{\partial \ln \eta_L}{\partial t} + \frac{\partial \ln L}{\partial t} \right) = \quad (10)$$

$$= \alpha \frac{\partial \ln K}{\partial t} + \beta h_E + \beta \cdot 0 + (1 - (\alpha + \beta))(h_L + n)$$

We denote with κ (don't mistake it with k) the ratio of capital to output:

$$\kappa = \frac{K}{Y} \Rightarrow \ln \kappa = \ln K - \ln Y \Rightarrow \frac{\partial \ln \kappa}{\partial t} = \frac{\partial \ln K}{\partial t} - \frac{\partial \ln Y}{\partial t}$$

¹ Correspondance between thermodynamical efficiency (η_{TD}), and productive efficiency (eg. η_E) can be easily achieved by applying the equation $\eta_L = 1/(1-\eta_{TD})$.

Substituting this into (10) yields:

$$\begin{aligned} \frac{\partial \ln \kappa}{\partial t} &= \frac{\partial \ln K}{\partial t} - (\alpha \frac{\partial \ln K}{\partial t} + \beta h_e + (1 - (\alpha + \beta))(h_L + n)) = \\ &= (1 - \alpha) \frac{\partial \ln K}{\partial t} - \beta h_e - (1 - (\alpha + \beta))(h_L + n) \end{aligned} \quad (11)$$

Utilising the identity $\frac{\partial \ln K}{\partial t} \equiv \frac{\dot{K}}{K}$, and using the definition of \dot{K} from (1) we get, that

$$(1 - \alpha)(s \frac{Y}{K} - \delta) - \beta h_e - (1 - (\alpha + \beta))(h_L + n) = \frac{\partial \ln \kappa}{\partial t} \quad (12)$$

If we examine the usual growth path then we require that the share of output and capital remains constant, thus the RHS of (12) is zero, then rearranging the equation to κ yields equilibrium capital:

$$\kappa_e = \frac{s}{\frac{\beta h_e}{1 - \alpha} + \frac{(1 - (\alpha + \beta))h_L}{1 - \alpha} + \frac{(1 - (\alpha + \beta))n}{1 - \alpha} + \delta} \quad (13)$$

The denominator is the weighted average of the two efficiency growth factors which we denote as h :

$$h = \frac{(1 - (\alpha + \beta))h_L}{1 - \alpha} + \frac{\beta h_e}{1 - \alpha} \quad (14)$$

Thus the equilibrium path of capital expansion is reduced to the following:

$$\kappa_e = \frac{s}{h + \frac{(1 - (\alpha + \beta))n}{1 - \alpha} + \delta} \quad (15)$$

It is well visible that changes in energy and labour intensity have significant impact and efficiency improvements reduce equilibrium capital intensity requirements. Let us now examine the per capita output change using

$$\frac{\partial \ln(y)}{\partial t} = \frac{\partial \ln(\frac{Y}{L})}{\partial t} = \frac{\partial (\ln Y - \ln L)}{\partial t} = \frac{\partial \ln Y}{\partial t} - \frac{\partial \ln L}{\partial t} = \frac{\partial \ln Y}{\partial t} - \frac{\dot{L}}{L} = \frac{\partial \ln Y}{\partial t} - n \quad (16)$$

and

$$\kappa Y = K \Rightarrow \ln K = \ln \kappa + \ln Y \quad (16b)$$

Substituting the above and the equilibrium intensity, κ_E into (10) yields

$$\begin{aligned} \frac{\partial \ln(Y)}{\partial t} &= \alpha \frac{\partial \ln K}{\partial t} + \beta h_E + (1 - (\alpha + \beta))(h_L + n) = \alpha \left(\frac{\partial \ln \kappa}{\partial t} + \frac{\partial \ln Y}{\partial t} \right) + \beta h_E + (1 - (\alpha + \beta))(h_L + n) \\ \Rightarrow (1 - \alpha) \frac{\partial \ln(Y)}{\partial t} &= \alpha \frac{\partial \ln \kappa}{\partial t} + h(1 - \alpha) + (1 - (\alpha + \beta))n \Rightarrow \frac{\partial \ln(Y)}{\partial t} = \frac{\alpha}{1 - \alpha} \frac{\partial \ln \kappa}{\partial t} + h + \frac{(1 - \alpha - \beta)n}{1 - \alpha} = \\ &= h + n - \frac{\beta}{1 - \alpha} n \end{aligned}$$

Using equation (16) yields

$$\frac{\partial \ln(y)}{\partial t} = h - \frac{\beta}{1 - \alpha} n = \frac{\gamma h_L}{1 - \alpha} + \frac{\beta h_e}{1 - \alpha} - \frac{\beta}{1 - \alpha} n = \frac{\gamma h_L + \beta(h_e - n)}{\beta + \gamma} \quad (17)$$

This results shows that the negative impact of population growth in the intensive form of the production function is proportional with the ratio of energy/resource used (β), the rate of efficiency improvement increases per capita output growth. The macroeconomic impact of population growth is also prevalent through the increasing energy consumption which results in decreasing per capita production and per capita consumable energy (we have fixed the amount of E). Increasing efficiency on the other hand *directly increases* economic output.

3. Impact of Energy Efficiency Improvement

We fix our energy consumption, and as a simplification we assume that labour use has reached its optimal efficiency which can not be further improved, and $\eta_L=1$. We also assume that population and labour supply of wealthier societies increases faster after reaching a critical per capita income level (Y_e/L_e)

$$n_t = \nu \left(\frac{Y_t}{L_t} - \frac{Y_e}{L_e} \right) \quad (18)$$

where n is population growth rate and ν is a constant parameter. We seek an equilibrium where productivity of unit of labour is constant, labour-capital ratio is constant and we assume that the rate of energy efficiency improvement equals population growth rate: $n=h_e$ ensuring that population increase is not increasing energy consumption (E_t = constant, assume for simplicity that $E_t =1$), then expressing Y/L from (18),

$$\frac{Y}{L} = \frac{Y_E}{L_E} + \frac{n_t}{\nu} = \frac{Y_E}{L_E} + \frac{h_E}{\nu} \quad (20)$$

Furthermore constant labour efficiency implies $h_L = 0$, substituting back to (13) yields:

$$\kappa_e = \frac{s}{\frac{\beta h_e}{1-\alpha} + \frac{(1-(\alpha+\beta))h_L}{1-\alpha} + \frac{(1-(\alpha+\beta))n}{1-\alpha} + \delta} = \frac{s}{\frac{\beta h_e}{1-\alpha} + \frac{(1-(\alpha+\beta))n}{1-\alpha} + \delta} = \frac{s}{h_e + \delta} \quad (21)$$

Thus equilibrium capital growth rate equals the ratio of saving rate and the sum of the rate of energy efficiency improvement and amortisation rate assuming that energy efficiency improvements are assured by new infrastructural investments, renewables, energy saving measures, etc. Along the balanced growth path (κ_e) substituting into the output per capita equation and exploiting our assumption on efficiency statics yields output per capita as :

$$\begin{aligned} Y &= K^\alpha (\eta_E E)^\beta (\eta_L L)^\gamma \\ \frac{Y}{L} &= \frac{K^\alpha (\eta_E E)^\beta (\eta_L L)^\gamma}{L} = \frac{\kappa_e^\alpha Y^\alpha}{L^\alpha} \cdot \frac{\eta_E^\beta E^\beta}{L^\beta} \cdot \frac{\eta_L^{1-\alpha-\beta} L^{1-\alpha-\beta}}{L^{1-\alpha-\beta}} \\ \frac{Y^{1-\alpha}}{L^{1-\alpha}} &= \left(\frac{Y}{L}\right)^{1-\alpha} = \frac{\kappa_e^\alpha \eta_E^\beta}{L^\beta} \Rightarrow \frac{Y}{L} = \sqrt[1-\alpha]{\kappa_e^\alpha \eta_E^\beta L^{-\beta}} = \kappa_e^{\frac{\alpha}{1-\alpha}} \eta_E^{\frac{\beta}{1-\alpha}} L^{\frac{-\beta}{1-\alpha}} \end{aligned} \quad (22)$$

Here we used that $\alpha+\beta+\gamma=1$, $\kappa=K/Y$, $E=1$, and that labour efficiency does not improve further and is equal to 1. If we express L from the last equation of (22) and substitute (21) we get that

$$\left(\frac{L}{\eta_E}\right)^{\frac{\beta}{1-\alpha}} = \kappa_e^{\frac{\alpha}{1-\alpha}} \left(\frac{L}{Y}\right) \Rightarrow \frac{L}{\eta_E} = \kappa_e^{\frac{\alpha}{\beta}} \left(\frac{L}{Y}\right)^{\frac{1-\alpha}{\beta}} \Rightarrow L = \left(\frac{s}{h_e + \delta}\right)^{\frac{\alpha}{\beta}} \left(\frac{Y_e}{L_e} + \frac{h_e}{v}\right)^{\frac{1-\alpha}{\beta}} \eta_E \quad (22b)$$

Applying the $y^* = Y_e/L_e$ denotation yields

$$L = \left(\frac{s}{h_e + \delta}\right)^{\frac{\alpha}{\beta}} \left(\frac{v}{y^* v + h_e}\right)^{\frac{1-\alpha}{\beta}} \eta_E \quad (23)$$

This result shows that employment can be further increased by energy efficiency improvements. If we denote the first two factors of the RHS of (23) with λ then this can be interpreted as a characteristic parameter typical for a given economy:

$$\left(\frac{s}{h_e + \delta}\right)^{\frac{\alpha}{\beta}} \left(\frac{v}{y^* v + h_e}\right)^{\frac{1-\alpha}{\beta}} = \lambda \quad (24)$$

Substituting (23) into (7) yields

$$Y = K^\alpha (\eta_E E)^\beta (\eta_L L)^\gamma = K^\alpha (\eta_E E)^\beta (\eta_L \lambda \eta_E)^\gamma = K^\alpha E^\beta \cdot \eta_E^{\beta+\gamma} \eta_L^\gamma \lambda^\gamma = K^\alpha \eta_E^{\beta+\gamma} \Theta \Rightarrow (25)$$

$$\Rightarrow Y = K^\alpha \eta_E^{\beta+\gamma} \Theta$$

where we applied the following notation

$$\eta_L^\gamma \lambda^\gamma = \Theta$$

and exploited that η_L is constant and energy use is stabilised ($E_i=1$), thus a single constant containing λ can be used. The constant Θ is a constant characterising a given country as it depends on several macroeconomic parameters.

The result attained in (25) shows that if energy use is stabilised and labour is used optimally than the output of the economy can be increased with energy efficiency in a higher ($\beta+\gamma$) proportion than expected from the factor share (β) of energy use from the production function.

Thus we gave a proof to the general idea that improving energy efficiency can assure economic development intensively, without increasing energy consumption. As energy efficiency here was used in a broad sense as a multiplier it can include renewables and any measures which result in a higher energetical rate of return on a unit of depletable energy source used.

4. Estimation and assessment of a domestic production function

The domestic production function in the form of (K,L,E) was estimated for a simple application of our results.

The data used for the estimation came from Eurostat and KSH. The validity of the estimation is limited, since the estimation was performed on data between 1994-2009, first because data availability was limited, and the methodology of GDP calculation was changed beginning from 1994. Not lastly, it is very likely that there was a structural break between the periods before and after 1993 (or 1990). The low number of elements nevertheless reduces the value of the estimation.

After running Eviews the following result is gained with good fitting ($R^2_{adj}=0.984$) for the logarithmised time series

$$\ln Y = 0.497 \cdot \ln E + 0.389 \cdot \ln K + 0.145 \cdot \ln L \Rightarrow Y = E^{0.48} K^{0.38} L^{0.14}$$

for macroeconomic production, energy used, capital goods, and labor utilised.

The next step is the assessment of the domestic Energy Efficiency Action Plan's effect on macroeconomic production. According to the Action Plan, 12% energy efficiency improvement would be achieved if the planned measures are implemented.

For simplicity everything else is assumed to remain unchanged, and the conditions under (25) to be fulfilled – among others energy use is stabilised –

then the macroeconomic output can be deduced with the aid of comparative statics:

That is, domestic product would be increased with 7% if the assumed 12% efficiency improvement is undertaken according to the data available. If no conditions are made then efficiency improvement would roughly enhance production by 5.6% compared to the base value everything else the same. Where a publication is referred to in the text, enclose the name of author(s) and the date of publication within brackets, see (Mujumdar, 1990). For two authors give both names and the date, see (Farkas and Rendik, 1997). For three or more authors give the name of the first author plus "et al.", and the date (Seres et al., 2004). If giving a list of references, separate them using semi-colons.

Conclusions

The above analysis shows that consideration of energy as a macroeconomic input factor significantly modifies equilibrium trajectories and solutions of the conventional model.

Increase of energy consumption in any case – although extensively – increases macroeconomic production. Combined with population increase nevertheless this extensive growth quickly meets its limitations of depleting resources and environmental problems.

With the introduction of energy efficiency and its dynamics numerous important results are gained in our opinion. One is that the equilibrium capital intensity can be reduced by increasing energy efficiency, another is that increase of production per capita is proportional (weighted) with energy efficiency improvements.

In the economies which stabilise their energy consumption improvement of energy efficiency leads to increases in macroeconomic output higher than proportional to energy's role in production.

This leads to the conclusion that in addition to political and environmental benefits energy efficiency measures have direct macroeconomic benefits beyond the trivial economic reasons (cost reduction, rationalisation).

Acknowledgements

The authors gratefully acknowledge the support of the TÁMOP-4.2.1.B-11/2/KMR-2011-0003 project titled „Az oktatás és kutatás színvonalának emelése a Szent István Egyetemen”.

References

- [1] Hotelling, H., (1931). The economics of exhaustible Resources. *Journal of Political Economy*, 39(2):137–175

- [2] Meadows, D.H., Meadows D.L., Randers J., and W.W. Behrens (1972), *The Limits to Growth*, Universe Books, New York.
- [3] Pezzey J.C.V., Toman M.A. (2002): *The Economics of Sustainability: A Review of Journal Articles*, Resources for the Future, Discussion Paper 02-03, 2002
- [4] Solow, R.M. (1974), *Intergenerational Equity and Exhaustible Resources*, Review of Economic Studies 41, Symposium on the Economics of Exhaustible Resources, pp. 29-45.
- [5] Stiglitz, J.E. (1974), *Growth with Exhaustible Natural Resources: Efficient and Optimal Growth Paths*, Review of Economics Studies 41, Symposium on the Economics of Exhaustible Resources, pp. 123-137.

On the properties of linear time varying systems

Sándor MOLNÁR

Department of Informatics, Institute for Mathematics and Informatics

Abstract

In this paper system properties of linear time varying systems are discussed. A family of subspaces is considered, which is related to the generalized Kalman's rank condition. It is shown that if special differential algebraic conditions for the time varying dynamics of the systems hold, then the subspaces are the reachability subspace of the system.

Keywords

Controllability and reachability, Differential algebra, Time varying linear systems, Matrix Lie-algebra

1. Introduction

Definition. 1 We call

$$\begin{aligned}\dot{x}(t) &= A(t)x(t) + B(t)u(t) \\ y(t) &= C(t)x(t) + D(t)u(t)\end{aligned}\tag{1}$$

a system with time-variant parameters, where functions

$$\begin{aligned}A : [0, T] &\rightarrow \mathbb{R}^{n \times n}, & B : [0, T] &\rightarrow \mathbb{R}^{n \times k} \\ C : [0, T] &\rightarrow \mathbb{R}^{l \times n}, & D : [0, T] &\rightarrow \mathbb{R}^{l \times k},\end{aligned}$$

are continuous on a fixed interval $[0, T]$.

Remark. R. Kalman solved all the fundamental problems concerning such systems. He proved the duality of reachability and observability, as well as that of controllability and reconstructability. He also showed the equivalence of the pairs reachability-controllability and observability-reconstructability for continuous time systems of the form (1). Therefore we are interested in only one system property, namely reachability.

Consider the initial value problem

$$\dot{x}(t) = A(t)x(t), \quad x(\tau) = I\tag{2}$$

in $\mathbf{R}^{n \times n}$. If the coefficient matrix is continuous, then it has a unique solution

$$t \mapsto \Phi(t, \tau) \in \mathbf{R}^{n \times n}$$

defined on the whole interval $[0, T]$, which is continuously differentiable as a two variable function at (t, τ) , and $\Phi(t, \tau)$ is invertible for all pairs (t, τ) . Consider the solution $t \mapsto \Psi(t, \tau)$ to the initial value problem

$$\dot{Y}(t) = -Y(t)A(t), \quad Y(\tau) = I$$

defined on the whole interval $[0, T]$. Then

$$\begin{aligned} \frac{d}{dt}(\Psi(t, \tau)\Phi(t, \tau)) &= \dot{\Psi}(t, \tau)\Phi(t, \tau) + \Psi(t, \tau)\dot{\Phi}(t, \tau) = \\ &= (-\Psi(t, \tau)A(t)\Phi(t, \tau) + \Psi(t, \tau)(A(t)\Phi(t, \tau))) = 0, \end{aligned}$$

that is, $\Psi(t, \tau)\Phi(t, \tau) = I$, which implies $\Psi(t, \tau) = \Phi(t, \tau)^{-1}$ in \mathbf{R}^n . Moreover, $\Phi(t, \tau) = \Phi(t, 0)\Phi(\tau, 0)^{-1}$, because $t \mapsto \Phi(t, 0)\Phi(\tau, 0)^{-1}$ is a solution to the equation $\dot{x}(t) = A(t)x(t)$ and $\Phi(\tau, 0)\Phi(\tau, 0)^{-1} = I$. Interchanging t and τ ,

$$\Phi(\tau, t) = \Phi(\tau, 0)\Phi(t, 0)^{-1} = \Phi(\tau, 0)\Psi(t, 0),$$

that is,

$$\begin{aligned} \frac{d}{dt}\Phi(\tau, t) &= \Phi(\tau, 0)\frac{d}{dt}\Psi(t, 0) = \Phi(\tau, 0)(-\Psi(t, 0)A(t)) = \\ &= -\Phi(\tau, 0)\Phi(t, 0)^{-1}A(t) = -\Phi(\tau, t)A(t), \quad \Phi(\tau, \tau) = I. \end{aligned}$$

Therefore

$$\Phi(t, \tau)^{-1} = \Phi(\tau, t).$$

Definition 2. We call

$$G_{\text{Rea}}[0, T] = \int_0^T \Phi(T, t)B(t)B(t)^* \Phi(T, t)^* dt$$

the reachability Kalman-Gram matrix.

Theorem 3 (Kalman's reachability theorem) The system (1) is reachable from state 0 if and only if the reachability Kalman-Gram matrix is invertible, or equivalently, positive definite.

Remark. A similar theorem holds for controllability. The controllability Kalman-Gram matrix is defined by

$$G_C[0, T] = \int_0^T \Phi(0, t) B(t) B(t)^* \Phi(0, t)^* dt.$$

If we define the dual system of (1*) as

$$\begin{aligned} \dot{x}(t) &= A(t)^* x(t) + C(t)^* u(t) \\ y(t) &= B(t)^* x(t) + D(t)^* u(t), \end{aligned} \tag{1*}$$

in (1*) the input could be denoted by y and the output by u , indicating the exchange of their roles.

Theorem 4 (Kalman's duality theorem). The system described in (1) is controllable if and only if (1*) is reconstructable, and (1) is reachable if and only if (1*) is observable.

Remark. Since the dual of the dual system is the original system, (1) is observable if and only if (1*) is reachable, moreover (1) is reconstructable if and only if (1*) is controllable.

The observability Kalman-Gram matrix is

$$G_0[0, T] = \int_0^T \Phi(T, t)^* C(t)^* C(t) \Phi(T, t) dt,$$

and reconstructability is equivalent to the invertability (or positive definiteness) of the reconstructability Kalman-Gram matrix

$$G_{Re}[0, T] = \int_0^T \Phi(0, t)^* C(t)^* C(t) \Phi(0, t) dt.$$

In the following we investigate the reachability of the systems (1) and the more general system given in canonic form.

$$\begin{aligned} \dot{x}(t) &= A(t)x(t) + \sum_j B_j(t)u^{(j)} \\ y(t) &= C(t)x(t) + \sum_j D_j(t)u^{(j)}. \end{aligned} \tag{3}$$

Several publications [3,5,6] deal with the system described in (1). Based on these we focus on the general canonic system (3), especially the theoretical construction of the persistent excitation condition, which plays an important role in the existence of a multivariable Kalman-like rank condition for LTV systems.

Definition 5. Let L be a vector space over \mathbf{R} endowed with a multiplication-like operation, the so-called Lie multiplication or Lie bracket: If $l_1, l_2 \in L$ then $[l_1, l_2] \in L$, $l_1 \mapsto [l_1, l_2]$ and $l_2 \mapsto [l_1, l_2]$ are linear mappings and

1. $[l, l] = 0$ for all $l \in L$
2. $[l_1, l_2] + [l_2, l_1] = 0$ for all $l_1, l_2 \in L$,
3. $[l_1, [l_2, l_3]] + [l_2, [l_3, l_1]] + [l_3, [l_1, l_2]] = 0$ for all $l_1, l_2, l_3 \in L$.

endowed with a Lie multiplication is called a Lie algebra.

Remark. Condition 2. means anticommutativity $[l_1, l_2] = -[l_2, l_1]$, and condition 3. measures non-associativity.

Indeed,

$$[l_1, [l_2, l_3]] = -[l_2, [l_3, l_1]] - [l_3, [l_1, l_2]] = [l_1, l_2], l_3 - [l_2, [l_3, l_1]],$$

because if $[l_2, [l_3, l_1]] = 0$ then the remaining equation

$$[l_1, [l_2, l_3]] = [l_1, l_2], l_3$$

means associativity.

Examples.

1. Let $L = \mathbf{R}^{n \times n}$. If we define $[A, B] = AB - BA$ then $(\mathbf{R}^{n \times n}, [\cdot, \cdot])$ is a Lie algebra.
2. Let $\Omega \subset \mathbf{R}^n$ be an open set and consider the vector space of analytic functions $f : \Omega \rightarrow \mathbf{R}^n$ over \mathbf{R} . Let the Lie bracket be defined by

$$[f, g](x) = f'(x)g(x) - g'(x)f(x). \tag{4}$$

Denote the vector space of all \mathbf{R}^n -value functions (the analytic vector space on Ω) over \mathbf{R} by $A(\Omega)$ endowed with the Lie multiplication (4).

Then we obtain the Lie algebra $(A(\Omega), [\cdot, \cdot])$.

3. Similarly, on the vector space $C^\infty(\Omega)$ over \mathbf{R} of vector fields C^∞ defined on an open set $\Omega \subset \mathbf{R}^n$ we can define the Lie multiplication as in (4). Then we obtain the Lie algebra $(C^\infty(\Omega), [\cdot, \cdot])$.

Definition 6. Consider system (3). The sub-Lie-algebra $L \subset R^{n \times n}, (L, [\cdot, \cdot])$ generated by

$$\{A(t) : t \in [0, T]\} \subset R^{n \times n}$$

is defined as the smallest sub-Lie-algebra for which $\{A(t) : t \in [0, T]\} \subset L$ holds.

Remarks. Such a sub-Lie-algebra exists because the set of the containing sub-Lie-algebras is non-empty, $R^{n \times n}$ is an element, and the intersection of these is the minimal sub-Lie-algebra generated by $\{A(t)\}$.

Since $R^{n \times n}$ has finite dimension (n^2), the sub-Lie-algebra $L \subset R^{n \times n}$ is also finite dimensional.

Let $A_1, A_2, \dots, A_l \in L$ be a basis of L . In this basis

$$A(t) = \sum_{i=1}^l a_i(t) A_i,$$

and the Lie bracket $[A_i, A_j] \in L$

$$[A_i, A_j] = \sum_{k=1}^l \Gamma_{ij}^k A_k.$$

Since $X \mapsto [A_i, X] = AdA_i(X)$ is a linear mapping on the vector space L (which is also a Lie algebra), the matrix representation of AdA_i in the basis A_1, A_2, \dots, A_l can be expressed with the help of the numbers Γ_{ij}^k .

Let $X = \sum_{j=1}^l x_j A_j$. Then

$$[A_i, X] = \left[A_i, \sum_{j=1}^l x_j A_j \right] = \sum_j x_j \left(\sum_{h=1}^l \Gamma_{ij}^h \right) A_h,$$

$\sum_j \Gamma_{ij}^h x_j$ is the h -th component of the matrix-vector product

$$\begin{pmatrix} \Gamma_{i1}^1 & \Gamma_{i2}^1 & \dots & \Gamma_{il}^1 \\ \Gamma_{i1}^2 & \Gamma_{i2}^2 & \dots & \Gamma_{il}^2 \\ \vdots & \vdots & \vdots & \vdots \\ \Gamma_{i1}^l & \Gamma_{i2}^l & \dots & \Gamma_{il}^l \end{pmatrix} \begin{pmatrix} x_1 \\ x_2 \\ \vdots \\ x_l \end{pmatrix} = \Gamma_i \mathbf{x}$$

and, because of the the correspondences $AdA_i X \leftrightarrow \Gamma_i \mathbf{x}$, $X \leftrightarrow \mathbf{x}$, Γ_i is the representation of the matrix AdA_i in the basis $A_1, A_2, \dots, A_l \in \mathbb{L}$.

According to the Cauchy formula, the solution to system with initial condition $x(0) = \xi$ is

$$x(t) = \Phi(t, 0)\xi + \int_0^t \Phi(t, \tau)B(\tau)u(\tau)d\tau,$$

and similarly, in the case of the generalized canonic system (3)

$$x(t) = \Phi(t, 0)\xi + \int_0^t \Phi(t, \tau) \left(\sum_j B_j(\tau)u^j(\tau) \right) d\tau.$$

For systems with constant coefficients, the solution basis $\Phi(t, \tau)$ are the solutions to

$$\dot{x}(t) = Ax(t), \quad x(\tau) = I$$

i.e.,

$$\Phi(t, \tau) = \exp A(t - \tau).$$

Moreover, if the system's structure matrix $A(t)$ has the form $A(t) = a(t)A$ then the basis solutions are $\Phi(t, \tau) = \exp A \int_{\tau}^t a(s)ds$.

In the case of a general time-varying system

$$\dot{x}(t) = \sum_{i=1}^l a_i(t)A_i x + \sum_j B_j(t)u^{(j)}(t)$$

the basic solutions take the form

$$\Phi(t, \tau) = \exp A_1 g_1(t, \tau) \exp A_2 g_2(t, \tau) \dots \exp A_l g_l(t, \tau).$$

Again, we assume that A_1, A_2, \dots, A_l is a basis in the Lie algebra \mathbb{L} generated by $A(t)$ and also that matrix $\Gamma_i \in \mathbb{R}^{k \times l}$ is the representation of AdA_i . Then the existence of the above representation is guaranteed by the Wei-Norman Theorem.

Wei-Norman Theorem. Let $\gamma(t) = g(t, \tau) \in R^k$ be a solution to the so-called Wei-Norman nonlinear differential equation

$$\left(\sum_{i=1}^l \exp \Gamma_i \gamma_i \exp \Gamma_2 \gamma_2 \dots \exp \Gamma_{i-1} \gamma_{i-1} E_{ii} \right)^{-1} \gamma = \mathbf{a}$$

$$\gamma(\tau) = 0 \tag{5}$$

Then

$$\Phi(t, \tau) = \exp A_1 g(t, \tau) \exp A_2 g(t, \tau) \dots \exp A_l g(t, \tau).$$

Remarks.

The solution locally exists, because the initial condition $\gamma(\tau) = 0$ implies that the matrix to be inverted at $\tau = 0$ is the identity, which is invertible, thus also invertible in an appropriate neighbourhood of τ , and so can be made explicite. It is well-known (cf. [1]) that

$$\exp A_i g_i(t, \tau) = \sum_{j=0}^{n-1} q_{ij}(g_i(t, \tau)) A_i^j \tag{6}$$

is a polynomial of A_i with maximal degree $n-1$, a quasipolynomial of $g_i(t, \tau)$ that is, a polynomial of $g_i(t, \tau)$, $\sin \alpha_i g_i(t, \tau)$, $\cos \beta_i g_i(t, \tau)$ and exponential of $\exp \lambda_i g_i(t, \tau)$, where λ_i are the real parts and α_i, β_i are the imaginary parts of the eigenvalues of A_i . (The basic results can be found in the classical monographs of matrix theory and ordinary differential equations, such as F. R. Gantmacher, The Theory of Matrices, Chelsea Publishing Company, New York, N.Y., 1974.)

Substituting (6) into the exponential product we obtain

$$\Phi(t, \tau) = \sum_{\mathbf{n}} Q_{\mathbf{n}}(\mathbf{g}(t, \tau)) A_1^{n_1} A_2^{n_2} \dots A_l^{n_l},$$

where $Q_{\mathbf{n}}$ is a quasipolynomial of $\mathbf{g}(t, \tau) = (g_1(t, \tau), g_2(t, \tau), \dots, g_l(t, \tau))$ (certain product of quasipolynomials $g_{ij}(g_i(t, \tau))$).

2. Reachability of the canonic system

Lemma 7. Consider the final states of the generalized linear system with time-variant coefficients (3), with the initial condition $x(0) = 0$. Then

$$x(T) = \int_0^T \Phi(T, t) \left[\sum_{j=0}^J \left(\sum_{|\alpha+\beta|=j-j} C_{\alpha, \beta} \left(A^{(\alpha)}(t) \right)^\beta \right) B_j^{(j)}(t) \right] u(t) dt.$$

Here we apply the following notation:

for integers $0 \leq \alpha_1, \alpha_2, \dots, \alpha_\gamma, 1 \leq \beta_1, \beta_2, \dots, \beta_\gamma,$

$$\alpha = (\alpha_1, \alpha_2, \dots, \alpha_\gamma), \quad \beta = (\beta_1, \beta_2, \dots, \beta_\gamma),$$

$$|\alpha| = \sum |\alpha_i|,$$

$$\left(A^{(\alpha)}(t) \right)^\beta = \left(A(t) \right)^{\beta_1} \left(A(t) \right)^{\beta_2} \dots \left(A(t) \right)^{\beta_\gamma}.$$

Proof. By the Cauchy formula,

$$x(T) = \int_0^T \Phi(T, t) \left(\sum_j B_j(t) u^{(j)}(t) \right) dt. \tag{7}$$

If the highest order derivative of u that appears is $u^{(J)}(t)$ then we assume that for all $j = 0, 1, 2, \dots, J - 1$, the boundary conditions $u^{(j)}(0) = 0, u^{(j)}(T) = 0$ hold. This assumption does not affect the subspace of the reachable final states in \mathbb{R}^n .

$$\begin{aligned} x(T) &= \int_0^T \Phi(T, t) B_0(t) u(t) dt + \sum_{j=1}^T \int_0^T \Phi(T, t) B_j(t) u^{(j)}(t) dt = \\ &= \int_0^T \Phi(T, t) B_0(t) u(t) dt + \sum_{j \geq 1} [\Phi(T, t) B_j(t) u^{(j-1)}(t)]_0^T - \\ &- \sum_{j=1}^T \int_0^T \frac{d}{dt} (\Phi(T, t) B_j(t)) u^{(j-1)}(t) dt = \int_0^T \Phi(T, t) B_0(t) u(t) dt + \\ &+ \int_0^T \Phi(T, t) (A(t) B_1(t) - B_1'(t)) u(t) dt + \sum_{j \geq 2} \int_0^T \Phi(T, t) (A(t) B_j(t) - B_j'(t)) u^{(j-1)}(t) dt. \end{aligned}$$

Repeating this for the last term, we obtain the equations of the next step:

$$\begin{aligned} \sum_{j \geq 2} \int_0^T \Phi(T, t) (A(t) B_j(t) - B_j'(t)) u^{(j-1)}(t) dt &= \sum_{j \geq 2} [\Phi(T, t) (A(t) B_j(t) - B_j'(t)) u^{(j-2)}(t)]_0^T - \\ - \int_0^T \frac{d}{dt} (\Phi(T, t) (A(t) B_2(t) - B_2'(t))) u(t) dt &- \sum_{j \geq 3} \int_0^T \frac{d}{dt} (\Phi(T, t) (A(t) B_j(t) - B_j'(t))) u^{(j-2)}(t) dt = \end{aligned}$$

$$\begin{aligned}
 &= \int_0^T \Phi(T, t) \left(A(t)^2 B_2(t) - 2A(t)B_2'(t) - A'(t)B_2(t) + B_2''(t) \right) u(t) dt + \\
 &+ \sum_{j \geq 3} \int_0^T \Phi(T, t) \left(A(t)^2 B_j(t) - 2A(t)B_j'(t) - A'(t)B_j(t) + B_j''(t) \right) u^{(j-2)}(t) dt.
 \end{aligned}$$

Again, integrating by parts in the last term, we have a similar equation:

$$\begin{aligned}
 &\sum_{j \geq 3} \int_0^T \Phi(T, t) \left(A(t)^2 B_j(t) - 2A(t)B_j'(t) - A'(t)B_j(t) + B_j''(t) \right) u^{(j-2)}(t) dt = \\
 &= \int_0^T \Phi(T, t) \left(A(t)^3 B_3(t) - 2A(t)A(t)'B_3(t) - A'(t)A(t)B_3(t) - 3A(t)^2 B_3'(t) + 3A'(t)B_3'(t) + \right. \\
 &+ 3A(t)B_3''(t) - B_3'''(t) \left. \right) u(t) dt + \\
 &+ \sum_{j \geq 4} \int_0^T \Phi(T, t) \left(A(t)^3 B_j(t) - 3A(t)^2 B_j'(t) - 2A(t)A'(t)B_j(t) + \right. \\
 &+ 3A(t)B_j''(t) - A'(t)A(t)B_j(t) + 3A'(t)B_j'(t) + A''(t)B_j(t) - B_j'''(t) \left. \right) u^{(j-3)}(t) dt.
 \end{aligned}$$

After the J -th step, no derivative of $u(t)$ appears in the integral. Then (applying the above notation)

$$\begin{aligned}
 x(T) &= \int_0^T \Phi(T, t) B_0(t) u(T) dt + \int_0^T \Phi(T, t) \left(A(t)B_1(t) - B_1'(t) \right) u(t) dt + \\
 &+ \int_0^T \Phi(T, t) \left(A(t)^2 - A'(t)B_2(t) - 2A(t)B_2'(t) + B_2''(t) \right) u(t) dt + \\
 &+ \int_0^T \Phi(T, t) \left((A(t)^3 - 2A(t)A(t)' - A(t)'A(t))B_3(t) - \right. \\
 &\quad \left. - (3A(t)^2 - 3A'(t))B_3'(t) + 3A(t)B_3'' - B_3''' \right) u(t) dt + \\
 &+ \dots = \\
 &= \int_0^T \Phi(T, t) \left[\sum_{j=0}^J \left(\sum_{|\alpha+\beta|=j-\bar{j}} C_{\alpha, \beta} \left(A^{(\alpha)}(t) \right)^\beta \right) B_j^{(\bar{j})}(t) \right] u(t) dt,
 \end{aligned}$$

which was to be proved.

Definition 8. The reachability Kalman-Gram matrix for generalised systems is defined as

$$G_{\text{Rea}}[0, T] = \int_0^T \Phi(T, t) \left[\sum_{j=0}^J \left(\sum_{|\alpha+\beta|=j-\bar{j}} C_{\alpha, \beta} (A^{(\alpha)}(t))^{\beta} \right) B_j^{(\bar{j})}(t) \right] \cdot \left[\sum_{j=0}^J \left(\sum_{|\alpha+\beta|=j-\bar{j}} C_{\alpha, \beta} (A^{(\alpha)}(t))^{\beta} \right) B_j^{(\bar{j})}(t) \right]^T \Phi(T, t)^T dt.$$

Theorem. *The general time-varying linear system on the interval $[0, T]$ is completely reachable if and only if the Kalman-Gram matrix $G_{\text{Rea}}[0, T]$ is invertible, or equivalently, positive definite.*

Proof. The proof is similar to the case of classical time-varying linear systems:

Let L be the Lie algebra generated by $\{A(t) : t \in [0, T]\} \subset R^{n \times n}$ and let $A_1, A_2, \dots, A_l \in L$ be a basis. In this basis

$$A(t) = \sum_{i=1}^l a_i(t) A_i.$$

Similarly, for the matrices $B_0(t), B_1(t), \dots, B_j(t)$, if

$$V = V\{B_0(t), B_1(t), \dots, B_j(t) : t \in [0, T]\} \subset R^{n \times k}$$

is the subspace of the vector space $R^{n \times k}$ spanned by $B_j(t)$ then a basis $B_1, B_2, \dots, B_{\bar{j}}$ can be chosen in V such that

$$B_j(t) = \sum_{\bar{i}=1}^{\bar{j}} b_{j\bar{i}}(t) B_{\bar{i}}.$$

Since $\Phi(T, t)$ can be written as a polynomial of A_1, A_2, \dots, A_l , a quasi-polynomial of the solutions g_1, g_2, \dots, g_l to the Wei-Norman equation, and the fonction $\sum_{j=0}^J \left(\sum_{|\alpha+\beta|=j-\bar{j}} C_{\alpha, \beta} (A^{(\alpha)}(t))^{\beta} \right) B_j^{(\bar{j})}(t)$ in the integral form of $x(T)$ can be written as a polynomial of A_1, A_2, \dots, A_l and $B_1, B_2, \dots, B_{\bar{j}}$ and a differential polynomial of $a_i(t)$ and $b_{j\bar{i}}(t)$ (with integer coefficients and first degree $B_{\bar{i}}$). Exchanging adjacent terms, the powers of A_i can be arranged in the natural

order (have the form $A_1^{m_1}, A_2^{m_2}, \dots, A_l^{m_l}$, where all m_i satisfy $0 \leq m_i < n$, or $\mathbf{0} \leq \mathbf{m} < \mathbf{n}$) using the equations $A_{i_1} A_{i_2} = A_{i_2} A_{i_1} + \sum_{h=1}^l \Gamma_{i_1 i_2} A_h$ and $A_i^n = \sum_{\hat{i}=0} C_{\hat{i}} A_i^{\hat{i}}$ assuming that the characteristic polynomial of A_i has the form

$$\lambda^n = \sum_{\hat{i}=0}^{n-1} C_{\hat{i}} \lambda^{\hat{i}}.$$

Then we have

$$x(T) = \sum_{\mathbf{0} \leq \mathbf{m} < \mathbf{n}} \sum_{\hat{i}=0}^i A_1^{m_1}, A_2^{m_2}, \dots, A_l^{m_l} B_{\hat{i}} \int_0^T P_{\mathbf{m}, \hat{i}}(\mathbf{g}(T, t), a^{[\infty]}(t), b_1^{[\infty]}(t), \dots, b_j^{[\infty]}(t)) u(t) dt.$$

Here $P_{\mathbf{m}, \hat{i}}(\mathbf{g}(T, t), \mathbf{a}^{[\infty]}(t), \dots, b_j^{[\infty]}(t), \dots)$ are quasi-polynomials of $g_1(T, t), g_2(T, t), \dots, g_l(T, t)$ and differential polynomials of $a_1(t), a_2(t), \dots, a_l(t)$,

$$b_{11}(t), b_{12}(t), \dots, b_{l\hat{i}}(t), b_{21}(t), \dots, b_{2\hat{i}}(t), \dots, b_{j1}(t), b_{j2}(t), \dots, b_{j\hat{i}}(t).$$

This implies that the reachable subspace of the general system on $[0, T]$ must be a subset of the image

$$\text{Im} \left\{ \dots, A_1^{m_1}, A_2^{m_2}, \dots, A_l^{m_l} B_{\hat{i}}, \dots \right\}$$

which is the same as in the case of classical canonical systems.

The reachability subspace is extended because the derivatives can also be inputs, therefore let $V_0 = V \left\{ B_0(t); t \in [0, T] \right\} \subset \mathbb{R}^{n \times k}$,

$$V_J = V \left\{ B_0(t), B_1(t), \dots, B_j(t); t \in [0, T] \right\} \subset \mathbb{R}^{n \times k'}$$

be the subspaces generated by the corresponding matrices $B_j(t)$. Choose a basis of V_J such that the first \hat{I}_0 element form a basis of V_0 :

$$V_0 = V \left\{ B_1, B_2, \dots, B_{\hat{I}_0} \right\},$$

$$V_J = V \left\{ B_1, B_2, \dots, B_{\hat{I}_0}, B_{\hat{I}_0+1}, B_{\hat{I}_0+2}, \dots, B_{\hat{I}_j} \right\}$$

From this it is obvious that for the general system, the image of the corresponding generalized Kalman-Gram matrices (briefly Kalman matrices in

the following) contain the image of the general Kalman matrices of the classical system.

From the proofs for the classical system one can deduce the excitation condition which guarantees that the reachability subspace of the general system coincides with the image of the image of the general Kalman matrix of the system. Suppose that ξ is a vector in the image of the Kalman matrix, $\text{Im}\{\dots, A_1^{m_1}, A_2^{m_2}, \dots, A_l^{m_l} B_i, \dots\} = K_{\text{gen}}$.

K_{gen} does not equal the reachable subspace of the general system over $[0, T]$ if and only if there exists $\xi \neq 0$, $\xi \in K_{\text{gen}}$, such that $\langle \xi, x(T) \rangle = 0$ for all possible inputs $u(t)$.

This means

$$\begin{aligned} 0 &= \langle \xi, x(T) \rangle = \\ &= \left\langle \xi, \sum_{0 \leq m < n} \sum_{\hat{i}=0}^{\hat{l}} A_1^{m_1} A_2^{m_2}, \dots, A_l^{m_l} B_{\hat{i}} \int_0^T P_{m, \hat{i}}(\mathbf{g}(T, t), \mathbf{a}^{[\infty]}(t), \dots, b_j^{[\infty]}, \dots) u(t) dt \right\rangle = \\ &= \int_0^T \left\langle \sum_{0 \leq m < n} \sum_{\hat{i}=0}^{\hat{l}} P_{m, \hat{i}}(\mathbf{g}(T, t), \mathbf{a}^{[\infty]}(t), \dots, b_j^{[\infty]}, \dots) \right. \\ &\quad \left. (A_l^T)^{m_l} (A_{l-1}^T)^{m_{l-1}} \dots (A_1^T)^{m_1} B_{\hat{i}}^T \xi, u(t) \right\rangle dt. \end{aligned}$$

By the classical Lagrange lemma, if the above holds for every „nice”, e.g. continuous function then

$$\sum_{0 \leq m < n} \sum_{\hat{i}=0}^{\hat{l}} P_{m, \hat{i}}(\mathbf{g}(T, t), \mathbf{a}^{[\infty]}(t), \dots, b_j^{[\infty]}, \dots) (A_l^T)^{m_l} (A_{l-1}^T)^{m_{l-1}} \dots (A_1^T)^{m_1} B_{\hat{i}}^T \xi = 0 \quad (8)$$

The analytic functions $\exp \lambda g, \cos \alpha g, \sin \alpha g$ in the quasi-polynomials $P_{m, \hat{i}}$ can be replaced by new variables $\bar{g} = \exp \lambda g$, $\hat{g} = \cos \alpha g$, $\check{g} = \sin \alpha g$. The corresponding differential equations are:

$$\begin{aligned} \dot{\bar{g}} &= \lambda \dot{g} \exp \lambda g = \lambda \dot{g} \bar{g}, \text{ and} \\ \dot{\hat{g}} &= -\alpha \dot{g} \sin \alpha g = -\alpha \dot{g} \check{g}, \\ \dot{\check{g}} &= \alpha \dot{g} \cos \alpha g = \alpha \dot{g} \hat{g}. \end{aligned} \quad (9)$$

To make these differential equations explicit, consider the Wei-Norman differential equation

$$\left(\sum_{i=1}^I \exp \Gamma_1 g_1 \exp \Gamma_2 g_2 \dots \exp \Gamma_{i-1} g_{i-1} E_{ii} \right) \mathbf{g} = \mathbf{a}, \mathbf{g}(0) = \mathbf{0},$$

where

$$E_{ii} = \delta_{ij} = \begin{pmatrix} 0 & & & 0 \\ & \ddots & & \\ & & 1 & \\ & & & \ddots \\ 0 & & & & 1 \end{pmatrix} \in \mathbf{R}^{I \times I}.$$

The exponential products are exponents in the multiplication table of the Lie algebra $\Gamma_1, \Gamma_2, \dots, \Gamma_{I-1}$ (the Christoffel symbols) []. Again, we can introduce the non-polynomial terms $\exp \frac{\alpha}{g}$, $\cos \alpha g$, $\sin \alpha g$ as new variables, which means adding more differential equations of the type (9) that are polynomial. Thus the Wei-Norman equation becomes polynomial but non-explicit.

The equation can be made explicit in the original derivatives $\dot{\mathbf{g}}$:

$$\dot{\mathbf{g}} = \left(\sum_{i=1}^I \exp \Gamma_1 g_1 \exp \Gamma_2 g_2 \dots \exp \Gamma_{i-1} g_{i-1} E_{ii} \right)^{-1} \mathbf{a},$$

and equations (9) also become explicit with fractional denominators:

$$\det \left(\sum_{i=1}^I \exp \Gamma_1 g_1 \exp \Gamma_2 g_2 \dots \exp \Gamma_{i-1} g_{i-1} E_{ii} \right).$$

Multiplying the system of explicit equations by these, in the end we obtain an implicit polynomial differential equation with variables $\mathbf{g}, \bar{\mathbf{g}}, \hat{\mathbf{g}}, \check{\mathbf{g}}$, where each equation contains only one derivative, that is, a regular differential equation which can be made explicit in the derivatives (with fractional right hand sides).

Thus the quasi-polynomials $P_{m,i}(\mathbf{g}(T,t), \mathbf{a}^{[\infty]}(t), \mathbf{b}_1^{[\infty]}(t), \mathbf{b}_2^{[\infty]}(t), \dots, \mathbf{b}_I^{[\infty]}(t))$ can be replaced by polynomials

$$\bar{P}_{m,i}(\mathbf{g}(T,t), \bar{\mathbf{g}}(T,t), \hat{\mathbf{g}}(T,t), \check{\mathbf{g}}(T,t), \mathbf{a}^{[\infty]}(t), \mathbf{b}_1^{[\infty]}(t), \mathbf{b}_2^{[\infty]}(t), \dots, \mathbf{b}_I^{[\infty]}(t))$$

of variables $\mathbf{g}, \bar{\mathbf{g}}, \hat{\mathbf{g}}, \check{\mathbf{g}}$ and differential polynomials of functions $\mathbf{a}(t), \mathbf{b}_0(t), \mathbf{b}_1(t), \dots, \mathbf{b}_J(t)$.

Denote the variables $\mathbf{g}, \bar{\mathbf{g}}, \hat{\mathbf{g}}, \check{\mathbf{g}}$ by $\mathbf{x} = (x_1, x_2, \dots, x_N)$ and by $\mathbf{u} = (u_1, u_2, \dots, u_K)$, and rewrite the above implicit polynomial differential equation as

$$F(\mathbf{x}, \dot{\mathbf{x}}, \mathbf{u}, \ddot{\mathbf{u}}, \dots) = 0.$$

We also rewrite equation (8) using \mathbf{x}, \mathbf{u}

$$\sum_{0 \leq m < n} \sum_{i=0}^l \bar{P}_{bm, \hat{i}}(\mathbf{x}, \dot{\mathbf{x}}, \mathbf{u}, \ddot{\mathbf{u}}, \dots) (A_i^T)^{m_i} (A_{i-1}^T)^{m_{i-1}} \dots (A_1^T)^{m_1} B_i^T \xi = 0.$$

Define the output equation

$$y = \sum_{0 \leq m < n} \sum_{i=0}^l \bar{P}_{m, \hat{i}}(\mathbf{x}, \mathbf{u}, \dot{\mathbf{u}}, \dots) (A_i^T)^{m_i} (A_{i-1}^T)^{m_{i-1}} \dots (A_1^T)^{m_1} B_i^T \xi = G(\mathbf{x}, u, \dot{u}, \dots, \xi).$$

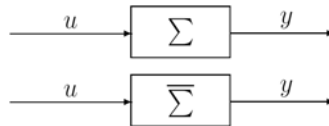
Thus we have an input-output system

$$\begin{aligned} F(\mathbf{x}, \dot{\mathbf{x}}, \mathbf{u}, \dot{\mathbf{u}}, \dots, \xi) &= 0 \\ \mathbf{y} &= G(\mathbf{x}, \mathbf{u}, \dot{\mathbf{u}}, \dots, \xi), \end{aligned} \tag{\Sigma}$$

which is polynomial and implicit in the derivatives $\dot{\mathbf{x}}$, with the regularity condition $\partial_{\dot{\mathbf{x}}} F(\mathbf{x}, \dot{\mathbf{x}}, \mathbf{u}, \dot{\mathbf{u}}, \dots, \xi) \neq 0$. Here \mathbf{u} are the inputs, \mathbf{x} are the states and \mathbf{y} are the outputs. Consider another representation possibly with different states but with the same inputs and outputs

$$\begin{aligned} \bar{F}(\bar{\mathbf{x}}, \dot{\bar{\mathbf{x}}}, \mathbf{u}, \dot{\mathbf{u}}, \dots, \xi) &= 0 \\ y &= \bar{G}(\bar{\mathbf{x}}, \mathbf{u}, \dot{\mathbf{u}}, \dots, \xi). \end{aligned} \tag{\bar{\Sigma}}$$

Let (Σ) and $(\bar{\Sigma})$ be input-output systems. We call them equivalent if for every input-output pair (\mathbf{u}, \mathbf{y}) , has a solution \mathbf{x} if and only if has a solution $\bar{\mathbf{x}}$. In this case the two systems



behave in the same way. Σ and $\bar{\Sigma}$ can be written more briefly also allowing the derivatives of the outputs \mathcal{Y}

$$J(\mathbf{x}, \dot{\mathbf{x}}, \mathbf{u}, \dot{\mathbf{u}}, \ddot{\mathbf{u}}, \dots, \mathbf{y}, \dot{\mathbf{y}}, \ddot{\mathbf{y}}, \dots, \xi) = 0, \quad (10)$$

and

$$\bar{J}(\mathbf{x}, \dot{\mathbf{x}}, \mathbf{u}, \dot{\mathbf{u}}, \ddot{\mathbf{u}}, \dots, \mathbf{y}, \dot{\mathbf{y}}, \ddot{\mathbf{y}}, \dots, \xi) = 0.$$

Diop [1] proved the existence of a finite, purely algebraic algorithm which gives differential polynomials

$$\begin{aligned} \hat{J}(\mathbf{u}, \dot{\mathbf{u}}, \ddot{\mathbf{u}}, \dots, \mathbf{y}, \dot{\mathbf{y}}, \ddot{\mathbf{y}}, \dots, \xi) \\ \hat{G}(\mathbf{u}, \dot{\mathbf{u}}, \ddot{\mathbf{u}}, \dots, \mathbf{y}, \dot{\mathbf{y}}, \ddot{\mathbf{y}}, \dots, \xi) \end{aligned}$$

such that the system (10) is equivalent to the input-output system $\mathbf{u} \mapsto \dot{\mathbf{y}}$ defined by the implicit equation and the non-equality condition

$$\begin{aligned} \hat{J}(\mathbf{u}, \dot{\mathbf{u}}, \ddot{\mathbf{u}}, \dots, \mathbf{y}, \dot{\mathbf{y}}, \ddot{\mathbf{y}}, \dots, \xi) = 0 \\ \hat{G}(\mathbf{u}, \dot{\mathbf{u}}, \ddot{\mathbf{u}}, \dots, \mathbf{y}, \dot{\mathbf{y}}, \ddot{\mathbf{y}}, \dots, \xi) \neq 0. \end{aligned} \quad (11)$$

The latter has no state variable \mathbf{x} , thus we can call the Diop algorithm a state elimination algorithm.

Definition 9. (10) and (11) define equivalent input-output systems if for any input-output pair (u, y) , (10) has a solution with respect to the state \mathbf{x} , i.e., the triple (x, u, y) is a solution to (10) if (u, y) is a solution to the polynomial equation

$$\hat{J}(\mathbf{u}, \dot{\mathbf{u}}, \ddot{\mathbf{u}}, \dots, \mathbf{y}, \dot{\mathbf{y}}, \ddot{\mathbf{y}}, \dots, \xi) = 0$$

and

$$\hat{G}(\mathbf{u}, \dot{\mathbf{u}}, \ddot{\mathbf{u}}, \dots, \mathbf{y}, \dot{\mathbf{y}}, \ddot{\mathbf{y}}, \dots, \xi) \neq 0$$

holds.

Remark. We get this latter by dividing by a differential polynomial in each step of the algorithm, and since the divisor naturally cannot be 0, this must be assumed. Their products form the differential polynomials $\hat{G}(\mathbf{u}, \dot{\mathbf{u}}, \ddot{\mathbf{u}}, \dots, \mathbf{y}, \dot{\mathbf{y}}, \ddot{\mathbf{y}}, \dots, \xi)$. If this product $\neq 0$ then neither of its terms can be 0.

Now returning to the original input-output system (Σ) , taking the „input” $\mathbf{u} = (\mathbf{a}, \mathbf{b}_0, \mathbf{b}_1, \dots, \mathbf{b}_j)$ ordered continuously in a row, we have

$$F(\mathbf{x}, \dot{\mathbf{x}}, (\mathbf{a}, \mathbf{b}_0, \mathbf{b}_1, \dots, \mathbf{b}_j), (\dot{\mathbf{a}}, \dot{\mathbf{b}}_0, \dot{\mathbf{b}}_1, \dots, \dot{\mathbf{b}}_j), \dots, \xi) = 0,$$

$$G(\mathbf{x}, (\mathbf{a}, \mathbf{b}_0, \mathbf{b}_1, \dots, \mathbf{b}_j), (\dot{\mathbf{a}}, \dot{\mathbf{b}}_0, \dot{\mathbf{b}}_1, \dots, \dot{\mathbf{b}}_j), \dots, \xi) = 0.$$

Substituting the input-output pair $((\mathbf{a}, \mathbf{b}_0, \mathbf{b}_1, \dots, \mathbf{b}_j), 0)$ into the state eliminated system obtained from system (Σ) , the equivalence of the systems yields the equation and non-equality

$$\begin{aligned} \hat{J}((\mathbf{a}, \mathbf{b}_0, \mathbf{b}_1, \dots, \mathbf{b}_j), (\dot{\mathbf{a}}, \dot{\mathbf{b}}_0, \dot{\mathbf{b}}_1, \dots, \dot{\mathbf{b}}_j), \dots, 0, 0, 0, \dots, \xi) &= 0 \\ \hat{G}((\mathbf{a}, \mathbf{b}_0, \mathbf{b}_1, \dots, \mathbf{b}_j), (\dot{\mathbf{a}}, \dot{\mathbf{b}}_0, \dot{\mathbf{b}}_1, \dots, \dot{\mathbf{b}}_j), \dots, 0, 0, 0, \dots, \xi) &\neq 0 \end{aligned} \quad (12)$$

which give a sufficient condition that for all inputs \mathbf{u} , the end state $x(T)$ is orthogonal to the given vector

$$\xi \in \text{Im} \left\{ \dots, A_1^{m_1}, A_2^{m_2}, \dots, A_T^{m_T} B_j, \dots \right\} \quad (13)$$

Definition 10. We say that the time-variant coefficients $\mathbf{a}, \mathbf{b}_0, \mathbf{b}_1, \dots, \mathbf{b}_j$ persistently stimulate the system if the subspace of the reachable states coincides with the image space of the generalized Kalman matrix, i.e., it is the largest possible subspace. According to our equations, if the coefficients satisfy the conditions (12) then state ξ must be 0.

The most interesting special case is when the image space of the generalized Kalman matrix is the whole space R^n . Then the coefficients $\mathbf{a}, \mathbf{b}_0, \mathbf{b}_1, \dots, \mathbf{b}_j$ persistently stimulate the system if and only if the system is totally reachable on the interval $[0, T]$.

Thus if the coefficients do not persistently stimulate the system then

$$\begin{aligned} \hat{J}((\mathbf{a}, \mathbf{b}_0, \mathbf{b}_1, \dots, \mathbf{b}_j), (\dot{\mathbf{a}}, \dot{\mathbf{b}}_0, \dot{\mathbf{b}}_1, \dots, \dot{\mathbf{b}}_j), \dots, 0, 0, 0, 0, \dots, \xi) &= 0 \\ \hat{G}((\mathbf{a}, \mathbf{b}_0, \mathbf{b}_1, \dots, \mathbf{b}_j), (\dot{\mathbf{a}}, \dot{\mathbf{b}}_0, \dot{\mathbf{b}}_1, \dots, \dot{\mathbf{b}}_j), \dots, 0, 0, 0, 0, \dots, \xi) &\neq 0 \\ \xi &\neq 0 \end{aligned}$$

can be solved. Regarding the equation as an implicit function of ξ , it can be solved for ξ ,

$$\xi = \hat{f}((\mathbf{a}, \mathbf{b}_0, \mathbf{b}_1, \dots, \mathbf{b}_j), (\dot{\mathbf{a}}, \dot{\mathbf{b}}_0, \dot{\mathbf{b}}_1, \dots, \dot{\mathbf{b}}_j), \dots) \quad (14)$$

Writing this into the two non-equalities we have that the condition of „persistent non- excitation” is the paralel fulfillment of the two non-equalities:

$$0 \neq \hat{G}\left(\mathbf{a}, \mathbf{b}_0, \mathbf{b}_1, \dots, \mathbf{b}_J\right), \left(\dot{\mathbf{a}}, \dot{\mathbf{b}}_0, \dot{\mathbf{b}}_1, \dots, \dot{\mathbf{b}}_J\right), \dots, 0, 0, \dots, \\ \hat{f}\left(\mathbf{a}, \mathbf{b}_0, \mathbf{b}_1, \dots, \mathbf{b}_J\right), \left(\dot{\mathbf{a}}, \dot{\mathbf{b}}_0, \dot{\mathbf{b}}_1, \dots, \dot{\mathbf{b}}_J\right), \dots \\ 0 \neq \hat{f}\left(\mathbf{a}, \mathbf{b}_0, \mathbf{b}_1, \dots, \mathbf{b}_J\right), \left(\dot{\mathbf{a}}, \dot{\mathbf{b}}_0, \dot{\mathbf{b}}_1, \dots, \dot{\mathbf{b}}_J\right) \dots$$

The negation is the condition for persistent excitation,

$$0 = \hat{G}\left(\mathbf{a}, \mathbf{b}_0, \mathbf{b}_1, \dots, \mathbf{b}_J\right), \left(\dot{\mathbf{a}}, \dot{\mathbf{b}}_0, \dot{\mathbf{b}}_1, \dots, \dot{\mathbf{b}}_J\right), \dots, 0, 0, \dots, \\ \hat{f}\left(\mathbf{a}, \mathbf{b}_0, \mathbf{b}_1, \dots, \mathbf{b}_J\right), \left(\dot{\mathbf{a}}, \dot{\mathbf{b}}_0, \dot{\mathbf{b}}_1, \dots, \dot{\mathbf{b}}_J\right), \dots$$

or

$$0 = \hat{f}\left(\mathbf{a}, \mathbf{b}_0, \mathbf{b}_1, \dots, \mathbf{b}_J\right), \left(\dot{\mathbf{a}}, \dot{\mathbf{b}}_0, \dot{\mathbf{b}}_1, \dots, \dot{\mathbf{b}}_J\right) \dots$$

Returning to the solvability of the implicit function of ξ we can obtain (14).

Again, Diop's elimination theorem (algorithm) can be applied. Regard the vector ξ as a state that can be eliminated. For this we would need a state equation, a dynamics, that is, a differential equation for ξ . But since ξ is a constant, the dynamics is simply $\dot{\xi}=0$.

References

- [1] Diop, S. (1991). Elimination in control theory, *Math Control Signals Systems, Signals*, 4, 17-32.
- [2] Fliss M. (1991). Controllability Revisited, in *Mathematical System Theory: The influence of R. E. Kalman*, A.C. Antoulas (Ed.), Springer-Verlag, Berlin.
- [3] Molnár S. and Szigeti F. (2011). A generalisation of Fuhrmann's rank condition for discrete dynamic systems, *Int. J. System of Systems Engineering*, Vol. 2(4), pp. 279-289. DOI: 10.1504/IJSSE.2011.043864
- [4] Silverman L.M. (1967). Controllability and Observability in Time-Variable Linear Systems, *SIAM Journal on Control*, Vol 5(1), pp. 64–73. (10 pages). DOI: 10.1137/0305005
- [5] Szigeti F. (1992). A Differential-Algebraic Condition for Controllability and Observability of Time Varying Linear Systems, *Decision and Control, Proceedings of the 31st IEEE Conference on*, pp. 3088-3090, Tucson, AZ, USA. DOI: 10.1109/CDC.1992.371050
- [6] Szigeti F. (1992). Kalman's Rank Conditions for Infinite Dimensional Time Dependent Linear Systems. In: *Proc. Conf. EQUADIFF*. pp. 927–931, Barcelona, Spain.

- [7] Wei, J. and E. Norman (1964). On Global Representations of the Solutions of Linear Differential Equations as a Product of Exponentials, Proc. Amer. Math. Soc. 15(12), pp. 327-334.

Real-time state observers for solar heating systems

Richárd KICSINY

Department of Mathematics, Institute for Mathematics and Informatics

Abstract

Nowadays it is important to investigate and develop solar thermal heating systems as an environmental friendly technology. In the paper, physically-based linear and nonlinear mathematical models are introduced, which can be applied to a wide range of solar heating systems to analyze and develop them.

A Luenberger type state observer and a global nonlinear state observer are introduced for the linear and nonlinear mathematical models, respectively. The observers enable us to estimate the unmeasured state variables of a solar heating system in real-time.

Comparing calculations and measurements, the usability of the observers is demonstrated for a particular solar heating system producing domestic hot water at the campus of the Szent István University, Hungary.

1. Introduction

It often occurs in technical practice that all variables determining the state of some system are not observed (not measured) as function of time, because for example the needed measurement cannot be carried out physically, since it may be either too complicated, or too expensive. In such a case the estimate of the unobserved (unmeasured) state variables is needed.

In many cases, the problem can be solved by the methods of mathematical systems theory (for a recent reference see Zak (2003)), by determining a so-called *state observer* (or shortly *observer*).

If the estimate of the unobserved state variables is performed in real-time – which means that at any time step of the measurements, the estimated values of the state variables are generated and available by the next time step – then we cannot only monitor the system but also apply a feedback control strategy to it, e.g. for stabilization or optimization.

Nowadays, there is no doubt on the importance to investigate and develop solar heating systems as environmental friendly technology, so the design and application of observers for such systems is an important scope, since all state variables are generally not observed in practice (in commercial solar heating systems), although the knowledge of them could be used for energetic evaluation and controlling purposes.

This paper is a short summary of two works on real-time observers for solar heating systems (Kicsiny and Varga (2012), Kicsiny and Varga (2013)). A linear

mathematical model for solar heating systems (Buzás et al. (1998), Buzás and Farkas (2000)) is used in Kicsiny and Varga (2012), where a classical Luenberger type observer is applied in a novel way, that is, in real-time processes and for solar heating systems. The same novelties (real-time application, solar heating system environment) hold for Kicsiny and Varga (2013), where the nonlinear (and more reasonable) version of the mentioned linear model is worked out, to which a global state observer (Lei et al. (2007), Wei (2006)) is applied.

2. Mathematical models

The linear mathematical model of Buzás et al. (1998) and Buzás and Farkas (2000) corresponds to a quite general kind of solar heating systems, the scheme of which can be seen in Figure 1:

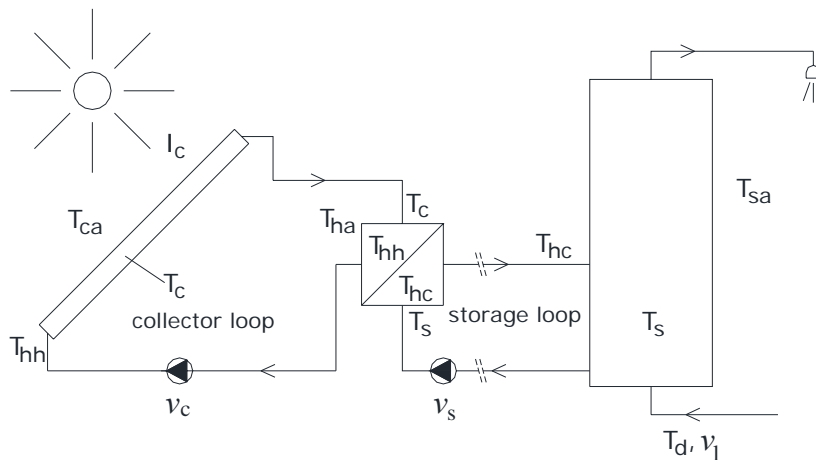


Figure 1. Scheme of the investigated solar heating systems

Notation: T_c : temperature of the solar collector, °C; T_{hh} : temperature at the hot (collector) side of the heat exchanger, °C; T_{hc} : temperature at the cold (storage) side of the heat exchanger, °C; T_s : temperature of the solar storage, °C; I_c : solar irradiance on collector surface, W/m^2 ; T_{ca} : ambient temperature of the solar collector, °C; T_{ha} : ambient temperature of the heat exchanger, °C; T_{sa} : ambient temperature of the solar storage, °C; T_d : tap water temperature, °C; v_c : volumetric flow in the collector loop, m^3/s ; v_s : volumetric flow in the storage loop, m^3/s ; v_l : consumption load of the solar storage, m^3/s .

The linear mathematical model is the following system of ordinary differential equations:

$$\dot{x} = Ax + Bu, \quad (1)$$

where

$$x = \begin{bmatrix} T_c \\ T_{hh} \\ T_{hc} \\ T_s \end{bmatrix}, \quad u = \begin{bmatrix} I_c \\ T_{ca} \\ T_{ha} \\ T_{sa} \\ T_d \end{bmatrix}, \quad B = \begin{bmatrix} \frac{A_c \eta_0}{\rho_c c_c V_c} & \frac{U_L A_c}{\rho_c c_c V_c} & 0 & 0 & 0 \\ 0 & 0 & \frac{A_a k_a}{2} & 0 & 0 \\ \frac{c_h m_h}{2} + \rho_c c_c \frac{V_h}{2} & 0 & 0 & 0 & 0 \\ 0 & 0 & \frac{A_a k_a}{2} & 0 & 0 \\ \frac{c_h m_h}{2} + \rho_c c_c \frac{V_h}{2} & 0 & 0 & 0 & 0 \\ 0 & 0 & 0 & \frac{A_s k_s}{\rho_s c_s V_s} & \frac{v_l}{V_s} \end{bmatrix},$$

$$A = \begin{bmatrix} -\frac{U_L A_c}{\rho_c c_c V_c} - \frac{v_c}{V_c} & \frac{v_c}{V_c} & 0 & 0 \\ \frac{\rho_c c_c v_c}{\frac{c_h m_h}{2} + \rho_c c_c \frac{V_h}{2}} & -\rho_c c_c v_c - \varepsilon k_h A_h - \frac{A_a k_a}{2} & \frac{\varepsilon k_h A_h}{\frac{c_h m_h}{2} + \rho_c c_c \frac{V_h}{2}} & 0 \\ 0 & \frac{\varepsilon k_h A_h}{\frac{c_h m_h}{2} + \rho_c c_c \frac{V_h}{2}} & -\rho_s c_s v_s - \varepsilon k_h A_h - \frac{A_a k_a}{2} & \frac{\rho_s c_s v_s}{\frac{c_h m_h}{2} + \rho_s c_s \frac{V_h}{2}} \\ 0 & 0 & \frac{v_s}{V_s} & -\frac{v_l - v_s}{V_s} - \frac{A_s k_s}{\rho_s c_s V_s} \end{bmatrix},$$

where the following parameters are used: A_c : collector surface area, m^2 ; η_0 : optical efficiency of the collector; ρ_c : collector fluid density, kg/m^3 ; c_c : specific heat capacity of the collector fluid, $J/(kgK)$; V_c : volume of the solar collector, m^3 ; U_L : overall heat loss coefficient of the solar collector, $W/(m^2K)$; c_h : specific heat capacity of the heat exchanger material, $J/(kgK)$; m_h : mass of the empty heat exchanger, kg ; V_h : total volume of the heat exchanger, m^3 ; εk_h : heat transfer coefficient inside the heat exchanger, $W/(m^2K)$ (where $\varepsilon=1$, based on Buzás and Farkas (2000)); A_h : surface area of the heat transfer inside the heat

exchanger, m^2 ; k_a : heat loss coefficient of the heat exchanger to the ambiance, $W/(m^2K)$; A_a : surface area of the heat exchanger to the environment, m^2 ; ρ_s : density of water, kg/m^3 ; c_s : specific heat capacity of water, $J/(kgK)$; V_s : volume of the solar storage, m^3 ; A_s : outside surface area of the storage, m^2 ; k_s : heat loss coefficient of the storage to the environment, $W/(m^2K)$.

In the nonlinear model of Kicsiny and Varga (2013), \dot{T}_s is determined in the same way as in the linear model, but εk_h is replaced with $k_3 \left(\frac{v_c + v_s}{2} \right)^{\frac{4}{5}} + k_4$ (where k_3 and k_4 are heat exchanger parameters) in the corresponding places in the determination of \dot{T}_{hh} and \dot{T}_{hc} . Furthermore, \dot{T}_c is determined in the following way, which involves nonlinearity:

$$\dot{T}_c = \begin{cases} \frac{A_c \eta_0}{\rho_c c_c V_c} I_c + \frac{k_1 A_c}{\rho_c c_c V_c} (T_{ca} - T_c) - \frac{k_2 A_c}{\rho_c c_c V_c} (T_{ca} - T_c)^2 + \frac{v_c}{V_c} (T_{hh} - T_c), & \text{if } (T_{ca} - T_c) \in]-\infty, \Delta T_1[\\ \frac{A_c \eta_0}{\rho_c c_c V_c} I_c + A + \frac{v_c}{V_c} (T_{hh} - T_c), & \text{if } (T_{ca} - T_c) \in]\Delta T_1, +\infty[\end{cases} \quad (2a)$$

where ΔT_1 is the maximum point of $\frac{k_1 A_c}{\rho_c c_c V_c} (T_{ca} - T_c) - \frac{k_2 A_c}{\rho_c c_c V_c} (T_{ca} - T_c)^2$ as a function of $T_{ca} - T_c$ and $A = \frac{k_1 A_c}{\rho_c c_c V_c} (\Delta T_1) - \frac{k_2 A_c}{\rho_c c_c V_c} (\Delta T_1)^2$ (k_1 and k_2 are collector parameters).

The nonlinear model proved to be a bit more accurate than the linear one, c.f. Kicsiny and Varga (2012) and Kicsiny and Varga (2013).

3. State observers

After complementing system (1) with $y = Cx$, where vector y contains the observed state variables from x according to C (e.g. $[0 \ 1 \ 0 \ 0]$,

$$\begin{bmatrix} 1 & 0 & 0 & 0 \\ 0 & 0 & 1 & 0 \end{bmatrix}, \begin{bmatrix} 1 & 0 & 0 & 0 \\ 0 & 0 & 1 & 0 \\ 0 & 0 & 0 & 1 \end{bmatrix}), \text{ the used Luenberger type state observer}$$

(Luenberger (1964)) is the following:

$$\dot{z} = Fz + Bu + Hy, \quad (3)$$

where $F = A - HC$ and H is such that the real parts of all eigenvalues of F are negative.

Then the state estimate vector $z(t)$ (with four coordinates) asymptotically approaches vector $x(t)$ in model (1) (see Kicsiny and Varga (2012) for more details).

Thus the unobserved state variables of x can be (asymptotically) estimated with the corresponding coordinates of z .

In Kicsiny and Varga (2013), a global state observer (Lei et al. (2007), Wei (2006)) has been applied to the nonlinear model of Section 2 aiming at the same estimating purposes.

Global means that vector $z(t)$ approaches vector $x(t)$ from any initial condition, in contrast to local observers that generally used in nonlinear systems, in which $z(t)$ approaches $x(t)$ only if the initial condition of system (3) is close enough to the initial condition of the corresponding mathematical model.

Application

In Kicsiny and Varga (2012), the above methodology has been applied to a solar domestic water heating system at the campus of the Szent István University, Hungary (Farkas et al. (2000)) after validation as follows.

The system has a collector field with 33.3 m² area and a solar storage with 2 m³ volume.

For any given date, the measurements of all state variables (T_c, T_{hc}, T_{hh}, T_s), v_c, v_s, v_l , and the coordinates of u are available. Nevertheless, only T_c and T_s are considered observed (measured) now, the monitored values of T_{hh} and T_{hc} serve only for comparison purposes. The measured day is 3rd April, 2011.

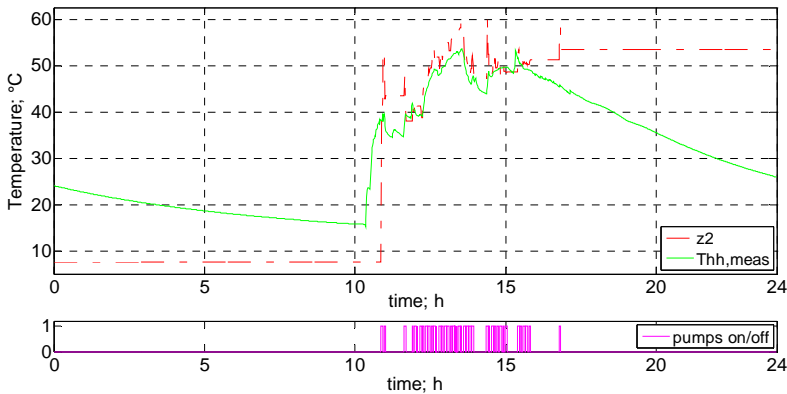


Figure 2. $z_2, T_{hh,meas}$ and the operating state of the pumps on 3rd April, 2011

Figure 2 and 3 compare the measured and estimated (z_2, z_3) state variables of T_{hh} and T_{hc} , respectively. The operating state of the pumps (on/off) can be

also seen in each figure. The estimating process can be applied only if the pumps are on (see Kicsiny and Varga (2012) for more details), so the error evaluation has been made for this time.

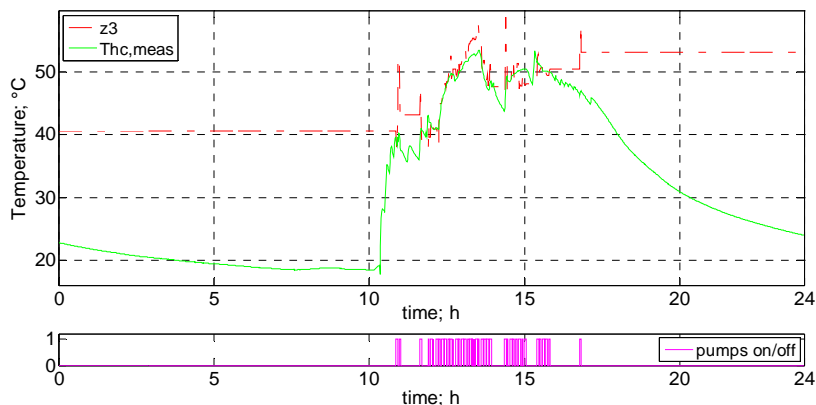


Figure 3. z_3 , $T_{hc,meas}$ and the operating state of the pumps on 3rd April, 2011

The average of the absolute difference between the estimated and measured temperatures for the time when the pumps are on is 2,9°C and 1,8°C in case of the hot and cold sides of the heat exchanger, respectively. In proportion to the difference between the maximal and minimal measured temperature values, the average of the absolute error for the time when the pumps are on is 7,5% and 5,2% in case of the hot and cold sides of the heat exchanger, respectively.

Similar results have been gained with the nonlinear global state observer in Kicsiny and Varga (2013).

Conclusion

The studied linear and nonlinear state observers are based on a linear and a nonlinear mathematical model with physical foundations (white-box models), so they can be required to approximate well the real operation of solar heating systems. This expectation is fulfilled as it can be stated that, considering the comparison with measurements and taking the aims of the observers (studying the processes and maybe developing the efficiency of solar heating systems), they model the real processes characteristically right and, for the general engineering practice, with convenient accuracy.

It should be also stated that the state estimate vector z approaches the real data more reasonably if the pumps are on. This is not surprising, since the existence of an observer is mathematically guaranteed only in case of switched on pumps.

The state observers enable us to make a real-time estimate of the unmeasured state variables of solar heating systems, which can be used for several purposes

(e.g. energetic and efficiency calculations, working out feedback control strategies, etc.).

The linear and nonlinear observers are global, in contrast to the generally used local ones, so they are relevant for real-time monitoring of systems far from equilibrium.

The proposed observer methodology can be used not only for solar heating but also for any systems modelled with similar ordinary differential equations, and this occurs in many fields of engineering sciences.

References

- [1] Zak, S. H. (2003), *Systems and Control*, Oxford University Press, New York-Oxford.
- [2] Kicsiny, R., Varga, Z. (2012), Real-time state observer design for solar thermal heating systems. *Applied Mathematics and Computation* 218, pp. 11558-11569.
- [3] Kicsiny, R., Varga, Z. (2013), Real-time nonlinear global state observer design for solar heating systems. *Nonlinear Analysis Real World Applications* 14, pp. 1247-1264.
- [4] Buzás, J., Farkas, I., Biró, A., Németh, R. (1998), Modelling and simulation of a solar thermal system. *Mathematics and Computers in Simulation* 48, pp. 33-46.
- [5] Buzás, J., Farkas, I. (2000), Solar domestic hot water system simulation using block-oriented software. *The 3rd ISES-Europe Solar World Congress (Eurosun 2000)*, Copenhagen, Denmark, CD-ROM Proceedings (2000) pp. 9.
- [6] Lei, H., Wei, J., Lin, W. (2007), Design of dynamic high-gain observers for a class of MIMO nonlinear systems. *Control Theory and Related Topics, In Memory of Xunjing Li* (ed. by S. Tang, J. Yong), World Scientific Publishing Co. Pte. Ltd., Singapore, 2007.
- [7] Wei, J. (2006), Observation and estimation of nonlinear systems. PhD thesis, Case Western Reserve University.
- [8] Luenberger, D. G. (1964), Observing the state of a linear system. *IEEE Transactions on Military Electronics* 8, 2, pp. 74-80.
- [9] Farkas, I., Buzás, J., Lágymányosi, A., Kalmár, I., Kaboldy, E., Nagy, L. (2000), A combined solar hot water system for the use of swimming pool and kindergarten operation. *Energy and the Environment*, Vol. I. /ed. by B. Frankovic/, Croatian Solar Energy Association, Opatija (2000), pp. 81-88.

Institute for Process Engineering



Professor Dr. János BEKE
Director of the Institute

Dear Reader,

It is a great pleasure to introduce a small part of our research activities that is determined by the structure of the institute. The Institute for Process Engineering is a notable education and research unit at the School of Mechanical Engineering that can be originated in the integrations of two earlier independent departments (Automotive and Thermal Technologies, and Energetics and Food Industry). The current institute consists of three professional working areas (Automotive Technologies, Energetics and Measurement Technologies)

On the base of our mission statement our educational and scientific activities pay special respects to the following topics: a) Basic technical knowledge forming the appropriate engineering approach, b) Engineering thermodynamics, electrical engineering and electronics, c) Basic and applied knowledge of energy conversion, energy utilization and energy economy, d) Special technical knowledge for development of environmental industry and utilization of alternative energy sources, e) Basic and applied knowledge of automotive and off-road techniques and technologies, f) Disciplines of measurement technology and process engineering needed to control, regulate and automate different engineering processes, g) Environmental- and market-conscious development of production and processing technologies.

In the last year we mainly focused on the following scientific topics:

- Making measurements to develop soil database and a computer simulation to determine the dynamical properties of vehicles at the point where they leave the road and derive an appropriate run-off-the-road accident simulation model.
- Challenges and possibilities of utilizing different types of the environmental energies in connection with the Hungarian national energy policy.
- Investigation of environmental-friendly de-icing methods for roads, bridges, overpasses etc by using heat energy.
- Analysing the role of wind energy in fulfilling the duties of the energy sector – before all – from technical and energetic points of view.
- Modelling different mechanical engineering processes based on up to date metrological methods. Inside this activity we tested typical, but rarely used models that seem suitable to simulate energetic processes.

More details and other information can be found: www.fomi.gek.szie.hu

De-Icing of Road Surfaces (Bridges) with Heat

László TÓTH, Norbert SCHREMPF, János BEKE
Department of Energetics, Institute for Process Engineering

Abstract

The rapid changes of weather, like sudden cooling, especially when it comes with moisture can cause dangerous traffic situations (personal injuries and significant property damage) for those who use roads, bridges, interchanges. These weather conditions are responsible for the most of winter traffic jams.

The maintenance of these roads means mechanical removal of snow or scattering of surfaces (to decrease freezing of surfaces). The usage of salt is disadvantageous because it causes corrosion, it is texture wrecking and it is harmful to the environment.

The bridges and overpasses cool down earlier than the average roads. The road maintainers have the responsibility to guarantee the safe transport on winter roads.

Tasks of road maintainers (prevention):

- bridges, overpasses;
- airport roads, highways;
- hilly bus routes;
- roads of residential institutions (hospitals, food supplies).

In developed countries (Japan, USA, Germany, etc.) already 20-25 years ago more environmental friendly solutions were evolved. In our work we analyse the heating of a non-identified real bridge (and overpass) with additional calculations.

This article was written with the help of a TÁMOP 4.2.1.B-11/2/KMR-2011-0003 „INCREASING THE QUALITY OF LEARNING AND RESEARCH” program

Keywords

De-icing, geothermic energy, heat pump

1. Introduction

Heating with stored sun energy

The well documented experimental unit, **SERSO** was put in operation in 1994 in Switzerland. It is constructed to avoid icing on bridges. The construction is still operable.

The system collects *heat from sun energy* and it stores it in underground probes. (Fig.1). The stored heat is used in wintertime. The temperature of road surface is always calibrated above 0°C before snowing. This way the de-icing is continuous and the interruption of traffic can be avoided. The experiences show that the

maximum summer surface temperature decreased, whilst the minimum winter temperature increased. This helped to lengthen the lifetime of the tread of the road.

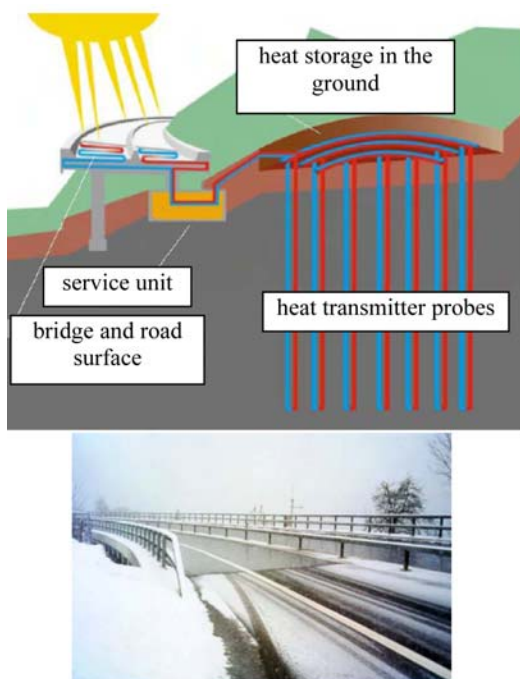


Figure 1. SERSO system and winter view

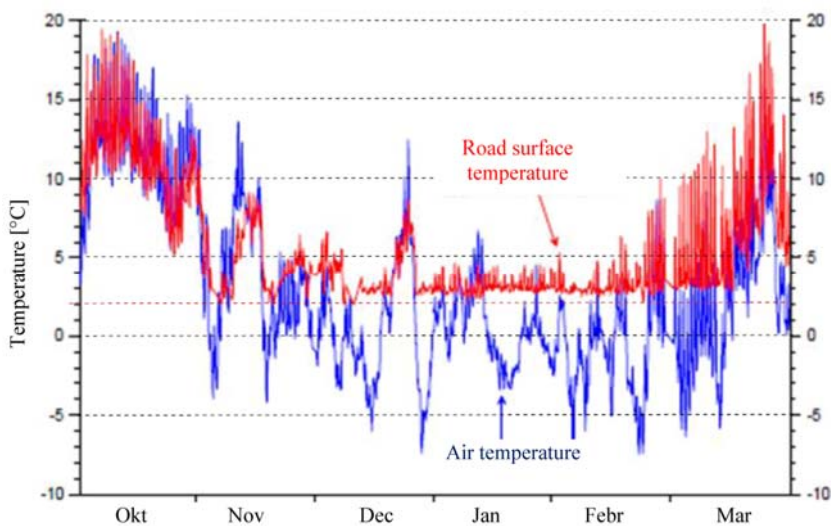


Figure 2. The temperature of air and road surface in winter heating time, SERSO

The heated surface is 1300m². The heat is stored in 55000m³ cubic capacity. It is operated by a 65 m depth system which consists of 91 closed probes. The yearly operating time is ~1000 hours heating at winter and ~1000 hours cooling in summer time.

At winter the input temperature is 10°C bigger than the actual air temperature. The energy demand of the road is 30-100MWh which needs a system performance of 100W/m². With the continuous winter operation the sudden big heat transfer demand can be avoided (melting down the snow layer). The installation costs of the experimental SERSO system is huge: 2500 Euro/m². It is twice as big as other service units. The operation cost is 4.0€/m²/year

Sun collector system

In 1982 the first sun collector system (Denver, Colorado) was installed with a sealed big buffer tank, heat exchanger and exothermic tubes. More controllers are needed for system efficiency. The needed heat amount was calculated with a computer program. According to experience 39.7kWh/m² amount of energy is needed in the winter season to keep the temperature on 1.0°C for which 200W/m² performance is needed. This performance is not enough in case of a big storm, when the roads are frozen. According to measures 1.3kWh/m² energy is needed to melt 2.5 cm snow. The temperature must be kept between 59 and 86°C in the buffer tank. According to experience storage of 541m³ is needed for a 930m² surface bridge.

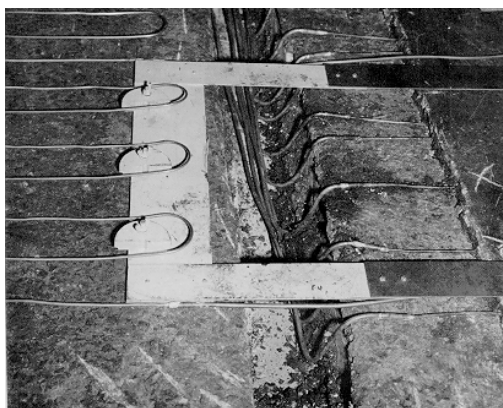


Figure 3. Electric cables in the bridge structure (New Jersey)

Heating with electricity

In Denver experiments were done on the Mississippi road with infra-red lamp heating. The lamps were put at the lower part of the bridge, the capacity was 75W/m².

In 1961 *electric heating cables* (Fig.3) were installed in a ramp of a bridge in New Jersey.

The cables were laid down in two lines. The ramp was 256 m long. The heating cables were buried in a 13mm thick sand-bitumen layer. Above it a 38 mm layer was placed. The needed performance was in average 400W/m^2 which was enough to melt 25 mm of snow. The yearly operation cost was ~ 5 dollar/ m^2 .

Similar systems were built in Ohio, Oregon and in Texas.

Heating with natural gas

In Lincoln (Nebraska) (Fig.4) 9.5 mm tubes were used 152 mm deep with 250 mm splitting and with 127 mm long upfront and backward cables. The system was built in 1993 and a gas water-heater gives the needed heat. The bridge was 367 m long and 3.7 m wide. The heat medium was a mixture of propylene-glycol and water. 454 mass flow provides the 473W/m^2 heating demand. The heating system is controlled by a sensor. The boiler starts to operate when the bridge temperature is below 4°C and stops when the temperature of the bridge reaches 13°C .



Figure 4. Heating system Nebraska, Lincoln



Figure 5. The bridge over the Buffalo river (Virginia)

The bridge over the Buffalo river (Virginia) is 35.7 m long and 13.4 m wide. (Fig.5) The structure is made from steel girders and bitumen. The heat demand of the bridge is 630W/m^2 and the heating system consists of steel tubes. Near the bridge a propane boiler heats 50% mixture of glycol and water. The tube in the tube (89/152mm) runs besides the bridge.

The heat is conducted with tubes (outer diameter 22 mm, inner cross section is 13 mm). These tubes are 178 mm far from each other.

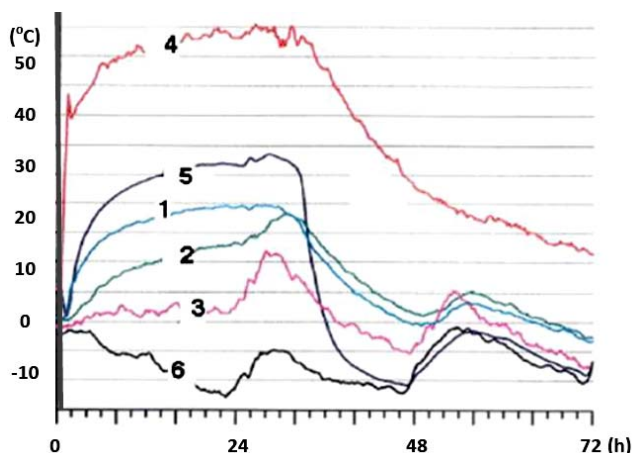


Figure 6. Temperature of structure units 1-outer surface, 2- inner surface, 3 – lower surface, 4 – heating fluid input temperature, 5 – heating fluid output temperature, 6 – air temperature

The heating starts when the sensor senses moisture and the surface temperature is $1.7\text{ }^{\circ}\text{C}$. The heating switches off when the sensors does not sense moisture for longer than 10 minutes or the surface temperature is bigger than $4.4\text{ }^{\circ}\text{C}$.

2. Bridges heated with thermal energy

A 122 m long hot water heating system was installed into a bridge in Oregon (1950). The system used thermal water well. 13 mm copper tubes were laid down in which frost-proof material was circulated. Because of continuous circulation the system can keep the surface of the bridge snow and freeze-free.

In 1970 in Larimi the lateens heat energy of evaporating fluid condensation was used. In the heating system which consisted of 60 tubes, ammonium was used. The lower part of bridge was heated. This heat was enough to prevent freezing and to melt snow. Its biggest disadvantage was the difficulty of tube mounting. The 40% of the whole cost is the drilling cost and the tube mounting cost.

In Oregon the heated surface of a two lane bridge is 576m^2 . 15.9 mm outer diameter polyethylene tubes with 12.7mm inner diameter were used. The tubes were 114 mm far from each other. The circulated fluid is 35% propylene-glycol

which by-passes the heat exchanger with 49°C and returns with 32°C. The energy which is distracted from the well comes with 568l/min mass flow. The heating starts when there is temperature and moisture sensing. The heating is operating between 1.7°C and 2.8°C. The primer side pump operates before the heating is started. The plastic tubes run between bitumen steel. The system was built in 1995 and it is still running efficiently.

In Amarillo (Texas) a two lane bridge (17.7 m wide, 44,5 m long, heated surface is 799m²) is the example. The aim was to avoid icing, the heat demand was 129W/m². The geothermal energy is gained from closed system probes (50 pieces). The probes have 102mm diameter and they are 53.6 m deep. The heat transfer medium is 50% of propylene glycol and water (11.3 m³). On secondary side the tubes have 32 outer diameter and 19 mm inner diameter. The splitters and collectors are under the bridge. The sensor in the bridge body automatically starts the heating when the temperature is 1.7°C (Fig.7).



Figure 7. Heating tubes in the road surface

In Turkey 50-75 mm polyethylene tubes were layered in the bridge, with 150-300 mm spread. At this area 600 mm thick snow layer is not rare. They are heating with geothermal energy. The heat comes from closed probe holes 30-90 m deep.

There are more examples of working systems (Japan, Germany, and Sweden).



Figure 8. The bridge in winter time



Figure 9. The water well during construction

In Canada, Essex a water well system was developed. It is easier and cheaper. The basic unit is more expensive and it can be used only appropriate conditions. (Fig. 8, and 9).

According to literature experience, we examined the possibilities of closed probe heat pump systems in Hungary. In Hungary the heat density ($q = -\lambda \text{grad}T$) is 90-100mW/m², which is advantageous in case of heat pump technology.

Hungarian Practice

In Hungary the de-icing is done with salt-sand scattering and with snow monitors in general. Advantage: ongoing and cheap. Disadvantage: it is more time consuming, it takes time for the machines to get to the scene. Under this time interval ice can form under the snow. Its biggest disadvantage is the negative effect of salt. Salt harms the structure of the bridges and harms the environment as well.

The night freezing is followed by daytime melting, when the salty water spills into the bitumen cavities and it can crack the layer. The interaction of the bitumen and salt is dangerous, the iron structure can corrode. The steel under mechanical stress is corrosion sensitive.



Figure 10. The impact of salt on the bitumen structure

The mentioned disadvantages can be avoided with heat pumping.

Heat pump systems can be good solutions for heating and cooling of buildings, heating water, or for de-icing roads and bridges. With this method the lifetime of bridges can be lengthened, if in the summer season the road surface is cooled. For our model we used the features of an imaginary bridge or overpass.

3. The features of the selected model

The heated surface is 400m^2 , one lane is 3 m wide, the width of the road is 6m and the length of the bridge is 66.7m. The outside temperature is -15°C . The ground is solid rock; the heat outcome is 60W/m . The basic element of the system is the compressor heat pump which is connected to a 100 m deep closed probe. The average temperature of the 100m deep probe is 14°C .

The new structure of the bridge (Fig.11):

1. 250 mm wide ferroconcrete plate
2. 50 mm insulation
3. 120 mm concrete with diameter 20 mm heating tubes inside (2mm wall thickness)
4. 40mm bitumen layer
5. Geocell insulation:

The Geocell insulation is often used at garages and has more positive features for our example.

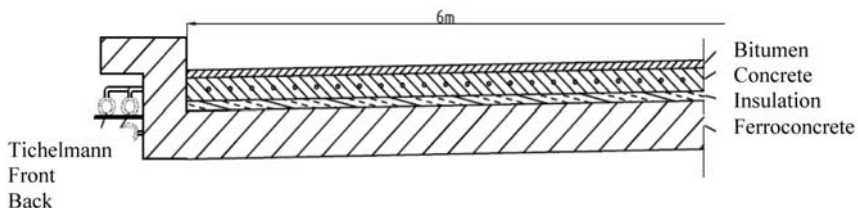


Figure 11. Cross section of the bridge

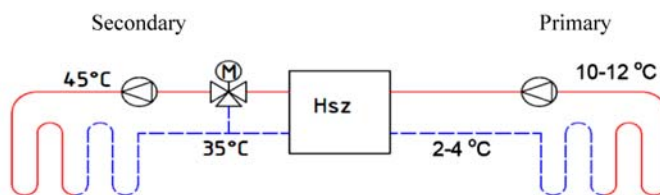


Figure 12. Temperature features of front and back side

Due to the Tichelmann tubes in the bridge the control is more efficient and easy. The heat-transmitting medium is 40% ethylene glycol-water mixture. Its freezing point is -25°C and the boiling point is 104.4°C .

The surface of the wrap is 4°C which is enough to be completely freeze-free. With the control of mass flow we adjust the secondary side front temperature to 45°C and the back to 35°. On primary side we adjust the back temperature of glycol to 10-12°C and the front side to 2-4°C. (Fig.12).

The probes are 7 m far from each other. On secondary side the tube's cross section is 20mm and it is 2mm thick.

Secondary side heat calculations: (for the heat calculations we used measurement programs, we do not introduce the method itself

Needed heat-flow for de-icing of the surface:

$$\dot{Q}_{\text{needed}} = \alpha * A_{\text{complete}} * (t_{\text{surface}} - t_{\text{outer}}) = 182400 \text{ W} = 182.4 \text{ kW}$$

where:

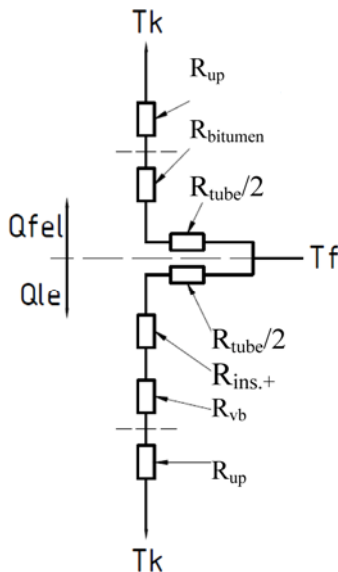
α – outer side heat transfer factor of the wall $\left[\frac{\text{W}}{\text{m}^2 \text{ K}} \right]$

A_{complete} – heated surface of the bridge $[\text{m}^2]$

t_{surface} – planned surface temperature $[\text{K}]$

t_{outer} – temperature of air which contact the bridge $[\text{K}]$

The bridge contacts the air above and under as well and the mass flow spreads in the tubes upwards and downwards. On the basis on this method we defined the layers as cascading resistors (we analysed layer thickness and t- tube spreads).



Summary of resistors above the tube:

$$\Sigma R_{\text{up}} = \frac{R_{\text{tube}}}{2} + R_{\text{bitumen}} + R_{\text{up}} \quad \left[\frac{\text{K}}{\text{W}} \right]$$

Summary of resistors under the tube:

$$\Sigma R_{\text{down}} = \frac{R_{\text{tube}}}{2} + R_{\text{ins.}+} + R_{\text{vb}} + R_{\text{down}} \quad \left[\frac{\text{K}}{\text{W}} \right]$$

Heat flow in t tube spread (upwards) :

$$\dot{Q}_{\text{up}} = \frac{T_{\text{middle}} - T_{\text{outer}}}{\Sigma R_{\text{up}}} \quad [\text{W}]$$

Heat flow in t tube spread (downwards) :

$$\dot{Q}_{\text{down}} = \frac{T_{\text{middle}} - T_{\text{outer}}}{\Sigma R_{\text{down}}} \quad [\text{W}]$$

Figure 13. Layers and their resistance

Heat flow of the complete bridge cross section:

$$\sum \dot{Q}_{up} = \dot{Q}_{up} \cdot \frac{bridge\ length}{t} \cdot [W]$$

Heat flow of the complete bridge cross section downwards:

$$\sum \dot{Q}_{down} = \dot{Q}_{down} \cdot \frac{bridge\ length}{t} \cdot [W]$$

Needed heat flow for the tube, with which the \dot{Q}_{needed} can be satisfied:

$$\sum \dot{Q} = \sum \dot{Q}_{up} + \sum \dot{Q}_{down} = 201,5kW$$

COP = 4.0 calculated vaporizing side performance: 157.9kW, for it 28 probes are needed (100 m deep)

Table 1. Chosen heat pump: Viessmann Vitocal 300-G Pro BW2180

Heating performance	248kW
Cooling performance	200.8kW
Electric performance	50.2kW
COP	4.84
Work medium	R410A

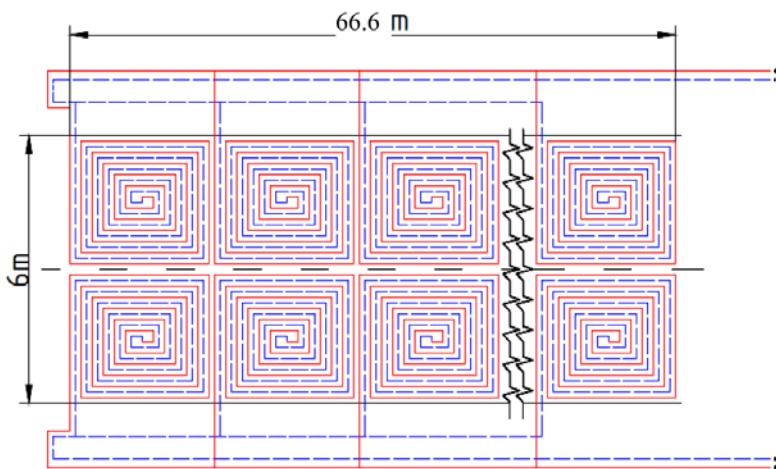


Figure 14. Secondary side Tichelmann construction and spreader tubes

According to secondary side hydraulic calculations (Fig.14), 82 m tube is needed with an inner cross section of 16mm and 40 units are needed. The needed mass flow per tube is 0.1385liter/s, the flow velocity is 0.689m/s, $Re=5286$ and the complete mass flow is $19.95m^3/h$. The cross section of the main spreaders is 100mm and the divider's cross section is 70 mm. Secondary side hydraulic lifting height is 15.

Primary side

Tubes of the probes: ϕ 32/26mm hard polyethylene tube with simple U construction (Fig.14)

Needed mass flow per probes: 0.187kg/s, flow velocity 0.335m/s, $Re=4172$, complete mass flow 4.87 kg/s, hydraulic lifting height 5,7 m. Cross section of spreader/collector main tubes (needed 94mm), chosen $\phi 100mm$, spreaders/collectors to probes: $\phi 75mm$.

Starting protocol:

The aim is to avoid icing on roads with snow melting. For this the road surface temperature must be kept above $2^{\circ}C$. When the sensor senses fast cooling under $6^{\circ}C$ ($0.5^{\circ}C/10perc$) and the road surface is under $3^{\circ}C$, the primary and the secondary probes start and the heat pump start as well. The heating is operating until the road surface temperature is permanently ($>1,h$) above $2^{\circ}C$.

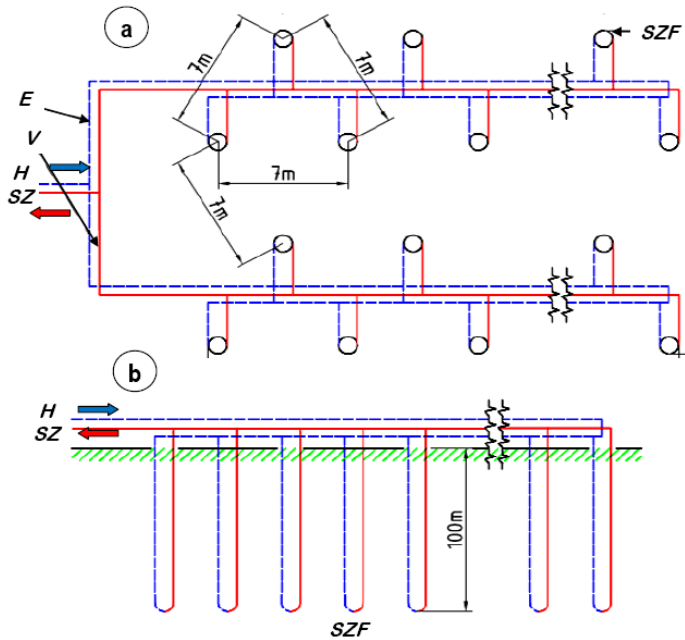


Figure 15. Primary side construction
(a – top view. b – connection cross section)
E - front, V - back, SZF- probe holes, HSZ – heat pump connection.

Important notes:

- The tubes must be fixed to the steel bars, to ensure the 125 mm tube spreading.
- The spreading back and front tubes must be insulated with 50mm thick rock wool. The tubes must be set up with metal coating and mechanical protection. The tubes must be supplied with loader and un-loader switches.
- A three way valve must be installed in the secondary branch for leading the 35°C fluid back in the system.

4. Economical background

Complete costs for the geothermic heat pump system (machine units, planning construction works, operation trial, guarantee): 92.0 million HUF.

Building costs of a new bridge: (similar to existing Hungarian examples): 360.0 million HUF.

Operation cost for 1600 operation hours :1.05 million HUF.

Yearly interest rate and stock cost for 30 years: ~3.5 million HUF

The system cost is the 25% of the bridges cost, and the 20% of the installed bridges cost. If the bridge is maintained in every 10 years, which is 10% of the whole investment: 44.0 million HUF. For one year it is 4.4 million HUF.

If the bridge needs to be maintained every 15 years, than the saving is 1.5million HUF/year. The cost of salt scattering approx. 0.3million HUF.

From the data it can be seen that the return of investment is 35-40 years. But the aim of the investment is not to reach profit, but to avoid dangerous traffic situations and to increase the safety of traffic.

5. Recommendation

This investment needs big stock and its return is very long and not even probable. But if we take into account that the lifetime of the bridge is increasing, and the probability of accidents decreases (e.g. the access of hospitals is better), than the investment is worth to start.

Not just salt scattering, but the summertime high temperature can cause harm in the bridges. Strong sunlight softens the bitumen, and heavy vehicles can make holes on the road which may cause accidents. In summertime the fluid is circulated with the secondary side pump, which causes heat loss. In extreme hot weather the heat pump must be started in cooling modus. With this temperature the construction becomes more balanced. This causes extra cost, which lengthens the lifetime of the bridge.

In case of multiple usages the economic aspects are better:

The installed system can be used for other tasks, because it can produce energy in summer time.

The cooling temperature of the heat pump is 200.8 kW which is enough to cool a nearby building. It even can create hot water for personal usage.

If these heat quantities are sold, than the utilization interval is longer and the return of the investment improves.

References

Article

- [1] L. David Minsk: 1999 Heated Bridge Technology Report on ISTEA, Sec. 6005 Program Washington, DC 20590 Publication No. FHWA-RD-99-158
- [2] J. D. SPITLER, 2000 Bridge Deck Deicing using Geothermal Heat Pumps Oklahoma State University Stillwater, OK, U.S.A.
- [3] Ádám, B.- Tóth, L.: 2011. Talajok hőtechnikai ellenőrzése függőleges elrendezésű hőszondák telepítéséhez, MAGYAR ENERGETIKA Nr. 5, 34-38 pp ISSN: 1216-8599, (in Hungarian)
- [4] Tóth, L. Ádám, B.: 2010. Adatok magyarországi sekélyszondás hőszivattyús rendszer telepítéséhez, Mezőgazdasági Technika, Gödöllő, 51. évf. 8. sz. 2-5p. ISSN 0026 1890, (in Hungarian)

Publication:

- [5] NRW: GeoVerSi - Geothermie sorgt für Verkehrssicherheit. Studie des Ministerium für Verkehr, Energie und Landesplanung des Landes Nordrhein-Westfalen, Düsseldorf, 2005
- [6] Tóth, L.: 2012. Alternatív energiaellátási rendszerek az agrárgazdaságban, Magyar Agrárkamara, Szaktudás Kiadó Ház, Budapest, ISBN 978-615-5224-22-5, 312 p. (in Hungarian)

Proceedings'

- [7] W. J. Eugster: 2007 Road and Bridge Heating Using Geothermal Energy. Overview and Examples. Proceedings European Geothermal Congress

Websites:

- [8] <http://www.bkk.hu/fejleszteseink/margit-hid-felujitasa/> (in Hungarian)
- [9] http://www.siriusprodukt.hu/files/CaCl2_alkalmazasa.pdf
- [10] <http://www.betonopus.hu/notesz/fagyallobeton.pdf> (in Hungarian)
- [11] www.specialterv.hu (in Hungarian)
- [12] http://www.engineeringtoolbox.com/ethylene-glycol-d_146.html
- [13] <http://www.bkk.hu/fejleszteseink/margit-hid-felujitasa/> (in Hungarian)

Run-Off-Road Vehicle Speed Analysis from Terrain Tracks

László MÁTHÉ, Péter KISS, Lajos LAIB,
György PILLINGER, Gábor MAGDICS

Department of Automotive Technology, Institute for Process Engineering

Abstract

Analysis of a „run-off” accident requires a knowledge of the physical properties of the soil, otherwise any evaluation can only be approximate. In order to reconstruct a run-off accident one must examine the soil’s mechanical parameters and create a soil database. The purpose of our project was to make measurements for a later soil database and a computer simulation to determine the speed of a vehicle at the point where it left the road. A series of measurements were performed for this purpose at the Department of Automotive Technology of the Szent István University to obtain data for a soil database as part of a project to develop a run-off-the-road accident simulation model. The model is designed to determine the speed of the vehicle as it leaves the road. Knowledge of this speed is crucial in the investigation of such accidents, and investigators have to estimate it from vehicle tracks left on the road and on the adjacent terrain. The model may be validated and verified by determining the soil-vehicle resistances on relevant terrain. In our paper we introduce a set of computations capable of computing the vehicle’s initial velocity.

Keywords

accident analysis, soil-tire interaction, terramechanics, soil-mechanical parameters

1. Introduction

The results of terramechanics research can be usefully applied to describe the motion of vehicles moving on terrain. These include agricultural and forestry vehicles [Kiss and Laib, 1999] [Nam et al., 2010], military and civilian off-road vehicles, mining and earthmoving machines and planetary rovers developed for space research [Patel et. al., 2010]. Vehicles which leave the built road and continue their way on terrain also belong to this category.

In some road accidents, the vehicle leaves the surfaced road and runs on to the adjacent terrain. An important item of information in the analysis of such accidents is the vehicle’s speed, a knowledge of which permits the circumstances of the accident to be reconstructed. There are developed and widely-accepted methods of analysis for road accidents, but hardly any methods for terrain

accidents. Hugemann [2007] has stated that computer simulation analysis of accidents occurring on terrain can only give approximate results. It is necessary to measure the soil mechanics parameters to make a good assessment of terrain accidents. Accident analysis must incorporate the soil-tire interaction and the effect of soil mechanics parameters on the vehicle's mobility.

Recent developments in vehicle-terrain interaction theory offer a means of assessing the motion of a vehicle on terrain. Different areas of application typically use different results of vehicle-terrain interaction theory.

Aim of research

The main aim of the research presented here is to determine the initial speed of a vehicle entering terrain at the moment it runs off the road. Staff of the Department of Automotive Engineering of Szent István University carried out a series of field measurements with the primary aim of recording data for set up a later soil database to be used in the simulation of motion of vehicles involved in run-off accidents. The measurements were used to determine travel resistances which acting against the rolling of the wheel, a required parameter for the determination of speed.

A vehicle leaving a surfaced road enters the adjacent terrain with a certain kinetic energy. Its motion is affected by larger terrain obstacles and by vibrational acceleration induced by micro-obstacles. The deceleration and halting of the vehicle is influenced by travel resistances arising from the vehicle-soil interaction. The run-off speed (initial speed) of a vehicle which comes to a halt on the terrain may be calculated indirectly knowing the travel resistances and the distance traveled on the terrain.

2. Acting forces and resistances on the vehicle on terrain

For the general case of a vehicle running on to terrain, the energies of the phenomena acting on it are described by the equation of motion generally used for vehicles supplemented with the energy losses of vibration acceleration and macro-obstacles:

$$\begin{aligned} \frac{m \cdot \Delta v^2}{2} = & \text{Energy lost to travel resistances} + \\ & + \text{Energy lost to vibration acceleration} + \\ & + \text{Energy lost to macro-obstacles} \end{aligned} \quad (1)$$

Where Δv is the change of speed of vehicle after leaving the road and m is vehicle mass.

In the case when the vehicle stops after traveling a distance s on the terrain, the run-off speed is calculated from:

$$\frac{1}{2} \cdot m \cdot \Delta v^2 = F_t \cdot s \quad (2)$$

Where F_t is the tractive force (against the vehicle's motion).

This is what the simulation model is designed to determine. Deceleration and stopping are largely governed by the resistances arising from the vehicle-terrain interaction. The run-off speed can therefore be calculated indirectly from the equation of vehicle motion and the energy equation derived from it.

Travel resistances

The following equation describes the motion of the vehicle in the direction of travel and expresses that the tractive force is equal to the total of travel resistances:

$$F_t = F_{rr} + F_{air} + F_s + F_{slip} \quad (3)$$

Where F_{rr} is rolling resistance, F_{air} is the air resistance, F_s is slope resistance, and F_{slip} is slip loss.

Substituting into equation (2):

$$\frac{1}{2} \cdot m \cdot \Delta v^2 = (F_{rr} + F_s + F_{air} + F_{slip}) \cdot s \quad (4)$$

If the vehicle stops on the terrain, i.e. its speed becomes zero, then Δv is equal to the run-off speed ($v_{run-off}$):

$$v_{run-off} = \sqrt{\frac{2 \cdot (F_{rr} + F_s + F_{air} + F_t + F_{slip}) \cdot s}{m}} \quad (5)$$

Knowledge of the vehicle's speed is crucial in accident investigations. Investigators attempt to determine the speed of the vehicle in each case from tracks left on the surfaced road or the terrain. The biggest problem arises with the terrain, whose effects can be approximated by only empirical quantities.

Determination of the speed requires a knowledge of the coefficient of rolling resistance on the specific soil. After an accident, the only information available comes from the tracks, the cone index measurement, and the soil type. There are several mobility models in the literature, of which the Turnage model [Rebati and Loghavi, 2006] was selected as the most appropriate for the present research. This model uses the soil cone index (CI) and the vehicle parameters (wheel width, B ; wheel diameter, D ; profile height, h ; tire deflection, δ ; and load on front wheel, W). Using this mobility model, the empirical formula by McAllister [Rebati and Loghavi, 2006] may be used to determine the rolling resistance factor.

The Turnage mobility model is stated as

$$M = \frac{CI \cdot B \cdot D}{W} \cdot \left(\frac{\delta}{h}\right)^{0.5} \cdot \left(\frac{1}{1 + \frac{B}{2 \cdot D}}\right) \quad (6)$$

Using this model, McAllister derived two relations to determine the rolling resistance factor in terms of the construction of the tire. For diagonal ply tires, the following applies:

$$C_{RR} = \frac{0.323}{M} + 0.054 \quad (7)$$

Where C_{RR} is the coefficient of rolling resistance and M is defined in equation (6). Rolling resistance may be partly or fully substituted by the bulldozing phenomenon or, in case of overturning, vehicle body friction.

Field measurements

The main purpose of the field measurements was to determine the rolling resistance factor and the bulldozing factor on soils of various load-bearing capacity (cone index). Measurements of deceleration distance were also carried out on a moving vehicle left to roll in neutral to determine the motion resistances of the vehicle on terrain.

Determination of coefficient of rolling resistance by pulling test

The test field had an area of 300x100 m. The tests were carried out on the same field on soil in three different conditions: wheat stubble, harrow-tilled wheat stubble and subsequent tilling by cultivator. Measurements were also made on concrete. The measurements were carried out on 60 m test strips (Figure 1), comprising a 10 m approach and deceleration sections and 25 m measurement section. For each soil condition, measurements were made with four different tire inflation pressures, so that there were four measurement sections on each area – stubble, harrowed and cultivated. To enable determination of the vertical soil deformation, every measurement had to be carried out on an undeformed area of ground. The vehicles used for the measurements were a John Deere 6600 tractor, the pulling vehicle, and GAZ-69 four-wheel drive vehicle, which was pulled.

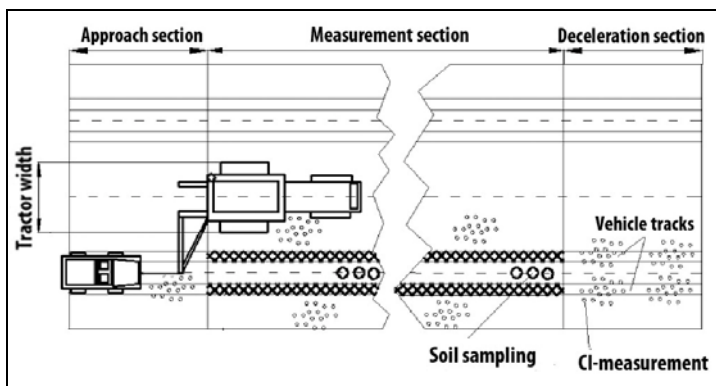


Figure 1. Pulling test.

A special drawbar mechanism was designed to ensure that the vehicle did not travel along the tracks of the tractor towing it. One of the main parameters measured was the pulling force, which was the towing force applied to the towed vehicle. The tire inflation pressures on the front and rear axles were 1.5, 1.8, 2.1, 2.4 bar. Speed of travel of towed vehicle was $v = 10$ km/h.

Measurement on concrete surface

Towing on concrete corresponds to the deformable tire-rigid track interaction. Comparison of the measurement on concrete with those on agricultural land yields the tire deformation loss. Here, the vehicle was not towed using the drawbar designed for terrain, because there is no significance in having a virgin (undeformed) surface. The towed vehicle was coupled behind the tractor, and the pulling force and accelerations were measured.

Measurement procedure:

- The boundaries of the measurement section over which the wheels of the test vehicle have to pass were marked out.
- The towing vehicle coupled to the towed vehicle was set up on the measurement area in accordance with the ground plan.
- The tractor started to pull the vehicle, and after the towing speed (10 km/h) was reached, the time, distance and five acceleration measurements began.
- Upon reaching the end of the measurement section, the tractor and towed vehicle slowed down and stopped.
- The measurement was repeated three times for all four tire inflation pressures.

Measurement on arable land

The special drawbar used for towing on arable land enabled the test vehicle to travel over an undisturbed surface. The main measurements in the arable-land tests were of rolling resistance, pulling force, slip, soil deformation and wheel accelerations.

Measurement procedure:

- The measurement section was surveyed and marked out with posts and ropes.
- The route of the towed vehicle was marked out.
- The soil profile was recorded on the designated track at 10 cm intervals, with 101 measurements on each wheel track path before and after towing, a total of 404 recordings for each pulling test.
- Soil samples were taken from the soil surface between the two tracks, every five meters, using three sampling cylinders.
- The cone index was measured on the vehicle tracks before and after the test.
- The moisture content was measured by in-situ instruments beside every soil sampling point and in the route marked out for the tire track.
- The tractor and vehicle were set up on the marked-out section.
- The vehicle was towed at 10 km/h.
- The soil mechanics measurements were repeated after the vehicles had traversed the test section, as described above.

Bulldozing effect

Field measurements were also carried out to measure the bulldozing effect and thus obtain the coefficient of bulldozing resistance for the model. The measurements were performed using a towed vehicle. The vehicle was accelerated to three different speeds, and then the vehicle brake was applied to cause bulldozing at the wheel. The speeds were 10, 15 and 20 km/h, and each test was performed on a previously undisturbed surface of stubble, harrowed and cultivated land. After the tire sank into the soil and caused bulldozing, the depth of sinking and the height of soil building up in front of the wheel were measured. The pulling force and acceleration were also measured in the tests.

Measurement with driven vehicle

The purpose of the measurement was to test the deceleration of the vehicle in varying terrain conditions (soil conditions). The measurements were carried out on concrete, a grassy surface, stubble, and harrowed and cultivated soil. The measurements were performed with a driven vehicle at tire inflation pressure of 2.1 bar and speeds of 10, 20 and 30 km/h. After the vehicle reached the desired speed and reached a designated measurement point, the driver put the vehicle into neutral and allowed it to freewheel. When it stopped, the distance between the measurement point and the stopping point was measured. This gave information on how the travel resistances slowed down and stopped the vehicle on soil of different cone index, and how far the vehicle traveled before it stopped.

Equipment used

The following equipments were used at the tests: Purpose-designed drawbar mechanism, converted forklift (Figure 3); 50 kN load cell; 3-axis acceleration sensors; Spider-8 data collection and measurement computer (GDS Instruments, Hampshire, United Kingdom); Shaft encoder (“fifth wheel”); Eijkelkamp Penetrologger (Eijkelkamp, Giesbeek, The Netherlands); PCE-SMM-1 field soil moisture meter (PCE Instruments, Southampton, United Kingdom); Terrain profile recorder; Soil sampling cylinders; Wheel load weighers to measure vehicle weight.



Figure 3. Purpose-designed drawbar mechanism

3. Results

Table 1 shows the physical characteristics of the test field. The measurements were performed with the help of staff of the Institute of Soil Science (Szent István University).

Table 1. Physical properties of the test field.

Field condition:				
Soil type:				
Moisture content (% dry basis)	[%]	15.8	11.5	10.8
Pore volume	[%]	36	38	42
Dry bulk density	[g/cm ³]	1.61	1.65	1.52
Vegetation:	-	Stubble+weeds	A few weeds	No plants

Constant quantities:

- $m_v = 1600$ kg Vehicle weight with driver
- $v = 10$ km/h Vehicle speed
- $CI_{\text{concrete}} = 80$ N/mm² Load-bearing capacity of concrete
- $F_{\text{air}} = 6.266$ N Air resistance (at a speed of 10 km/h)

The rolling resistance factor for each soil type and tire inflation pressure was calculated from the test figures. The results are shown on Table 2.

Table 2. Pulling test results and calculated coefficients of rolling resistance.

	TIP [bar]	F _t [N]	slope angle [°]	slip [%]	F _{rr} [N]	F _s [N]	F _{slip} [N]	C _{RR} [-]
Concrete	1.5	336.1	0	0.6	327.8	0	2.0	0.021
	1.8	258.1	0	1.1	248.9	0	2.8	0.016
	2.1	211.2	0	1.9	200.9	0	4.0	0.013
	2.4	167.7	0	2.9	156.5	0	4.8	0.010
Stubble field	1.5	1326.8	0.92	2.8	1031.3	252.0	37.1	0.066
	1.8	1583.5	1.10	2.8	1231.5	301.3	44.3	0.078
	2.1	1527.3	1.17	2.8	1157.7	320.4	42.7	0.074
	2.4	1463.4	0.90	3.0	1166.6	246.5	43.9	0.074
Disc- tilled field	1.5	749.2	1.13	2.8	412.4	309.5	20.9	0.026
	1.8	1438.7	0.91	2.8	1142.8	249.2	40.2	0.073
	2.1	1378.6	1.22	2.8	999.5	334.1	38.6	0.064
	2.4	1693.2	1.07	2.8	1346.4	293.1	47.4	0.086
Cultivator-tilled field	1.5	2817.4	1.21	4.8	2344.4	331.4	135.2	0.149
	1.8	2876.6	1.29	4.8	2378.8	353.3	138.0	0.152
	2.1	2667.4	1.22	4.8	2198.9	334.1	128.0	0.140
	2.4	2841.7	1.11	4.8	2394.9	304.0	136.4	0.153

Table 3 gives the cone index values characterizing the soil's load-bearing capacity.

Table 3. Soil cone index and moisture content in undisturbed soil.

	Depth[cm]					Moisture content [% dry basis]	
	5	10	15	20	25		
Field condition	Cone index (CI) [MPa]					Avera.	
Stubble field	0.434	0.692	0.854	1.183	1.511	0.935	15.04
Disc-tilled	0.590	1.473	1.711	1.903	2.449	1.625	13.05
Cultivated	0.034	0.108	0.546	1.461	2.010	0.832	10.63

Table 4 gives the figures from the bulldozing test and the calculated coefficient of bulldozing resistance (C_{BR}).

Table 4. Coefficients of bulldozing resistance.

	TIP [bar]	m_v [kg]	CI [MPa]	v [km/h]	F_{tmax} [N]	C_{BR} [-]
Stubble field	2.1	1600	0.935	10	12780	0.814
				15	14210	0.905
				20	11170	0.712
Disc-tilled field	2.1	1600	1.625	10	16310	1.039
				15	16760	1.068
				20	19280	1.228
Cultivator-tilled field	2.1	1600	0.832	10	20730	1.321
				15	17410	1.109
				20	18510	1.179

Table 5 shows the deceleration lengths traveled after the driven vehicle was put into neutral. The tests were performed at various speeds at constant tire inflation pressure.

Table 5. Deceleration length test results.

	TIP [bar]	m_v [kg]	CI [MPa]	C_{RR} [-]	V [km/h]	S [m]
Concrete	2.1	1600	80	0.013	10	20.73
					20	74.10
					30	164.98
Grass	2.1	1600	1.864	-	10	11.20
					20	28.15
					30	64.60
Disc-tilled field	2.1	1600	1.625	0.064	10	3.43
					20	10.35
					25	10.80
					30	18.20
Cultivator-tilled field	2.1	1600	0.832	0.140	10	2.50
					20	7.48
					30	15.15
					35	22.50

4. Discussion

The measurements on arable land were required to construct the model being developed for the research project. They will provide the basic data for the model's soil database. The most important data are the rolling and bulldozing resistances, the cone index and the moisture content.

The coefficients of rolling resistance in each measurement area were determined at various tire inflation pressures, and are given in Table 2. The coefficient of rolling resistance was between 0.010 and 0.021 on concrete, 0.066 and 0.078 on stubble, 0.026 and 0.086 on disc-tilled soil, and 0.140 and 0.153 on cultivator-tilled soil, depending on the tire inflation pressure. The coefficient of bulldozing resistance determined from the bulldozing tests is shown on Table 4. Its magnitude was between 0.712 and 0.905 on stubble, 1.039 and 1.228 on disc-tilled soil, and 1.109 and 1.179 on cultivator-tilled soil. The cone index and moisture content are given in Table 3. The cone index in undisturbed soil was 0.618-1.163 MPa on stubble, 1.466-1.795 MPa on disc-tilled soil and 0.699-1.025 MPa on cultivator-tilled soil. The soil moisture content on the test field varied between 9.25 and 16.75 %. Table 5 gives the deceleration distances measured for a vehicle rolling in neutral after reaching a specified speed.

Conclusion

The measurement results demonstrate that rolling resistance decreased as cone index increased. On loose soils, coefficients of rolling resistance are higher than on a hard surface. This was borne out by measurement on concrete.

The change in the coefficient of bulldozing resistance is related to the load-bearing capacity of the soil. The coefficient of bulldozing resistance rose above 1.00 on cultivator-tilled and harrowed areas and approached this figure on harrowed areas. The lower figure for stubble was due to the thin covering of vegetation which reduced the potential for bulldozing to occur.

The longest deceleration distances were measured on concrete, where there was least resistance acting on the vehicle. The next longest were on the grassy field, whose surface also presents a low travel resistance. The distances on harrowed and cultivator-tilled areas were almost identical. The vehicle deceleration here was highest, owing to the high coefficients of rolling and bulldozing resistance.

With knowledge of the vehicle mass, the distance traveled on the terrain, and the effects of the soil parameters, then if the other forces acting on the vehicle are known, the speed of the vehicle as it left the road may be calculated.

Acknowledgement

Research was supported/subsidized by the TÁMOP-4.2.2.B-10/1-2010-0011 „Development of a complex educational assistance/support system for talented students and prospective researchers at the Szent István University” project.

References

- [1] Hugemann, W. (2007): Unfallrekonstruktion, Band 1.Grundlagen (Accident Reconstruction, Vol. 1. Bases). Münster, Germany, Schönbach-Druck GmbH, pp. 222-226.
- [2] Kiss, P. and Laib, L. (1999): Determination of the absorbed energy by the soil in the soil-tire interaction. Proceedings of the 13th International ISTVS Conference pp. 361-373. Munich, Germany
- [3] Nam, J. S., Park, Y. J. and Kim, K. U. (2010): Determination of rating cone index using wheel sinkage and slip. *J Terramechanics* 47(4):243-249.
- [4] Patel, N., Slade, R. and Clemmet, J. (2010): The ExoMars rover locomotion subsystem. *J Terramechanics* 47(4):227-243.
- [5] Rebati, J. and Loghavi, M. (2006): Investigation of rolling resistance prediction models for pneumatic tire of agricultural vehicles. *Iran Agricultural Research* 25(1):77-88.

Utilisation possibilities of environmental energy carriers

László TÓTH, János BEKE, Péter SEMBERY
Department of Energetics, Institute for Process Engineering

Abstract

Hungary as the member country of European Union has joined the common binding target of 20% renewable energy from final energy consumption by 2020, and aims at increasing the share of renewable energy sources from gross final energy consumption to 14.65%. In this reason the gross quantity of renewable energy sources would add up to 165-170 PJ by 2020, which is to be used for electric power supply, traffic, heating and cooling purposes. The increase in the generation of renewable electric power has increased primarily due to biomass utilization up to now. By 2010, the amount of renewable electric power reached 2,9 TWh/year, being equal to 7.1% of the net domestic electric power generation. Biomass was started to be utilized in greater quantities in 2004, the largest part of which was used to generate electric power. The reason for this was that user infrastructure did not require substantial investments, only traditional coal burning power stations had to be converted to multi-fuel power stations.

Keywords

biomass, renewable energy, energy policy

1. Introduction

The overall energy consumption in Hungary is about 1160-1200 PJ. This means the amount of primer energy sources, and real consumption is approximately 30-35% lower. The difference comes from conversion losses and the own consumption of energy converters. The major consumers include the inhabitants, traffic, industry and service industries.

Hungary has also joined the European Union's binding target of 20% renewable energy from final energy consumption by 2020, and aims at increasing the share of renewable energy sources from gross final energy consumption to 14.65% (Government Decision No 1002/2011 (I.14.)). By this, the gross quantity of renewable energy sources would add up to 165-170 PJ by 2020, which is to be used for electric power supply, traffic, heating and cooling purposes.

The increase in the generation of renewable electric power has increased primarily due to biomass utilization up to now. By 2010, the amount of renewable electric power reached 2600-2900 GWh/year, being equal to 7.1% of the net

domestic electric power generation. The volume of biomass utilization became stable by 2009-2010, within which the amount of biogas consumption slightly increased, on the other hand, wind energy consumption raised to a significant extent, adding up to 620 GWh/year in 2010 [2].

2. Utilisation course of environmental energy carriers

Biomass was started to be utilized in greater quantities in 2004, the largest part of which was used to generate electric power. The reason for this was that user infrastructure did not require substantial investments; only traditional coal burning power stations had to be converted to multi-fuel power stations. The disadvantage of the technology is that the so-called waste heat produced during the generation of electric power in power stations can only be utilized to an insignificant extent, which causes a very low energy transformation efficiency of 20-30% (Figure 1).

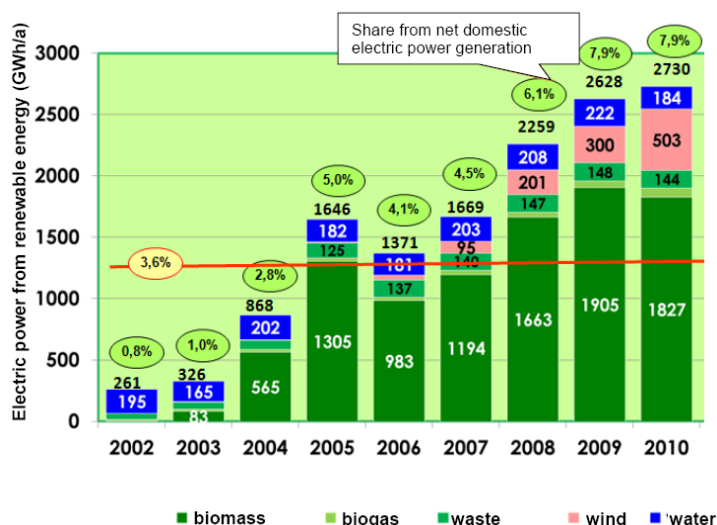
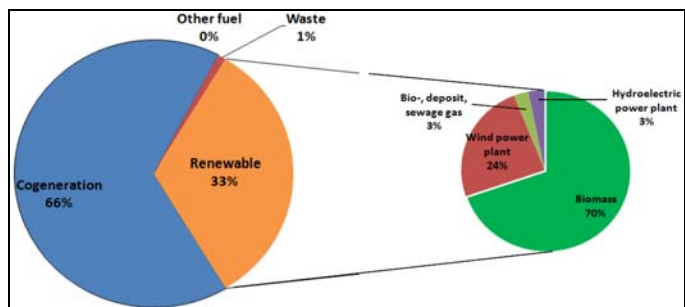


Figure 1. Generation of electric power from alternative energy sources

This quick rise was promoted by the support of the government given to the generation of electric power from biomass, irrespectively of the efficiency of production and utilization. Significant subsidies were provided to cogeneration (CHP) gas-fired power stations as well. Thus, 80-90 thousand million Hungarian forints were flown annually to cogeneration small power plants and renewable electric power suppliers as subsidy by 2010. From which 19-20 thousand million Hungarian forints were subsidy on electric power produced from biomass and 8-9 thousand million Hungarian forints were subsidy on other renewable sources like

water, wind, geothermic, solar and other energy sources. The largest part of the subsidy was used to develop cogeneration power plants (Figure 2):



	mill. HUF
Cogeneration	56680
Waste	827
Other fuel	0
Renewable	28007
Biomass	19520
Wind power plant	6812
Hydroelectric power plant	802
Bio-, deposit, sewage gas	873

Figure 2. The amount (in HUF) and rate of state subsidy in 2010

Even forestry experts agreed on that it was time to cut down and use the surplus, aged and sometimes ill trees although it occasionally led to misuse. The price of wood and the income of forest managers considerably increased. [6].

Seeing that deforestation was excessive in some places and the efficiency of transformation was low, the government withdrew the subsidy by 2011 from large non-cogeneration biomass-fired power plants and small amortised CHP gas-fired power plants. As a result, the amount of electric power output reduced to 1375 GWh in 2011, as against to the planned amount of 1870 GWh. Some ‘worn-out’ biomass-fired power plants were even closed down.

The government intends to implement a really ambitious plan on the utilization of renewable energy sources by 2020. The *National Action Plan* (NAP) specifies the production of electric power capacity of approximately 1530 MW by 2020 in the frame of a 14.65% renewable energy program (Figure 3).

The NAP continues to calculate with biomass as the major renewable energy source. Solid biomass primarily includes firewood produced by traditional silviculture, agricultural by-products and plant-chips from energy plantations. Significant improvement is expected in the fields of biogas, agricultural wastes

and residual materials from communal sewage purification plants. Wind energy utilization is of high volume, and is intended to be increased by 120%.

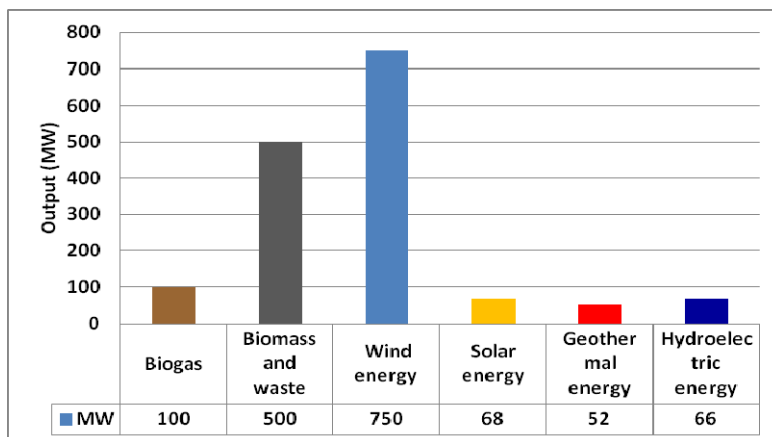


Figure 3. Expected electric power production capacity by 2020 [7].

To reach the planned renewable electric power production of 5500-5600 GWh/year by 2020, *biomass* (including biogas) production and partially wind energy have to be increased significantly. Importance of heat pump can appreciate as well. Utilization of thermal energy based on electric power raises economy questions due to the multiple transformations. It can be found many examples for spread of heat pump application. [4, 5].

Biomass

From biomass we can produce heat energy, electric power and various gaseous, liquid or solid fuels (such as oil, alcohol, gas, biogas, chips, pellets, etc.).

Oil, alcohol and gas are used as fuels, while solid processed materials, for instance chips, pellets, briquettes are mainly utilized to produce heat. [9].

It has to be acknowledged and should not be disregarded that the production of various biomasses requires substantial amount of energy (e.g. for converting herbaceous plant biomass into hard fuel pellet). Efficiency is demonstrated by the OUTPUT/INPUT (O/I) rate comparing the chemically bonded energy content of the end-product before use to the total energy content of all the energy sources used for production. In professional literature sometimes very beneficial rates are stated, for instance the O/I rate for hard stem energy plantation collected to the edge of fields is 15-20. It has to be noted that this rate is reduced by transportation, shopping and preparation, depending on the energy requirement of technologies, to O/I = 3-6 or even lower. [8].

From the aspect of energetics, the amount of so-called *net energy gain* is to be examined, taking into consideration, in addition to the above, conversion losses as well. When only electric power is produced from biomass, the I/O rate does not

exceed 3.0. When only thermal energy is generated (for heating) the O/I rate can be as many as 6, which is, of course, reduced by transportation.

These figures also indicate that biomass is not practical to be used only for generating electric energy. Combined production is much more advantageous when all the heat is utilized in addition to the generation of electric power. In this case, the efficiency rate is almost equivalent to heating (Figure 4).

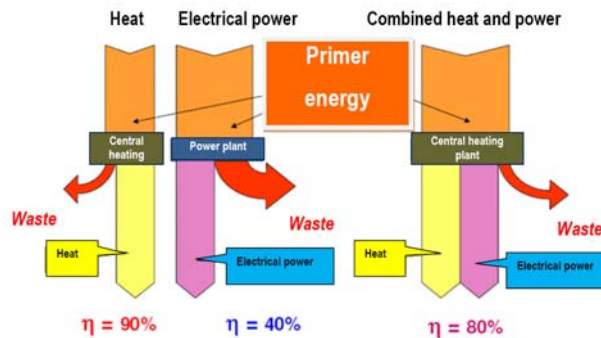


Figure 4. Efficiency of SHP and CHP power generation [10].

There are a lot of estimations known on the total energetic biomass potential of Hungary. Some of which calculates with 200-300 PJ/year as the possible upper limits. It is estimated that the average biomass production from agriculture is approximately 100 PJ, while the maximum production is 170 PJ. The most important factor of uncertainty is the possible utilization of various biological by-products as the amount of cereal straw, corn-stalk, grape-shoot, etc. depends highly on weather.

Biofuels

The amount of cereals and oil seed crops used for biofuels adds up to 4% of the annual raw material production of the world.

In 2010, 21 million m³ biodiesel was produced in the world, 56% of which was produced in Europe. Biodiesel is mixed into diesel oil in the rate of 5%. This rate has to be doubled by 2020. The required production capacity (23 million m³) is practically available, which is now operated with a utilization rate of 56%. In several countries where biodiesel was offered as a separate fuel, it was withdrawn from the supply of filling stations as price differences dropped to the minimum in comparison to traditional diesel oil, significantly reducing its market advantage.

In Hungary, biodiesel is marketed as a component of traditional diesel oil mixed in at a rate of 4.7%, which is to be increased to 8% by 2020. The biodiesel production capacity established so far in the country (180 thousand tons) is capable of meeting the demand of fuel producers and distributors.

To achieve the mixing quota planned and undertaken by 2020, 240 thousand m³ biodiesel will be required. This can be obtained from the processing of oil-seed

rape (95%) and a minimum amount of sunflower produced in Hungary at the present level of production. It is also possible to increase the production capacity. Biodiesel production and utilization in Europe may be influenced by the market prices of oil-seed crops which has shown continuous increase lately.

Bioethanol is used as a component of petrol-driven motor vehicles mixed in the fuel E85 and partially as a separate fuel. Last year, 4.4 million m³ bioethanol was produced in the European Union, and 6.1 million m³ was mixed in petrol, 27.9% of which came from import. European bioethanol producing capacity adds up to 7 million m³, but it only operates with a utilization rate of 62.8 due to the high raw material (cereal) prices. In order to reach the targets by 2020, the EU has to increase bioethanol production to at least the double of the present amount, i.e. to 12-14 million m³. Within the EU, only France, Spain and Hungary are capable of exporting bioethanol.

In Hungary, significant bioethanol production capacity has been established. In the near future, production capacity in the country will reach 810 thousand m³/year. The majority of the product is exported as the amount used at present in Hungary is 75 thousand m³/year, which will be increased to not more than 140 thousand m³/year by 2020.

Biogas

Biogas production based on agricultural primary and secondary by-products and other biological wastes has increased substantially in the world. Europe is in the vanguard as more than 8500 biogas plants are operated here.

In Hungary, 46 biogas-producing plants are run at this time with an overall electric power generation capacity of 37 MW, from which 31 plants use agricultural raw materials and the rest produces biogas from food and communal wastes or sewage sludge. The majority of the plants built in the vicinity of livestock farms and mainly using animal slurry and plant-based raw materials (silage, hay, residuals of cereal cleaning, etc) or food industry wastes have an output of 600-700 kW. The results of the common research between Szent István University and the University of Szeged show that the beneficial effect thermal pre-treatments for aerobic biodegradability and biogas yield. [1, 3].

Using the biogas-producing capacity installed in the recent past, the country is able to produce 150-170 GWh/year electric power. This amount can be tripled or quadruplicated by 2020. It is important to ensure that waste heat is also utilized (for heating, drying, heating green-houses, warm-water fish-breeding) as this is required for the economic operation of plants. A solution could be the purification and concentrating of biogas (biomethane), enabling it to be fed into the natural gas network or used as fuel in motor vehicles.

3. Ecological sustainability

Experts involved in agriculture and soil management are right in criticising the utilization of cereal straw and corn-stalk for energy purposes and state that these materials are needed to maintain soil fertility and provide nutrition for the soil as

a living organism. Accordingly, a substantial part of these materials has to be returned in the soil to maintain the original structure, water storage capacity of soil and to provide materials (carbon, minerals, microelements, etc.) required for plant growth. These experts claim that by continuously removing the yield from the field we degrade the soil, reducing its productivity as well as the nutritive value of the plants produced there.

The removing of some by-products such as grape-shoots, fruit trimmings does not mean significant ecological harm, however, they are not really important from energetic aspects either as their energy density is so insignificant in an unprocessed form that their transportation is not economic for distances above 20-25 km. Many people have reservations, with good reasons, about the utilization of wood produced in our forests in electric power plants, and the state subsidy provided for this.

Between 2004 and 2010, an annual amount of 6.4 PJ (400 thousand tons) wood was fired in Hungarian power plants, which requires over 500 thousand hectares of forests in addition to the usual timber felling. This was enough for 5% of the domestic electric power demand.

In the case of energy forests, much smaller areas are needed as much larger amounts of wood can be produced with 2- or 3-year turns. Professional literature contains very different data for this as well ranging from 2.0 to 14.0 tons of annual yield per hectare. Misinterpretations in evaluations are caused by that the moisture content of wood is not defined when yield is given. Fire-wood was traditionally used after a 3-year delay period in air-dry condition, which is not possible these days. Even if the wood is cut in winter with low moisture content and is used after a delay period in the next heating season, the moisture content will not be lower than 40-50% and the maximum net calorific value will only be 11-13 MJ/kg.

Calculating with the averages of values defined in literature for agricultural by-products, about 6500000 tons could be collected annually. Energy content is calculated in the next table:

By-product	Energy content	Energy content	Operational energy rate	Fossil requirement
Tons/year	GJ/tons	PJ/year	O/I	PJ/year
6 500 000	13	85	5/1	17

Thus, calculating with 50% transformation efficiency, the amount of utilized energy is 42.25 PJ/year, which does not reach 5% of total domestic energy need, and it requires a fossil usage of 17 PJ/year. [11].

Biomass utilization for the purposes of electric power generation diminished considerable even in 2011 because the state subsidization of electric power was ceased. In accordance with the NAP, the restoration of the subsidy cannot be expected. Biomass utilization for heating can only be performed in larger village

or city central heating plants (industrial, public utility, private sector). The majority of these will apply cogeneration systems favourable from the aspect of energy efficiency as only these types will obtain state subsidy in the future. Such facilities can be utilized for longer times and with higher effectiveness. The same applies to labour utilization, and the return of invested capital is of higher chance.

4. Alternative electric power program

Figure 5 demonstrates the planned increases in electric power by 2020.

The plan shows that the present biomass production is intended to be increased by about 70%. Accordingly, the increase in biomass has to be doubled in comparison to the level of the year 2012 to achieve the target by 2020. However, the development requires substantial costs: 580-650 million euros (160-180 thousand million Hungarian forints) only for the power plants, which will give an overall amount of about 300-350 thousand million Hungarian forints together with infrastructural facilities.

Ecological sustainability also sets a limit to the plan as the expected increases in food production also have to be taken into consideration.

The concept of decentralized biomass-firing small power plants is reasonable especially when raw materials can be provided from the vicinity of the settlement. It also facilitates local employment, but their construction does not seem feasible in many cases under the present economic trends as they require significant resources.

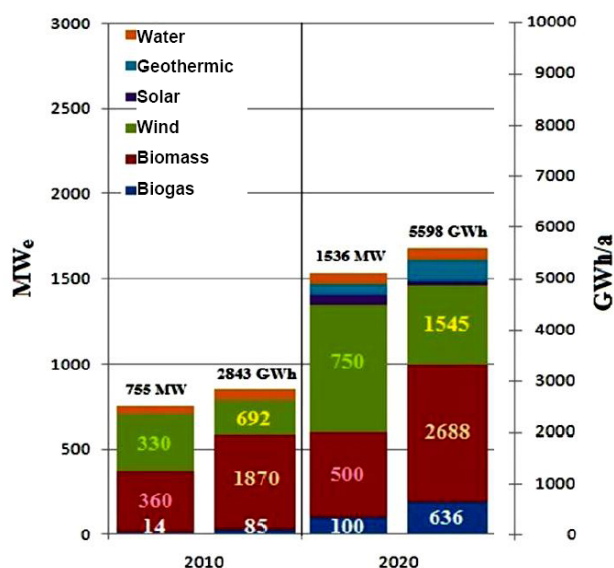


Figure 5. Planned quantity (MW) of various renewable energy sources and expected production (GW) [7].

Conclusions

- Utilization of energy carriers of biological origin can be improved; however the primer and final energy production will not be economically sustainable without outer financial support.
- The usable mass of bioenergetic resources must be determined in aspect of ecological sustainability.
- Notable and long-term investments can be established in countable economical and legislative conditions only.
- The improvement of environmental energy production requires appropriate energy reservoirs.

Acknowledgement

This study was supported by TAMOP 4.2.1.B-11/2/KMR-2011-0003

References

- [1] Beszédes S., Szabó G., Géczi G.: 2012. Application of Thermal and Microwave Pre-treatments for Dairy Wastewater Sludge *Annals Of Faculty Of Engineering Hunedoara/International Journal of Engineering* 10;(3) pp. 231-235.
- [2] Büki G.: 2010 Megújuló energiák hasznosítása Magyar Tudományos Akadémia Köztestületi Stratégiai Programok, Budapest, 1-79 p. ISBN 978-963-508-599-6
- [3] Géczi G., Beszédes S., Szabó G.: 2012. Élelmiszeripari szennyvizek biológiai lebontásának növelése termikus előkezelésekkel *Mezőgazdasági Technika* 53;(3) pp. 2-4.
- [4] Komlós F., Fodor Z., Kapros Z., Vajda J., Vaszil L.: 2009. Hőszivattyús rendszerek ISBN 978-963-06-7574-1 p.215.
- [5] Korzenszky P.E., Géczi G.: 2012. Heat Pump Application in Food Technology *Journal Of Microbiology Biotechnology and Food Sciences* 2:pp. 493-500.
- [6] Marosvölgyi B.: 2005. A biomassza-bázisú energiatermelés mezőgazdasági háttere VI. Energiapolitikai Fórumon, a Magyar Tudományos Akadémia, 2005, április.
- [7] National energy strategy (Nemzeti energia stratégia) 2010-2030.
- [8] Rónay D.:_szerk. 2006. Biomassza alapú energiaforrások termelése és hasznosítása Budapest, Tanulmány.
- [9] Sembery P. Tóth L.: 2005. Hagyományos és megújuló energiák, Szaktudás Kiadó Ház. Budapest, 522 p.
- [10] Stróbl A.: 2012 Tájékoztató adatok a magyarországi villamosenergia-rendszerről, A piacnyitás (2003) óta eltelt időszak fontosabb adataiból, MAVIR, 2012. április 15. kézirat, ábragyűjtemény.
- [11] Zsebik A.: 2007. Gázmotorok jövedelmezősége, megtérülése; 2007 március; http://www.eh.gov.hu/gcpdocs/200809/gm_meh_02_honlapra.pdf

Institute for Environmental Engineering Systems



Professor Dr. István FARKAS
Director of the Institute

Dear Reader,

The Institute for Environmental Engineering Systems consists of two departments as Department of Environmental and Building Engineering and Department of Physics and Process Control. There are several research activities going on in the Institute having interrelations in order to find new scientific solutions concerning to the environmental engineering requirements. It gives a strong opportunity for sustainable development and allowing common way of approach in the solution of different nature of problems. From the results of the current research activity the following topics are selected out to publish in the recent issues of the Journal:

Thermal performance of different exterior building boundaries:

- This research aims at to define the energy flows between the exterior boundaries of buildings and their environment when energy input as well as energy removal were applied to such constructions. The current paper analyses the different criteria by which the boundary constructions of different energy input abilities could be compared with another one, and looks for response factors which refer to the change of energy flows between boundary constructions of dissimilar structure and their environment.

Spectral sensitivity of photovoltaic modules:

- In the paper the results of the spectral measurements of the different type of photovoltaic modules (amorphous and polycrystalline silicon ones) were compared for the power data of the same period in order to get relationship between them. From the long-time analysis of the power distribution a periodical yearly change can be recognized which shows seasonal dependence. As the system lifetime is almost 8 years, a long time analysis of the possible power degradation was also carried out.

Effect of volumetric flow rate on energy production of vacuum tube solar collector:

- In the present work the vacuum tube solar collector energy production and its efficiency dependence on the volumetric flow rate of the solar liquid were studied. The pump of the solar system was connected to the solar loop via performance control unit to provide the different constant volumetric flow rate of solar liquid. On the basis of the measured data it can be said that during the different radiation conditions at a given system the optimal volumetric flow rate of the solar liquid are different, therefore the flow control is justified.

Effect of volumetric flow rate on energy production of vacuum tube solar collector

Piroska VÍG, István FARKAS

Department of Physics and Process Control, Institute for Environmental Engineering Systems

Abstract

In the present work the vacuum tube solar collector energy production and its efficiency dependence on the volumetric flow rate of the solar liquid are studied. The pump of the solar system is connected to the solar loop via performance control unit to provide the different constant volumetric flow rate of solar liquid. On the basis of the measured data it can be said that during the different radiation conditions at a given system the optimal volumetric flow rate of the solar liquid are different, therefore the flow control is justified.

Keywords

solar energy, efficiency, solar collector, volumetric flow rate

1. Introduction

For application of active solar systems the basic target is how to use them at higher efficiency. In order to achieve this goal it is important to know about their operation at a given location and meteorological conditions. The dependence of energy production of photovoltaic modules and solar collectors on orientation, angle (Duffie, Beckman, 2006), the effects of shading (Sharma, 2013) and the advantages and disadvantages of the solar tracking (Mousazadeh et al, 2009) are thoroughly investigated topics. The solar thermal system efficiency dependence of stored water temperature is also a well-studied issue.

The efficiency of the vacuum tube solar collector is about 70% (Farkas, 2003), only slightly reduced than increase the difference between the average temperature of the solar fluid and the ambient temperature. However, the actual efficiency is influenced by several factors. In the present paper the efficiency dependence of the volumetric flow rate of the solar liquid was specifically studied. The optimal flow rate for the highest efficiency and power were examined on the base of the measured data during the given radiation and temperature conditions. This work is going to give a basis for to set up an optimal volumetric flow rate which also considered as control problem.

2. System description

The measurements were carried out with the solar system which was built for educational and demonstration purposes, in the Department of Physics and

Process Control, Szent István University, Gödöllő, Hungary. The type of the vacuum tube solar collector is SP-SS8/1800A-15, include 15 tubes with heat pipe system. The collector area is 1,695 m² with south orientation and 45° inclination. The type of the solar storage is Styleboiler, ISSWW 300V. The 300 litres volume solar storage is coated with insulation layer, contained inside heat exchangers and temperature sensor outputs.

50-50% mixture of propylene glycol and distilled water is circulated in the solar loop. The type of the pump is Grundfos UPS 25-50, the pump ensures a constant flow rate of solar fluid, can be adjusted in three levels. For the constant, but these different flow rate had been implemented a power regulator (thyristor) connected to the pump.

For the monitoring and the control of this domestic hot water system the temperature, radiation, and flow rates data were gathered and recorded. The type of the pyranometer is Kipp & Zonen CM11. It is installed in the collector plane. The temperature data were gathered with PT100 resistance thermometers and thermocouples.

The data acquisition system is based on the ADAM 4000 Series modules, the control is also carried out with ADAM modules. The Fig. 1 shows 3 photos about the studied collector, the storage tank and the power regulator of the pump.



Figure 1. Pictures about vacuum tube solar collector, solar storage tank and power regulator of the pump

3. Measured data

The measured data were gathering between July and August in 2013. The data acquisition system recorded data every minute. During the data collection period the sky was absolutely clear, solar radiation fluctuation-free. The following figures show the measurement data of 6615 minutes with sequentially append.

The Fig. 2 shows the collector inlet and outlet solar fluid temperature and ambient temperature, the Fig. 3 shows the global solar radiation, the Fig. 4 shows the volumetric flow rate of solar fluid and the temperature difference of solar fluid and the Fig 5 shows the average temperature of stored water.

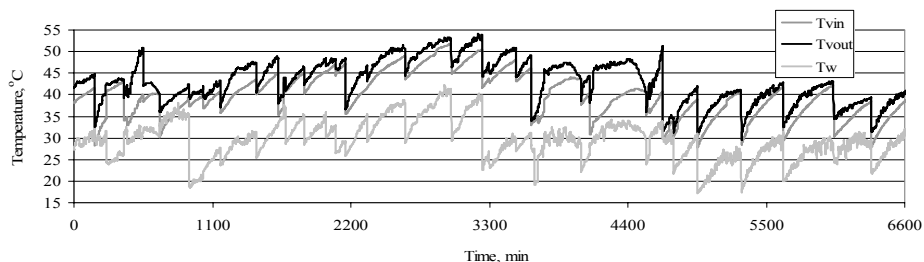


Figure 2. Solar fluid inlet temperature, outlet temperature and collector ambient temperature

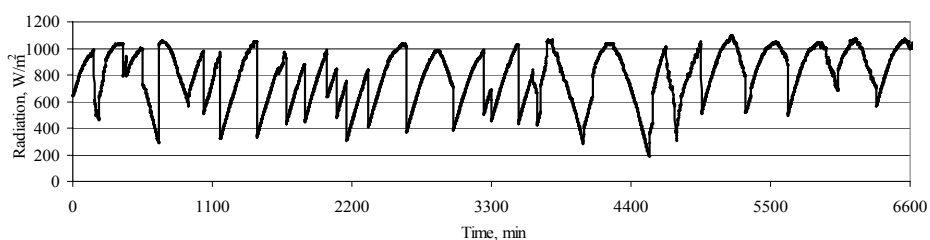


Figure 3. The measured global solar radiations

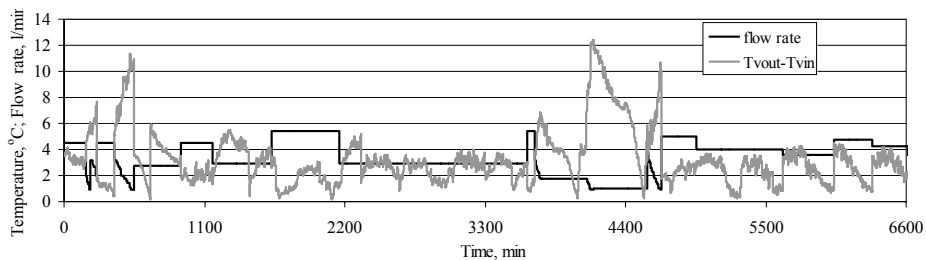


Figure 4. The flow rate of solar fluid and its temperature changes in the collector

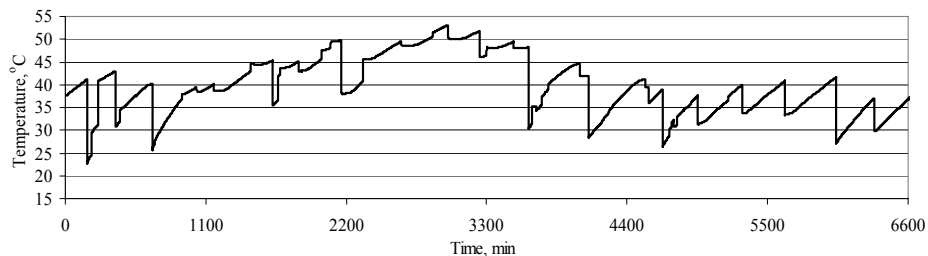


Figure 5. Average temperature of the stored water

In the Table 1 the intervals of the measured values and their accuracy are summarized.

Table 1. Data intervals and accuracy

Symbol of quantities	Interval	Error
\dot{v} [l/min]	0,86 – 5,56	0,02
I [W/m ²]	188 – 1080	1,00
T _w [°C]	17,9 – 41,8	0,10
T _{vin} [°C]	27,1 – 51,7	0,10
T _{vout} [°C]	29,0 – 53,9	0,10
T _s [°C]	21,2 – 53,1	0,10

The calculations and conclusions are valid in the studied collector and inside the table showed validity range.

4. Volumetric flow rate effect on energy production and efficiency

The utilized energy by the collector is given by Eq. (1), and energy reaching the collector by solar radiation is given by Eq. (2).

$$Q = \int c \dot{m}(t) (T_{vout}(t) - T_{vin}(t)) dt, \quad (1)$$

$$E = \int I(t) A(t) dt. \quad (2)$$

The efficiency of the collector is the ratio of these two values. In case of per-minute data, taking into consider that the collector absorber surface constant and heat expansion of solar fluid negligible in the applied interval follows Eq. (3).

$$\eta(i) = \frac{c \rho}{A} \frac{\dot{v}(i) (T_{vout}(i) - T_{vin}(i))}{I(i)}. \quad (3)$$

In the additional Figs the calculated efficiency values by Eq (3) are shown in depending on different parameters.

The efficiency values accuracy is 12.4% by the law of error propagation. The Fig. 6 shows the efficiency values time dependence similarly than Figs 2-5.

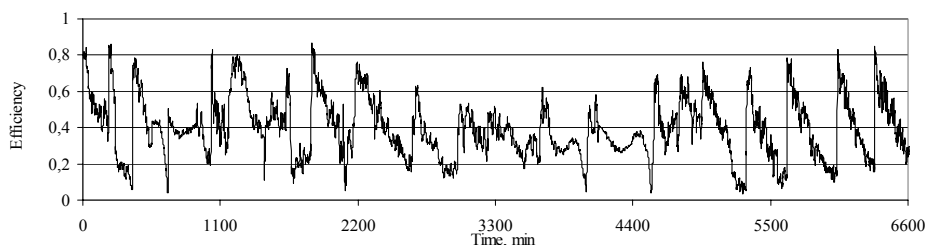


Figure 6. Collector efficiency

The efficiencies are highest when the radiation high, the stored water temperature is not very high and flow rate also large. Smaller efficiencies next to the low flow characteristics even when the flow rate high while the stored water hot, and/or low the radiation. The Fig. 7 shows the calculated efficiency values based on measured data according to the flow rate.

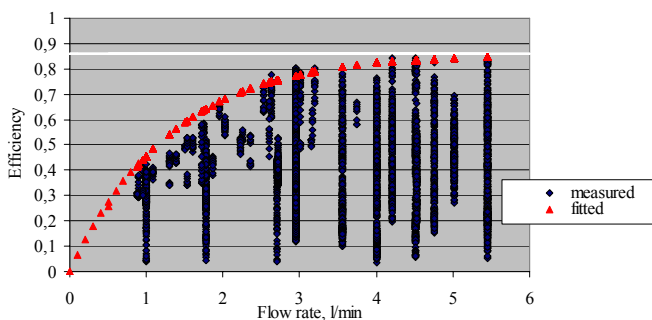


Figure 7. Efficiency vs flow rate

On the base Fig. 7 it can be said, in low flow rate interval, if flow rate increase, than efficiency increase. This result is in accordance with Yousefi et al. (2012) result. In addition the maximum efficiency values, which were determined from measured data, fitting to the saturation curve is also observed. The equation of this curve is given by Eq. 4:

$$\eta(\dot{v}) = 0,862(1 - e^{-\dot{v}/1,618}). \quad (4)$$

Correlation coefficient of the curve fitting is characterized by $r=0,9836$. The maximum efficiency value is 0,862, which approximates in 95% at 3,8 l/min flow rate if the other conditions are optimal. So, if a pump on/off operated and maximal collector efficiency is important the 3,8 l/min flow rate is recommended.

The Fig. 8 shows the power of the collector versus flow rate of the solar fluid.

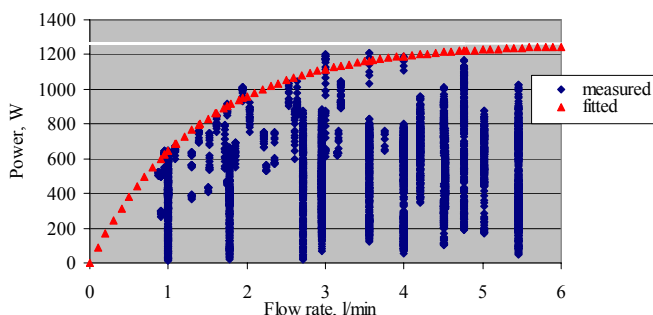


Figure 8. Power vs flow rate

The behaviour of the maximum powers are similar than the behaviour of the maximum efficiency. The maximum power which was calculated from the measured data is 1208 W, when the used flow rate was between 3-4 l/min flow rate. The equation of the fitted curve are given by eq. 5, with $r=0,9844$ correlation coefficient.

$$P(\dot{v}) = 1264(1 - e^{-\dot{v}/1,4}). \quad (5)$$

So, the maximum available power at this collector is 1264 W. The Fig. 9 shows the efficiency against global solar radiation.

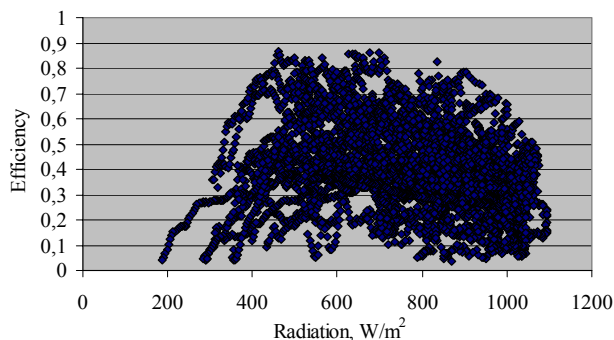


Figure 9. Efficiency vs solar radiation

The results show that relatively high efficiencies are available if the radiation relatively low, 350-400 W/m², but other conditions are ideal. It is also supported that the vacuum tube solar collector in winter also can be operated effectively.

The Fig. 10 shows the power of the collector versus solar radiation, the Fig. 11. shows the efficiency versus solar fluid temperature difference while passes through the collector and the Fig. 12. shows the efficiency values versus differences between collector average and collector ambient temperature.

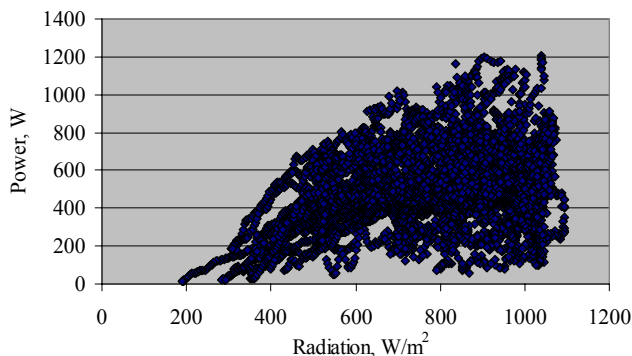


Figure 10. Power vs solar radiation

The maximum values of the set of points shows that if the radiation increases, than the can be gathered power by collector also increase, in this case if the other conditions are optimal. Also it can be stated that if the other conditions are not optimal, the power is degraded.

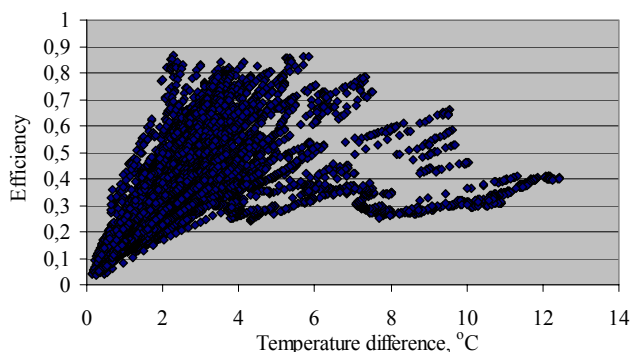


Figure 11. Efficiency vs solar fluid temperature change

On the based the Fig. 11 the optimal difference between outlet and inlet solar fluid temperature is between 2 and 6 °C, if this difference is outside this interval, the efficiency decrease.

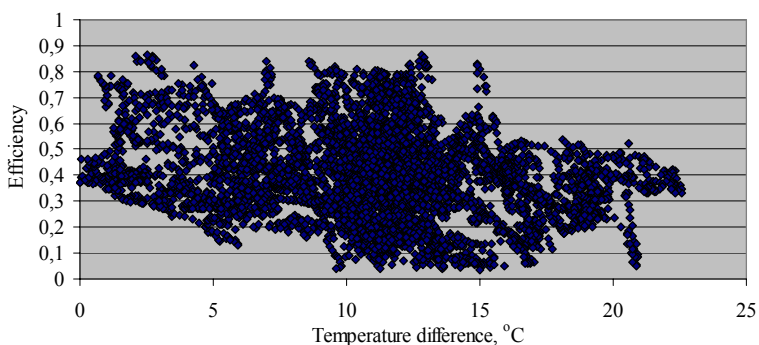


Figure 12. Efficiency vs collector average and ambient temperature difference

It can be seen that the temperature difference between collector average and collector ambient temperature increase until 15°C the collector is not very sensitive, the maximum efficiency does not decrease significantly, as in the case of a vacuum tube collectors can be expected. If this temperature difference more than 15 °C the efficiency decrease can be observed.

The control of a continuously ideal flow rate working solar system is the complex task. For this aim necessary is considered the energy of the whole system. If the temperature of the stored water is high or solar radiation is low than with lower flow rate the outlet fluid temperature are higher, so it can continue heated the solar fluid and increase the time of solar energy utilization. Used lower flow rate in the area of the switch on/off, is reduce length of the transient periods, which is also an advantage if the energy of the whole system are considered. The based on the results it can be said that near the working maximal efficiency of the collector the gathering maximum power in the user-side are also aims, than, the optimal flow rate considered control is justified.

The determination of the extra power which come from such control, the possibilities of the realization of the control, determination investment and operating costs are the further work.

Conclusions

- The efficiency of the collector is influenced by flow rate of solar liquid also, near the radiation and temperature conditions.
- The optimal flow rate for maximal collector efficiency in the event of on/off-controlled pump and the maximum power of the collector were determined in case of examined collector.
- For the view point of the usable energy, if the conditions are not ideal, to use the lower flow rate is may gives greater useful solar energy, so it makes sense to examine the control which taking into account the optimal flow rate as well.

- To determine the growth of efficiency which came from control with taking into account the optimal flow rate it is the object of a further research.

Nomenclature

A	collector absorber area [m ²]
c	3194 J/kgK, solar liquid specific heat
E	energy from radiation [J]
i	variable, indicating per minute data
I	global radiation in a collector plane [W/m ²]
m	mass flow rate [kg/s]
Q	exploited heat by collector [J]
t	variable, time
T _s	stored water temperature [°C]
T _{vin}	inlet solar liquid temperature [°C]
T _{vout}	outlet solar liquid temperature [°C]
T _w	collector ambient temperature [°C]
v	volumetric flow rate [m ³ /s]
P	power [W]
ρ	1040 kg/m ³ , solar liquid density
η	efficiency

Acknowledgements

The research was carried out with the support of the OTKA K 84150 project.

References

- [1] Duffie, J.A., Beckman, W.A. (2006), *Solar Engineering of Thermal Processes*, (third ed.) Wiley, New Jersey
- [2] Farkas, I. (2003), *Solar energy in agriculture*, Mezőgazda Kiadó, Budapest (in Hungarian)
- [3] Mousazadeh, H., Keyhani, A., Javadi, A. (2009), A review of principle and sun-tracking methods for maximizing solar systems output, *Renewable and Sustainable Energy Reviews* Volume: 13 Issue: 8, pp. 1800-1818.
- [4] Rojas, D., Beermann, J., Klein, S. A. (2008), Thermal performance testing of flat-plate collectors, *Solar Energy*, Volume: 82 Issue: 8, pp. 746-757.
- [5] Sharma, V.M., Nayak, J. K., Kedare, S.B. (2013), Shading and available energy in a parabolic trough concentrator field, *Solar Energy*, Volume: 90, pp. 144-153.
- [6] Yousefi, T., Veysi, F., Shojaeizadeh, E., Zinadini S. (2012), An experimental investigation on the effect of Al₂O₃-H₂O nanofluid on the efficiency of flat-plate solar collectors, *Renewable Energy*, Volume 39, Issue 1, March 2012, pp. 293-298.

Spectral sensitivity of photovoltaic modules

Ivett KOCSÁNY, István SERES, István FARKAS

Department of Physics and Process Control,
Institute for Environmental Engineering Systems

Abstract

During the almost 8 years of operation of the 10 kWp photovoltaic (PV) system installed at the Szent István University, enough amount of data were collected to start analysis of the working of the different type of photovoltaic modules: amorphous and polycrystalline silicon ones. As the energy production of the different technologies is measured separately, such data give the basis to the analysis. From the long-time analysis of the power distribution a periodical yearly change can be recognized which shows seasonal dependence. The rate of the normalized energy production was used for the analysis. As the effect is partly considered to the spectral dependence of the PV modules spectral measurements were carried out for a limited period of time. In the paper the results of the spectral measurements were compared for the power data of the same period in order to get relationship between them. As the system lifetime is almost 8 years, a long time analysis of the possible power degradation was also carried out.

Keywords

Measurements, solar radiation, solar energy, PV module power, efficiency degradation

1. Introduction

Presently, direct conversion of solar energy into electricity is being accepted as an important form of power generation. This electricity generated by a process known as the photovoltaic effect using photovoltaic (PV) system, which are made from semiconductor materials (Rakić and Pichler, 2011) The performance of photovoltaic systems is influenced by spectrum of solar irradiance even under the same total solar irradiance (Grottke et al., 2006). In term of wavelength (λ), the spectrum (light) of solar irradiance can be divided into three main regions i.e. ultraviolet region (around 5% of the irradiance), visible region (around 43% of the irradiance) and infrared region with (around 52% of the irradiance) (Rusirawan and Farkas, 2012). In this paper, effects of spectral irradiance on overall efficiency of PV modules will be analysed, under Gödöllő meteorological conditions. For the comparison two types of PV module technologies accurately poly-crystalline silicon (pc-Si, ASE 100 type) and

amorphous silicon (a-Si, DS 40 type) the components of 10 kWp grid connected PV array system were used. (During the system planning the two different technologies were installed to be able to compare their operation at the same location under the same operating conditions).

2. Experimental setup

The grid-connected PV array system was installed on the roof of a Dormitory building of Szent István University (SZIU), and is structured into 3 sub-systems. Sub-system 1 consists of 32 pieces of ASE-100 type modules from pc-Si (wafer based crystalline silicon technology), and sub-system 2 and 3 consists of 77 pieces of DS-40 type of modules from a-Si technology (thin film technology), respectively. The total power of the system is 9,6 kWp with the total PV surface area 150 m². Every sub-system uses a separate inverter (Sun power SP3100-600 for sub-system 1 and SP2800-550 for the other two sub-systems), which converts the produced DC electrical energy to the 230 V AC, 50 Hz electrical grid (Farkas and Seres, 2008). The schematic installation of grid-connected PV array at Szent István University can be seen in Fig. 1. The arrays are tilted at 30°, and facing 5° East from South.

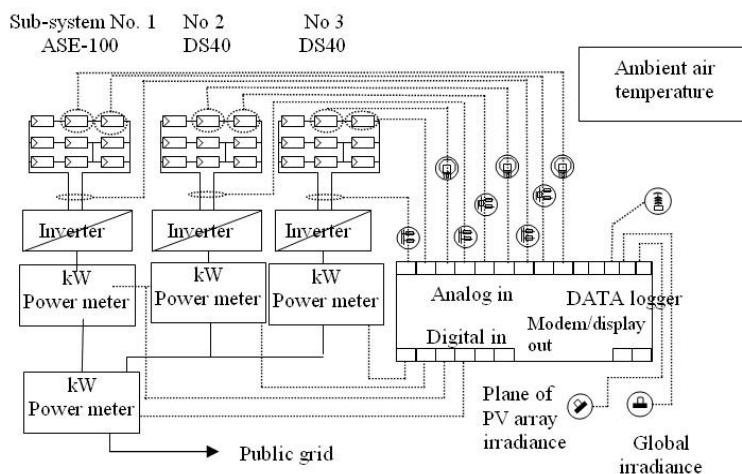


Figure 1. Schematic diagram of a 10 kWp grid-connected PV array at Szent István University, Gödöllő

As the data logger computer are relatively far from the measurement point (inverter room and sensor connection boxes), signal converters were installed to the system to serve as an amplifier. The signal converters converts all different output signals of the sensors (e.g. different voltage levels) to 4-20 mA signal, what is sent to the AD converter unit of the data logger PC. The quantities measured by the data logging system are the follows:

- Irradiation (in the module plane by a silicon reference sensor, and the total horizontal radiation by a pyranometer),
- Temperature (environmental and module temperature for each type, measured by Pt100 sensors),
- PV array (DC) voltage, current and power,
- AC voltage, current and power supplied to the electrical grid.

Numerous studies were conducted on the performances of PV modules, but most of them using energy analysis method (Seres et al., 2009). In this paper, effects of wavelength of solar radiation on the overall efficiency of PV modules will be initialized. Beside as comparison purpose, further outcome of this research is trying to find a possibility to increase the performance both PV modules.

From the long-time energy data the possible power degradation of the subsystems with different technologies is also checked.

3. Energy issues of photovoltaic modules

The efficiency was clarified for six randomly selected modules of each type under standard test conditions, at the TISO test site in Switzerland. The recent efficiency calculations are different from that, as the PV array efficiency was calculated from the irradiation data and from the measured DC energy data. The irradiation data were measured on horizontal surface by Kypp & Zonen pyranometer, and also in the module plain by a silicon reference sensor. For the comparison the irradiation data on the module plain were used. The DC power data were compared to input power from the irradiation and the rate of them was calculated as the module efficiency.

Efficiency analysis

The efficiency depends on several parameters (spectral distribution of the incoming light, temperature of the module, etc.) but this time only an overall efficiency is calculated from the measured 10 minutes average values. This analysis has been carried out separately for the ASE and DC subsystems, as well. The time dependence of the efficiency can be seen in Fig. 2 for a selected day.

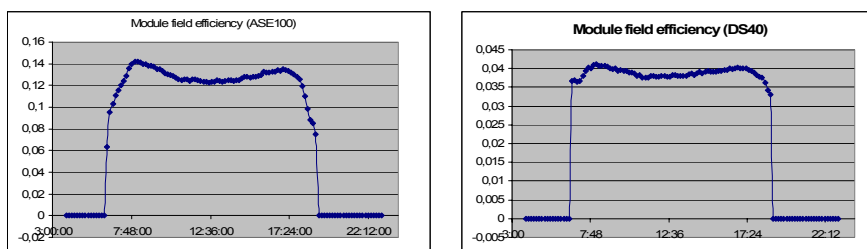


Figure 2. PV array efficiency

The average module efficiencies can be read from the curves as about 13% for the crystalline and 4 % for the amorphous silicon modules. From the figures it can also be seen that the module efficiency is lowering a bit in the hottest hours. The highest temperature was reached (the value is about 50 °C) between 11- 13 h. The reason is the temperature dependence of the efficiency.

From the measured data some efficiency values can also be achieved. As the PV system is a multi-component system, the efficiency of the different parts can be calculated and the multiplication of these values provides the system efficiency. In our case not all the part efficiencies are determined, but calculations were carried out for the module efficiency and for the inverter efficiency. The cable losses are not taken into the calculations.

The inverter efficiency was calculated from the measured DC and AC power values. As the data logging records 10 minutes average values, the efficiency was also calculated in series for the same day as the module efficiencies (Fig. 3). It can be seen that the average inverter efficiency is above 90%.

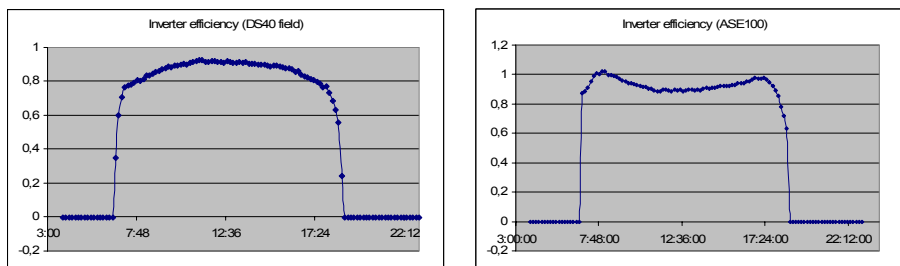


Figure 3. Inverter efficiencies for the two different subsystems

The periodical change of the energy production

It is normal, that the energy production of a solar system shows periodical change as the solar irradiation is changing the same way. In Fig. 4 and Fig. 5 the seasonal change of the energy production can be recognized very easily.

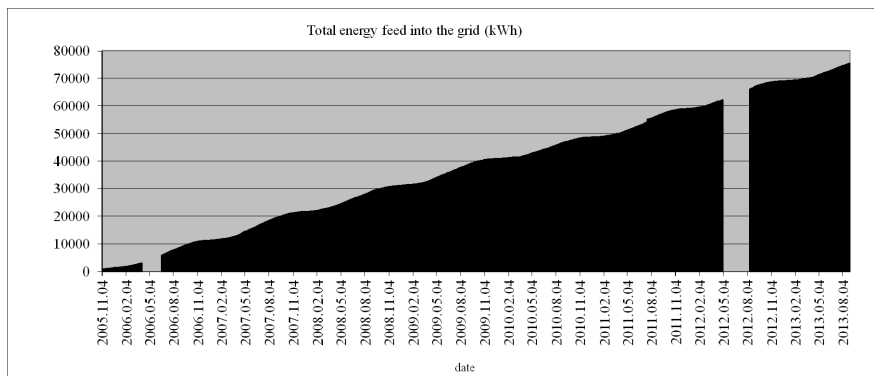


Figure 4. The overall energy production during the operation

From Fig. 4 it can be seen, that during the summer period the gradient of the curve is higher (more energy is generated, while in the winter time the gradient is almost zero. In the two empty region of the function the system was working, just the distribution data was lost.

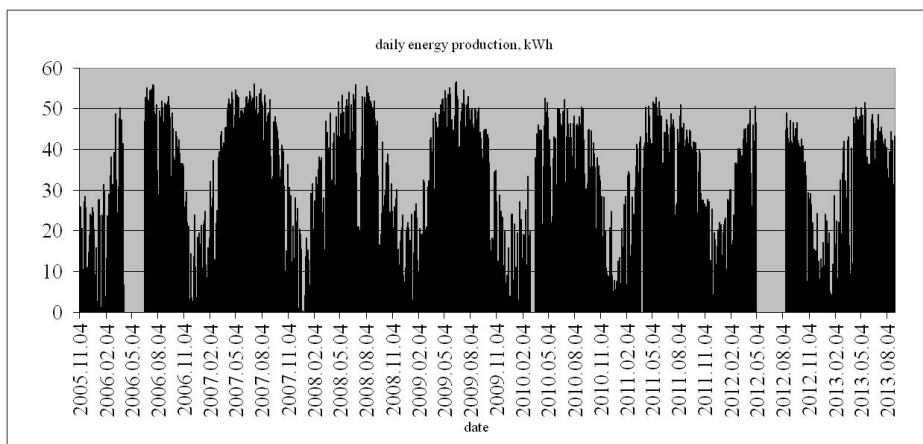


Figure 5. The daily energy production during the operation

From Fig. 5 some decrease in the energy production can be recognized, but as the graph shows the produced energy, and it is depending among them on the irradiation data, the reduction can be caused by lower irradiation on the examined period. Only the cross relation between them can answer for any degradation.

4. Comparison of different PV technologies

As the system has three subsystems, an important question was how the system energy production is shared among them. It is not correct to compare simply the energy production of the subsystems, as the nominal power of the polycrystalline subsystem (ASE) is about 10 percent higher than the two other ones (DS1 and DS2). The differences between the energy productions of the subsystems are measured continuously as all the subsystems are measured separately. From the data it can be seen, that subsystems 2 and 3 are working almost exactly the same way, and the power of subsystem 1 is obviously higher (Fig. 6.).

It can be seen from Fig 5 that each DS40 module fields are producing almost exactly the same energy, but the rate of the energy production of the ASE and DS subsystems is definitely higher than one. From the values it can be seen, that the ASE subsystem produced about 30% more energy than the DS, and the difference is higher in the winter time and lower in the summer time. As the

difference in the energy production of the subsystems is partly coming from the different nominal power, a normalized energy production rate was determined. In this case the normalized energy production is used as the energy production of 1 kWp nominal power part of the subsystems, so it was calculated by dividing the energy production with the nominal power of the given subsystem. The rate of the normalized energy production can be seen in Fig. 7.

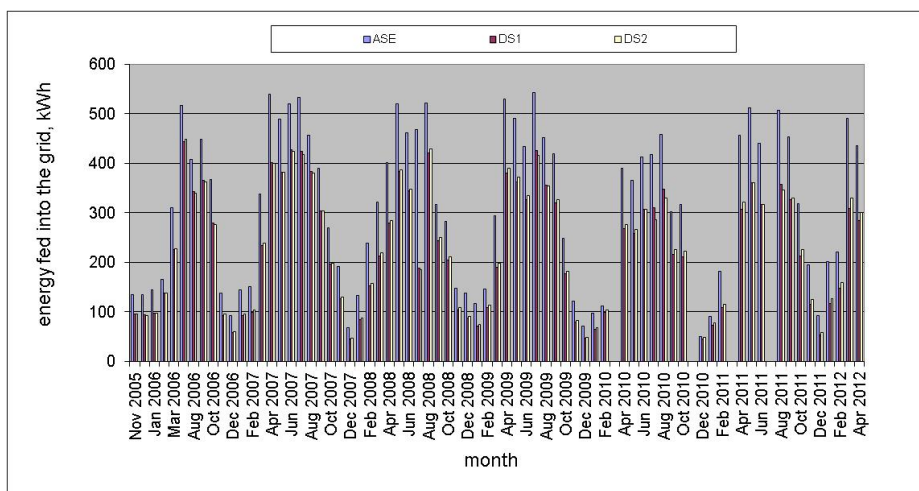


Figure 6. Comparison of the energy production of the subsystems

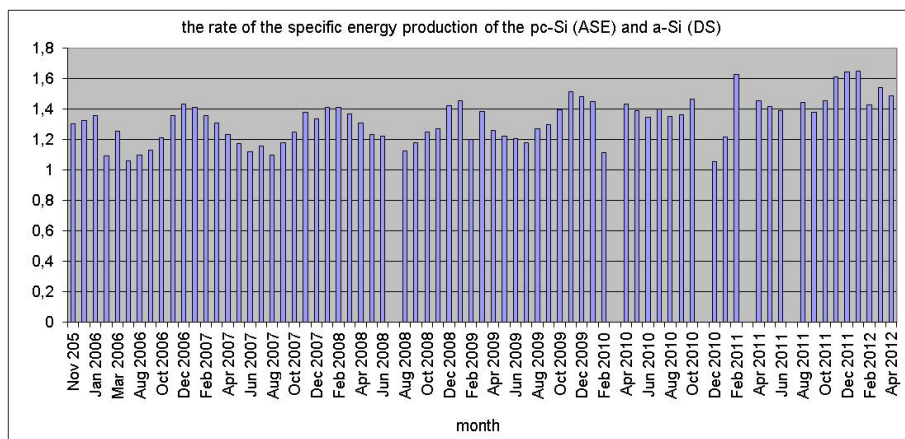


Figure 7. The rate of the normalized energy production

From the graph it can be seen, that there is a seasonal change in the energy production of the different technologies due to the different radiation conditions. The difference is smaller during the summer months (15-20%) and higher during winter time (up to 40%), or even higher, this effect will be analyzed yet in the Degradation section.

Spectral dependence of the different technologies

If we analyze what can be the reason for the presented differences in the energy production, two main effects has to be taken into the account, the different temperature dependence and the different spectral dependence of the used technologies.

The different temperature dependence can generate some differences in the module power, but when the radiation id hitting the surface, its temperature goes up, even under low ambient temperature. The other main reason is the spectral dependence. During the different seasons the spectra of the solar radiation is different because of the different AM values (the sunrays has to travel longer route in the air during high AM values, which means higher scattering value of the blue component, so the radiation became red, the red and IR components is relatively stronger. On the other hand the air humidity has effect of the spectra as well, but the humidity generally depends on the season.

5. Degradation of PV modules

The solar applications, among them the PV modules are continuously under the radiation of the sun, but some parts of the solar spectra (e.g. UV and shorter wavelengths), can cause structural changes in the wafers, which means degradation of the nominal power of the modules. Fortunately, the magnetic field of the Earth protects us from the cosmic radiation (its charged particles are coming mainly from the Sun) and the ozone layer stops the UV radiation, so the incoming radiation energy in these harmful ranges is minimal. However during long time, the cumulative effect of the UV radiation means lover energy production.

The almost 8 years of operation can be long enough to be recognizing the degradation of the power generation if it exists. In Fig. 8 the yearly energy production of the system can be seen. Between 2006 and 2010 a decrease can be recognized in the energy production, but in the last two (whole) years it went up again to the original level.

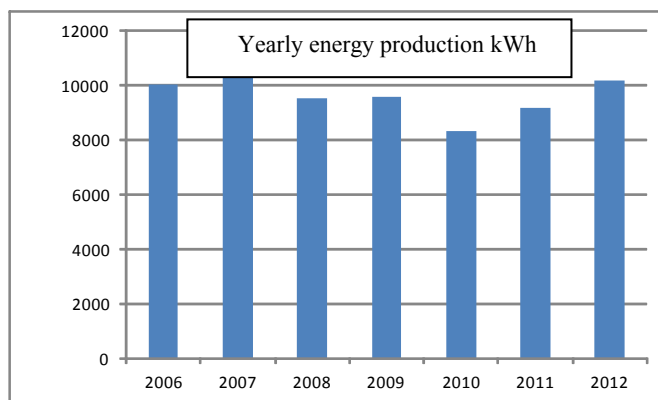


Figure 8. The yearly energy production of the 10 kWp system

However from this graph nothing can be concluded to the system degradation, as the energy production is depend first of all from the solar irradiation. If a cross effect between the solar irradiation and the energy production of the given year is presented, then some conclusions can be drawn.

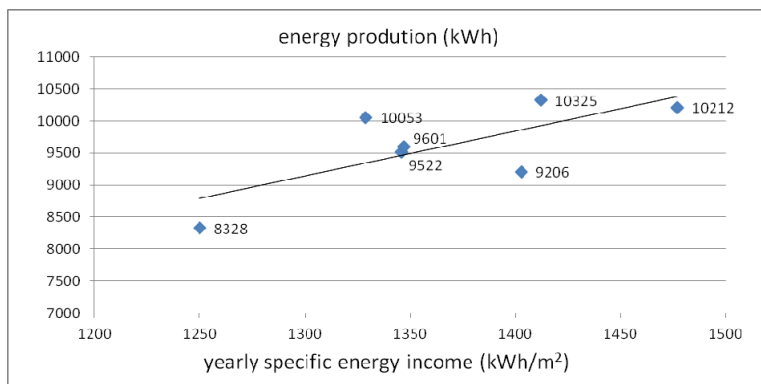


Figure 9. The energy production vs the solar irradiation (energy income), yearly values

From the graph in Fig. 9 it can be seen, that some degradation can be recognized, as the production of the first two years are above the trend line, and the values of the last three years are below that. Of course for the correct percentages of the degradation more data have to be analyzed.

If we want to see how the degradation effect of the different technologies, a comparison has to be made between the used technologies. To do this the percentage rate of the energy production of the subsystems from the total energy production was determined for the different years (Fig. 10).

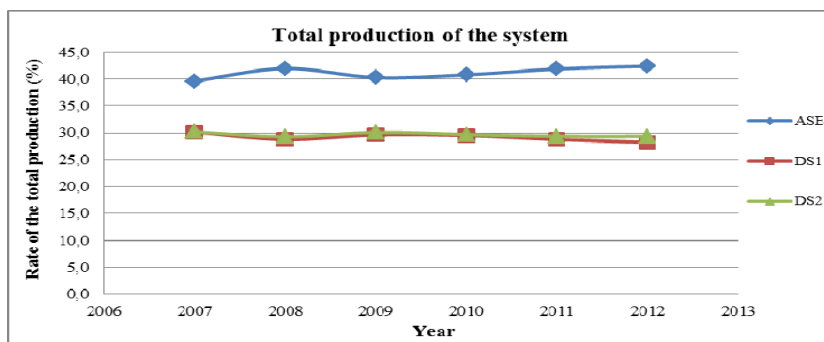


Figure 10. Percentage of the energy production of the different subsystems (yearly data)

From the data we can conclude that probably the degradation is stronger for the a-Si modules (DS-40) then for the pc-Si modules (ASE100), but for achieving numerical values the data of longer time is necessary.

Conclusions

During the study the seasonal period of the energy production was recognized, and beside the periodic change of the incoming total radiation the spectral change of the solar radiation was also considered. This spectral change has different effect for the different PV technologies, which can show from the measured data of the different subsystems.

Beside the spectral effect of the incoming radiation, the degradation of the PV modules was also investigated. From the measurement results some degradation can be recognized, and from comparing the energy production of the subsystems, more degradation can be seen for the a-si (DS) modules than for the po-Si (ASE) but to make it exact, more measurement data has to be collected.

Acknowledgement

The research was carried out with the support of the OTKA K84150 project.

References

- [1] Grottke, M., Helm, P., Kiessling, A., Friesen, G., Realini, A., Gehrlicher, K. (2006): PV enlargement: PV module technologies in performance comparison results of a 3 years project program, Proceedings of the 21st European Photovoltaic Solar Energy Conference, 4-8 September 2006, Dresden, Germany, pp. 3263-3266.
- [2] Farkas, I., Seres, I. (2008): Operational experiences with small-scale grid-connected PV system, Szent István University, Faculty of Mechanical Engineering, Mechanical Engineering Letters, Vol. 1, pp. 64-72.
- [3] Rakić, M., Pichler, G. (2011): Comparison of visible and infrared spectrum of light sources. Science Direct, Optics Communications, Vol. 284, pp. 2881-2885.
- [4] Seres, I., Farkas, I., Kocsany, I. and Weihs, P. (2009): Comparison of PV modules under different spectral conditions, Szent István University, Faculty of Mechanical Engineering, Mechanical Engineering Letters, Vol. 3, pp. 81-89.
- [5] Rusirawan, D., Farkas, I. (2012): Spectral irradiance effects on exergetic performances of photovoltaic module: initial study, Szent István University, Faculty of Mechanical Engineering, Mechanical Engineering Letters, Vol. 8, pp. 77-84.

Thermal performance of different exterior building boundaries

Zoltán DODOG

Department of Building Facility and Environmental Engineering,
Institute for Environmental Engineering Systems

Abstract

This research aims at to define the energy flows between the exterior boundaries of buildings and their environment when energy input as well as energy removal are applied to such constructions. There are only specific design methods for these structures. The current paper analyses the different criteria by which the boundary constructions of different energy input abilities could be compared with another one, and looks for response factors which refer to the change of energy flows between boundary constructions of dissimilar structure and their environment.

Keywords

building boundaries, heat insulation, renewable energy, energy input

1. Introduction

The trend aiming to increase the thermal insulation capability of exterior building boundaries in order to reduce the energy consumption of buildings has existed since the 70's. Today in the case of certain boundary constructions the thickness of the insulation layer already exceeds the thickness of bearing structures (constructions). In addition to applying an insulation layer upon the framework there are other alternatives to reduce energy loss, including, for instance, the so-called active heat insulation (Meggers et al., 2012), which means getting low enthalpy heat carrying materials inside the structure. The essence of this solution is that by increasing the temperature of the expediently selected layer of the wall structure we get to reduce the heat flow bringing on heat loss from the interior. Evaluating the usage of active heat insulation from an energetic point of view necessitates a thorough survey. Based on the values of temperature of exterior and interior spaces correlating to the temperature of the environmental heat source we can distinguish several typical operational statuses (Dodog, 2013), where the main energy flow rates and directions inside the structure are different in each of these statutes. None of these named cases are of a steady state condition. The most important disturbing factor is the daily and seasonal changes in external temperature but there are several other factors that

influence energy flows inside the structures. In this paper examination focus on itself the boundary construction and looks for different factors which refer to the change of energy flows between these constructions and their environment.

2. Modelling approach

In this paragraph exterior building boundaries will be examined, how heat exchange can apply in the construction, and what are the possibilities for modelling such system.

Exterior building boundaries

During the architectural and building engineering design phase engineers like to use formulas presuming steady state, thus models created to define the heat flows inside the real exterior building boundaries implement several simplifications. Besides unknown influencing factors there are some known ones that do have impact on heat flows formed in real exterior building boundaries, but that impact is mostly insignificant and so it can be neglected from the point of view of practice. Building walls and slabs can be made of various homogeneous and inhomogeneous materials, in a number of different layer structure versions. The thermal conductivity of the material, which is the most important parameter influencing heat flows, is usually only on a rough estimate, and furthermore, its value can be affected by the temperature or moisture content of the material. On the surface of boundary constructions heat transport occurs by convection, while towards surrounding surfaces it happens by radiation. Most of the time heat transport is calculated by means of formulas that contain several omissions, when dealing with values of thermal conductivity they rely on references found at manufacturers and in the literature, the experimental values of heat transfer coefficient are approximate. In spite of the fact that these calculations are thus merely approaching the physical quantity values referring to the actual phenomenon, we can still use them well in practice as they approach the phenomenon with reasonable accuracy.

In case of steady state processes energetic calculations generally based on these factors:

- geometrical dimensions, layer structure,
- physical properties of building materials: thermal conductivity, specific heat,
- inside and outside temperature, heat transfer coefficient.

In practice boundary constructions are made of more than one kind of building materials and they have a complex spatial geometry, therefore it is impossible to determine their spatial heat distribution and heat flows in a purely analytical way. An interference like cooling and heating of the boundary constructions requires an even more complex model, where the solution of the descriptive equation can be approached by means of applying numerical methods (Minkowycz et al., 2006), with large scale calculation capacity.

Active insulation

Energy can be led into the building structure by using several methods: the most frequently used technologies are the tube row heat exchangers, using water as transmission medium, and the electric heating, which transforms electric energy into heat energy (as they can be seen on Fig. 1).



Figure 1. Capillary tube heat exchanger and electric heating

The boundary construction, be it in an upright, horizontal or even slant position, can be, in most cases, structurally divided into three easily separable layers: framework, energy transport and heat insulation. In the case of active heat insulation this is also the actual order of layers from the interior (Fig. 2).

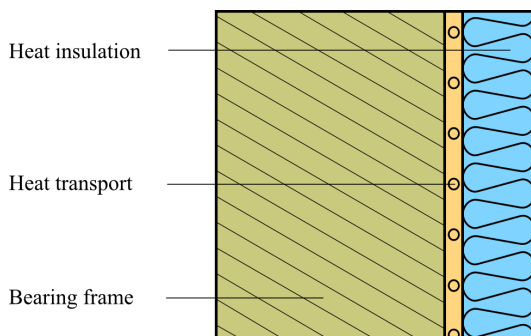


Figure 2. Cross-section of wall with heat exchanger

Modelling

Heat transfer by conduction is the flow of thermal energy within solids and non-flowing fluids, driven by thermal non-equilibrium, commonly measured as a heat flux at a control surface. The general equations for heat conduction are the

energy balance for a control mass, and the constitutive equations for heat conduction which relates heat flux to temperature. Applying to an infinitesimal volume, yield the partial differential equation (PDE) known as heat equation:

$$\left(\frac{\partial T}{\partial t}\right) = \kappa \left(\frac{\partial^2 T}{\partial x^2} + \frac{\partial^2 T}{\partial y^2} + \frac{\partial^2 T}{\partial z^2}\right). \quad (1)$$

Analytical solutions to heat transfer problems reduced to solving the PDE (1), within a homogeneous solid, under appropriate initial and boundary conditions. Several different approaches may be used to find analytical solutions: dimension reduction, reduction by similarity, separation of variables, Green's function integrals, Laplace transforms, etc.,

Numerical solutions are the rule in solving practical heat transfer problems, because the analytical formulation in terms of partial differential equations is not analytically solvable except for very simple configurations. Numerical methods transform the continuous problem to a discrete problem, thus, instead of yielding a continuous solution valid at every point in the system and every instant in time, and every value of the parameters, numerical methods only yield discrete solutions, valid only at discrete points in the system, at discrete time intervals, and for discrete values of the parameters. The numerical approach has two crucial advantages, it can provide a solution to any practical problem and the discretization can be refined as much as wanted for specific goal.

Several numerical methods have been developed (Minkowycz, 2006), each with its own advantages and complexities, from simple ones like the lumped method or the finite difference method, which can be developed from scratch for every new problem to the standard finite element method that, once developed can be routinely applied to whatever complex case we have at hand. The most common numerical methods may be grouped as integral methods and differential methods. Among them, the most used differential methods are:

- residual minimization,
- finite differences,
- finite elements,
- boundary elements.

Another classification may be in terms of the continuity of the base functions as global methods, global fitting and residual minimization, and local methods. The great advantage of local methods is that the base functions can be very simple. The first step in all local methods is a spatial discretisation of the domain, followed by node assignment, and the choice of base functions.

Research steps

The aim of this research is to make energy flows between the system and its surroundings easily determinable in the case of boundary constructions categorized as per certain criteria. When comparing various boundary constructions the insulation layers mostly differ only in their layer thickness and

material, so their thermal resistance can very well describe these layers. Whereas the heat transport factor of thermal insulation materials stays in a relatively narrow range, there are way larger differences to be seen in the case of frameworks. The energy input layer is of special significance; observations have shown that the spatial heat distribution is largely influenced by the thermal properties of materials surrounding the tubes as well as by the density of tubes.

The research must examine the potential criteria that can be used for categorizing boundary constructions. It must deal with questions of how structures of varying geometry and building materials of various heat transport factors influence the balance heat flows of the construction.

The subject of the survey is an idealized vertical boundary structure (Fig. 3.) that consists of three layers and heat on the surface is transported only by means of convection while inside the construction only by means of heat conduction. The boundary conditions are determined by the temperature of the media circulated in the energy transport tubes and by the external and internal temperature values. Radiation between surfaces of the wall and environment is neglected.

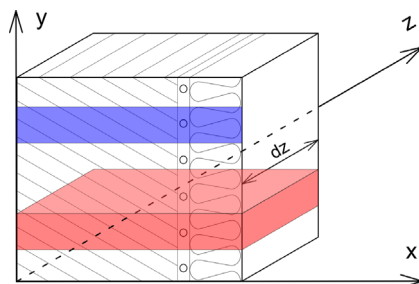


Figure 3. Representative wall segment

With appropriate choice, the structure can be divided into uniform elemental blocks (red block on Fig. 3) that fit together along the x-axis with adiabatic surfaces. In this case the survey can be narrowed down to the thin slice of such a block, parallel to x-y plane, where the external energy transport can be calculated from the change in temperature around the tube. In the appropriately thin segment of the block such change is negligible, which means that the heat transport between the block segments along the z-axis can be considered zero, however temperature change could be present and it refers to energy transfer. In this case

$$\left(\frac{\partial T}{\partial y}\right) = 0; \quad \text{and} \quad \left(\frac{\partial T}{\partial z}\right) = 0, \quad (2)$$

therefore the segments (blue slice on Fig. 3), can be examined in two dimensions, the finite element grid needs to be spread on the x-y plane.

3. Results and discussion

In the course of simulations the experimental factors will be set between limits (shown in Table 1). The inside temperature can vary within the comfort range while the outside temperature can vary within the generally used design temperature value. Geometrical sizes and physical properties of building and insulation materials are also set between frequently used limits.

Table 1. Scope of experimental factors

Factors	Limits	Unit
Framework thickness of construction	10-80	[cm]
Heat insulation thickness of construction	0-30	[cm]
Thermal conductivity of framework	0.1-2.00	[Wm ⁻¹ K ⁻¹]
Thermal conductivity of heat insulation	0.1-0.02	[Wm ⁻¹ K ⁻¹]
Inside temperature	20-26	[°C]
Outside temperature	-13-26	[°C]
Temperature of heat source	0-26	[°C]

The subject of the survey is the wall structure with geometrical dimensions and boundary conditions seen in Fig. 4. The first consideration is to determine how the balance heat flows change in the framework when we replace it with a structure of different heat insulation capacity and thickness in a manner that the heat transfer resistance remains unchanged. Reducing the framework thickness simultaneously with the heat transfer ability there were only a very small change in the typical heat flows of the system, the relative difference always stayed below the threshold of the FEM method. This can be explained by that the heat flux vectors in this layer have little component in the y-direction, which means that in the framework layer heat flow approaches the state of being one-dimensional.

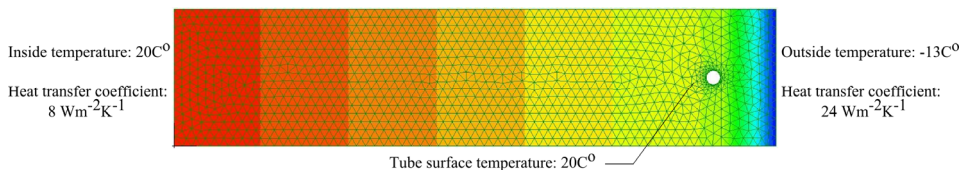


Figure 4. Wall segment examination between specific conditions

The second consideration is to ascertain how the density of tubes of the energy input layer influence energy flows. It is clear that by reducing the space between the tubes the transportable energy quantity is increasing, so a theoretical increase of the number of tubes to infinite would result a homogeneous transport layer

where the heat flow is truly one-dimensional. In practice, the y-direction heat flow component are always present at tube distances of discrete values, thus we need to deal with the question as to in what ratio the standard energy flows change when changing the tube placing density. Simulations showed, with fixed temperature as boundary condition in tube inner surface, changing the tubes density lead to vary heat flows of the system, and had influence on heat flow crossing tube surface. That means, changing geometrical sizes have more impact on the system simultaneously, no linear relationship between energy flows of the system.

In the third case the question to be looked into is how the standard energy flows of the system change when changing the heat transport factor of the energy transport layer in the case of a given boundary construction. Simulations proved, modified input layer heat transport factor affect not only the heat distribution on the wall surfaces, but the energy flows of the system too.

Conclusion

In the case of framework layers of identical heat transfer resistance, their geometric measures and the heat transfer factor of the materials are indifferent from the viewpoint of standard energy flows of boundary constructions. This stands for the heat insulation layer, too, although in a limited sense. Under circumstances of ordinary usage the forming balance heat flows are influenced for the most part by tube distance, if we look at the options providing different geometric layouts, and the heat transfer factor and geometric arrangement of the filling material between tubes. Using the results of the series of simulations carried out on the models it will be possible to determine the impact of the individual influencing factors, mathematically too.

Nomenclature

t	time	s
T	temperature	K
x	length co-ordinate	m
y	length co-ordinate	m
z	length co-ordinate	m
α	heat transfer coefficient	$\text{Wm}^{-2}\text{K}^{-1}$
κ	thermal diffusivity	m^2s^{-1}
λ	thermal conductivity	$\text{Wm}^{-1}\text{K}^{-1}$

Acknowledgement

The research was supported/subsidized by the TÁMOP-4.2.2.B-10/1-2010-0011 „Development of a complex educational assistance/support system for talented students and prospective researchers at the Szent István University” project.

References

- [1] Chen, Y., Zhou, J. and Spitler, J.D. (2006), Verification for transient heat conduction calculation of multilayer building constructions, *Energy and Buildings*, Vol. 38, pp. 340–348.
- [2] Dodog Z.: (2013) Electric analogies in heat transfer of exterior building boundaries supplied a heat input layer, *Magyar Épületgépészet*. Vol. 17/3, pp. 5-10. (in Hungarian)
- [3] Meggers, F., Baldini L., Leibundgut H. (2012), An Innovative Use of Renewable Ground Heat for Insulation in Low Exergy Building Systems, *Energies*, Vol. 5, pp. 3149-3166.
- [4] Minkowycz, W.J., Sparrow, E.M. and Murthy, J.Y. (2006), *Handbook of Handbook of Numerical Heat Transfer*, 2nd edition, John Wiley and Sons, Inc., Hoboken, New Jersey.

Institute for Mechanical Engineering Technology



Professor Dr. Gábor KALÁCSKA
Director of the Institute

Dear Reader,

The Institute for Mechanical Engineering Technology (consists of three departments: Department of Material and Engineering Technology, Department of Maintenance of Machinery, Department of Mechatronics) carried out more research topics launched formerly during the year 2012 – 2013. Three of them are shown briefly in the following articles.

Those are about:

- Tribology research of engineering polymers, devoting special attention to different composites. PA6 as a strategic base polymer matrix and PEEK as an advanced matrix were investigated. New test set-up and measuring systems have been designed with regard to the running-in phase of friction as well.
- Material sciences, where the carbon nano-tube network-design seeking the weak points under tensile load were modelled. New algorithm and junction model have been developed.
- Mechatronics area. A new method and an instrument has been developed to recognize object's location. Through applying Doppler effect an image is going to be developed about the object in question but the people with poor sight will not be able to see this. For this reason the second step of this project is to make the image audible.

As a result of more-year-long research activity one PhD work dealing with rubber/steel hybrid parts was completed in 2013. The surface preparation of the steel part and 2D and 3D characteristics of micro-topography were studied before joining the rubber. Also the vulcanization technology was investigated.

Additionally it has to be mentioned that the workshop and laboratory equipments were developed during 2013.

More information about the Institute:

www.geti.gek.szie.hu

Development of tribology model systems for research of PA6 and PEEK polymer composites

László ZSIDAI¹, Zoltán SZAKÁL²

¹Department of Maintenance of Machinery,

Institute for Mechanical Engineering Technology

²Department of Material and Engineering Technology,

Institute for Mechanical Engineering Technology

Abstract

Our present work prepares a research, what is starting now, that composites based on PA6 and PEEK polymer matrix is aimed at the making a map of the features of tribology. I give a short introduction from the significance of the tribological small-scale examination of the polymers and his present state. I plan to use reciprocating Cylinder on plate and standard pin on disc test. From the research expected results may serve as a basis reliable and energy saving constructions for the industry. It gives reasons for the research that they expand increasingly better in the mechatronic and the precision engineering the clear polymer-polymer contacts.

Keywords

tribology, PA6, PEEK, polymer, composites

1. Introduction

My work is trended towards the examination of the reliability of engineering plastics in sliding (tribology) polymer-polymer and polymer-metal contact systems, through the complex tribology exploration of characteristics.

It turned because of my interest, some important viewpoints the polymers towards the research of tribology, these are next:

- Beside the corrosion and fatigue, the friction and wear are the basic failure mechanisms of the moving machine elements.
- Because of the strength, chemical resistance and self-lubricating ability of polymers, they can be chosen as sliding material in many applications of machine construction.
- The tribological performance of polymer/steel sliding pairs can be further improved by altering the polymer composition with additives, Bahadur (1992).
- The tribology investigations are very difficult and expensive, since many times one–one tests are not enough for accurate determination of the tribological behaviour. Consequently, standards recommend simplified laboratory tests with small-scale specimens.

The reasons for these so-called, small-scale tests are quite obvious, e.g. simple test rig with low forces and power, reduced cost for preparing test specimens, easy of control of environment. Moreover many small-scale results are available in literature to be referenced, e.g. Sukumaran, et al. (2012), Zsidai, et al. (2002). They are useful to compare the properties of different materials, but induce unrealistic edge effects.

The small-scale test results obtained recently give more and more new knowledge about the tribology behaviours of modern constructional materials. This is true mainly for the standardised "tribo" systems, because of these are easily obtained and there is a possibility to make fast tests. Unfortunately we have only little information about the tribological properties of polymers concerning some extreme cases e.g. high load under different condition, unfavourable contact geometry and also there is a lack of data about the tribological effect of inner component in case of composites.

As an examined materials from among the engineering polymers are the several of the variants composites based on PA6 (polyamide 6) and PEEK (Polyether ether ketone) polymer matrix (with a lubricant charged and/or are with thread strengthening), and the mating plates are steel (and polymer) I plan his application.

Several studies on the tribological behaviour of common engineering plastics e.g. Uetz, Wiedemeyer (1985), Kalacska, et al., (1997), Yamaguchi (1990), Kalácska (2007, 2013) in contact with steel have been published and compared by, e.g., Tanaka (1982), and Evans (1982). We can found In the research character in connection with base polyamide, Byett (1992), De Velde, De Baets (1997), Keresztes (2010) and the base PEEK, Yamamoto et al. (2002) in sources also. The number of the articles dealing with the composites is growing nowadays, e.g., Friedrich et al. (1995), Sumer et al. (2008) and Schroeder et al. (2013).

I characterize the polymers with complex tribology examinations, taken into consideration the material testing (tensile and hardness examinations) his results.

Our equipment's make it possible to do (dry) sliding friction tribo tests in adhesion and abrasion systems near different parameters (velocity, load, surface roughness, temperature), different motion and with contact relations (continuous and altering, circle and lineal).

Aims

Regarding the above written the main aim of my research work is to investigate the friction and wear behaviour of engineering polymer composites. During the evaluation of the results of my research work I put emphases on describing the system-independent phenomena beside the points that are:

- Comparison of friction and wear behaviour of different composites in connection with their chemical and mechanical properties. Description of the basic failure process of engineering plastics during dry sliding in different conditions.
- Definition of the safety of the polymers against overload, to determine the effect of different internal (filled) lubrications on the tribological behaviour of polymers.

- Investigation the effect of inner component in case of composites on the sliding friction comparing to the base polymers, taking the adhesion and the heat conduction of the mating surfaces into account. Further aims of the research: to determine the optimal operational conditions of the selected polymers, and to give a help for the selection of a proper polymer for a certain condition.

2. Test rigs

Base Principles

The tribological properties of polymers strongly depend on the sliding (tribo) friction systems. The experiences express the difficulty of determination of the tribological properties from only one-one friction tests with the same parameters. It is necessary to use different tribo test systems with different parameters to establish a better database of polymers.

I selected two examination systems based on the above ones:

- CYLINDER ON PLATE reciprocating test rig
- PIN ON DISC standard tribo test with continuous sliding friction

My reasons the next:

Most of the tribology test systems do not apply or there is no possibility of use high normal pressure between the sliding surfaces. It mainly depends on the contact geometry, where we can increase the load with the decrease of contact area e.g. counter formal contact (line or point). The literature we can see mostly dynamic friction results measured under steady condition. Regarding the global friction and wear behaviour of engineering polymers we must target the investigation of static friction coefficient as well to approach e.g. the disadvantageous stick-slip phenomenon. That's why I selected the CYLINDER ON PLATE reciprocating test rig (like HFRR) to determine both friction coefficients.

It is generally true from the literature and tribotesting practices that most of the tribology test rigs provide a continuous sliding friction (e.g. PIN ON DISC, BLOCK ON RING, FOUR BALL TESTS, etc.). Because of this beside the observed phenomena, PIN ON DISC test gives a good comparison with the previous (from literature) results.

Description of the CYLINDER ON PLATE reciprocating test rig

The experimental set-up as pictured in figure 1. is essentially a variant of the cylinder on plate reciprocating tribotest rig.

The reciprocating sliding friction is created by a polymer cylinder (1), which moves against a lower steel plate (2) in counter formal contact. The polymer specimen is fixed to the static fixture (3) the oscillating motion of the mating (steel) plate is provided by a controlled variable speed motor (4) through a crank transmission for the adjustment of the stroke. The steel plate is fixed to the moving plate holder (5) and is moving on a linear guide way (6). The horizontal

movement is impeded by the load cell (7) like a friction force. The machine is equipped with a manual loading system, which consists of a load arm (8), mechanically pulled down by weights (9). The normal displacement of the cylindrical specimen towards the steel plate, as a result of the wear, is measured by a contactless proximitor (10).

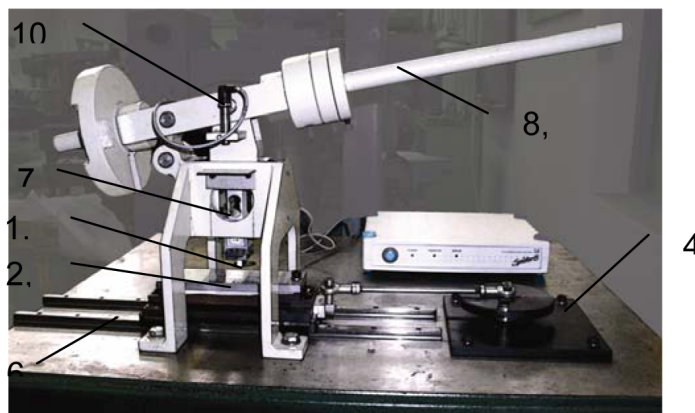


Figure 1. Experimental set-up of the cylinder on plate reciprocating tribotest

Description of the PIN ON DISC standard tribo-test with continuous sliding friction

The figure 2. shows the practical construction of the (Dynamic) PIN ON DISC tribometer with its different elements, the sliding motion of the samples, the way of load transfer and the selection of the frictional track. Vibrations of the test equipment are reduced by a massive cast support. With a turn-free attachment in order to ensure a homogeneous contact surface, the cylindrical polymer sample is fixed into a clamp head (1), and is mechanically pushed against the mating disc with a constant (or changeable) load by means of a lever system (2) and dead weights (3). The radius of the frictional track is determined by the position of the cross guiding rail (4). The end surface of the polymer cylinder is facing the metal counter face plate (5), providing continuous sliding friction (Kalácska et.al 1999). The rotating metal counter face (original steel plate or polymer plate) is fixed to the supporting table, providing a continuous rotational motion. In this way, a conformal contact is ensured between the end surface of the polymer cylinder and the steel or polymer disc, which can be regarded as a rigid body as opposed to the plastic sample.

The so-called bulk temperature is measured in the bulk of polymer with a thermocouple. The wear is characterised by the drop in height of the polymer cylinder, and is measured with a contactless proximitor.

The measurements according to the German standard DIN 50322 suit to the VI. wear test category, (DIN 50322, 1986).

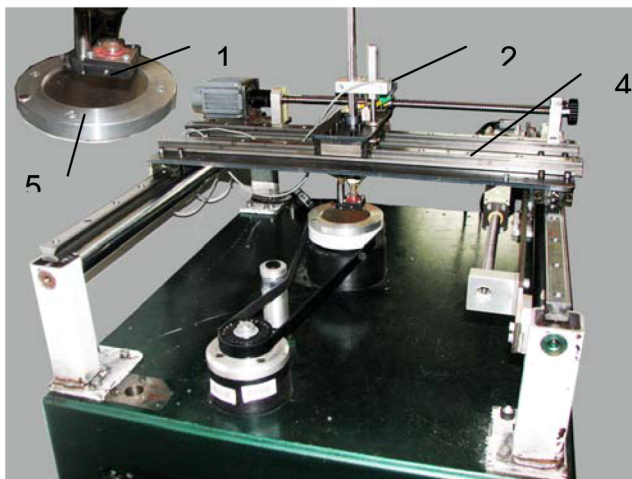


Figure 2. Experimental set-up of the cylinder on plate reciprocating tribotest

Test method

I will use the examination logical order used in the course of my earlier researches that is shown on the figure 3.

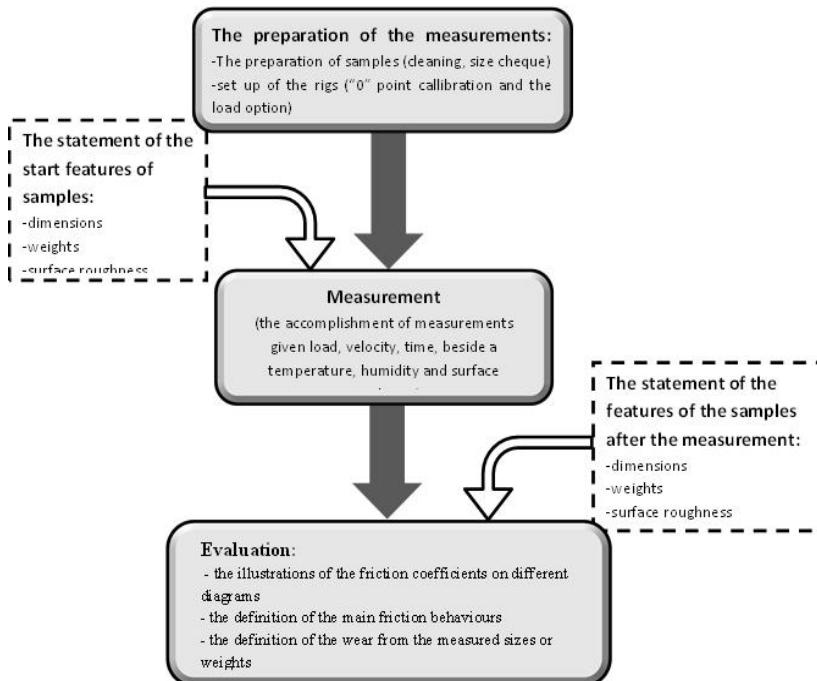


Figure 3. The order of the logical steps of the tribological measurement process, and the contact between them

Locations of the research

I carried out the investigations at same place for tribology and material science also. The tribology tests, which are presented in this paper, will make in *SZIU, Faculty of Mechanical Engineering – Institute for Mechanical Engineering Technology, Gödöllő, Hungary*, in the frame of the research fellowship *BOLYAI (BO/00127/13/6)*.

Presumably, some additional tests, like chemical tests, SEM analysis and investigations of wear depth will make at other institute at SZIU and at BME-Budapest.

3. The investigated materials

The selection of the tested polymers and composites was made on the database of polymer producers, end-users and expertizing companies at this field. The finally selected engineering polymer materials can be taken as generally used engineering materials in the industry in sliding systems. Some of the like polyamides are well-known but some composites are just being spread.

The materials are two composites groups. One of them is with PEEK and the other is with PA6 base matrix are included in the experiments.

Material of the polymer specimens

PA6's composites

The basis polymer constructions well can be added different addition-, strengthening composite materials with a modified characteristic differing with substances, so can be created.

Onto the satisfaction of the technical users' wide-ranging claims they stand for a provision: glass, carbon fibres, lubricant, MoS₂, soot, elastomer, antioxidant, composites with a mineral content, concerned it mentioned associating composites produced with the different combinations of substances. Fibre reinforced and/or lubricant filled base material is available to ensure special properties (better sliding, wear resistance, greater strength, dimensional stability).

Main areas of use: bearing bushings, wear pads, sleeve bearing, guide and conveyor rollers, rope pulleys, cams, gear wheels, gear racks, hob gears, buffer blocks, chain gears, hammer heads, blades, strippers, insulating elements, gasket rings, insulators, etc. [Kalácska 2007]

PEEK's composites

The *polyether ether ketone* in other grouping at which distinguished features are HPM (high-performance materials) his group can be enumerated. The PEEK is semi-crystalline engineering plastics with excellent heat resistant.

There are unfilled natural and PTFE-, graphite-, carbon-, glass fibre-reinforced composites. PEEK can be used well in case of extremes of operating condition (low or high temperatures, strong chemical effects, high mechanical and tribological loads and radiation). PEEK can be used in the field of e.g.:

conventional machine production, aviation, nuclear and chemical industry, transportation. Typical machine elements made of PEEK: gears, pump elements, sealing, valves, slide bearings, linings, controllers, pistons, jigs...etc.

The main properties of the base polymer matrix from the manufacturer are showed in table 1. [Kalácska 2007]

Table 1. The main properties of the test polymers

PA 6	PEEK
<ul style="list-style-type: none"> • High strength properties: 70–110 MPa (flow, breaking, crushing), • Toughness (notched Charpy): 12 kJ/m²– does not break, • Good sliding properties : $\mu=0,15-0,5$ (dry sliding on smoothed and ground steel), • Wide temperature range for application: from –40°C to +140°C, • High hardness (Rockwell): M 85 – M 98, • Good fatigue strength and damping capability, • Good wear resistance, • Favourable creep resistance: 18 – 26 MPa, tension for 1% extension in 1000 h, • Density: 1,15 – 1,16 kg/dm³ 	<ul style="list-style-type: none"> • High mechanical strength (75 - 130 MPa) and hardness, • High temperature of applicability (250-310 °C), • Good strength at elevated temperatures • Excellent wear resistance of tribo-composite versions • Good stiffness and dimension stability at high temperatures, too • Difficult to burn • Excellent electrical insulation for natural version • Good resistance to high energy radiation

There could be different effect of the different base polymer matrix on the friction and wear due to the modified mechanical properties and surface energy, too. I use different forms of the polymer specimens for the tests:

- In CYLINDER ON PLATE tribo systems the diameter $\varnothing 6$ mm, length $l=12$ mm
- In PINS ON DISC tribo systems the diameter, $\varnothing 5$ mm, length $l=10$ mm

Material of the mating part for tribo tests

The counter plates are made of hardened and tempered 40CrMnNiMo8 steel (German standard DIN 1.2738). Steel surfaces are hardened and tempered to approximately 300 HB.

In case of CYLINDER ON PLATE tests the dimension of the steel plate is 80x60x10mm. Two different methods for preparing the steel surfaces are used. The first consists of grinding the surface to a roughness $R_a = 0.1-0.3 \mu\text{m}$. In order to obtain a lower roughness, the steel substrates are polished with SiC-paper (grid 400 and 600) to a R_a -value of 0.02–0.08 μm . The grinding grooves are made parallel to the sliding direction during the wear tests. Roughness is measured perpendicular to the sliding direction. The roughness parameters and the normal force define the real contact zone. These roughness parameters can be defined in Descartes and wavelength space [Barányi (2011)].

In case of PIN ON DISC tests the diameter of the steel disc is 100 mm and the thickness is 10mm. The grinding grooves are concentric therefore they do not have a determined trend for the friction.

The information about the size of mating plate could be very important in the future work in connection with the friction heat conduction.

Conclusions

From the research expected results may serve as a basis reliable, modern, with a polymer basis, to the formation of a substance and energy saving constructions for the industry. It gives reasons for the research that they expand increasingly better in the mechatronic and the precision engineering the clear polymer-polymer contacts. The making a map of these contacts is the users' fundamental claim.

The largest significance of the given results their informative role furthering the practical application, based on which is increasable the reliability of tribology features. Beside the technical viewpoints, we wait the results about the environment protection one (lubricant reduction –self lubrication) and the economic benefits (exchanging more expensive polymer for cheaper one) also.

I keep the most critical part of the research the examination of composites with thread strengthening, because of their tribology tests half-baked and their behaviour is depend on many factors. The results offer a potential opportunity on the international conferences and in professional journals truth onto publishing, patents protecting.

Acknowledgements

The author (László Zsidai) would like to thank MTA (Hungarian Academy of Sciences) for supporting this work in the frame of the research fellowship BOLYAI (BO/00127/13/6).

Special thanks go to SZIU Institute for Mechanical Engineering Technology for the labours and the QuattroPlast for the delivery of material specimens.

References

- [1] Barányi I, Kalácska G, Czifra Á (2011): Three dimensional surface microtopography analysis based on wavelength method, Synergy 2011 - II. International Conf., Gödöllő, 2011.10.09-2011.10.15. pp. 1-4.
- [2] DIN 50322 (1986): Kategorien der Verschleißprüfung, Deutsche Norm 50322, Beuth Verlag
- [3] Evans, Dc; Senior, Gs (1982): Self-lubricating materials for plain-bearings, Tribology International Volume: 15 Issue: 5 Pages: 243-248

- [4] F. Van De Velde, P. De Baets, The friction and wear behaviour of polyamide 6 sliding against steel at low velocity under very high contact pressures, *Wear* 209 (1997) 106–114.
- [5] Friedrich, K; Lu, Z; Hager, AM (1995): Recent advances in polymer composites' tribology ,*WEAR* Volume: 190 Issue: 2 Pages: 139-144
- [6] G. Kalácska, et al., (1997): *Műszaki műanyagok gépészeti alapjai (Mechanical Basics of Polymers)*, Minervasop Bt. Sopron,
- [7] G. Kalácska- L. Zsidai- M. Kozma- P. De Baets: Development of tribological test-rig for dynamic examination of plastic composites. *Hungarian Agricultural Engineering*. N.12/1999. Hungarian Academy of Sciences. p. 78-79.
- [8] H. Uetz, J. Wiedemeyer, (1985): *Tribologie der Polymere*, Carl Hanser, Munich,
- [9] J. Sukumaran, M. Ando, P. De Baets, V. Rodriguez, L. Szabadi, G. Kalácska, V. Paepegem (2012): Modelling gear contact with twin-disc setup, *Tribology International* 49 (2012) 1-7
- [10] J.H. Byett, C. Allen(1992) :Dry sliding wear behavior of polyamide-66 and polycarbonate composites, *Trib. Int.* 25 (1992) 237, Pages: 237-246
- [11] Kalácska G. ed. (2007): *Műszaki polimerek és kompozitok a gépész-mérnöki gyakorlatban.* 3C-Grafika Kft. p. 1-315. ISBN-10: 963-06-1566-5, ISBN 13: 978-963-06-1566-2
- [12] Kalácska G. (2013): An engineering approach to dry friction behaviour of numerous engineering plastics with respect to the mechanical properties. *eXPRESS Polymer Letters* Vol.7, No.2 (2013) pp. 199-210.
- [13] Keresztes R., Kalácska G. (2010): Research of machining forces and technological features of cast PA6, POM C and UHMW-PE HD 1000. *Sustainable Construction & Design*. 2010. Vol.1. p. 136-144.
- [14] S. Bahadur, D. Gong (1992): The action of fillers in the modification of the tribological behavior of polymers. *Wear* 158 (1992) 41.
- [15] Schroeder, R.; Torres, F. W.; Binder, C.; et al. (2013): Failure mode in sliding wear of PEEK based composites , *WEAR* Volume: 301 Issue: 1-2 Pages: 717-726
- [16] Sumer, M.; Unal, H.; Mimaroglu, A. (2008): Evaluation of tribological behaviour of PEEK and glass fibre reinforced PEEK composite under dry sliding and water lubricated conditions ,*WEAR* 265 Issue: 7-8 Pages: 1061-1065
- [17] Tanaka K. (1982): Transfer of semi-crystalline polymers sliding against a smooth steel surface *WEAR* 75 Issue: 1 Pages: 183-199
- [18] Y. Yamaguchi (1990): *Tribology of Plastic Materials*, Tribology Series 16, Elsevier, Amsterdam DIN 50322, Kategorien der Verschleißprüfung, Deutsche Norm 50322, Beuth Verlag, 1986.
- [19] Yamamoto, Y; Takashima, T Source (2002): Friction and wear of water lubricated PEEK and PPS sliding contacts ,*WEAR* Volume: 253 Issue: 7-8 Pages: 820-826

- [20] Zsidai L., et al. (2002): The tribological behaviour of engineering plastics during sliding friction investigated with small-scale specimens. *Wear*, 253 673-688. p.

Drawing process of carbon nanotube „y” junctions

Tamás PATAKI, Attila KÁRI-HORVÁTH, Zoltán SZAKÁL

Department of Material and Engineering Technology,

Institute for Mechanical Engineering Technology

Abstract

We examined the behaviour of carbon nanotubes, and their structures. These structures under tensile forces begin to deform naturally. But this deformation consists of two major parts. One is a topological deformation, which characterizes the change of the bond angles. The other is the real strain increasing the bond length. Normally the structure of carbon nanotubes is built up on graphene surfaces. The graphene structure is designed, so the neighbour atoms are located on a circle of 1.4 angstrom (Å), at 120 degrees. With the developed calculation method I found that under the modelled strain the bond angles change their structure first, and then it will be followed by the change of the bond length.

Keywords

nanotube, graphene, bond degree, bond length, tensile strength

1. Introduction

The topology of nanotube has been investigated [1-3]. How to build up, and therefore what type of electrical properties have they [3]. These tests and studies have shown the ground state of build structures. The nanotube can have different chirality, and of course, not only the electrical properties change but also mechanical and the tribological properties too [4-14]. These changes were calculated in single-walled nanotubes molecular mechanics methods [4, 5, 15-17]. On a super square network were calculated deformations and distortions. This calculation was made of the structure as a whole [16-21]. The individual bonds did not cover in detail.

2. Methods and materials

Neither method was specified what kind of changes pass off under load. The articles found in the literature do not cover the length and angle of the joints. These parameters can be changed under load. The original structure changes

continuously until it reaches the point when it breaks. The nano tubes due to the elongation of two parts, one for the bond angles and bond lengths of the other changes. The angles are easier to change, they change first, then the harder varying lengths will lengthen. At the beginning the bonds are 1.4 angstrom (\AA), and the bonding angles are 120 degrees. On the figures (fig. 1-4) you can see the changing of the bond angle and the bond length.

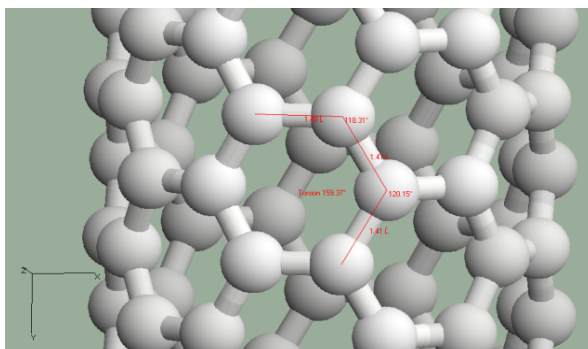


Figure 1. Basic structure

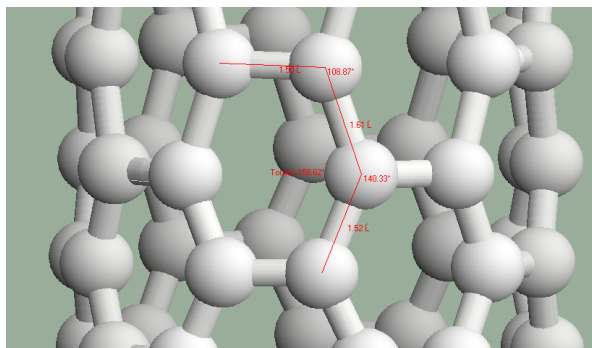


Figure 2. 400 step (4 nm)

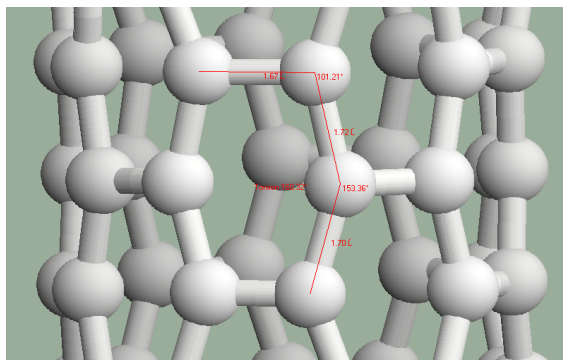


Figure 3. 600 step (6 nm)

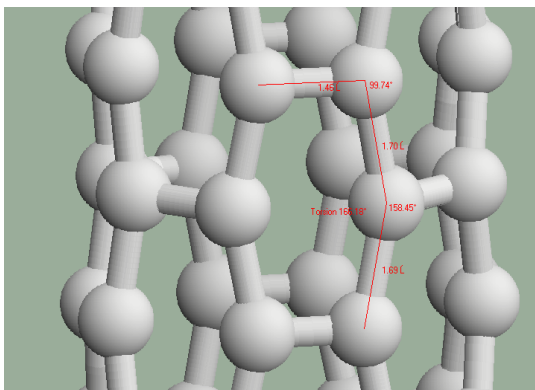


Figure 4. 879 step (8,79 nm) Befor it's broken

The table (tabl. 1) shows changes taking place during the entire process. And this can you see on the two graphs too. (fig. 5-6)

Table 1. The collected datas

step	Angström	degree_1	degree_2	mean distance
0	0	119,86	120,17	1,4
100	1	116,28	126,75	1,41
200	2	114,63	131,13	1,41
300	3	111,92	135,68	1,43
400	4	108,87	140,33	1,46
500	5	105,55	147,29	1,51
600	6	101,21	153,36	1,59
700	7	100,85	155,74	1,63
800	8	100,26	157,13	1,69
879	8,79	99,78	158,45	1,71

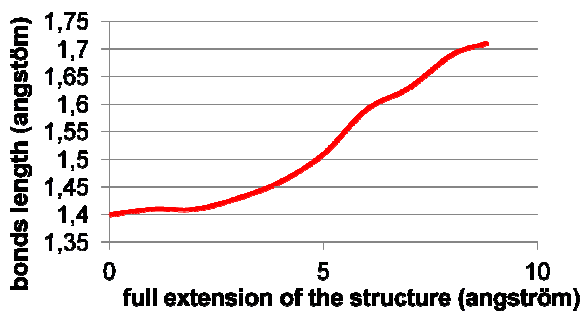


Figure 5. Changing of bond length

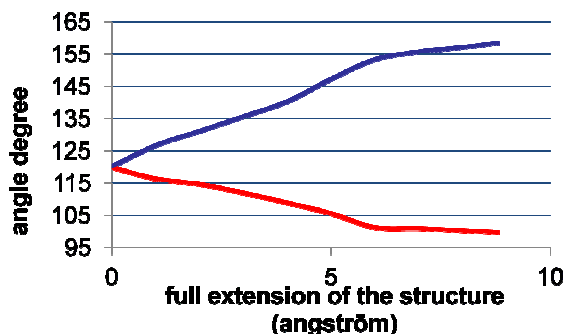


Figure 6. Changing of bond degree

References

- [1] Li, C.Y., Chou, T.W.: Elastic moduli of multi-walled carbon nanotubes and the effect of van derWaals forces. *Compos. Sci. Technol.*
- [2] Li, C.Y., Chou, T.W.: Single-walled carbon nanotubes as ultrahigh frequency nanomechanical resonators. *Phys. Rev. B* **68**, 073405 (2003)
- [3] Li, C.Y., Chou, T.W.: Elastic properties of single-walled carbon nanotubes in transverse directions. *Physical Review B* **69**, 073401 (2004)
- [4] Li, C.Y., Chou, T.W.: Modeling of elastic buckling of carbon nanotubes by molecular structural mechanics approach. *Mechan. Mater.* **36**, 1047–1055 (2004)
- [5] Li, C.Y., Chou, T.W.: Mass detection using carbon nanotubebased nanomechanical resonators. *Appl. Phys. Lett.* **84**(25), 5246–5248 (2004)
- [6] Mátyás ANDÓ, Gábor KALÁCSKA, Tibor CZIGÁNY: Development and Examination of different cast polyamide 6 composites. *Synergy and Technical Development, Gödöllő 2009* 06-199 1-6p.
- [7] Matyas ANDO, Gabor KALACSKA, Tibor CZIGANY: Development of magnesium catalyzed polyamid 6 matrix composites. *Erősített Műanyagok 2008 Nemzetközi BALATON Konferencia, Keszhely 2008b.* 1-9 p.
- [8] Matyas ANDO, Gabor KALACSKA, Tibor CZIGANY: Development of Technical Polymer Composites for Agricultural Engineering Application. *Gépészet 2008, Budapesti Műszaki és Gazdaságtudományi Egyetem, Budapest 2008 G-2008-K-07* 1-7p. Mylvaganam K., Zhang L.C., *Carbon* 42:2025-2032, 2004.
- [9] Kalácska Gábor, Andó Mátyás, Deák Ferenc, Sárosi Gyula: Öntött poliamid 6 alapú nano- és mikro kompozitok fejlesztése különleges gépészeti alkalmazásokhoz. *MTA AMB Kutatási és Fejlesztési Tanácskozás. Gödöllő, SZIE Gépészmérnöki Kar - FVM Mezőgazdasági Gépesítési Intézet, 2007.* 3. kötet 195-199 p.
- [10] Andó Mátyás, Kalácska Gábor, Czigány Tibor: Öntött poliamid 6 kompozitok vizsgálata és anyagfejlesztése. *MTA AMB Kutatási és Fejlesztési*

- Tanácskozás. Gödöllő, SZIE Gépészmérnöki Kar - FVM Mezőgazdasági Gépesítési Intézet, 2008. 1. kötet 251-255 p. Agrawal P.M., Sudalayandi B.S., Raff L.M., Komanduri R., *Comput. Mater. Sci.* 41:450-45, 2008a.
- [11] G. Kalácska, L. Zsidai, R. Keresztes, A. Tóth, M. Mohai, J. Szépvölgyi.: Effect of nitrogen plasma immersion ion implantation of polyamide-6 on its sliding properties against steel surface. *Wear* 290-291. (2012) pp. 66-73.
- [12] Kalácska G. (2013): An engineering approach to dry friction behaviour of numerous engineering plastics with respect to the mechanical properties. *eXPRESS Polymer Letters* Vol.7, No.2 (2013) pp. 199-210. DOI: 10.3144/expresspolymlett.2013.18
- [13] G. Kalácska, L. Fazekas, R. Keresztes, A. Tóth, J. Szépvölgyi: Cold flame-sprayed and oil-impregnated porous metallic coatings. Elsevier. *Applied Surface Science*. 257 (2011) pp. 9532-9538.
- [14] Keresztes R., Kalácska G.: Research of machining forces and technological features of cast PA6, POM C and UHMW-PE HD 1000. = *Sustainable Construction & Design*. 2010. Vol.1. p. 136-144. ISSN 2032-7471, ISBN 978-9-49072-600-3
- [15] Li, C.Y., Chou, T.W.: Vibrational behaviors of multiwalled carbon-nanotube-based nanomechanical resonators. *Appl. Phys. Lett.* **84**(1), 121–123 (2004)
- [16] Pan, Z.W., Xie, S.S., Lu, L., Chang, B.H., Sun, L.F., Zhou, W.Y., Wang, G.: Tensile tests of ropes of very long aligned multiwall carbon nanotubes. *Appl. Phys. Lett.* **74**(21), 3152–3154 (1999)
- [17] Zhou, L.G., Shi, S.Q.: Molecular dynamic simulations on tensile mechanical properties of single-walled carbon nanotubes with and without hydrogen storage. *Comput. Mater. Sci.* **23**, 166–174 (2002)
- [18] Yakobson, B.I., Campbell, M.P., Brabed, C.J., Bernholc, J.: High strain rate fracture and C-chain unraveling in carbon nanotubes. *Comput. Mater. Sci.* **8**, 341–348 (1997)
- [19] Li CY, Chou TW. A structural mechanics approach for the analysis of carbon nanotubes. *Int J Solids Struct* 2003;40:2487–99.
- [20] Liu B, Huang Y, Jiang H, Qu S, Hwang KC. The atom-scale finite element method. *Comput Method Appl M* 2004;193:1849–64.
- [21] Liu B, Huang Y, Jiang H, Qu S, Yu MF, Hwang KC. Atomic-scale finite element method in multiscale computation with applications to carbon nanotubes. *Phys Rev B* 2005;72:035435.

Development of orientation strategy and guidance tool for visually impaired people

Viktor ERDÉLYI, László JÁNOSI
Department of Mechatronics,
Institute for Mechanical Engineering Technology

Abstracts

In this paper a new method and an instrument has been developed to recognize object's location, orientation and size. The basic idea is the application of sense of locality of bats. Applying Doppler effect an image will be developed about the object in question but the people with the lack of power of vision will not be able to see this. The second step of this project is to make the image audible. Applying a special transformation all pixel of an image will be adequate with a respective sound effect.

Keywords

Doppler effect, image process, sense of locality

1. Introduction

Target

My target is to develop a virtual imaging method based on sonic reflection and to create a device which is able to generate images using ultrasonic technology.

Background

In the world of animals some mammals use ultrasonic orientation, however there are some „night vision” techniques used by warriors of certain tribes centuries before the invention of electronics. As well known the bat use ultrasound for exploring its prey and for orientation. Dijkgraaf (1949) Matsuda et. al. (2013) This technique is called „echolocation” which means ultrasonic navigation. Bats' echolocation is discovered by Donald Griffin and Robert Galambos in 1938. Griffin (1958) It seemed to be obvious, that animals, Jones (2005), and even humans can use this method for orientation in darkness. Let's use this technique extended by electronics for virtual imaging!

2. „Echolocation”

Principle of operation

If we compare the technical practice with the echolocation technology, the simplest analogy is the active sonar. The meaning of SONAR is SOund NAvigation Ranging

Navigation And Ranging Operation is the following: Jones (2005) The animal or the location equipment emits a sound impulse which reflects from surfaces and gets back to the emitter. The „emitter” calculates the distance from the elapsed time between emitting and receiving the pulse. The horizontal azimuth is calculated from the loudness and time difference between the signals received by two sensors or ears. The navigation method inspired by animals patented by an English meteorologist, Lewis Richardson in 1913. Hill 1962

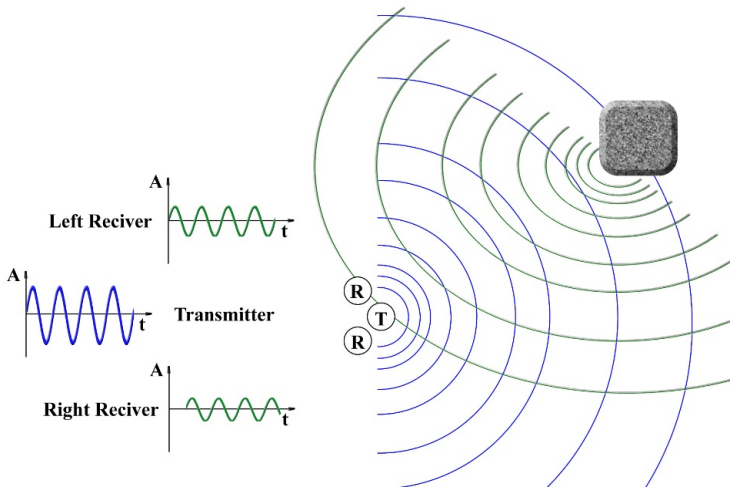


Figure 1. Working principle of „echolocation”

According to Suga et. al. (1975) the emitted sound can be examined from several points of view.

– **Frequency**

- Frequency modulation (FM): during the FM ping the modulated search sound's frequency changes in a wide range.
- The sweeping starts from higher frequencies. Constant frequency (CF): During a CF search the frequency range is narrow; the search sound's frequency can be considered as constant.

– **Intensity** in the world of animals the search sound's intensity varies between 60 and 140dB. The amplitude is reduced in small distances, because the reflected sound's pressure could damage the bat's ear.

– **Pulse time** Bats change the interval of the search sound between 0,2 and 100 ms, depending the distance to be measured. When hunting pings are more frequent, this results in a better image resolution of their environment. Shorter pulses are used measuring smaller distances.

FM sweep

The biggest advantage of wide-range-sweeping ultrasound is the possibility of precision distance measurement. In J.A Simmons'(1975) experiment, bats were

able to detect 0,5 mm difference between two surfaces using FM sweep. The emitted sound sweeps in a wide frequency range which helps them to detect the reflection time more precisely, and has a better cross-correlation. The accuracy can be improved if the search sound has harmonics. The disadvantage of FM method is the limited range of operation. It works with small distances only Suga et. al. (1975).

CF sweep

The biggest advantage of CF is the bigger range, and the capability to measure speed from the Doppler's effect.

As the bat search for moving prey, and the red shifts, and the blue shifts from Doppler's effect help him to sense the target moving direction, Suga et.al. (1975).

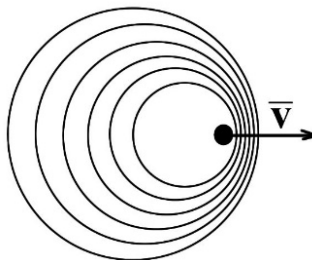


Figure 2. Doppler effect

$$f = \left(\frac{c + v_r}{c + v_s} \right)$$

Where:

f: frequency of the reflected sound

c: speed of sound

v_r : the bat speed relative to the medium

v_s : speed of the reflector (prey) relative to the medium

f_0 : the frequency of the emitted sound

Neurological mechanism in the brain

As the bats find their way with their sound, their ear and the part of their brain which is responsible for hearing are modified specifically. The human basically orientates himself with his vision. The experiences prove that the brain section, which is responsible for hearing – the temporal lobe –, is much more supplied with blood if the human is blind. Also the occipital lobes, which provide the ability to see, is not wither over time, but help to process the information that heard. Burton (2003).

3. Design of instrument working on „echolocation” effect

Initial consideration

During the preparation phase of the device design, the capabilities of the human brain were considered, which are different from species, specialized for this navigation method. Also the ancient „night vision” method was studied, which based on the reflection of the human-made voices.

Criteria which are considered:

- Transportability: Very low weight
- Lifetime of the battery: Little battery with long operation time
- Using of spatial hearing: The basic capability of the human body

Knowing these criteria the distance measurement method was chosen with permanent wavelength.

The working method of the planned device

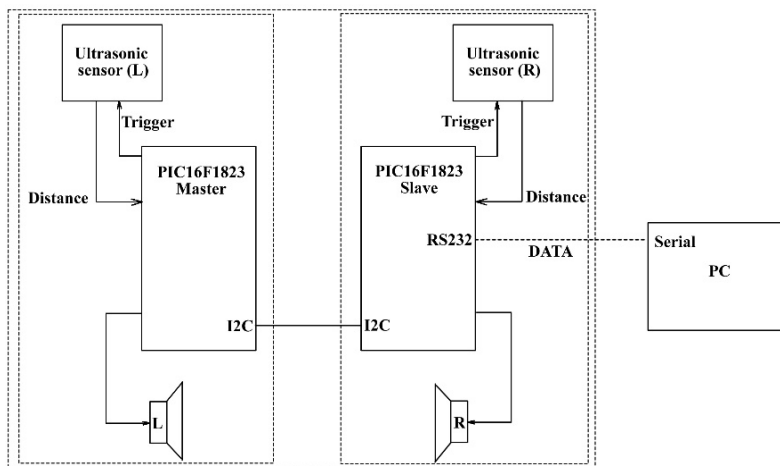


Figure 3. Schematic diagram of the system

Two intelligent ultrasonic distance measurement sensor (which are located 200mm from each other) are instructed by a trigger, after that, there will be a signal impulse on the output of the sensor, which length is proportional with the distance.

The length of the impulse and the knowledge of the sensor’s properties we can determine the distance between the sound source and the object.

With the strength of the sound, which captured with ears, the brain can determine the location and the distance of the object as if the obstacle makes the sound.

The two microcontroller gives the trigger in the same time, that way not just the amplitude of the sound, but also the frequency shifting can be evaluated.

If we compute the distance values – which are appear on the output of the intelligent distance measurement sensors – with a microcontroller, we get a sound that can be heard in the earphone. With that sound, even the human mind can build the 3D „picture” from the virtual area.

Engineering

The circuit was designed by DesignSpark program. The prototype will be produced of DIP parts, which require bigger space, but easier the assembly. If the device will work satisfactorily, the final circuit will be made of SMD parts. That way the constructed device will be much smaller – which is important point of the portability.

The circuit also got a communication channel. By using it, the measured data are available to everybody. To access these data, you will need an RS232 serial data cable, and the MATLAB program. The required programs are written in C and C# languages.

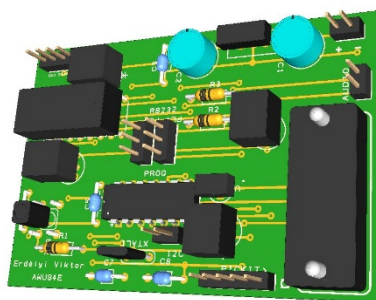


Figure 4. 3D model of the prototype PCB

4. Expected results

This device can help the blinds and the visually impaired people to find their way. It makes the obstacles visible by sound as if those make the sound. The prototype of this research can serve many other projects.

References

- [1] D. R. Griffin (1958). Listening in the dark. Yale Univ. Press, New York.
- [2] H. Burton (2003) The Journal of Neuroscience, 23(10): p.4005-4011;
- [3] Hill, M. N. (1962). Physical Oceanography. Allan R. Robinson. Harvard University Press. p. 498.
- [4] Jones G. (2005). "Echolocation" Current Biology 15(13): p.484-488.
- [5] Naohiro Matsuta, Shizuko Hiryu,, Emyo Fujioka, Yasufumi Yamada, Hiroshi Riquimaroux and Yoshiaki Watanabe (2013) Adaptive beam-width

- control of echolocation sounds by CF–FM bats, *Rhinolophus ferrumequinum nippon*, during prey-capture flight *The Journal of Experimental Biology* 216 p. 1210-1218
- [6] S. Dijkgraaf (1949). Spallanzani und die Fledermäuse. *Experientia* 5: p.90-92
- [7] Stuart Parsons and Gareth Jones (2000) Acoustic identification of twelve species of echolocating bat by discriminant function analysis and artificial neural networks *The Journal of Experimental Biology* 203, p. 2641–2656
- [8] Suga N, Simmons J.A. & Jen P.H. (1975) Peripheral specialization for fine analysis of doppler-shifted echoes in the auditory system of the "CF-FM" bat *Pteronotus parnellii*. *Journal of Experimental Biology*, 63 p.161-192.

**Invited Papers from „Synergy”
International Conference 2013**

Development of an autonomous driven robotic platform used for ht-phenotyping in viticulture

H.-P. SCHWARZ¹, Ph. RÜGER¹, A. KICHERER², R. TÖPFER²

¹Department of Viticultural Engineering, Geisenheim University

²Julius Kühn-Institut; Federal Research Centre for Cultivated Plants,
Institute for Grapevine Breeding,

Abstract

A major contribution to improve sustainability of viticulture is the cultivation of fungus resistant grapevine cultivars. Their development, however, can be accelerated by application of novel technologies to increase efficiency of selection in grapevine breeding programs. To assist evaluation of plants innovative phenotyping tools are demanding. Therefore, in an interdisciplinary approach PHENOvines will focus on the development of tools to accelerate grapevine breeding by high-throughput (HT)-phenotyping.

For this purpose a robot with a sensor unit will be constructed which is designed to run autonomously based on GPS coordinates through the vineyard to monitor yield parameters.

Keywords

high throughput phenotyping, robotics, automation, viticulture, yield monitoring

1. Introduction

During the 19th century (1845, 1878) two mildew pathogens (powdery mildew (1845) and downy mildew (1878)) and phylloxera (1863) were introduced accidentally into European viticulture. Ever since then the mildews have been causing continuous plant protection measures, high costs and today environmental concerns. These pathogens caused resistance breeding activities which in the late 1990s led to first cultivars like ‘Regent’ that successfully entered the market.

During the last decade grapevine breeding changed its toolbox considerably. The use of molecular markers which have been developed for powdery mildew (Welter et al., 2007), downy mildew (Hoffmann et al., 2008), phylloxera (Zhang et al., 2009), and other traits (Töpfer et al., 2011) is a paradigm shift. Marker assisted selection (MAS) is now an integral part of modern grapevine breeding. As a consequence of resulting technical improvements, phenotyping is becoming the current bottleneck. The phenotypic characterisation and genotypic elucidation of the genus *Vitis* and its genetic resources is a basic requirement in

order to accelerate grapevine breeding and to get access to new sources of resistance or other traits like phenological behaviour, yield or wine quality. Therefore robust, flexible, and guidable image analysis tools especially for field phenotyping are demanding.

2. HT-phenotyping

Phenotypic data acquisition is time-consuming, labour-intensive, often destructive, and in many cases of limited accuracy. As a consequence alternative strategies and techniques are currently under development to establish so called high-throughput phenotyping platforms which permit a more accurate accumulation of large quantities of phenotypic data. In a first step automated greenhouses in which plants are grown and analysed, e.g. by taking images automatically and regularly, are the basis for high-throughput (HT-) phenotyping of plants. Various fully automatic high-throughput plant growth and phenotyping platforms have been developed: A technology called PHENOPSIS (Granier et al., 2006) is used for *Arabidopsis thaliana*. The in-house System GROWSCREEN is used at Forschungszentrum Jülich to analyse different plant species (Walter et al., 2007). Other fully automatic greenhouse systems that screen plants non-destructively over a period of time are the TraitMill™ platform (Reuzeau et al., 2006) used for cereals and the high-throughput phenotyping platform developed by LemnaTec (LemnaTec). These high-tech applications are limited to contained uses and smaller plants. For some crops such as perennial crops like grapevine or fruit trees etc., similar techniques need to be transferred into the field. Particularly HT-phenotyping for breeding applications with perennial crops but also other crops requires specific adaptations or new developments.

Maximising yield is a goal in table grape breeding. In wine grape breeding, however, due to legal limitations for quality wine production in certain countries optimal yield is required for certain quality segments in the wine market. Yield as a trait has yet not been molecularly dissected in grapevine. For diversification and acceleration of breeding it is important to distinguish the various parameters contributing to yield in order to identify QTL regions. Major parameters are berry size, the number of berries per cluster and the number of clusters per cane. Up to now yield estimation in breeding as well as in viticultural practice is very vague throughout the vegetation period. The OIV descriptors (OIV, 2009) are one approach to characterise grapevine features like berry width (OIV221) or berry shape (OIV223). Image analysis was applied in viticulture for assessing the berry morphology (Kicherer et al., 2013, Tardaguila et al., 2013, Wycislo et al., 2008). To break down the most important yield parameters, the BAT (Berry Analysis Tool) was introduced by Kicherer et al. (2013) as an intermediate step within the PHENOvines project and in cooperation with the CROP.SENSE.net project. The automated image interpretation enables the acquisition of the number, size and volume of grapevine berries (Fig.1). The aim of the project is

to use this preliminary work of the assessment of yield parameters in the lab for creating a phenotyping platform for field application. So far different approaches have been made in viticulture to use machine vision within the vineyard. Dunn and Martin (2004) used image analysis for yield assessing while Tardaguila et al. (2013) acquired canopy features. In both cases a digital camera was used to capture the images.

Within the PHENOvines project a robust, high-resolution camera unit will be built and used as a sensor on the platform for image acquisition. This will be based on experience of Bonn University concerning the construction of a camera unit, gained in the CROP.SENSE.net project. The pictures generated will be stored in a database. They will be analysed by using the software tools of MathWorks. Furthermore the robot can be equipped with additional sensors for field evaluation as they become available.

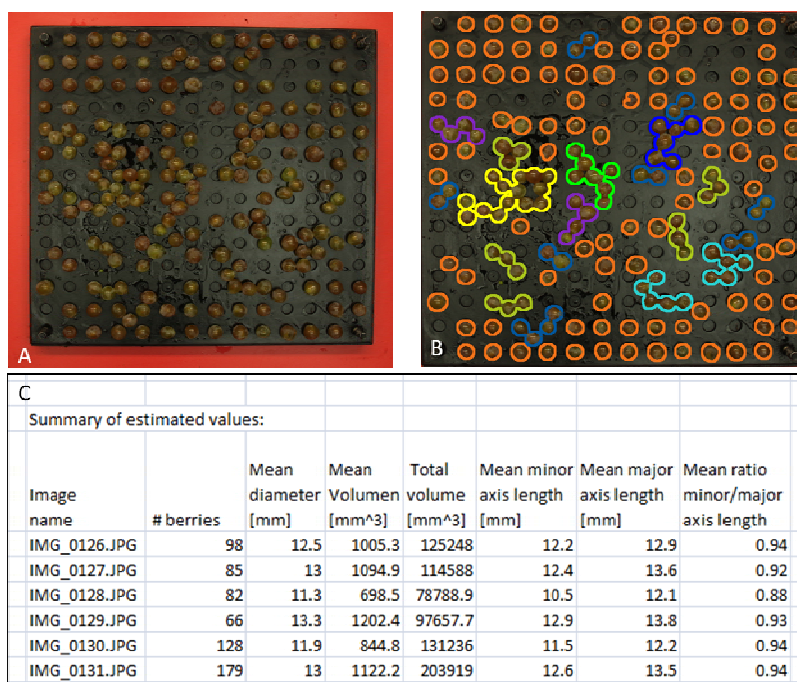


Figure 1 BAT (Berry Analysis Tool).A: Original image. B: Result image. C: Result table.

3. Autonomous driven robotic platform

Automated guided vehicle systems for in-facility use are established in several industrial sectors. Utilising different guidelines, like buried wires, these vehicles are moving only on predefined paths through the production facilities. In outdoor applications, especially off-road, the system requirements are more ambitious. Vehicle guidance systems in agricultural environments use either

virtual guidelines or real ones (Keicher and Seufert 2000). Plant oriented (relative positioning) path following systems for tasks like spraying and hoeing use the crop row for guidance. Sensor principles used include machine vision, time of flight cameras, ultrasonic, infrared, laser or mechanical sensing (Keicher, 2002). The position oriented (absolute positioning) systems, e.g. used for sowing or weeding on fallow land, are applying virtual guidelines like a predefined track. The sensor principles utilised here include inertial navigation systems and global navigation satellite systems (GNSS). Because inertial navigation is based on inertia to calculate the actual position (and thus is precise only for short periods), it is used to supplement GPS Systems to enhance accuracy. Satellite navigation nowadays is the established system for car navigation as well as for automatic steering devices on agricultural machinery.

In the 1970s, the Global Positioning System (Navigational Satellite Timing and Ranging – Global Positioning System “NAVSTAR GPS”) was developed by the US Ministry of Defense. Initially used exclusively for military needs, it was designated for public use after selective availability had ended in 1995. Nowadays it’s the most common guiding system for vehicles. Its accuracy is about +/- 10 m.

In navigation systems for cars, the accuracy of the signal is sufficient. In terms of agricultural application such as harvesting, planting, spraying, fertilising and, especially with automatic steering devices, one needs a more precise system. This is provided by the differential GPS. The accuracy in this case is +/- 2 cm. Two different measuring systems are known (Müller, 2009):

- | | |
|----------------------------|------------------------------|
| 1. real time kinematic | a) RTK |
| real time differential GPS | b) RT-dGPS |
| 2. post processing | a) static (+/- 0.003 m) |
| | b) fast static (+/- 0.005 m) |
| | c) kinematic (+/- 0.01 m) |

Today more than 30 different guiding system solutions are available for farmers (Böhrnsen, 2009). They are mostly used on large farms in Eastern Europe and in North and South America. Kübler (2010) saved over 9 % on herbicides and fertilisers using a GPS supported tractor including sensor systems. This tractor is guided by a GPS based steering system. The automatic documentation is standard in these systems. The field robot system is the next step for the mechanisation in the future. Working in the field following a pre-programmed order, these autonomous vehicles would be able to work 365 days a year 24 hours a day (Ruckelshausen, 2010).

The established automatic guidance systems for agricultural vehicles unite GPS and inertial navigation for high precision navigation. Adding a machine vision or ultrasonic system to avoid obstacles and for in-row navigation, a driverless vehicle for autonomous field operation is possible.

Some first applications have been established in viticulture. The growth variability of vineyards is well known, though only a few results have been reported (Bramley, 2005). Thus far, the focus was mainly on high or low vigour

using the Normalised Difference Vegetation Index (NDVI). All the research is done either in transit, by aerial imagery in the red and infra-red range or using the rapid eye system, i.e. satellite technology (Langner, 2009).

Construction of the carrier vehicle

As part of the first work package the exact required specifications within the following key points were developed:

Size of the chassis (L x W x H) 200 cm x 50 cm x 100 cm)

- Lifting capability up to 250 kg
- Low-vibration drive, speed 4-6 km h⁻¹
- Easily adjustable mounting system with sensors for positioning axes
- Navigation system of the robot based on GPS coordinates
- Ability to set the route on the PC (path planning) and transmission of data using external media including the data plots
- Fulfil the usual safety standards

Within the framework of these aspects, the expected operating conditions were defined and the resulting load profiles were determined. Analysing the purpose of the planned operation cycles of the robot's drive and implements and deriving the necessary driving power is required. With the collected data, vehicle simulations were created and implemented to determine the achievable energy efficiency of different concepts and to define the architecture of the driving system. This led to the choice of an electrical drive concept, the exact dimensions of the vehicle chassis and chain drive elements, together with batteries and a combustion engine as power supply and storage system.

In addition, the conditions for the carried equipment, thus the implements were to be specified. In the case of the camera unit, these are the same position, the necessary adjustment axes and areas, as well as weight, forces and moments likely to be encountered.

The design of the drive components then allowed the evaluation and selection of components available on the market. The determination of the components to be used and the design of the drive control allowed the definition of the interfaces to the navigation system and the user.

Structure of the navigation system

First, the use of sensor systems for navigation had to be evaluated in vines. Recourse could be drawn on the experience from previous projects with the use of GNSS, image processing, ultrasonic and infrared systems. It would be useful to have some redundancy in order to bridge the short-term failure of a single system. Since the task requires the use of a highly accurate GNSS system (the position data of the individual vines are needed in order to assign them to the appropriate images), additional infrared, ultrasonic or camera systems would be required only for controlling the distance to the canopy and for detecting start of line, end of line and obstacles that may occur (safety aspect).

The vehicle navigation in a row, the turning manoeuvres and path planning together with route mapping are major work packages carried out with the use of

GIS software. For safety and system testing first a semi-autonomous mode with an overriding remote control should be implemented.

Implementation

After design and construction of the carrier vehicle, the navigation system and the camera unit, all parts must be linked to the robot. The application of the control devices in the carrier vehicle and the testing of the overall system then take place in experimental vineyards. For this purpose, the robotic platform and the camera unit are equipped with metrology systems in order to ensure the adequate operation of the overall system. As a final step, a SWOT analysis will be done to evaluate the project as a whole.

Nomenclature

BAT	Berry Analysis Tool
GIS	Geo Information System
GNSS	Global Navigation Satellite System
GPS	Global Positioning System
HT	High-throughput
MAS	Marker assisted selection
NDVI	Normalised Difference Vegetation Index
OIV	Organisation Internationale de la Vigne et du Vin; vine feature descriptions
RTK	Real Time Kinematic

Acknowledgements

We gratefully acknowledge the financial support of Projektträger Jülich and the Federal Ministry of Education and Research (BMBF). This work was funded by BMBF in the framework of the PHENOVines project (FKZ 0315968A and B).

References

- [1] Böhrnsen, A. (2009), Mit Spuranzeige fahren oder automatisch lenken. In *Profi* (7), 74–77.
- [2] Bramley, R. G. V. (2005), Understanding variability in winegrape production systems, Within vineyard variation in quality over several vintages. In *Australian Journal of Grape and Wine Research* (11), 33–42.
- [3] Dunn, G. M. and Martin, S. R. (2004), Yield prediction from digital image analysis: A technique with potential for vineyard assessments prior to harvest, *Australian Journal of Grape and Wine Research*.
- [4] Granier, C., Aguirrezabal, L., Chenu, K., Cookson, S. J., Dauzat, M., Hamard, P., Thioux, J. J., Rolland, G., Bouchier-Combaud, S., Lebaudy, A.,

- Muller, B., Simonneau, T. and Tardieu, F. (2006), PHENOPSIS, an automated platform for reproducible phenotyping of plant responses to soil water deficit in *Arabidopsis thaliana* permitted the identification of an accession with low sensitivity to soil water deficit, *New Phytologist*, 169, 623-635.
- [5] Hoffmann, S., Di Gaspero, G., Kovacs, L., Howard, S., Kiss, E., Galbacs, Z., Testolin, R. and Kozma, P. (2008), Resistance to *Erysiphe necator* in the grapevine 'Kishmish vatkana' is controlled by a single locus through restriction of hyphal growth, *Theoretical and Applied Genetics*, 116, 427-438.
- [6] Keicher, R. (2002), Bestandsorientierte automatische Nachführung landwirtschaftlicher Arbeitsmaschinen in Reihenkulturen mit Hilfe der digitalen Bildverarbeitung, Dissertation, Institut für Landtechnik Gießen, Justus-Liebig-Universität.
- [7] Keicher, R. and Seufert, H. (2000), Automatic guidance for agricultural vehicles in Europe. In *Computers and Electronics in Agriculture* (25), 169–194.
- [8] Kicherer, A., Roscher, R., Herzog, K., Šimon, S., Förstner, W. and Töpfer, R. (2013), BAT (Berry Analysis Tool): A high-throughput image interpretation tool to acquire the number, diameter, and volume of grapevine berries. *Vitis*, 52 (3), 129-135.
- [9] Kübler, H. (2010), Perspectives for FMIS, Automation and Robotics in Agriculture, Erfurt, KTBL.
- [10] Langner, R. K. (2009), Presentation of Rapid Eye, A new System for Agro Risks, Geisenheim, 2009.
- [11] Lemnatec, Get an impression of your image, <http://www.lemnatec.com/>.
- [12] Müller, R. (2009), Principles and Methods of GNSS, Script, Department of Viticultural Engineering, Geisenheim University.
- [13] OIV (2009), Descriptor list for grape varieties and *Vitis* species (2nd edition), Organisation Internationale de la Vigne et du Vin, Paris, <http://www.oiv.org>.
- [14] Reuzeau, C., Frankard, V., Hatzfeld, Y., Sanz, A., Van Camp, W., Lejeune, P., De Wilde, C., Lievens, K., De Wolf, J., Vranken, E., Peerbolte, R. and Broekaert, W. (2006), Traitmill™: A functional genomics platform for the phenotypic analysis of cereals, *Plant Genetic Resources: Characterisation and Utilisation*, 4, 20-24.
- [15] Ruckelshausen, A. (2010), Semi autonomous and autonomous Systems, Automation and Robotics in Agriculture, Erfurt, KTBL.
- [16] Tardaguila, J., Diago, M. P., Millan, B., Blasco, J., Cubero, S. and Aleixos, N. (2013), Applications of computer vision techniques in viticulture to assess canopy features, cluster morphology and berry size, In: S. Poni (Ed.) *Proceedings of the 1st International Workshop on Vineyard Mechanization and Grape and Wine Quality*, Piacenza, Italy, June 27-29 2012, 77-84, Leuven, Belgium, International Society for Horticultural Science (ISHS).
- [17] Töpfer, R., Hausmann, L., Harst, M., Maul, E., Zyprian, E. and Eibach, R. (2011): New horizons for grapevine breeding, In: H. Flachowsky, M. V.

- Hanke (Eds.) *Methods in Temperate Fruit Breeding*, 79-100, Global Science Books.
- [18] Walter, A., Scharr, H., Gilmer, F., Zierer, R., Nagel, K. A., Ernst, M., Wiese, A., Virnich, O., Christ, M. M., Uhlig, B., Junger, S. and Schurr, U. (2007), Dynamics of seedling growth acclimation towards altered light conditions can be quantified via GROWSCREEN: A setup and procedure designed for rapid optical phenotyping of different plant species, *New Phytologist*, 174, 447-455.
- [19] Welter, L. J., Gokturk-Baydar, N., Akkurt, M., Maul, E., Eibach, R., Töpfer, R. and Zyprian, E. M. (2007): Genetic mapping and localization of quantitative trait loci affecting fungal disease resistance and leaf morphology in grapevine (*Vitis vinifera* L), *Molecular Breeding*, 20, 359-374.
- [20] Wycislo, A. P., Clark, J. R., Karcher, D. E. (2008), Fruit shape analysis of *Vitis* using digital photography, *HortScience*, 43, 677-680.
- [21] Zhang, J. K., Hausmann, L., Eibach, R., Welter, L. J., Töpfer, R. and Zyprian, E. M. (2009), A framework map from grapevine V3125 (*Vitis vinifera* 'Schiava grossa' x 'Riesling') x rootstock cultivar 'Borner' (*Vitis riparia* x *Vitis cinerea*) to localize genetic determinants of phylloxera root resistance, *Theoretical and Applied Genetics*, 119, 1039-1051.

A micro-controller-based algorithm for fast and robust edge detection in white paprika sorting process

Z. GERGELY¹ J. BEKE²

¹Department of Measurement Technologies, Institute for Process engineering
Faculty of Mechanical Engineering, Szent István University

²Department of Energetics, Institute for Process Engineering,
Faculty of Mechanical Engineering, Szent István University

Abstract

There is no device available on the market of sorters (pickers) which is suitable especially for sorting the sweet white paprika, and capable of fulfilling the standard requirements. The most of the sorting machines is suitable for selecting roundish, sub-spherical vegetables and fruits (tomato, potato, apple, apricot, cantaloupe etc.) by applying the weight measurement. The function of the system is to qualify the paprika of which most important parameters are its size and shape – measuring them and processing the measured data have to be solved. The record of shape is realized by CCD photoelectric linear array sensors with the help of which the processing with regular accuracy can be provided. An algorithm running in the micro-controller developed by us provides the assorting process; it determines the size fraction from the length and the shoulder-width, the centre-line length, the perimeter and area data.

Keywords

sorting technologies, micro-controller, algorithm

1. Introduction

Now the sweet paprika is still picked manually in the small as well as the large-scale plants (farms or works) so paprika generally with peculiar sizes to the producers is put on the market. This does not fulfil the very severe requirements of today. Since at present there is no accurate device available on the market of sorters for sorting the sweet pointed, white paprika accordingly we set the development of a picking system based on the picture processing as a target.

The rapid propagation of the image processing is closely related to the explosive increase in the data processing rate and the store capacity of computers. But it is still a key problem today as well (especially with the real-time applications) to elaborate successfully algorithms with an acceptable running time.

The image processing starts with shooting and recording pictures. There are several usable options for this – conventional or infrared cameras, X-ray images

and ultrasonic detectors as well. The image is usually an intensity picture or map which certain luminance values assigns to the individual points of the objects; the recorded picture may be analogues or digital.

The wide assortment of new optical techniques looks promising in the rapid determination or, at least, estimation of the quality parameters of the crops. A super-rapid pattern recognition system differing from the earlier practice is shown in the following paragraphs; it facilitates the picking processes of the sweet white paprika with acceptable accuracy.

2. Method

For achieving a suitable picking performance, the complete recognition of 3 or 4 peppers has to be provided in a second (that is 10,800 to 14,400 bell peppers per hour at a travel speed of 1 m/s). It requires an extremely high-speed picture processing system and, in addition to this, the amount of data to be processed is also multiplied according to the multi-directional mapping. The complete image processing and recognition process shown in Figure 1.

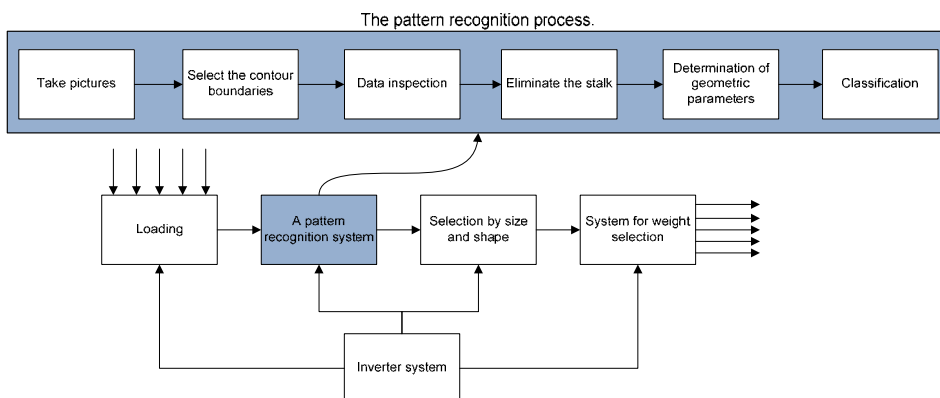


Figure 1. The complete paprika sorting process

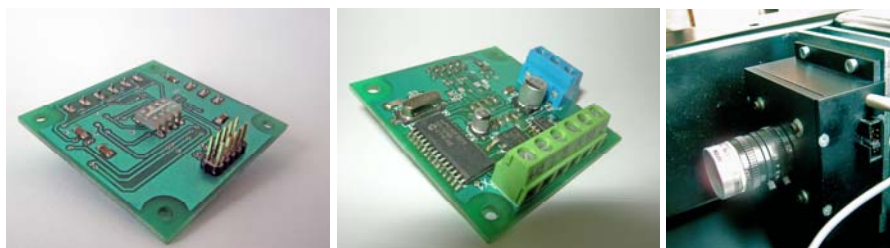


Figure 2. The used line CCD (left), the camera processor (middle) and the boxed design (right)

It turned out during the investigations that the above demands can be satisfied only by the CCD sensor with a low pixel number – by the line CCD sensors (with the type used by us), the complete pixel data can be read out in 102 μ s at the maximal read-out rate (Figure 2). An additional advantage is that the record of contour directly can take place; accordingly, the search of contour through software can be avoided and the recognition algorithm will be speeded up. To measurements used a general problem or target specific measurement system.

An embedded system (with microcontroller basis) was elaborated for the sorting algorithm. The pixel data of the CCD are received by a high-rate Microchip DSP. This unit includes the pattern recognition algorithm as well. The high speed of the DSP provides the real-time running of the algorithm (Figure 3). The whole control system as well as the operating software programmes has been developed by us alone. During the experiments the application of PCs was rejected since they did not run reliably in the severe industrial conditions (in spite of their industrial design).

To avoid the time-consuming rolling and moving of the crops, the projection has to be provided from several directions (Figure 4). It has been found in the course of our investigation that using more than two cameras does not improve significantly the accuracy, but greatly decreases the rate of processing.



Figure 3. The central processing unit

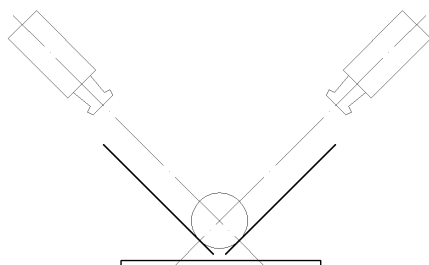


Figure 4. Projection from two directions

3. Results

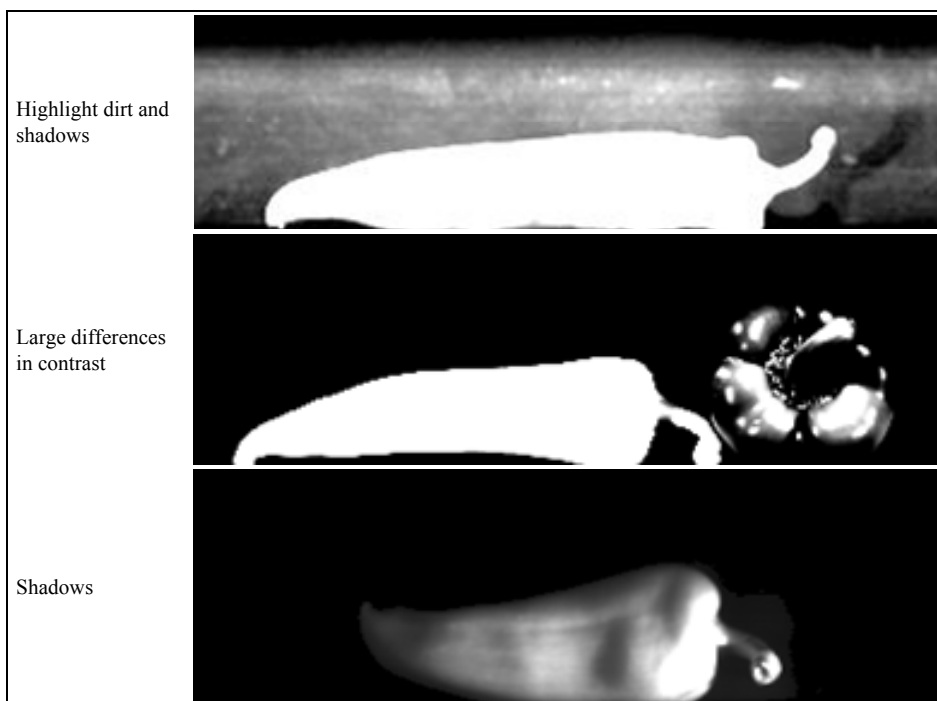
Under industrial conditions it is difficult to ensure that a good picture be created. There are many problems to be solved in the preparation and processing of

images. The biggest problem is a low contrast ratio. This problem caused by shadows and dust (Table 1). Both effects cause a significant reduction of the contrast. The standard, commonly used threshold algorithms have increased sensitivity of the shadows and dirt. This results in a significant reduction in accuracy. During this process it is very important to the strength and direction of illumination. In addition to these effects, the lighting inequalities need attention.

To resolve this problem, I created a self-developed algorithm for performing the analysis of images (Figure 5). This algorithm is based on the morphological analysis of image slices. Morphological analysis algorithm continuously analyzes the image slices from the cameras, and on the intensity function searches the key points. Faults can be due to the intensity difference can be eliminated completely (ideally). The figure shows that the morphological analysis algorithm finds very high accuracy to the actual edges. Test results of the composite image slices algorithm are shown in Figure 6.

Not only the pepper dimensions are relevant, very important to specify the degree of deformation as well. The working of the determining the malformation algorithm in a very simplified form is as follows: As it was mentioned above, only the contour of the pepper is recorded during the measurement. The elimination (image rejection) of the stalk is a serious problem; it is solved by differential map identification process (Figure 7).

Table 1. The main problems in the edge detection process



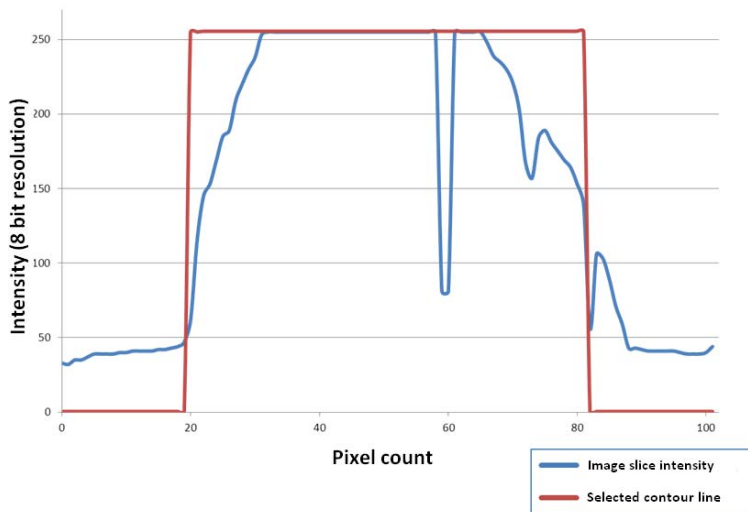


Figure 5. Results of self-developed morphological analysis of image slices

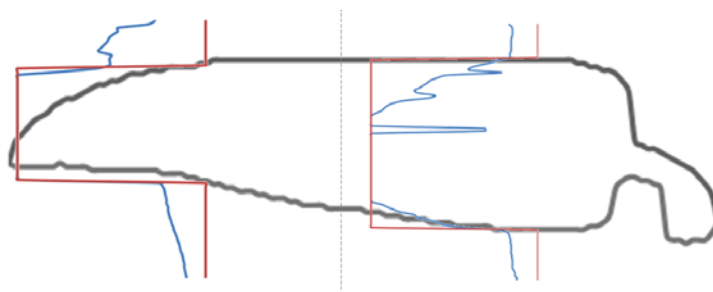


Figure 6. Result of the contour recording process

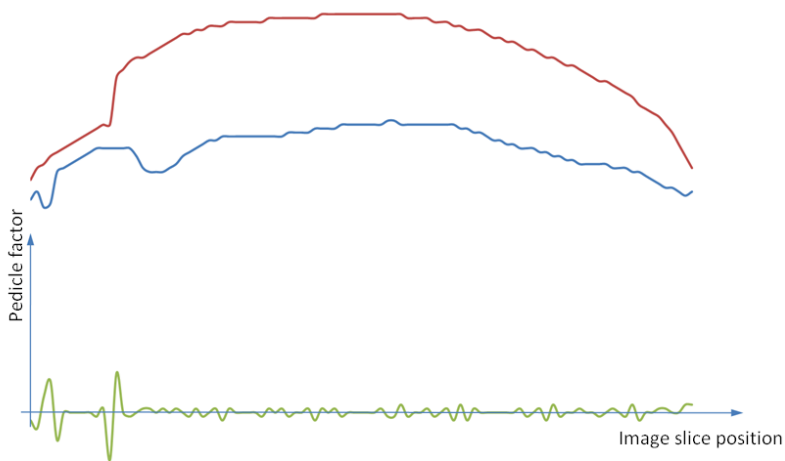


Figure 7. Pedicle elimination

The first step for determining the malformation: The centre-line (Figure 8, purple line) is constructed and its length is accurately computed with small triangles. The values gained in this way are compared to the length of the line drawn between the first and the last centre points of the paprika body (black line). The quotient of the two length values is the centre-line curvature degree. By this method, the curvature invisible in profile also can be filtered out.

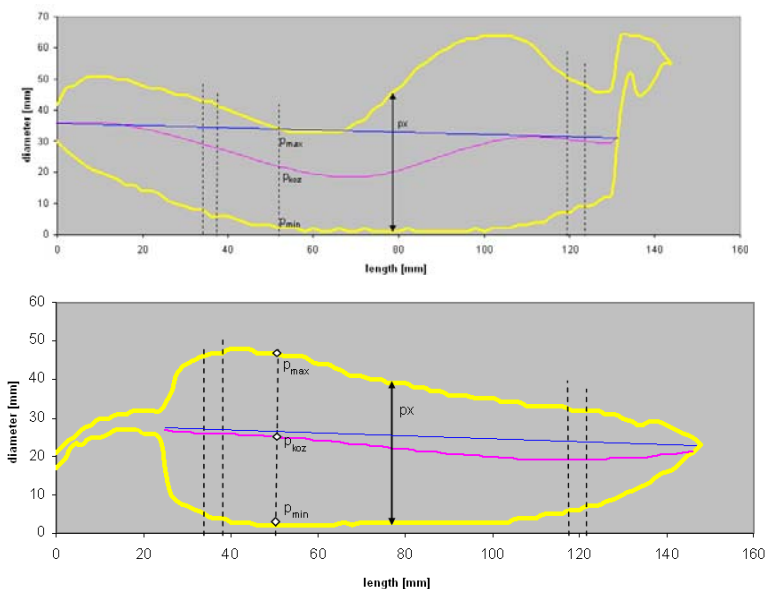


Figure 8. The contour recording process of a malformed and an un-deformed bell pepper

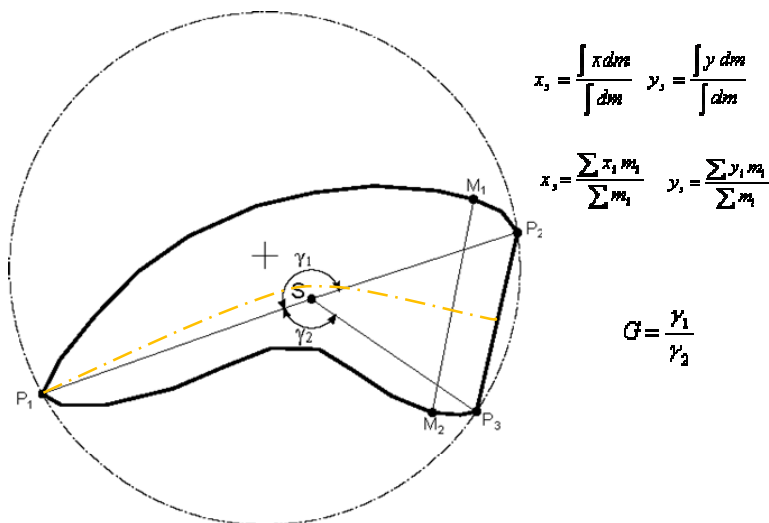


Figure 9. Determination of deformation

If that is done, there is second step for determining the deformation: Determination of malformation continued by calculating the centre of gravity of plane figure. After that will be assigned to P_1, P_2, P_3 points, are defined in the γ_1 and γ_2 angle (Figure 9). The ratio of the two angles determines the degree of deformity (G quotient), and direction. With this method, the small malformations are also determined (this is mainly important for long paprika, e.g. green hot peppers). For regular paprika (without malformation) the value of the coefficient is 1. Because the determination of the center line length and direction does not give a clear result for malformation, so comparing the two quotient of these two steps is essential. In this way, the deformation rate gives us very quickly identify and accurate results.

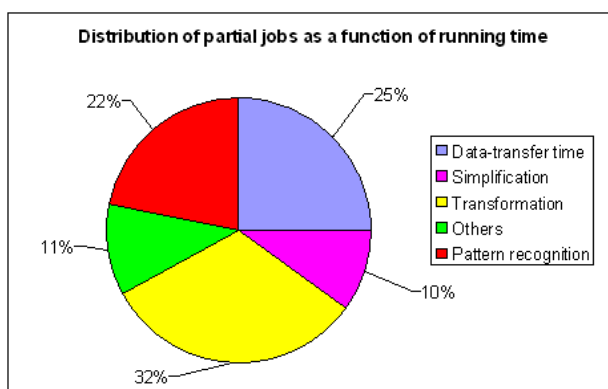


Figure 10. Distribution of the processes during the running time of an algorithm running by PC

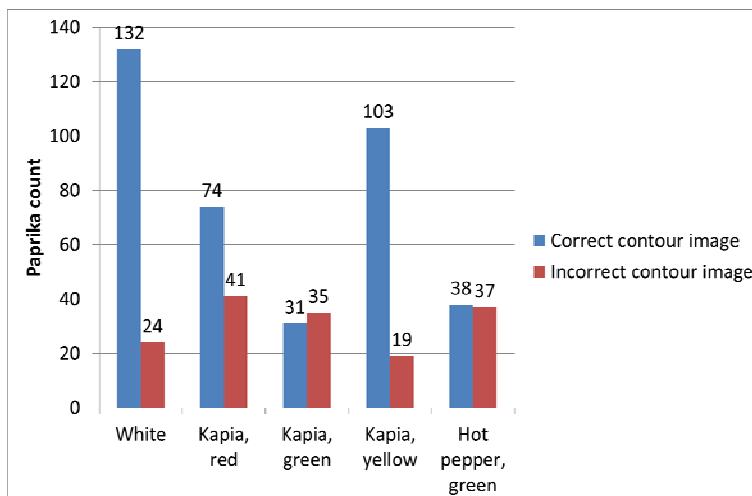


Figure 11. Results of standard, commonly used edge threshold-based detection algorithm

During the beginning phase of the research, many pattern-recognition algorithms had been tested but their running times were not acceptable. With the most algorithms, the re-simplification and the transformation of the pictures caused significant time losses. The time distribution of the processes in a general shape recognition algorithm running in the PC can be seen in *Figure 10*.

During the elaboration of the algorithm, particular attention was paid to the accuracy and the running rate suiting the requirements. In our self-developed system, the first processing of the data begins already in the camera during the reading-in accordingly the DSP receives the preliminary processed, suitably formatted and packed data flow. With this method, the amount of unnecessary transferred data could have been significantly decreased; accordingly, we managed to reduce the transfer time to its fraction, and minimize the time of transformation jobs as well.

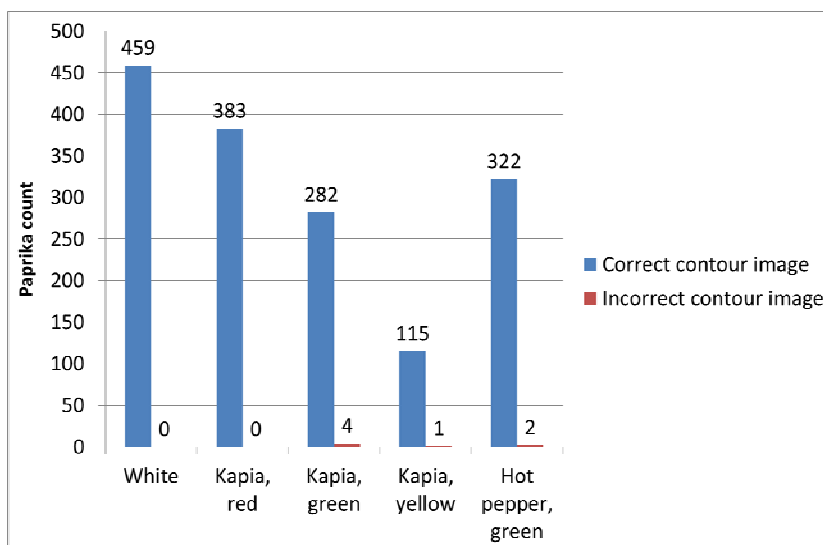


Figure 12. Results of self-developed morphological analysis

The paprika color can affect the accuracy of the algorithm, this appears most strongly in the case of green peppers. The conventional threshold-based algorithm works quite large, up to 50% error, if the pepper colour is green. Slightly better the error rate when testing with red pepper (but still high). In case of white pepper is a significant error rate, it is mainly due the low noise and error tolerance.

The test results are shown in Figure 11 and 12. The figures show that using morphological analysis greatly reduced the number of incorrect data. For white and red pepper the number of bad data is completely eliminated, for the green and yellow paprika, errors decreased significantly. Both results were significantly below the allowable 5% error margin.

Conclusions

When searching for the method of sorting, we have found that using the line CCD sensor is the most suitable process for recording contour.

The development of the measuring system was completed; the microcontroller- and morphologic algorithm based pattern recognition seems viable for the further applications as well. The correct determination of the parameters required by the standard is provided by the algorithm. Even in its present state, the algorithm is capable of recognizing easily the malformed peppers.

The designed measuring system and the algorithm very well performed its part during the long-term tests. The prototype system is working continuously at present as well; the evaluation of the data is also continuous.

Credits

We owe the ‘Furafol Hungary’ Ltd. thanks for their help and collaboration in our measurement and the required testing program.

Our paper is supported by the project TÁMOP-4.2.1.B-11/2/KMR-2011-0003.

References

- [1] Gergely, Z., Judák, E. (2008): „A microcontroller based algorithm for sorting white paprika”, Hungarian Agricultural Engineering, No. 2007-20. pp. 37-39. HU ISSN: 0864-7410
- [2] Gergely, Z. – Judák, E. (2008): „Automatizált paprikaválogatás beágyazott alakfelismerő rendszerrel” Mezőgazdasági technika, XLIX. évf. 2008/11. HU ISSN: 0026-1890
- [3] Gergely Z., Madár V., Judák E. (2007): Paprikaosztályozó rendszer kialakítása (Development of Paprika Classifying System) -MTA Agrárműszaki Bizottsága, Kutatási és Fejlesztési Tanácskozás XXXI. Gödöllő.
- [4] Gergely Z., Madár V., Judák E. (2006): Paprikaosztályozó berendezés a növényházi termesztésben - MTA Agrárműszaki Bizottsága, Kutatási és Fejlesztési Tanácskozás XXX. Gödöllő
- [5] Fűrész Gábor (2003): CCD alapismertetek. Budapest: MCSE egyesület.
- [6] Sing-Tze Bow (2002): Pattern Recognition and Image Preprocessing. Marcel Dekker Inc, New York.

The situation of application of wind power plant in the world and in Hungary

L. TÓTH, N. SCHREMPF, J. BEKE

Department of Energetics, Institute for Process Engineering
Faculty of Mechanical Engineering, Szent István University

Abstract

The worldwide wind capacity reached 282'275 Megawatt, out of which 44'609 Megawatt were added in 2012, more than ever before.

In Hungary the current wind energy capacity is 330MW, built of modern units, which are designed for the Hungarian wind circumstances. Because of this energy production is very good (740 GWh/year) and the capacity factor (24.1%) is good as well (the 4th best in Europe in 2012). With this we save approx. 220 million m³ /year natural gas whilst we avoid ~400 000 tons of CO₂ emission.

It is a fact that wind power plants (after the return of investment -9-10 years-) produce cheap energy. From financial side wind power plant utilization is one of the most perspective investments. Our analysis points out that the ambitious plan of Hungary for 2020 (the increasing of renewable energy utilization) is unlikely to be met without wind energy utilization.

This article was written with the help of a TÁMOP 4.2.1.B-11/2/KMR-2011-0003 „INCREASING THE QUALITY OF LEARNING AND RESEARCH” program

Keywords

Wind Power Plant, Wind Energy Capacity in Hungary, Cost of Wind Energy

1. Introduction

Overview of Hungarian development on the fields of wind energy

In the period of 1980-90 energetic wind measurements proved (made on measurement towers) that at bigger heights (100-120 m) at certain areas of Hungary there are right circumstances for wind energy utilization. The first wind measurement made for energetic purposes (1998-'99) was done by the experts of Szent István University at area of Kisalföld. The installation of the first wind power plant was in 2002 at Kulcs, in Middle Hungary, the wind power plant is an Enercon plant with kW performance. The height of the tower is 65 m. The location of it was chosen according of the measures of Szent István University (or as short SZIE). According to the wind measurement results it can be stated that Hungary is a proper place for wind energy utilization.

In 2005 the new law on electricity stated the government subsidies in the frames of the KÁT subsidy. This subsidy helped the investments to return in 9-11 years. After this a ‘so called’ wind tender was announced for Hungarian companies. Approx. 330 MW was installed in Hungary.

2. Features of Technological Development and Capacity Growth

In Hungary the big energy content winds are on 80-200 m, so the tower height is very important.

Capacity depends on rotor diameter as well, nowadays $D > 100\text{m}$ is typical. Expected biggest capacity (can be W_p as well):

$$P_{\max} = \frac{16}{27} \cdot \frac{1}{2} \cdot \rho \cdot A \cdot v_{\infty}^3 \quad (\text{kW}) \quad (1)$$

where:

ρ - air density [kg/m^3],

A -examined surface ($D^2\pi/4$) [m^2],

v_{∞} - wind speed until control [m/s].

Wind speed is important, see v^3 . Before wind power plant installation is made these parameters must be defined. (Fig.1) The change of v can be seen on Fig. 2.

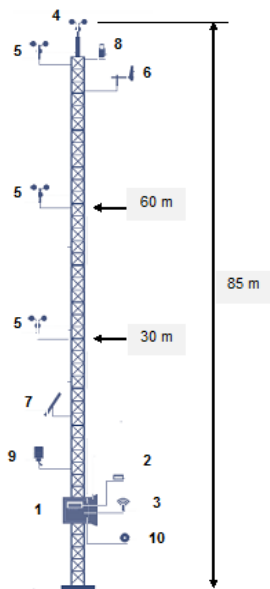


Figure 1. Hungarian development, 85 m tower height 1- gauge box, 2- data logger, 3- data transmitter, 4- anemometer (control), 5- anemometer at 30, 60 and 80 m height, 6- wind vane, 7 – energy source (solar cell, PV), 8- light signal, 9- moisture measurement gauge, 10- air pressure measuring gauge

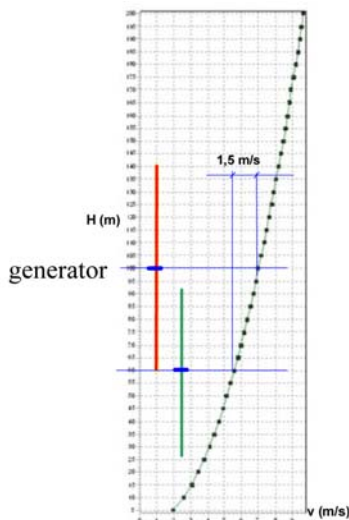


Figure 2. Data from the measurement system on Fig.1.
(wind speed difference 1,5 m/s, 60 and 100 m tower height)

Capacity of given wind power plants (P_x):

$$P_x = c_{px} \cdot \frac{1}{2} \cdot \rho \cdot A \cdot v_x^3 \quad (\text{kW}) \quad (2)$$

c_{px} is the capacity factor of given areas, defined with v_{nx} (mean wind speed) values. (c_{px} can be defined with experiments. Wind power plant producers give the P-v, c_p -v diagrams.)

On the c_p -v diagram at the biggest c_p value the P_n = nominal performance can be found. On the basis of the measured yearly energy production (kWh/year) and nominal performance the utilization number can be calculated (K_F):

$$K_F = \frac{E}{8760 \cdot P_n} \quad (3)$$

A $K_F \cdot 8760$ (hours in a year) gives the nominal utilization hours, which is h_n /year (pl. $8760 \times 0,23 = 201.8$ h/year on P_n performance). According to Hungarian calculations the operation of a wind power plant is economically efficient on 2000 h_n /year nominal performance (P_n), the investment returns in 9-10 years with KÁT subsidy.

Wind power plants utilizations in the world

Wind power plant production is the most dynamically developing branch of industry. Yearly installed capacity can be seen on Fig.3 with the focus on the biggest investors. Until 2007 Europe was the first, in 2008 the USA and in 2009

China. Now China installs the capacity of Europe and Europe altogether. The estimation of WWEA shows that in the year 2020 the built capacity will be as much as in the past 10 years. This is an investment of 240 million dollars/year. Until the end of 2020 100-1200 billion dollars are needed for this investment. This requires huge producer and developer basis. Hungary can only be a leader in wind energy industry if we use our corporate advantage.

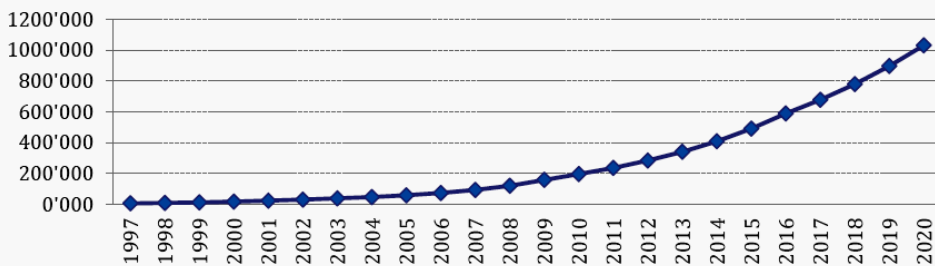


Figure 3. Total Installed Capacity 1997-2020 [MW] Development and Prognosis (Source: WWEA-2012.)

In the world approximately 700.000 small capacity household wind turbines were in operation in 2012 (Fig.4). Their capacity is in average 0.2-0.6kW. The 50 % of these devices is in China, and the 25% in the US. In Hungary currently 150-200 units are in operation, they solve local energy problems.

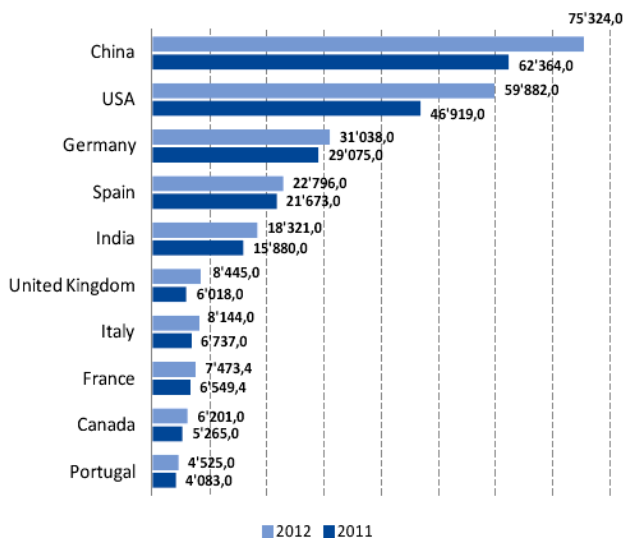


Figure 4. Top 10 Countries by Total Capacity [MW] (Source: WWEA 2012.)

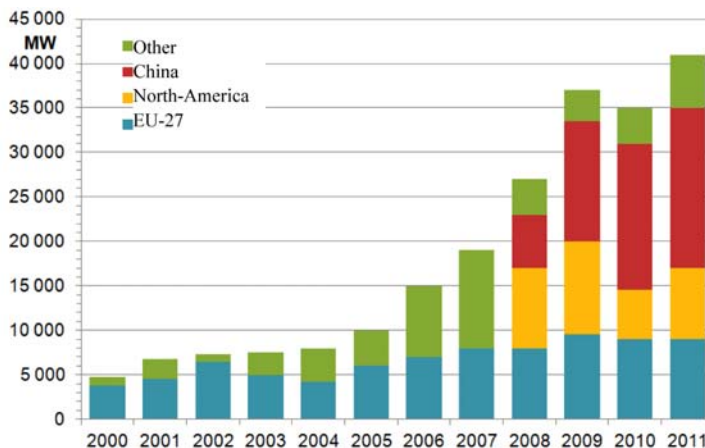


Figure 5. Development of the world's wind energy capacity
 Source: Mind Power Barometer – EUROBSERV'ER – February, 2013.
 *green: other, red: China, yellow: North America, blue:EU-27

In the last years China made the biggest development (Fig.5). Until 2006 Europe had the leading role in Europe. In 2008 the USA, and in 2009 China took over Europe. In 2011 China invested more in development than Europe and the US altogether.

The plan of Europe 27 countries is to triple the capacity until 2020. The trend shows that the plan can work. (Fig.6)

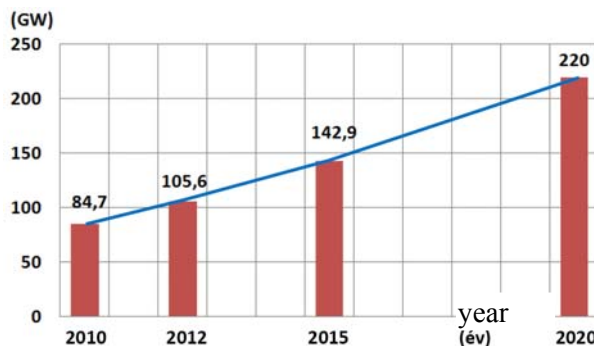


Figure 6. The plan of the Europe 27 countries Source: Wind Power Barometer – EUROBSERV'ER – February, 2013.

3. Costs

The utilization of the wind power plants

The production costs of the wind power plants have to be given with their utilization level since 2000. The Hungarian wind power plants are modern and

they are chosen for the wind conditions of Hungary. Unfortunately we are not in leading position in wind energy; we are at the 24th place (produced energy per capita).

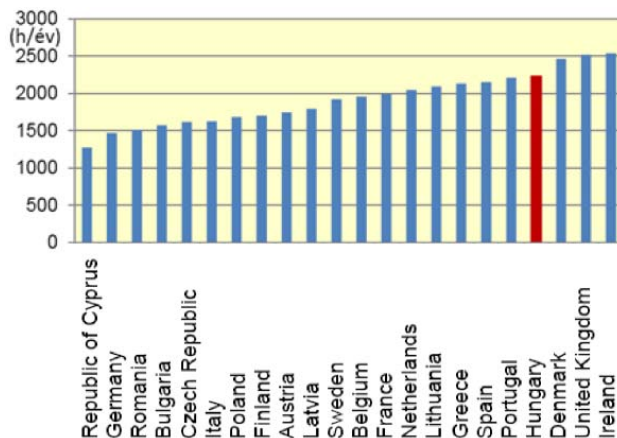


Figure 7. Utilization wind power plants (h_n/year) in EU 27 countries
Source: Wind Power Barometer – EUROBSERV’ER – February, 2013.

Energy production costs and costs of investments

On Fig.8 the curve represents the production cost per utilization level. The upper curve shows the data of maritime plants, and the lower the terrestrial plants. The maritime and the terrestrial plants differ in their material and in their construction. The terrestrial types have higher towers and big diameter rotors, but the blade angle change (pitch control) is happening faster.

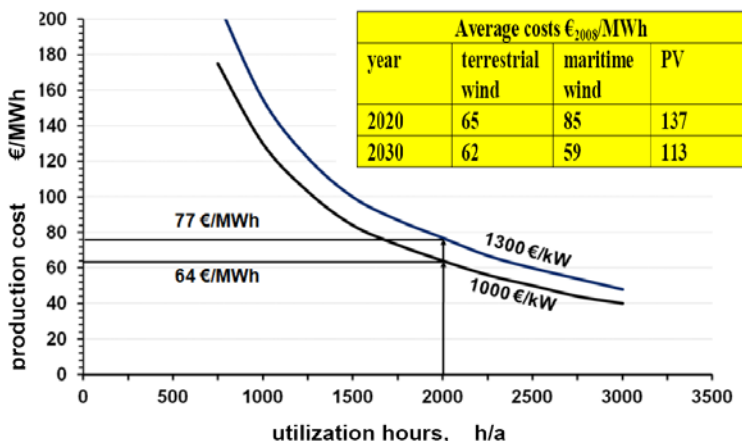


Figure 8. Energy production costs and the utilization time (hour)
source: Wind Power Barometer – EUROBSERV’ER – February, 2013.

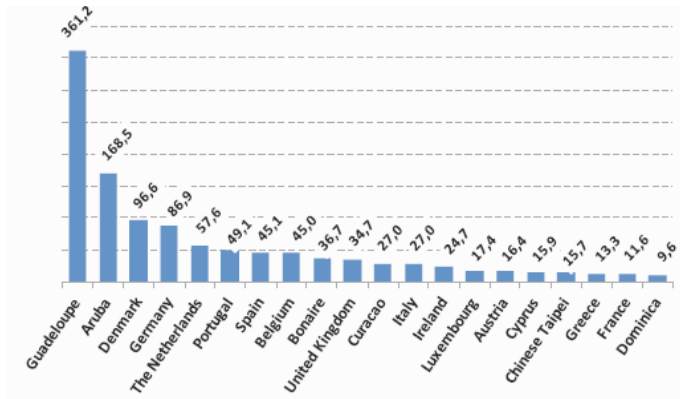


Figure 9. Installed Capacity per Land Area [kW/sqkm]

The maritime wind energy is more expensive. But the development of them is ongoing and because of this their costs will decrease. At maritime wind power plants a huge decrease of costs is estimated until 2020. The price of electricity is changing because of cheap surplus energy, and this may cause differences in stock prices. At those power plants where the investments returned there are only low external costs.

Costs

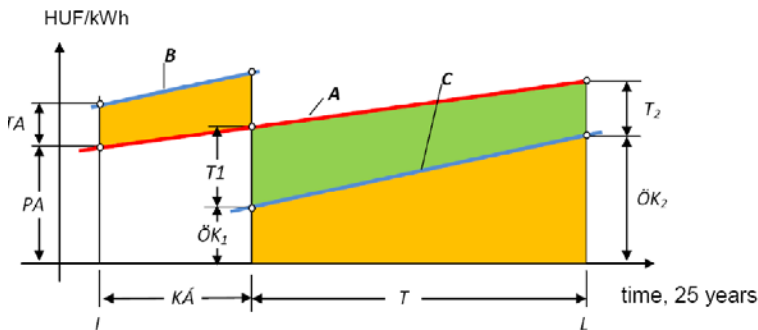


Figure 10. Costs of electricity during wind power plant lifetime

Abbreviations:

PA = market price of electricity
 TA = governmental subsidy (KÁT, or METÁR)
 A = trend of electricity price
 B = trend of subsidies
 I-L = lifetime of equipments = KÁ + T
 KÁ = subsidized interval
 T = interval after the payback of loan and subsidy
 ÖK1 = costs of wind energy production (utilization, repair, control costs) after KÁT

T₁ = the difference of electricity price and wind energy production costs after KÁT
 C = trend of electricity production (increasing utilization, repair and maintenance cost)
 ÖK₂ = costs of wind energy production (at de-installation of the plant).
 T₂ = costs of wind energy production (utilization, repair, control costs) a at de-installation of the plant
 T₁, T₂, A and C area = gaining of the society (min.3-4KÁT investment)

By land area, two small countries, Guadeloupe and Aruba, have the top position, again followed by Denmark and Germany. Also the Netherlands, Portugal, Spain, Belgium and the United Kingdom are amongst the top ten (Fig. 9). However, neither China, USA nor India are amongst the top 20: China holds position 27 (7'800 Watt per square kilometre), India ranks 32th (5'600 Watt/sqkm), and the USA are number 30 (6'100 Watt/sqkm).

This geographical distribution reveals that especially the countries with large land mass have still a huge potential which they could use to harvest wind power. The global average is currently 1,9 kW/sqkm.

If all countries had the same density like today Germany or Denmark, the world would see a total installed capacity of 12'000'000 MW, more than enough to cover the world's complete electricity demand.

For an example let's check the costs in long-term. Such example can be seen on Fig 10. After installation of the plant the costs are typical (KÁT interval). The maintenance, repair another costs does not reach the 25-30 % of overall costs, but they are 15-20% bigger the market price of electricity (PA). At the interval of return the wind power plan gains subsidy (min. 8-10 years). The energy production costs are 25-30% smaller at ÖK1 and at ÖK2. (It rises because of higher maintenance costs, etc.) At T the difference between average wind energy price and costs is bigger than the subsidies. *At governmental investments the profit is as well governmental.* In Germany the price of wind energy will be lower than market electricity price in 2015-2016. The power plants which were built before 2006 returned.

4. Current Hungarian Situation

Capacity

At 90 % of the Hungarian wind power plants the tower height is 90-120 m and the performance is 2 MW. The installation trend is shown on Fig.11. The energy production is 610-700 GWh/year. The utilization factor is ~21-24 %. At some parks 23-25 % value can be measured. With these data it can be proved the estimations were correct.

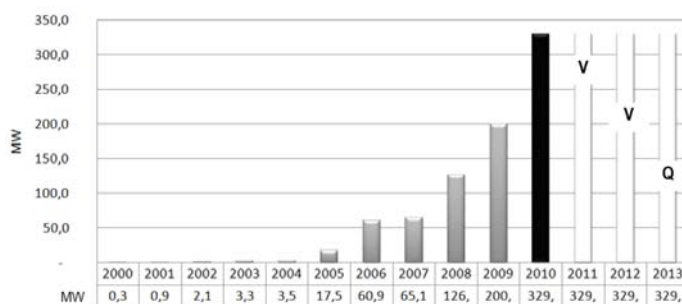


Figure 11. Trend of Hungarian wind energy capacity
(V = remains the same, Q = new installation is not likely)

The current wind energy capacity is equal to the energy of ~ 200 million m^3 natural gas, whilst $\sim 400\,000$ tons of CO_2 emission can be avoided.

Base numbers of Nemzeti Cselekvési Terv (national Energy Efficiency Plan)

According to NCST until 2020 750 MW wind energy capacity should be reached. This means that additional 410 MW must be built. (See Fig.1)

In 2009 a tender was announced, and companies competed for 1100 MW. The tender was not announced properly so the quotas were not distributed. New capacities can be built earliest in 2015. To reach the 750 MW can only succeed if new plants are built in an increasing tendency.

The wind power investments did not get subsidies. The mood for investment is good; three years ago 1000-1200 MW additional capacity could have been built. If we would like to reach the capacity defined in the NCST, than we need to build additional 900-1000 MW. With this at the end of 2020 1300 MW would operate. Of course, the investors the only invest if they see their investment to return.

In Hungary the government does not invest direct stock in the wind energy installation only KÁT subsidy. The KÁT subsidy returns in short term. With the usage of wind energy the fossil fuel addiction of the country is decreasing and income rises from selling CO_2 .

The lifetime of the modern wind power plants is 20 years, but with care it can be 25 years. In the future the energy produced by wind power plants will be cheaper than the energy produced by carbon plants or gas plants.

The technological increase and the increasing value of fuel prices cannot be neglected.

To be concrete if the investment returns then (approx. 10 years with subsidies) the price of electricity decreases to 8-10 HUF/kWh. There is no cheaper energy source, and the plants produce it for additional 10 years (it can be 20 years as well).

Wind energy as other alternative energy sources need network equalization.

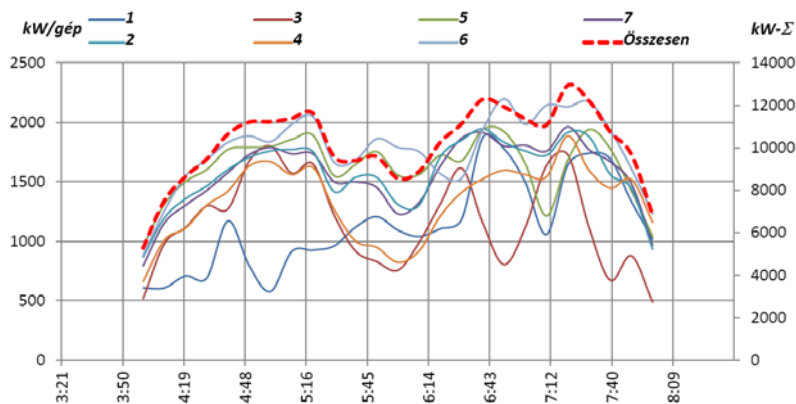


Figure 12. Wind power plant capacity (7 plants, 2 MW)

On Fig. 12 it can be seen that there can be 300-400 % differences in a 5h interval, and the total outcome changed 30-35%.

The wind parks have big network equalization effect. In Hungary the control price in 2011-2012 was 0.8-1.5 HUF/kWh. These costs do not influence the production costs.

It is important to state that the control of the electricity network can be done with bigger capacities as the current as well. The utilization level of the plant in Gönyű was only once 60 % since it is in operation. The plant capacity of Hungary is approx. 9000 MW, the max. consumption is approx. 6000-6500 MW. Yearly we use 1000-1500 MW import energy. It is not true that the existing 330 MW wind energy capacity or 3-4 times bigger would cause unsolvable problems in control.

References

- [1] Tóth, G. – Schrempf, N. – Tóth, L. (2005): A szélenergia prognosztizálása, üzemi tapasztalatok, MTA AMB, K + F Tanácskozása Nr. 29 Gödöllő, (in Hungarian)
- [2] Tóth, L. – Schrempf, N.: (2012) Szélenergia helye, várható szerepe Magyarország Megújuló Energia Hasznosítási Cselekvési Tervében (MCST) ENERGIAGAZDÁLKODÁS 53. évf. 5. szám, (in Hungarian)
- [3] Tóth, L. – Horváth, G. (2003): Alternatív energia, Szélmotorok, szélgenerátorok, Szaktudás Kiadó Ház, Budapest, 93-124. p., 281-321. pp. (in Hungarian)
- [4] Wilkes, J. – Moccia, J. – Dragan, M.: (2012) Wind in power, European statistics (EWEA) http://www.ewea.org/fileadmin/ewea_documents/documents/publications/statistics/Stats_2011.pdf
- [5] Stróbl, A.: (2012) Tájékoztató adatok a magyarországi villamosenergia-rendszerről, A piacnyitás (2003) óta eltelt időszak fontosabb adataiból, MAVIR, 2012. április 15. kézirat, ábragyűjtemény, (in Hungarian)
- [6] Stróbl, A.: (2013) Energetikai tájékoztatások szakirodalomból (ábragyűjtemény)
- [7] www.eurobserv-er.org. Wind Power Barometer – EUROBSERV’ER – 2013. febr.
- [8] Tóth, G. – Tóth, L. – Horváth, G. - Berencsi B. (2007): A hazai energia célú széltérkép elkészítésének feltételei. = MTA AMB Kutatási és Fejlesztési Tanácskozás. Gödöllő, Gödöllői Agrártudományi Egyetem – FVM Műszaki Intézet, 2. kötet 148-153. p. (in Hungarian)
- [9] Small Wind World Report 2012 Summary, BONN, 3 – 5 JULY 2012 Germany

Modeling conflicting interests in a water distribution problem with game theory

F. SZIDAROVSKY¹, S. MOLNÁR²,
M. MOLNÁR³, Cs. FOGARASSY⁴

¹Department of Systems and Industrial Engineering, University of Arizona, USA

²Institute of Mathematics and Informatics, Szent István University

³Institute of Economics, Szent István University

⁴Institute of Regional Economics and Rural Development, Szent István University

Abstract

The water distribution problem of the Mexican Valley is modeled first as a three-person noncooperative game. Each player has a five-dimensional strategy vector, the strategy sets are defined by 15 linear constraints, and the three payoff functions are also linear. A nonlinear optimization problem is first formulated to obtain the Nash equilibrium based on the Kuhn-Tucker conditions. The problem can also be considered as a conflict between the three players. The non-symmetric Nash bargaining solution is suggested to find the solution. Multiobjective programming is an alternative solution concept, when the water supply of the three players are the objectives, and the water authority is considered to be the decision maker. The water distribution strategies are determined by using these solution concepts and methods.

Keywords

Nonlinear game theory, water management, conflict resolution

1. Introduction

Game theory is the most commonly applied methodology in decision making problems, when the decision makers have conflicting interests. The solution of a noncooperative game is a decision vector such that no decision maker can unilaterally change the decision and receive higher benefit. This solution concept is known as the Nash equilibrium (Forgo et al., 1999).

The limited amount of natural resources creates a conflict between the users, since it is impossible to satisfy the demands of all users, so any user can receive more resources only in the expense of the others. It is well known that water shortage is one of the most worrying problems of the new millennium due to the increase of population, better living standards and the inefficiency of the way we use water (Brown, 2005). This problem already became serious in the neighborhood of large cities with very large population. Mexico City with its 19 million inhabitants is considered the most populated city in the world. It is

located in the Mexican valley where the very limited water resources are distributed between three users: Agriculture, industry and households. Therefore there is a conflict between them, and this conflict can be modeled by a three-person game, which will be the case study reported in this paper. There is a large variety of computer methods to find Nash equilibrium in non-cooperative games. A comprehensive summary is given for example, in Forgo et al. (1999) where a combination of the Kuhn-Tucker conditions and nonlinear optimization is discussed in detail. We will apply this method in our case study, when an alternative algorithm is also developed based on duality theory.

This problem can also be considered as a conflict between the users, so conflict resolution methodology is a reasonable alternative approach. In our case study the non-symmetric Nash bargaining solution is selected to find the solution. (Harsanyi and Selten, 1972). A summary of the most commonly used conflict resolution methods is given for example in Roth (1979).

In many countries, like in Mexico, the water supply is provided to the users by a governmental organization. Therefore we might also consider this problem as a single-decision maker's problem with three objective functions, where the water amounts supplied to the three users are the objective functions. A comprehensive summary of the most popular methods for solving multiobjective programming problems can be found for example, in Szidarovszky et al. (1986). The application of game theory, conflict resolution and multi-objective programming in natural resources management has a long history. The survey papers of Hipel (1992), Bogardi and Nachtnebel (1994) give excellent overview of earlier works. More recently Donevska et al. (2003) examined a similar problem to ours with water demands to agricultural and non-agricultural users in the Republic of Macedonia. Jensen et al. (1998) investigated multiple usage of irrigation water. A multi-objective design of water distribution systems under uncertainty was developed by Kapelan et al. (2005), and Bekele and Nicklow (2005) combined multi-objective optimization with evolutionary algorithms. Lizhong et al. (2008) used game theory for a water distribution problem for the South Saskatchewan Basin in southern Alberta, Canada.

In our case study the non-cooperative Nash equilibrium of the three player game of the water users in the Mexican Valley will be first determined. All payoff functions and constraints will be linear, so taking advantage of the special structure of the model, the general solution algorithm based on the Kuhn-Tucker conditions can be significantly simplified and by using duality theorem an alternative method can be developed. The non-symmetric Nash bargaining solution of the problem will be next determined, which requires the solution of a nonlinear optimization problem with linear constraints and quasiconcave objective function. In finding solutions based on the concepts of multiobjective optimization we will use the weighting method (Szidarovszky et al, 1986). This paper develops as follows. Section 2 will introduce the mathematical methodology. Section 3 will contain the model of the case study. Numerical results will be presented and the solutions obtained by the different solution

concepts and methods will be compared in Section 4. The last section will conclude the paper.

2. The Mathematical Methodology

We will first present a nonlinear optimization problem to find the Nash equilibria in a general class of n-person games, which will be later applied in the case study.

Consider an n-person noncooperative game, and assume that the strategy set of player $k(1 \leq k \leq n)$ is $X_k = \{\mathbf{x} \mid \mathbf{g}_k(\mathbf{x}) \geq \mathbf{0}\}$ where \mathbf{g}_k is a continuously differentiable vector variable, vector valued function, and the payoff of player k is $\phi_k(\mathbf{x}_1, \dots, \mathbf{x}_n)$, where ϕ_k is also continuously differentiable. Then $(\mathbf{x}_1^*, \dots, \mathbf{x}_n^*)$ is a Nash equilibrium, if for all k, \mathbf{x}_k^* maximizes the payoff of player k, $\phi_k(\mathbf{x}_1^*, \dots, \mathbf{x}_{k-1}^*, \mathbf{x}_k, \mathbf{x}_{k+1}^*, \dots, \mathbf{x}_n^*)$ subject to the feasibility constraint $\mathbf{g}_k \mathbf{x}_k \geq \mathbf{0}$. Assume that the Kuhn-Tucker regularity condition holds, then the Kuhn-Tucker necessary conditions imply the existence of a vector \mathbf{u}_k such that

$$\begin{aligned} \mathbf{u}_k &\geq \mathbf{0} \\ \mathbf{g}_k(\mathbf{x}_k) &\geq \mathbf{0} \\ \mathbf{u}_k^T \mathbf{g}_k(\mathbf{x}_k) &= 0 \\ \nabla_k \phi_k(\mathbf{x}_1, \dots, \mathbf{x}_n) + \mathbf{u}_k^T \nabla_k \mathbf{g}_k(\mathbf{x}_k) &= \mathbf{0}^T, \end{aligned} \quad (1)$$

where $\nabla_k \phi_k$ is the gradient vector (as row vector) of ϕ_k with respect to \mathbf{x}_k and $\nabla_k \mathbf{g}_k$ is the Jacobian matrix of \mathbf{g}_k . Consider next the optimization problem

Minimize $\sum_{k=1}^n \mathbf{u}_k^T \mathbf{g}_k(\mathbf{x})$ subject to

$$\begin{aligned} \mathbf{u}_k &\geq \mathbf{0}, \\ \mathbf{g}_k(\mathbf{x}_k) &\geq \mathbf{0}, \\ \nabla \phi_k(\mathbf{x}_1, \dots, \mathbf{x}_n) + \mathbf{u}_k^T \nabla_k \mathbf{g}_k(\mathbf{x}_k) &= \mathbf{0}^T, \quad k = 1, 2, \dots, n. \end{aligned} \quad (2)$$

Since $\mathbf{u}_k \geq \mathbf{0}$ and $\mathbf{g}_k(\mathbf{x}_k) \leq \mathbf{0}$, the objective function is zero if and only if the Kuhn-Tucker conditions are satisfied. Therefore every equilibrium of the n -person game is an optimal solution of. Hence the equilibrium of the game can be obtained by solving problem. The sufficiency of the Kuhn-Tucker conditions for

concave problems implies that if all components of \mathbf{g}_k and ϕ_k are concave in \mathbf{x}_k , then all optimal solutions of (2) with zero objective function value are equilibria.

Consider next the linear case, when $\phi_k(\mathbf{x}_1, \dots, \mathbf{x}_n) = \sum_k \mathbf{c}_k^T \mathbf{x}_k + \gamma_k$, and the strategy sets are defined by the linear constraints

$$\mathbf{A}_k \mathbf{x}_k \leq \mathbf{b}_k \quad (\text{Individual constraints}) \quad (3)$$

$$\sum_k \mathbf{B}_k \mathbf{x}_k \leq \mathbf{c} \quad (\text{Joint constraint}). \quad (4)$$

Using the previous notation,

$$\mathbf{g}_k(\mathbf{x}_k) = \begin{pmatrix} \mathbf{b}_k - \mathbf{A}_k \mathbf{x}_k \\ \mathbf{c} - \sum_{l \neq k} \mathbf{B}_l \mathbf{x}_l - \mathbf{B}_k \mathbf{x}_k \end{pmatrix}. \quad (5)$$

So conditions (1) become

$$\begin{aligned} \mathbf{v}_k, \mathbf{w}_k &\geq \mathbf{0} \\ \mathbf{b}_k - \mathbf{A}_k \mathbf{x}_k &\geq \mathbf{0} \\ \mathbf{c} - \sum_{l \neq k} \mathbf{B}_l \mathbf{x}_l - \mathbf{B}_k \mathbf{x}_k &\geq \mathbf{0} \\ \mathbf{v}_k^T (\mathbf{b}_k - \mathbf{A}_k \mathbf{x}_k) + \mathbf{w}_k^T (\mathbf{c} - \sum_{l \neq k} \mathbf{B}_l \mathbf{x}_l - \mathbf{B}_k \mathbf{x}_k) &= 0 \\ \mathbf{c}_k^T - \mathbf{v}_k^T \mathbf{A}_k - \mathbf{w}_k^T \mathbf{B}_k &= \mathbf{0}^T, \end{aligned} \quad (6)$$

where vector \mathbf{u}_k is broken up to two parts. So problem (2) can be rewritten in the form

$$\begin{aligned} \text{Minimize} \quad & \sum_{k=1}^n \left\{ \mathbf{v}_k^T (\mathbf{b}_k - \mathbf{A}_k \mathbf{x}_k) + \mathbf{w}_k^T (\mathbf{c} - \sum_{l=1}^n \mathbf{B}_l \mathbf{x}_l) \right\} \quad \text{subject to} \\ & \left. \begin{aligned} \mathbf{v}_k, \mathbf{w}_k &\geq \mathbf{0} \\ \mathbf{A}_k \mathbf{x}_k &\leq \mathbf{b}_k \\ \mathbf{c}_k^T - \mathbf{v}_k^T \mathbf{A}_k - \mathbf{w}_k^T \mathbf{B}_k &= \mathbf{0}^T \end{aligned} \right\} k = 1, 2, \dots, n \quad (7) \\ & \sum_l \mathbf{B}_l \mathbf{x}_l \leq \mathbf{c}. \end{aligned}$$

All constraints are linear, and the objective function is quadratic.

In computing the non-symmetric Nash bargaining solution assume that $\alpha_1, \dots, \alpha_n$ are the relative importance factors of the players. In addition, let ϕ_k denote the minimal value of the payoff of player k, which can be obtained by solving the single-objective optimization problem

Minimize $\mathbf{c}_k^T \mathbf{x}_k$ subject to

$$\begin{aligned} \mathbf{A}_l \mathbf{x}_l &\leq \mathbf{b}_l, \quad l = 1, 2, \dots, n \\ \sum_l^n \mathbf{B}_l \mathbf{x}_l &\leq \mathbf{c}. \end{aligned} \quad (8)$$

Then the non-symmetric Nash bargaining solution can be obtained by solving the following problem:

Maximize $\prod_{k=1}^n (\mathbf{c}_k^T \mathbf{x}_k - \phi_{k*})^{\alpha_k}$ subject to

$$\begin{aligned} \mathbf{A}_l \mathbf{x}_l &\leq \mathbf{b}_l, \quad l = 1, 2, \dots, n \\ \sum_l^n \mathbf{B}_l \mathbf{x}_l &\leq \mathbf{c}. \end{aligned} \quad (9)$$

Notice that (8) is a linear programming problem, and in the nonlinear model (9) only the objective function is nonlinear, all constraints are linear.

The application of the weighting method requires the solution of the following linear programming problem:

Maximize $\sum_{k=1}^n \alpha_k \mathbf{c}_k^T \mathbf{x}_k$ subject to

$$\begin{aligned} \mathbf{A}_k \mathbf{x}_k &\leq \mathbf{b}_k, \quad k = 1, 2, \dots, n \\ \sum_{k=1}^n \mathbf{B}_k \mathbf{x}_k &\leq \mathbf{c}, \end{aligned} \quad (10)$$

where α_k is the relative importance factor of player k as before.

It is usually assumed that $\alpha_k \geq 0$ for all k, and $\sum_{k=1}^n \alpha_k = 1$. If for some k, $\alpha_k = 1$ then in the objective functions of both problems (9) and (10) only the payoff of player k is optimized, the payoffs of the other players are completely ignored. Tradeoffs between the players are obtained if $\alpha_k > 0$ for all k.

3. The case study

The three players are: Agriculture, Industry and households. They can receive surface water, ground water and treated water. Surface and ground water supply

can be obtained from local sources and also can be imported from other neighboring watersheds. Let $k = 1, 2, 3$ denote the three users, so the decision variables of each of them are as follows:

s_k = surface water usage from local source

g_k = groundwater usage from local source

t_k = treated water usage

s_k^* = imported surface water usage

g_k^* = imported ground water usage.

So the strategy of each player is the five-element vector

$$\mathbf{x}_k = (s_k, g_k, t_k, s_k^*, g_k^*).$$

The payoff function of each player is the total amount of water received:

$$\phi_k = s_k + g_k + t_k + s_k^* + g_k^*. \quad (11)$$

The players have two common constraints. The supplied water amount cannot be smaller than a minimal necessary amount D_k^{\min} and cannot be larger than the demand, D_k , in order to avoid wasting water:

$$s_k + g_k + t_k + s_k^* + g_k^* \geq D_k^{\min} \quad (12)$$

$$s_k + g_k + t_k + s_k^* + g_k^* \leq D_k \quad (13)$$

In addition, each player has its own individual constraints.

The agricultural users ($k = 1$) have two major conditions. Introduce the following variables:

G = set of crops which can use only ground water

a_i = ratio of crop i in agriculture area

w_i = water need of crop i per ha

T = set of crops which can use treated water

$W = \sum_i a_i w_i$ = total water need of all crops per ha.

Ground water has the best irrigation quality and treated water has the worst. Therefore water quality sensitive crops can use only ground water, and only the least sensitive crops are able to be irrigated by treated water. The ratio of available groundwater cannot be smaller than the water need of crops that can use only ground water:

$$\frac{g_1 + g_1^*}{s_1 + g_1 + t_1 + s_1^* + g_1^*} \geq \frac{\sum_{i \in G} a_i w_i}{W},$$

which can be rewritten into a linear form

$$a_1 s_1 + (\alpha_1 - 1)g_1 + a_1 t_1 + \alpha_1 s_1^* + (\alpha_1 - 1)g_1^* \leq 0 \quad (14)$$

with $\alpha_1 = \frac{\sum_{i \in G} a_i w_i}{W}$. Similarly, the ratio of treated water availability cannot be larger than the ratio of water need of the crops which can use treated water:

$$\frac{t_1}{s_1 + g_1 + t_1 + s_1^* + g_1^*} \leq \frac{\sum_{i \in T} a_i w_i}{W},$$

which also can be rewritten into a linear form:

$$-\beta_1 s_1 - \beta_1 g_1 + (1 - \beta_1)t_1 - \beta_1 s_1^* - \beta_1 g_1^* \leq 0 \quad (15)$$

with $\beta_1 = \frac{\sum_{i \in T} a_i w_i}{W}$.

The industrial users ($k = 2$) also have their own constraints. Introduce the following variables:

B_g = minimum proportion of ground water that industry has to receive

B_t = maximum proportion of treated water that industry can use.

In order to keep a sufficient average quality of the water used by the industry, a minimum proportion of ground water is specified, since ground water has the best quality. The worst quality of treated water requires the industry to use only a limited proportion of treated water in its water usage:

$$\frac{g_2 + g_2^*}{s_2 + g_2 + t_2 + s_2^* + g_2^*} \geq B_g,$$

$$\frac{t_2}{s_2 + g_2 + t_2 + s_2^* + g_2^*} \leq B_t.$$

Both conditions can be rewritten into linear forms:

$$-\beta_g s_2 - (\beta_g - 1)g_2 + \beta_g t_2 - \beta_g s_2^* + (\beta_g - 1)g_2^* \leq 0 \quad (16)$$

and

$$-\beta_t s_2 - \beta_t g_2 + (1 - \beta_t)t_2 - \beta_t s_2^* - \beta g_2^* \leq 0. \quad (17)$$

Households ($k = 3$) have only treated water usage limitation, since it can be used for only limited purposes, such as irrigating in parks, etc.:

$$\frac{t_3}{s_3 + g_3 + t_3 + s_3^* + g_3^*} \leq B_d,$$

where

B_d = maximum proportion of treated water that households can receive.

This constraint is also equivalent with a linear inequality:

$$-\beta_d s_3 - \beta g_3 + (1 - \beta_d)t_3 - \beta_d s_3^* - \beta_d g_3^* \leq 0. \quad (18)$$

There are four additional interconnecting constraints by the limited resources:

$$s_1 + s_2 + s_3 = S_s \quad (19)$$

$$g_1 + g_2 + g_3 = S_g \quad (20)$$

$$s_1^* + s_2^* + s_3^* \leq S_s^* \quad (21)$$

$$g_1^* + g_2^* + g_3^* \leq S_g^*, \quad (22)$$

where

S_s = maximum available surface water amount from local source

S_g = maximum available ground water amount from local source

S_s^* = maximum available imported surface water amount

S_g^* = maximum available imported ground water amount.

In constraints (19) and (20) we require that all local resources have to be used before importing water from other watersheds.

This model is a three-person decision problem with objective functions (11) and feasible sets defined by constraints (12)-(20) with all nonnegative components.

4. Numerical results

The data for the numerical study are the updated versions of those given in the earlier paper of Salazar et al. (2010). The numerical values are given in Table 1.

Furthermore $S_s = 58$, $S_g = 1684$, $S_s^* = 453$, $S_g^* = 170$. These values and D_k^{\min} , D_k are measured in million m^3 /year, the other parameters are ratios, unitless quantities.

Table 1. Model Parameters

	$k = 1$	$k = 2$	$k = 3$
D_k^{\min}	594	177	1092.81
D_k	966	230	2123
α_1	0.41		
β_1	0.33		
B_g		0.666	
B_i		0.20	
B_d			0.06

Table 2. Equilibrium Solution

	$k=1$	$k=2$	$k=3$	Total
s_k	0	0	58	58
g_k	966	205.353	530.647	1702
t_k	0	0	75.702	75.702
s_k^*	0	24.647	428.353	453
g_k^*	0	0	169.000	169
Total	966	230	1262.702	

Table 3. Nash-Bargaining Results

	$k=1$	$k=2$	$k=3$	Total
s_k	0	58.00	0	58
g_k	526.463	101.878	1073.658	1702
t_k	318.780	46.00	98.986	463.766
s_k^*	0	0	453.000	453
g_k^*	120.757	24.122	24.122	169
Total	966	230	1649.766	

First the Nash equilibrium of the three-person noncooperative game is determined by solving the quadratic programming problem (7). The solution is presented in Table 2. The objection function value is zero at the solution showing that global optimum is obtained. The linearity of all constraints and payoff functions imply that the Kuhn-Tucker conditions are also sufficient, so any optimal solution of problem (7) provides equilibrium.

The non-symmetric Nash bargaining solution is then computed by solving the optimization problem. Because Mexico city has the largest population in the world, we give slightly higher importance to households than to the others by selecting $\alpha_1 = \alpha_2 = 0.3$ and $\alpha_3 = 0.4$. The solution is shown in Table 3.

The weighting method is finally applied with the same weights as before by solving the linear programming problem (10). The results are shown in Table 4.

Table 4. Weighting Method Solution

	$k=1$	$k=2$	$k=3$	Total
s_k	0	58	0	58
g_k	647.220	83.600	971.180	1702
t_k	318.780	35.400	101.692	455.872
s_k^*	0	0	453	453
g_k^*	0	0	169	169
Total	966	177	1694.872	

In order to find the individual maximum objective function values we repeated the computations by the weighting method with weight selections $w_1 = 1, w_2 = w_3 = 0$; $w_1 = w_3 = 0, w_2 = 1$ and $w_1 = w_2 = 0, w_3 = 1$. The maximal values became 966, 230 and 1960.021. For agriculture and industry these numbers show that their demands can be completely satisfied. However, for households the maximum possible water supply is only 91.89% of the total demand, meaning that there is no water distribution scheme which can satisfy all domestic demands. In all solutions all available surface and groundwater supplies are used, but the very restrictive constraints on the treated water ratio makes the use of more treated water impossible. In the cases of the equilibrium and the Nash bargaining solutions all demands of agriculture and industry are satisfied. Domestic needs are satisfied only on 59.43% and 77.71% levels, respectively. In the case of the weighting method agricultural demands are fully satisfied, industry receives only the minimum amount, and households get only 79.83% of their need.

Conclusion

The water distribution problem of the Mexican Valley was considered, where agriculture, industry, and households were the players in the game theoretic

models, and their water supplies were the objective functions in the case of multiobjective optimization.

The Nash equilibrium was first obtained by solving a special quadratic optimization problem with linear constraints, which was derived based on the Kuhn-Tucker conditions. The non-symmetric Nash bargaining solution was then obtained by maximizing the non-symmetric Nash product. The application of the weighting method required the solution of a special linear programming problem.

The numerical results well demonstrate that there is no water distribution scheme which can satisfy all domestic demand. In all solutions all available surface and groundwater supplies have to be used. Water supply can be increased either by using more treated water on the expense of worsening water quality, or by increasing surface and groundwater supplies. Importing more water from neighboring regions would result in serious social conflicts, so more investment is needed for further developments and incentives should be given to the users for more efficient water usage. Maybe a market driven pricing policy is needed in the near future

Acknowledgement

The authors gratefully acknowledge the generous support of the TÁMOP-4.2.1.B-11/2/KMR-2011-0003 project titled „Az oktatás és kutatás színvonalának emelése a Szent István Egyetemen”.

References

- [1] Bekele, E. G. and Nicklow, J. W. (2005). “Multiobjective Management of Ecosystem Services by Integrative Watershed Modeling and Evolutionary Algorithms.” *Water Resources Research* 41: W10406, doi:10.1029/2005WR004090.
- [2] Bogardi, J.J. and Nachtnebel, H.P. (1994). “Multi-criteria Decision Analysis in Water Resources Management.” UNESCO Publ. SC94/WS.14. UNESCO, Paris.
- [3] Brown, L.R. (2005) *Outgrowing the Earth: The Food Security Challenge in an Age of Falling Water Tables and Rising Temperatures*. Earthscan Publications Ltd., 120 Pentonville Road, London N1 9JN, UK; www.earthscan.co.uk.
- [4] Donevska, K., Dodeva, S. and Tadeva, J. (2003) “Urban and Agricultural Competition for Water in the Republic of Macedonia”. Internet resources, <http://afeid.montpellier.cemagref.fr/mpl2003/Conf/Donevska.pdf>.
- [5] Forgo, F., Szep, J. and Szidarovszky, F. (1999). *Introduction to the Theory of Games*. Kluwer Academic Publishers, Dordrecht.
- [6] Harsanyi, J. C. and Selten, R. (1972). A generalized Nash Solution for Two-Person Bargaining Games with Incomplete Information. *Management Science* 18:80-106.

- [7] Hipel, K.W. (1992). “Multiple Objective Decision Making in Water Resources.” *Water Resources Bulletin* 28(1):3-11.
- [8] Jensen, P.K., Hoek, W. V. D., Konradsen, F. and Jehangir, W. A. (1998). Domestic Use of Irrigation Water in Punjab. 24th WEDC Conference Sanitation and Water for All. Islamabad. Pakistan.
- [9] Kapelan, Z.S., Savic, D.A. and Walters, G.A. (2005). “Multiobjective Design of Water Distribution Systems under Uncertainty.” *Water Resources Research* 41. W11407.
- [10] Lizhong, W., Liping, F. and Hipel, K.W. (2008). “Basin Wide Cooperative Water Resources Allocation”. *European Journal of Operational Research* 190: 798-817.
- [11] Roth E. A. (1979) *Axiomatic Methods of Bargaining*. Springer-Verlag, Berlin/Heidelberg/New York.
- [12] Salazar, R., Szidarovszky, F. and Rojano, A. (2010) Water Distribution Scenarios in the Mexican Valley. *Water Resources Management*, 24(12): 2959-2970.
- [13] Szidarovszky, F., Gershon, M. and Duckstein, L. (1986). *Techniques of Multiobjective Decision Making in Systems Management*. Elsevier, Amsterdam

Cost and shift hours demand of transportation tasks in the field root vegetable production technology

L. MAGÓ

Department of Logistics and Materials Handling,
Institute for Engineering Management,
Faculty of Mechanical Engineering, Szent István University

Abstract

We present the up-to-date mechanized production technology of carrot production from ridge preparation till harvesting including transporting as well. By the presentation of experiences together with the performance and economic data of machines necessary for production, we are emphasizing the significant volume of transport tasks in the production technology.

The surveys conducted have proved that the machine work costs of carrot production are high. Considering machine costs it is advantageous if, as in the studied cases, harvesting is done by tractor-pulled working machines instead of expensive self-propelling harvesting machines with high operational costs, as the acquisition cost of connected working machines is more favourable and a better utilization and lower specific operational costs of power machines can be achieved by the use of tractors.

It can be stated that special attention is to be paid to the following operations: harvesting, *transport*, cultivation and plant protection works which are the most costly ones and which represent about 95-97 % of the total machine operational costs.

Keywords

transportation, field root production technology, machine investments and usage costs, logistics, shift hours demand

1. Introduction

Carrot is a very important vegetable for fresh consumption as well as for the deepfreezing and for the canning industry. In accordance with the growing methods there is a wide selection of varieties and different production technologies are applied.

We present the up-to-date mechanized production technology of carrot production from ridge preparation till harvesting including transporting as well. By the presentation of experiences together with the performance and economic data of machines necessary for production, we are emphasizing the significant volume of transport tasks in the production technology.

Table 1. The basic economic data of carrot production

Denomination of operation	Type of machine applied in the technology		Shift Performance (ha/h)	Price of		Direct cost of operation (EUR/ha)	
	working machine	power machine		working machine	power machine	working machine	power machine
Stubble stripping	Kühne 770 - 7,2 disc harrow	190 HP tractor	3	19164	109048	10	27
Deep ploughing	VN Euromat 3S Var.5blade upright	190 HP tractor	1	18000	109048	7	27
Ploughing-processing	S-2H/M	190 HP tractor	4,8	7452	109048	7	27
Transport of fertilizer	MBP 6,5	80 HP tractor	4	6016	13516	2	11
Fertilizer spreading	Tomado 5	110 HP tractor	4	9604	82000	6	20
Ridge bed preparation	Rumpstadt FH4x75 RSF 2000 T	190 HP tractor	0,6	15200	109048	13	27
Sowing	Agricola ANT-3-290	110 HP tractor	1,5	6400	82000	9	20
Renewal of ridge beds	Badalini Variax EP/85W 140 GLS	110 HP tractor	1	6600	82000	6	20
Spray transport	DETK-115 tanker	80 HP tractor	4,8	6800	13516	4	11
Plant protection-pre-emergence	HARDI Commander Plus 2200/18	110 HP tractor	4,8	21600	82000	12	20
Spray transport × 3	DETK-115 tanker	80 HP tractor	4,8	6800	13516	4	11
Plant protection-post-emergence×3	HARDI Commander Plus 2200/18	110 HP tractor	4,8	21600	82000	12	20
Spray transport × 6	DETK-115 tanker	80 HP tractor	4,8	6800	13516	4	11
Plant protection-stock treatment×6	HARDI Commander Plus 2200/18	110 HP tractor	4,8	21600	82000	12	20
Irrigation	Valmont Linear		1	98000		17	
Harvesting	GB-02	110 HP tractor	0,4	66000	82000	44	20
Transport to the depot	MBP 6,5	80 HP tractor		6016	13516	2	11
Lodging, loading	Telescopic loader				76000		22
Road transport	HL_92.02 road trailer			7536	33720	3	20
The basic economic data of the operations of harvesting of carrots meant for fresh consumption							
...
Harvesting	ASA LIFT Combi - 1000	110 HP tractor	0,1	59060	82000	34	20
							54

2. Method

Presentation of the production technology

The machine technology of production is presented on the basis of Table 1. The table shows the denomination of operation, the machine applied for the certain operation, and the type of the power machine connected to it together with the shift performance of the connected machines and the calculated shift performance of the working machine for the given economic year. Some of the economic data are also included: the selling price of the working machine and the power machine in the year 2011, the operational cost of the same per shift hour together with the operational cost of the connected machines. (Gockler-2012)

Stubble stripping by disc-harrow is unavoidable in order to work the stem remains of the forecrop into the soil and to prevent weeding. The next operation is deep ploughing. The ploughing processing is realized in the form of dragging. The subsequent delivery of nutrients is ensured through the transport and spreading of fertilizers. This is followed by the preparation of ridge beds, sowing and later on by the renewal of ridges. Plant protection is applied once as a pre-emergence treatment and three times afterwards as a post-emergence treatment. Stock treatment is applied six times. In the vegetation period of cultivated plants irrigation is necessary in order to achieve a high quality final product and a better crop yield. This is done by a linear irrigation system. (Dimény et al. 2004)

3. Results and discussion

Results of the economic survey

The results of the economic survey of carrot production on a 20 hectare area are shown in Table 2. Apparently, the machine working time necessary for the cultivation of the 20 hectare growing area in case of connected machines has been stipulated related to the individual operations. On this basis the direct operational cost of the connected machines can easily be calculated by multiplying the *direct operational cost of the machine per hour* (Table 1) with the effective working time. (Magó et al 2006) Furthermore, the additional cost of connected machines has also been stipulated which is affected by the capital return on fixed and current assets as well as by the general costs of farming. As a result the cost of the individual operations related to 20 hectare growing area has been defined the total of which equals the total production costs of carrot production on 20 hectares, and also the specific costs per hectare of the different harvesting methods for fresh consumption or for the canning industry have been stipulated.

It can be stated on the basis of the results that in case of *carrot production for canning purposes* the operational cost of the power machines (6631 EUR) is less than the half of that of the working machines (14.979 EUR). The total operational cost amounts to 21.610 EUR, 1080 EUR per hectare. In case the

goods are meant for the fresh market the above indexes are as follows: the operational cost of the working machines (14.990 EUR) is nearby equal to the operational cost of the power machines (15.612 EUR). The total operational cost is 30.602 EUR, 1530 EUR per hectare.

Table 2. The economic index numbers of the operations of carrot production on 20 hectares

Denomination of operation	Machine working hours	Cost of operation
	(h)	(EUR)
Stubble stripping	6	265
Deep ploughing	20	814
Ploughing-processing	4	164
Transport of fertilizer	5	75
Fertilizer spreading	5	161
Ridge bed preparation	33	1625
Sowing	13	467
Renewal of ridge beds	20	640
Spray transport	4	70
Plant protection-pre-emergence	4	162
Spray transport × 3	12	214
Plant protection-post-emergence × 3	12	489
Spray transport × 6	24	431
Plant protection-stock treatment × 6	24	979
Irrigation	20	444
Harvesting	50	4107
Transport to the depot	150	2299
Lodging, loading	20	515
Road transport	300	7689
Canning industry technology - total	726	21610
<i>Cost per hectare (EUR/ha)</i>		1080
The economic index numbers of the harvesting operation of carrot production for fresh consumption on 20 hectares		
...
Harvesting	200	14026
Fresh consumption technology - total	826	30602
<i>Cost per hectare (EUR/ha)</i>		1530

It can be stated that the drag picking method harvesting for fresh consumption causes an extra cost of about 450 EUR per hectare.

In view of the operational cost relations it can be stated that in case the final product is meant for industrial use the *cost of road transport is about 35 %*, and

the *delivery from the field to the depot by tractor about 10 %* of the total cost. It is followed by the harvesting operation with 19 %. Considering the cost of the other operations of the technology the significant ones are the plant protection with 11 %, the ridge bed preparation with 7,5 %, the deep ploughing and the renewal of ridge beds with 3 % each, while the cost proportion of the remaining operations is often less than 1 %. In case the final product is meant for the fresh market this order is different. The major cost factor is harvesting with 45 %, *road transport and delivery by tractor follows with 25 % resp. 6 %*, and in this case the cost of plant protection is 8 %, of ridge bed preparation 6 %, of deep ploughing 3 % and of the renewal of ridge beds 2 % of the total cost.

The figures of the present survey are calculated on the basis of high quality and mostly valuable power machines which ensure effective performance. (Husti 2004) Consequently the acquisition and operational costs of the power machines are also substantial. (Daróczy 2013) The prescribed operations can naturally be realized by using power machines of a lower technical level under strict control and in this case the operational cost of the machines can be less than that figuring in the survey. (Magó 2008)

The investment cost of the machines applied in the production technology amounts to 602 thousand EUR (*554 thousand EUR*¹), out of which the purchasing price of the working machines amounts to 288 thousand EUR, which equals about 48 % of the total investment cost (*292 thousand EUR – 53 %*), while the purchasing price of the power machines is 314 thousand EUR, about 52 % of the total cost of machines (*262 thousand EUR – 47 %*). In case of power machines it can be stated that one power machine with an engine capacity of 190 HP is needed for the hard cultivation works, while the tasks of nutrients delivery, plant protection and crop cultivation, sowing, harvesting tractor delivery are fulfilled by 110 HP main and a 80 HP aid machine. (Magó 2009a) For moving the goods in the depot a *telescopic loader is also required*, first of all in case of root vegetables meant for industrial use. For the road transport of the crop a *low-cost trailer can be used*. With the above method of applying power machines lower acquisition costs and a more effective utilization of power machines can be achieved.

Carrot production on 20 ha demands 726 shift hours of machine work, out of which the two lower capacity tractors represent a great proportion due to delivery of nutrients, sowing, ridge bed renewal, crop protection and harvesting and *transport by tractor* and the shift hour performance of the high capacity power machine in the course of cultivation is also significant. *Road transport with its 300 shift hour capacity demand is the most time-demanding operation*.

In case of production meant for fresh consumption the 110 HP tractor works even more shift hours due to the time-demanding harvesting. In this case the total number of the shift hours performed in the course of the technology is 826.

¹ Investment cost values in case of technology when the goods are meant for the fresh market.

Conclusions and proposals

The surveys conducted have proved that the machine work costs of field root vegetable production are high. Taking into consideration the extra work connected to grading and consumer packing substantial additional costs arise which can lead to specific costs per hectare exceeding 1500 EUR. In case of a 60 t/ha yield it can easily be calculated that operational costs of machines themselves exceed 3 EURO Cent/kg, and we have to take into consideration the costs of seeds, fertilizers, pesticides, labour and irrigation water.

Considering machine costs it is advantageous if, as in the studied cases, harvesting is done by tractor-pulled working machines instead of expensive self-propelling harvesting machines with high operational costs, as the acquisition cost of connected working machines is more favourable and a better utilization and lower specific operational costs of power machines can be achieved by the use of tractors. (Magó 2009b, 2013)

It can be stated that special attention is to be paid to the following operations: harvesting, transport, cultivation and plant protection works which are the most costly ones and which represent about 95-97 % of the total machine operational costs.

References

- [1] Daróczy M.: (2013) „The Contribution of Agricultural Machinery to Sustainable Agriculture“ Proceedings of the First International Symposium on Agricultural Engineering, 4th-6th October 2013, Belgrade–Zemun, Serbia, p. VIII. 19-27.
- [2] Dimény I., Fenyvesi L., Hajdú J.: (2004) Piactudatos zöldségtermelés. (Market Oriented Vegetable Production) MGI könyvek, FVM Mezőgazdasági Gépesítési Intézet, No. 3. 2004, 234. p.
- [3] Gockler L.: (2012) The Costs of Agricultural Machines in 2012, Mezőgazdasági Gépüzemeltetés 2011., FVM Mezőgazdasági Gépesítési Intézet. Gödöllő, 2012.
- [4] Husti I.: (2004) Why is the Mechanisation of Hungarian Small and Medium Size Farms so Difficult, Hungarian Agricultural Engineering. No. 17. p.: 74-75.
- [5] Magó L., Hajdú J., Nagy I.: (2006) The Economic of the Mechanisation of Field Root Vegetable Production by Ridge-till Technology, Collection of Extent Abstracts of the “2006 CIGR Section VI International Symposium on FUTURE OF FOOD ENGINEERING”, Warsaw, Poland, 26-28 April 2006. Proc. p. 136., Full Paper in the CD issue
- [6] Magó L.: (2008) Efficient Machine Utilisation in Small and Medium Size Field Vegetable Production Farms, Journal of Agricultural Machinery Science, Agricultural Machinery Association - Ege University, Bornova-Izmir, Turkey, 2008. Vol. 4., No. 1., p. 81-85.

- [7] Magó L.: (2009a) „Comparison of the Cost of Mechanisation of Field Vegetable Production Technologies”, Abstracts of the International Conference “Synergy and Technical Development in the Agricultural Engineering”, Gödöllő, Hungary, 31. August - 3. September 2009. p. 98.; Full Paper in CD Issue
- [8] Magó L.: (2009b) Determination of the Cost of Mechanisation of Field Vegetable Production Technologies, Hungarian Agricultural Engineering, Periodical of the Committee of Agricultural Engineering of the Hungarian Academy of Sciences, Vol. 22/2009. p. 56-59.
- [9] Magó L.: (2013) „The Significance of Post-harvest Transportation Tasks in the Field Root Vegetable Production”, Proceedings of the First International Symposium on Agricultural Engineering, 4th-6th October 2013, Belgrade–Zemun, Serbia, p. IV. 1-6.

Characterizing quality of tillage by means of stereo vision

T. RIEGLER¹, C. RECHBERGER¹, F. HANDLER², H. PRANKL²

¹Josephinum Research, Lehr- und Forschungszentrum Francisco Josephinum

²BLT Wieselburg, Lehr- und Forschungszentrum Francisco Josephinum

Abstract

In this paper the usage of passive image data acquisition technique for generating 3D-maps of the surface of soil by means of stereo vision is investigated. A stereo vision system is mounted onto an electrical powered movable slider of a linear motion frame. Quality of tillage can be characterized by average slope, statistic attributes of the 3D-map, roughness, volume change and working depth. To indicate the capability of the method for characterizing quality of tillage, accuracy and deviation of repeated measurements were analyzed. Stereo vision is an appropriate method for generating 3D-maps and consecutive measurement in outdoor environments.

Keywords

stereo vision, quality of tillage, roughness index, tilled volume, agricultural information technology

1. Introduction

Quality of tillage depends on many independent parameters which are the properties of soil and properties of the tillage system. Due to the enormous amount of influencing parameters it is important to characterize the quality of work for tillage by objective criteria. Characterizing quality of tillage can be achieved by several statistic attributes, roughness of the soil surface and volume change through tillage. Basing on the quality of tillage different tillage systems, tillage tools and even different settings of the same tillage system can be compared.

To determine surface roughness and volume change a method for generating a 3D-map of the surface is necessary. Different methods with varying accuracy, resolution, time for data acquisition and captured area are available. In this study the usage of a stereo vision system (SVS) to acquire 3D-maps of the soil surface is investigated and evaluated. Software was developed to utilize a conventional camera system by making use of image data processing techniques. For the comparison of different tools and settings, changes of the surface of an area with side length of one working width of a tillage system must be covered. The

benefit of image data processing techniques is the cost-saving hardware, a high degree of automation and the insensitivity to changeable lighting conditions through the passive acquisition method.

2. Related work

The tillage index of Colvin et al. (1984) bases on height differences perpendicular to direction of tillage, percentage of soil surface covered by plant residues, roughness of the soil surface and depth of tillage. According to soil surface roughness, Taconet and Ciarletti (2007) provide an overview of different roughness indices, grouped into elevation standard deviation, slope-angle and tortuosity index and elevation auto-covariance function. The parameters root-mean square (rms), autocorrelation function (ACF) and the associated correlation length are used to define the characterization of the agricultural soil roughness (Zhixiong et al., 2005). The roughness index RC_x and RC_y introduced by Taconet and Ciarletti (2007) as extension to roughness index RC of Currence and Lovely (1970) treats the demand of height differences perpendicular to the direction of tillage. The working depth is typically defined as the distance between work bottom and the ground surface mean level (Pochi and Fangigliulo, 2010), in other words the difference of the height readings before tillage and the working horizon.

In the past many different systems for the acquisition of height readings from manual to automatic systems were developed. A manual microrelief meter was used to measure the elevation of the soil surface for estimating the total porosity (Allmaras et al., 1966). For analyzing the soil surface roughness an automated profilometer was used. It took about 3-4 hours for taking 4 800 height readings of a plot of 60 x 80 in (152 x 203 cm) (Currence and Lovely, 1970). For estimating soil erodibility by wind a soil contacting microrelief meter covering an area of 1 m² with 800 recorded grid points was used by Zobeck and Hagan (1990). A wide spread method for automatic data acquisition is the use of laser scanners mounted on a linear motion frame. Investigations concerning the accuracy of laser scanners based on Guideline VDI/VDE (2002) are shown by Boehler et al. (2003). To analyze the roughness of seedbeds a laser profile meter mounted onto a linear motion frame with a stepper motor was used by Anken and Hilfiker (1996) covering an area of 1 x 50 cm. Several regional roughness indices are proposed and discussed from Guillobez and Arnaud (1998) by using a 3D profilograph with a laser cell recording 930 data points with a grid size of 3.2 mm. Droll and Kutzbach (2001) use a laser scanner to measure marks of tires on soft ground of an area of 1 000 x 180 mm with an average distance of 1.75 mm between measurements. A portable tillage profiler using a laser scanner was used by Raper et al. (2004). Zhixiong et al. (2005) uses a laser profiler with a spatial resolution of 1 mm for measuring the agricultural soil roughness. To predict the surface porosity in a cultivated field a laser profiler scanning an area of 2 x 1 m is used by Sun et al. (2009). Photogrammetry for investigating and

evaluating the behavior of different roughness indices in regard to their spatial sampling size and sampling form was used by Marzahn et al. (2012). Jester and Klik (2005) compared roller chain, portable laser scanner, pin-meter and stereo photography as soil roughness measurement techniques with regard to data acquisition and computational effort. While an overview of active optical range imaging sensors can be found in work of Besl (1988), Hebert (2000) gives an overview of different passive and active range sensing technologies.

3. Materials and methods

A stereo vision system (SVS) called Bumblebee 2 provided by Point Grey Research (Fig 1) is mounted onto an electrical 12 V powered movable slider of a linear motion frame (Fig 2). The linear motion frame has an extent of 4 m and the SVS is mounted at a height of 60 to 80 cm. The SVS consists of two cameras with CCD sensors which are mounted parallel. The camera system has a 1/3” CCD imaging sensor with 1032 x 776 max pixels (4.65 μm square pixels), a baseline of 12 cm and a lens focal length of 3.8 mm with 66° horizontal field of view (HFOV). A left-handed coordinate system is used, where the y-axis denominates the moving direction of the slider and consequently denominates across driving direction of a tillage system. The x-axis denominates the driving direction of the tillage system and denominates across the driving direction of the slider. The z-axis defines the elevation (see Fig 2 for definition of coordinate system).



Figure 1. Bumblebee 2

Software with programming language C#.NET was developed for Microsoft Windows 32 und 64 bit architecture under usage of libraries FlyCapture SDK (Version 1.8.3.27) Triclops SDK (Version 3.3.1.3) and VTK Visualization Toolkit (Version 5.8.0.607). The resulting report is generated as Microsoft Excel Worksheet.

To indicate the capability for characterizing the quality of tillage of the SVS and the developed software analysis of accuracy and deviation of repeated measurements were analyzed.

Since the correlation algorithm in the developed software needs a well structured non-uniform surface, it is difficult to measure the distance from the SVS to a plain surface. To show systematic errors and uncertainty of measurement in practical use the volume between two surfaces, modeled with sand of granulation 0.5 – 2.0 mm was used. For investigating systematic errors

and uncertainty of measurement two experimental arrangements were elaborated. First a rough surface was built and scanned as reference surface, where a well-defined volume of 6 and 12 dm³ was randomly added to the surface and scanned repeatedly afterwards. In a second arrangement also a reference surface was scanned and then consecutive about 10, 20, 30, 40, 50, 100, 150 and 200 dm³ were added randomly. As distinction to the first arrangement the surface was remodeled after each repetitive scan.



Figure 2. Linear Motion Frame

For evaluating the uncertainty of measurement in practical use 11 scans of the same surface before tillage, after tillage and of the working horizon were taken. For all calculated characteristics the arithmetic mean and the standard deviation were calculated.

All statistical analyses were carried out by means of Statgraphics Centurion XVI.I.

4. Results

Development of the software

A 3D-map is generated out of the images taken from the two cameras by a stereo vision processing pipeline. Images are shot continuously while moving the slider of the linear motion frame with a speed of about 0.13 m/s. The camera provides a 66 degree horizontal field of view resulting in a field of view of about 1 m at a typical operating distance of 0.8 m. Rectification for eliminating lens distortion and align images coplanar is the next step. Edge Detection ensures that different brightness in the images does not influence correspondence matching. Correspondence matching is the crucial point in stereo vision, which leads to a disparity map. By means of triangulation the disparity map is transferred in real world coordinates, resulting in a set of about 620 000 unorganized points. Subpixel interpolation, back and forth validation and surface validation increase the quality of stereo processing. According to field of view this results in a

resolution of about 60 points per cm². To combine fractional point set into one coordinate system a 3D rigid body transformation where z-coordinate remains unchanged is done. Final step is a 2D-Delaunay Triangulation where the surface is reconstructed by connecting points via edges so that triangles are formed. As result of these steps a comprehensive 3D-map of the scanned area (about 3.5 x 1 m) is available.

Quality of tillage

For characterizing the quality of tillage three subsequent scans of the examined area before tillage (BT), after tillage (AT) and of the working horizon (WH) by removing the loosened soil are taken. In Figure 3 examples of 3D-maps produced by tilling with a 3-bank stubble cultivator without rear roller at a working depth of 22 cm can be seen. From these 3D-maps (BT, AT and WH) descriptive and comparative characteristics are calculated:

(1) Average slope describes the trend of lopsidedness in y direction by calculating the line of best fit which minimizes the sum of square deviations. Comparing lopsidedness before and after tillage, marks introduced by tillage can be identified.

(2) Statistic attributes like arithmetic mean, median and standard deviation describe key features of the height readings of a 3D-map.

(3) The roughness index RC is calculated by correcting each height reading for row and column effects, to remove plot slope (Currence and Lovely, 1970). Taconet and Ciarletti (2007) state that the roughness index RC is a satisfactory index which describes the amplitude variation of the height residuals from the plane of best fit through the data.

(4) For non isotropic structure of the surface averages on one single coordinate can be performed. These roughness indices RC_x and RC_y are described by Taconet and Ciarletti (2007).

(5) Volume: As result of the stereo processing pipeline a triangulated 3D-map is available. By comparing the 3D-map before tillage and after tillage the volume increase resulting from loosening of soil can be determined. Comparing the 3D-map before tillage and of the working horizon the processed volume can be determined.

To calculate the volume difference between two 3D-maps the maps have to be cropped to the same size. This is done by calculating the bounding box of each 3D-map and then by taking the extent in x- and y-direction of the smaller value. Second step is the calculation of the volume difference to plane with $z = 0$. Therefore the center of gravity of each triangle is determined. From this center of gravity the height reading (z-value) is multiplied with the projected area to get the volume of the three-sided prism. This calculation of the spatial volume of each three-sided prism is done for each triangle of the 3D-map and summed up to get the total volume. The calculation of the volume to plane with $z=0$ is repeated with the second 3D-map. Consequently the difference between these two determined volumes gives the volume difference between the two compared 3D-maps.

(6) Working depth: The accurate measurement of depth of tillage is trivial in theory but difficult in practice. Surface of soil, even before tillage, does not build a plane so height readings depend on the location of measurement, just as the working horizon does not build a plane for accurate measurement. Height readings and subsequent depth of tillage can only be an average of multiple measurements. Complicating some tillage systems, like cultivators, provide a bumpy working horizon. Therefore we use the volume of the tilled and loosened soil as replacement for the depth of tillage. A definition of working depth for uneven working horizon will be necessary in the future.

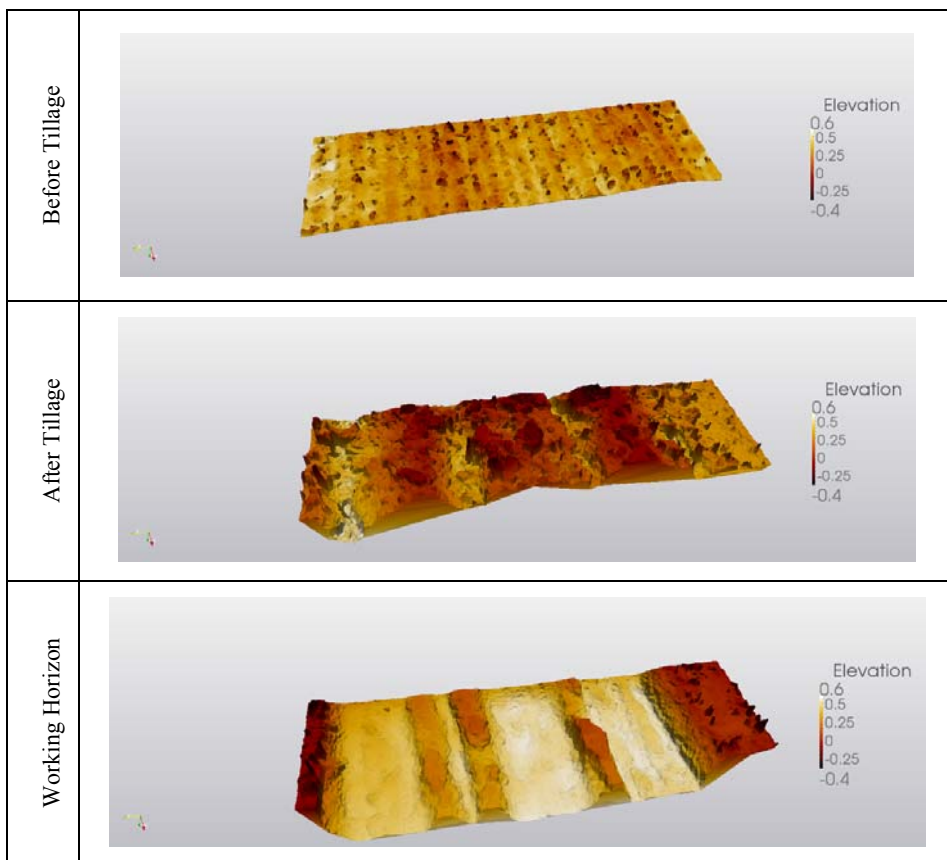


Figure 3. 3D-map of different surfaces

Evaluation of the system

Table 1 and Table 2 contain the results of the in-door experiments for evaluating the volume measurement. The mean differences between the actually added volume of sand and the measured volume (see column 6) are used as measurement for a systematic error. For repeated measurements of the same

surface (Table 1) the standard deviation of the measured volume is lower than the standard deviation of measured volume when remodeling the surface after each scan (Table 2).

Table 1. Uncertainty of measurement and systematic error of volume measurement

n	Added volume of sand [dm ³]	Scanned area [dm ²]	Arithmetic mean of measured volume [dm ³]	Standard deviation of measured volume [dm ³]	Mean difference between column 4 and 2
1	2	3	4	5	6
24	6.00	360.62	6.01	0.10	0.01
24	12.00	360.62	11.90	0.11	0.10

Table 2. Uncertainty of measurement and systematic error of volume measurement with remodeled surface after each scan

n	Added Volume of sand [dm ³]	Scanned Area [dm ²]	Arithmetic mean of measured volume [dm ³]	Standard deviation of measured volume [dm ³]	Mean difference between column 4 and 2
1	2	3	4	5	6
4	9.8	358.13	9.0	0.8	-0.8
4	19.6	358.13	21.2	2.3	1.6
4	29.2	358.13	30.3	2.2	1.1
4	38.9	358.13	39.4	2.2	0.5
4	48.6	358.13	49.2	2.5	0.6
4	97.1	358.13	98.0	0.9	0.9
4	145.6	358.13	145.9	2.2	0.4
4	194.1	358.13	193.6	0.6	-0.5

Table 3. Characteristics for the quality of work of a cultivator
(\bar{X} .. arithmetic mean, s .. standard deviation)

	Before tillage		After tillage		Working horizon	
	\bar{X}	s	\bar{X}	s	\bar{X}	s
Avg. Slope y [mm]	0	0	0	0	0	0
Arithmetic mean z [mm]	0	0	36	1	-68	1
Median z [mm]	0	0	36	1	-79	1
Roughness index RC [mm]	7.1	0.1	14.6	0.1	11.6	0.1
Roughness index RCy [mm]	13.7	0.1	18.6	0.1	34.8	0,1
Roughness index RCx [mm]	7.1	0.1	14.1	0,1	9.4	0.0

To show variation of characteristics in practical use, 11 scans of the same surface before tillage, after tillage and of the working horizon were taken. In *Table 3* and *Table 4* the arithmetic means and the standard deviations of the characteristics are shown. The Average Slope y describes the slope of the regression line (y/z) across the driving direction of the cultivator. An Average Slope y of 0 of the working horizon for example means that the cultivator works on the left and right side at the same working depth. The Arithmetic mean z and Median z after tillage represent the average enhancement of the soil surface caused by tillage while the Arithmetic mean z and Median z of the working horizon represent the average working depth. The roughness indices describe the roughness of the surface. Tillage causes an increase of roughness of the soil surface. Furthermore there is a difference in roughness of the working horizon in driving direction and across driving direction.

Table 4. Volume of soil between scanned surfaces
(\bar{x} .. arithmetic mean, s .. standard deviation)

Volume of soil	between surface before and after tillage		between surface before tillage and working horizon		between surface after tillage and working horizon	
	\bar{x}	s	\bar{x}	s	\bar{x}	s
Volume [dm ³ /m ²]	35.40	0.22	66.07	0,16	101,47	0,12

In *Table 4* the volume of soil between surface before and after tillage represents the increase of soil volume caused by tillage. In the present case the increase of soil volume amounts to 54 %.

The standard deviations of all calculated characteristics are relatively low which indicates a low uncertainty of measurement.

Conclusion

Passive image acquisition using a SVS system is capable to generate 3D-maps of soil surface by using a stereo vision processing pipeline. Further investigation may be necessary to process image data in real time. It was shown that the accuracy in practical use is in a feasible range for measuring surfaces of soil. Stereo vision is a method that is appropriate for generation of 3D-maps and consecutive measurement in 3D-space for outdoor environments. The method is suitable to characterize the quality of work for arbitrary working width of tillage implements though the manageability of the linear motion frame has to be considered. Practical experiments using further tillage system have to be done in the future to show the applicability for other tillage systems.

Acknowledgement

This work is part of the project “Future Farm Technology (FFT)” which is supported by the COMET-program of the Austrian Research Promotion Agency.



References

- [1] Allmaras, R. R., Burwell, R. E., Larson, W. E., Holt, R. F., & Nelson, W. W. (1966), Total porosity and random roughness of the interrow zone, U.S. Department of Agriculture, 7, 1-22.
- [2] Anken, T., & Hilfiker, T. (1996), Feines Saatbett: Hoher Energiebedarf und Feldaufgang, aber kein Mehrertrag bei Winterweizen, FAT-Berichte, 484, 1–9.
- [3] Besl, P. J. (1988), Active, optical range imaging sensors, Machine Vision and Applications, 1, 127–152.
- [4] Boehler, W., & Marbs, A. (2003), Investigating Laser Scanner Accuracy, XIXth CIPA Symposium, Antalya, Turkey, Sept. 2003
- [5] Colvin, T. S., Erbach, D. C., Buchele, W. F., & Cruse, R. M. (1984), Tillage Index Based on Created Soil Conditions, Transactions of the ASAE, 27, 370 – 371.
- [6] Currence, H., & Lovely, W. (1970), The analysis of soil surface roughness, Trans. ASAE, 13, 710–714.
- [7] Droll, P., & Kutzbach, H. D. (2001), Laserscanner zur 3D-Oberflächenvermessung, Landtechnik, 56, 148–149.
- [8] Guideline VDI/VDE. (2002), Optical 3-D measuring systems /Optical systems based on area scanning, Beuth Verlag GmbH Berlin.
- [9] Guillobez, S., & Arnaud, M. (1998), Regionalized soil roughness indices, Soil and Tillage Research, 45, 419–432.
- [10] Hebert, M. (2000), Active and passive range sensing for robotics, 2000 IEEE International Conference on Robotics and Automation, San Francisco, 102–110.
- [11] Jester, W., & Klik, A. (2005), Soil surface roughness measurement—methods, applicability, and surface representation, Catena, 64, 174–192.
- [12] Marzahn, P., Rieke-zapp, D., & Ludwig, R. (2012), Assessment of soil surface roughness statistics for microwave remote sensing applications using a simple photogrammetric acquisition system, ISPRS Journal of Photogrammetry and Remote Sensing, 72, 80–89.
- [13] Pochi, D., & Fangigliulo, R. (2010), Testing of Soil Tillage Machinery, Soil Engineering (pp. 147–168).

- [14] Raper, R. L., Grift, T. E., & Tekeste, M. Z. (2004), A portable tillage profiler for measuring subsoiling disruption, *Trans. ASAE*, 47, 23–27.
- [15] Sun, Y., Lin, J., Lammers, P. S., Damerow, L., Hueging, H., Zhang, H., & Sun, W. (2009), Predicting surface porosity using a fine-scale index of roughness in a cultivated field, *Soil and Tillage Research*, 103, 57–64.
- [16] Taconet, O., & Ciarletti, V. (2007), Estimating soil roughness indices on a ridge-and-furrow surface using stereo photogrammetry, *Soil and Tillage Research*, 93, 64–76.
- [17] Zhixiong, L., Nan, C., Perdok, U. D., & Hoogmoed, W. B. (2005), Characterisation of Soil Profile Roughness, *Biosystems Engineering*, 91, 369–377.
- [18] Zobeck, T. M., & Hagan, L. J. (1990), A microrelief index to estimate soil erodibility by wind, *Transactions in Agriculture*, 33, 151–155.

Simulation of grain harvesting

R. TÓTH, M. DARÓCZI

Institute for Engineering Management, Szent István University

Abstract

The monitoring and organization of various agricultural prime movers and harvesters in different circumstances is a difficult task due to the growing costs. Concerning this fact, the computerized modeling of certain technical processes can be the solution.

Simulation was used to model the grain harvesting and to get acquainted with the used technology. During simulation, the Arena simulation software was used. The simulation trial involved the harvest and the transportation with trailer. During the selection of the based data, the parameters of a selected harvester were used. The results of the modeling are in the English reports prepared by Arena. The methods and experiences obtained in the course of modeling are adaptable to other harvesting technologies and practice.

Keywords

grain harvesting, simulation, model

1. Introduction

Simulation is the imitation of the operation or a real-world process or system over time. The act of simulating something first requires that a model be developed; this model represents the key characteristics or behaviors/functions of the selected physical or abstract system or process. The model represents the system itself, whereas the simulation represents the operation of the system over time. (Banks, 2001)

Simulation refers to a broad collection of methods and applications to mimic the behavior of real systems, usually on a computer with appropriate software. In fact, “simulation” can be an extremely general term since the idea applies across many fields, industries and applications. These days, simulation is more popular and powerful than ever since computers and software are better than ever. (Kelton, 2003)

2. Materials and methods

Simulation can be used to show the eventual real effects of alternative conditions and courses of action. Simulation is also used when the real system cannot be

engaged, because it may not be accessible, or it may be dangerous or unacceptable to engage, or it is being designed but not yet built, or it may simply not exist. (Sokolowski, 2009)

Key issues in simulation include acquisition of valid source information about the relevant selection of key characteristics and behaviors, the use of simplifying approximations and assumptions within the simulation, and fidelity and validity of the simulation outcomes.

A computer simulation is an attempt to model a real-life or hypothetical situation on a computer so that it can be studied to see how the system works. By changing variables in the simulation, predictions may be made about the behavior of the system. It is a tool to virtually investigate the behavior of the system under study.

Traditionally, the formal modeling of systems has been via a mathematical model, which attempts to find analytical solutions enabling the prediction of the behavior of the system from a set of parameters and initial conditions. Computer simulation is often used as an adjunct to, or substitution for, modeling systems for which simple closed form analytic solutions are not possible. There are many different types of computer simulation, the common feature they all share is the attempt to generate a sample of representative scenarios for a model in which a complete enumeration of all possible states would be prohibitive or impossible.

Simulation allows the analysis of a system's capabilities, capacities, and behaviors without requiring the construction of or experimentation with the real system. Since it is extremely expensive to experiment with an entire factory to determine its best configuration, a simulation of the factory can be extremely valuable. There are also systems, like nuclear reactions and warfare, which are too dangerous to carry out for the sake of analysis, but which can be usefully analyzed through simulation. (Smith, 2000)

The Arena is an advanced, hierarchical structured simulation system which provides an interactive environment for building, graphically animating, verifying, and analyzing simulation models. Due to the hierarchical structure, you can design a unique Arena template that is specific to your particular project, company, or industry. (Benkő, 2011)

The basic building blocks for Arena models are called modules. These are the flowchart and data objects that define the process to be simulated and are chosen from panels in the Project Bar. Modules come in two basic flavors: flowchart and data.

Flowchart modules describe the dynamic process in the model. You can think of flowchart modules as being nodes or places through which entities flow, or where entities originate or leave the model. Data modules define the characteristics of various process elements, like entities, resources and queues. They can also set up variables and other types of numerical values and expressions that pertain to the whole model. (Kelton, 2003)

Simulation was used to model the grain harvesting and to get acquainted with the used technology. During simulation, the Arena simulation software was used.

The harvester applied during the simulation is Claas Lexion 600. During the selection of the base data the parameters of this harvester were used. The methods and experiences obtained in the course of modeling are adaptable to other harvesting technologies and practice.

Table 1. Technical specification of Claas Lexion 600

Engine power	368 kW
Net weight	17,5 t
Grain container capacity	12.000 l
Grain container capacity	12.000 l
Continuity desk width	9,12 m
Cutting frequency	1120 stroke/min

3. Results

The simulation trial involved the harvest and the transportation with trailer. The whole model of simulation can be seen in Figure 1.

The entrance point of the model is a Create module, called *Gabona tabla*. The entities created by this module are correspond to 0,1 t grain, which are started up with constant, 1 entity/minute intensity. In the *Ertekadas 1* Assign module, the cutting time was determined, which is used by the Process module called *Aratas*. The variable, called *Magtartaly tartalom* was defined by the *Ertekadas 2* Assign module, and the *Dontes 1* Decide module calculate on it. With the Hold module *Betakarito gep blokkolas*, a free trailer can be ordered. With the *Magtartaly urites* Delay module the grain unloaded from the container to the trailer.

The further parts of the model connect to the unload of the grain container. With the help of the first, *Dontes 2* Decide module, it can be determined, whether the trailer coming to the harvester is empty. It is a two way conditioned decision, using the *Potkocsi tartalom* variable. If the value of the variable is zero, the trailer arrives empty, if the value is different from zero, there is grain in the trailer. In that case, with the *Ertekadas 3* Assign module, the following variables have to be determined: the quantity that can be unloaded, the content of the trailer, and the content of the grain container after the unload. If the trailer arrives empty, the *Dontes 3* Decide module is necessary. In this case the proportion of the grain container capacity and the trailer capacity is determined. If the content of the grain container is equal to or bigger than the trailer capacity, the grain quantity of the grain container have to be determined with a variable, defined in *Ertekadas 4* Assign module. In case the quantity of grain in the grain container less than the trailer capacity, the grain container have to be unloaded by *Ertekadas 5* Assign module.

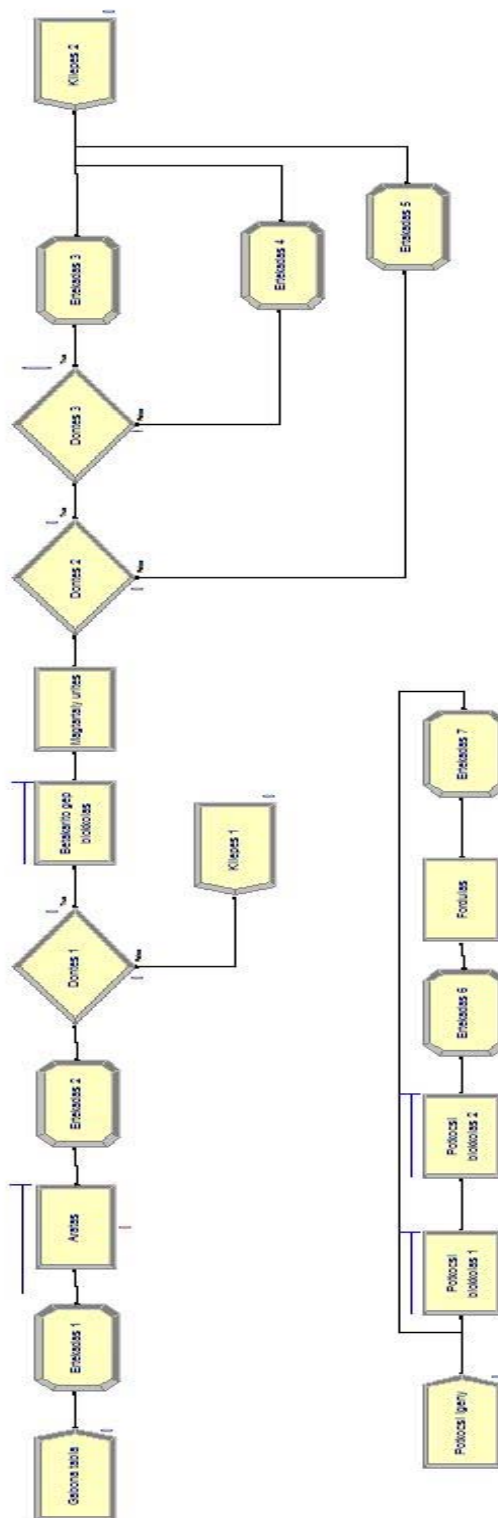


Figure 1. The model of simulation

It was necessary to model the availability of trailers. The number of available trailers can be given in *Potkocsi igeny* Create module. The unload is not continuous, the available trailer have to be holden with *Potkocsi blokkolas 1* Hold module, until the grain quantity in the grain container reaches 90%. By this time, the entity is released and the grain container can be unloaded. Because the capacity of the trailer and the grain container can be different, it can happen, that the trailer do not fill up with every unload. It is practical to exploit the whole capacity of the trailer, so the *Potkocsi blokkolas 2* Hold module will not release the trailer until the capacity and the content of the trailer is equaled. In this case the trailer is engrossed. This is nominated by the *Lekotottseg* attribute with value 1, given in the *Ertekadas 6* Assign module. The aim of the *Fordulas Delay* module, is to take the time into consideration, while the trailer transport the grain and come back after the unload. After that the trailer have to be made free, with the *Ertekadas 7* Assign module, where the *Lekotottseg* attribute get the value 0. After this the trailer get into the transportation again with a feedback.

To control the proper run of the simulation model, the following input parameters were used. (Table 2.)

Table 2. Input parameters of simulation model of grain harvesting

Input data	Parameter
Cutting time	0,08 min
Grain container capacity	12.000 l
Unload grain container	2 min
Available trailers	2
Trailer capacity	14 t
Turning time	60 min

The running time of simulation are 7200 minutes. The results of the modeling are in the English reports prepared by Arena. These reports contain information about the entities, the sources, the processes, the waiting queues, transportation, etc. The data can be different time parameters, cost and utilization indicators.

Through the examined duration 720 t of entity started up. The average working time of 0,1 t grain is 0,0013 h, (about 5 s). The waiting, queuing time is important. With these parameters, there was a free trailer every time the grain container filled up. The trailers waited average 1,27 hours in the first hold module. The minimum waiting time was 0,018 h, the maximum was 1,35 h. The report shows, that usually one trailer waited.

From the results of the model run with original parameters can be stated that the model results approximate the reality, it is operable. On the basis of the results of the simulation, two trailers can serve two harvesters with these parameters.

Conclusions

Simulation was used to model the grain harvesting and to get acquainted with the used technology. During simulation, the Arena simulation software was used. The simulation trial involved the harvest and the transportation with trailer. The waiting times and bottlenecks can be assigned by means of the model. The results of the modeling are in the English reports prepared by Arena. These reports contain information about the entities, the sources, the processes, the waiting queues, transportation, etc. The methods and experiences obtained in the course of modeling are adaptable to other harvesting technologies and practice.

Acknowledgement

The research was supported/subsidized by the TÁMOP-4.2.2.B-10/1-2010-0011 „Development of a complex educational assistance/support system for talented students and prospective researchers at the Szent István University” project.

References

- [1] Banks, J., Carson, J., Nelson, B., Nicol, D. (2001), Discrete-Event System Simulation, Prentice Hall, p. 3.
- [2] Benkő, J. (2011), Arena Modules for Modeling Kanban-Controlled Manufacturing, Mechanical Engineering Letters, Szent István University, Gödöllő p. 161.
- [3] Kelton, W. D., Sadowski, R. P., Sadowski, D. A. (2003), Simulation with Arena, McGraw-Hill
- [4] Smith, R. D. (2000) Simulation Article, Encyclopedia of Computer Science, 4th Edition
- [5] Sokolowski, J. A., Banks, C. M. (2009), Principles of Modeling and Simulation. Hoboken, NJ: Wiley, p. 6.

Investigation of soil-rigid wheel contact under three different circumstances using discrete element method

K. KOTROCZ¹, Gy. KERÉNYI²

¹Department of Machine and Product Design,
Budapest University of Technology and Economics

²Department of Machine and Product Design,
Budapest University of Technology and Economics

Abstract

This paper involves numerical simulations of the rigid wheel's sinkage. The Discrete Element Method (DEM) was used during all analysis and the cohesive nature of the soil was simulated by the so-called Parallel Bond contact model. In this article three types of soil was calibrated with different mechanical properties. The cohesion and the internal friction angle were determined by numerical direct shear tests. After that the interaction of the rigid wheel and the soil was simulated in all three circumstances to measure the wheel's vertical sinkage and the soil's compaction and to compare them with the theoretical values.

Keywords

soil, rigid wheel, DEM, soil deformation, numerical direct shear test

1. Introduction

The description of the soil wheel interaction always has been an important area of the researches because the agricultural machines are made contact with the soil by their wheels. As it is well known that a loaded wheel sinks into the soil. Thus lots of studies and papers were written about the sinkage and the rolling resistance in the last century, including the theoretical basics of these phenomena.

In addition numerical methods were developed to simulate the behaviour of the materials under static or dynamic loading processes. The best known is the Finite Element Method which can be used efficiently for homogeneous, isotropic materials. In contrast of these materials the soil consists of individual particles thus is not able to simulate with FEM correctly. Instead of FEM the so-called Discrete Element Method (DEM) can be used in case of granular assemblies which was developed by Cundall and Strack (1979). In DEM the soil can be simulated as a group of discrete elements. Each particle has its own displacement which can be determined from Newton's second law in every calculation cycle.

During our investigation we created three soil-models with different mechanical properties using the PFC2D software. Numerical direct shear tests were performed to calculate the soil’s cohesion and the internal friction angle. After that a lot of analyses were created to investigate the soil-rigid wheel contact and to measure the vertical sinkage of the wheel. Finally the results of the numerical tests were compared to the theoretical values.

2. Materials and methods

Theoretical sinkage of the rigid wheel

Bekker was the first who investigated the soil-wheel interaction. His experience was that a pneumatic tyre with sufficiently high pressure has small deformation and acts as a rigid wheel. In this case the sinkage of the wheel can be calculated as follows (Bekker, 1960):

$$z = \left[\frac{3 \cdot N}{(3 - n) \cdot b \cdot k \cdot d^{0.5}} \right]^{\frac{2}{2n+1}}, \quad (1)$$

where $N [N]$ denotes the vertical load, $b [m]$ is the width and $d [m]$ is the diameter of the wheel. There are two constants ($n [-]$ and $k [Pa \cdot m^{-n}]$) which depend on soil behaviour. The k stiffness constant can be calculated with the (2).

$$k = \frac{k_c}{b} + k_\phi. \quad (2)$$

Table 1. The mechanical parameters and the stiffness-constants of the three soil (McKyes, 1985).

Description / Stiffness constant	Unit	Soil-type nr. 1	Soil-type nr. 2	Soil-type nr. 3
Cohesion (c)	kPa	1.7	4.8	11.0
Internal friction angle (ϕ)	°	29.0	20.0	25.0
k_c	$Pa \cdot m^{-(n-1)}$	5.0	52.0	11.0
k_ϕ	$Pa \cdot m^{-n}$	1514.0	1127.0	1802.0
n	-	0.7	0.9	0.7

The $k_c [Pa \cdot m^{-(n-1)}]$ and $k_\phi [Pa \cdot m^{-n}]$ parameters are stiffness constants as well which are independent from the tyre’s width, but depend on the soil’s cohesion

and internal friction angle, respectively. This theory was summarised by Sitkei (1967) and McKyes (1985) as well. The values of these two constants can be found in Appendix 4 of McKyes (1985). Three types of soil were chosen from there, their parameters are shown in Table 1. The theoretical sinkage of the rigid wheel with given geometrical dimensions can be calculated with these parameters.

The properties of the discrete element models

Modelling the soil-wheel interaction in 2D the PFC2D discrete element software was used. First a box was created with given size, after that 5000 particles were generated to random positions within the box. To reach the porosity of 0.15 the radius of the discrete elements were multiplied. In Table 2 the geometrical values were summarized which were used in numerical direct shear tests and soil-wheel interaction simulations.

In PFC only non-deformable elements can be generated. The material properties can be simulated by using the most suitable contact model in the calculations so it is important to install the correct contact’s type between the particles. To simulate the soil’s cohesive behaviour the Parallel Bond model was used which was extended by Potyondy and Cundall (2004). With these two springs (the so-called parallel springs) the discrete elements can give tensile load to each other. To install the parallel bonds stiffness-, strength parameters and the parallel bond radius have to define in normal and shear direction as well. In addition each elements have its own stiffness, density and friction coefficient which are necessary to adjust before starting the simulation.

Table 2. The geometrical parameters of the simulations.

Geometrical parameters			
Walls (box and rigid wheel)			
		Direct shear test	Soil-wheel interaction
Length of the box	mm	50.8	300.0
Height of the box	mm	60.0	60.0
Width of the box	mm	60.0	40.0
Diameter of the wheel	mm	-	160.0
Width of the wheel	mm	-	40.0
Balls			
Number of balls	-	5000	
Radius	mm	0.27...0.61	0.66...1.5

After setting up the geometrical and mechanical parameters of the elements the numerical direct shear tests were performed. The box was loaded vertically

with different forces and the top section of the box was moved with the speed of 0.005 m/s. During the simulations the box’s vertical position and the shear force was measured. From the results the cohesion and the internal friction angle of the soil-model can be calculated as it is described by MyKyes (1985). Our goal was to calibrate the 11 contact parameters (shown in Table 3.) to the three chosen cohesion and internal friction angle values (see Table 1.).

Table 3. The mechanical parameters of the three soil model.

Mechanical parameters				
Walls (box and rigid wheel)				
Speed of the wheel	m/s	0.005		
Normal stiffness	N/m	1·10 ²⁰		
Shear stiffness	N/m	1·10 ²⁰		
Balls				
Friction coefficient	-	0.5		
Density	kg/m ³	1900		
		Soil type nr. 1	Soil type nr. 2	Soil type nr. 3
Ball normal stiffness	N/m	7·10 ⁶	4·10 ⁶	1·10 ⁷
Ball shear stiffness	N/m	7·10 ⁶	4·10 ⁶	1·10 ⁷
Parallel Bond normal stiffness	Pa/m	7·10 ⁶	4·10 ⁶	1·10 ⁷
Parallel Bond shear stiffness	Pa/m	7·10 ⁶	4·10 ⁶	1·10 ⁷
Parallel Bond normal strength	Pa	2·10 ⁵	1·10 ⁵	5·10 ⁵
Parallel Bond shear strength	Pa	2·10 ⁵	1·10 ⁵	5·10 ⁵
Parallel Bond radius	-	0.5		

After the direct shear tests a wider box was created to investigate the soil-wheel interaction with DEM. First the initial geometry was generated after that the calibrated contact parameters were added to the model. Finally the wheel was simulated as a rigid wall and was compressed to the soil with different vertical forces. During these simulations the tyre’s sinkage was measured and exported to evaluation.

3. Results and discussion

Results of the three numerical direct shear tests

The results of the direct shear simulations are shown in Figure 1...3 where the shear force was illustrated according to the x displacement of the box’s top side. In case of each normal loads (210 N, 345 N, 480 N, 615 N, 750 N and 1000 N, respectively) a point can be determined where the value of the shear force is not changing sufficiently from, so the average value of the shear force can be calculated from that point.

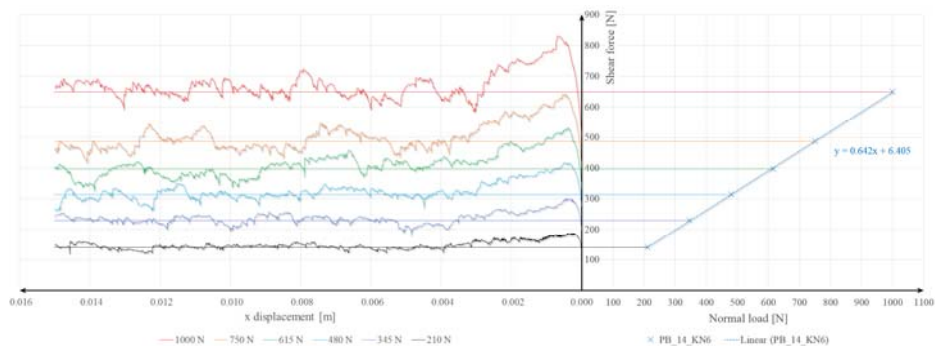


Figure 1. The results of the numerical direct shear tests in case of soil-type nr. 1.

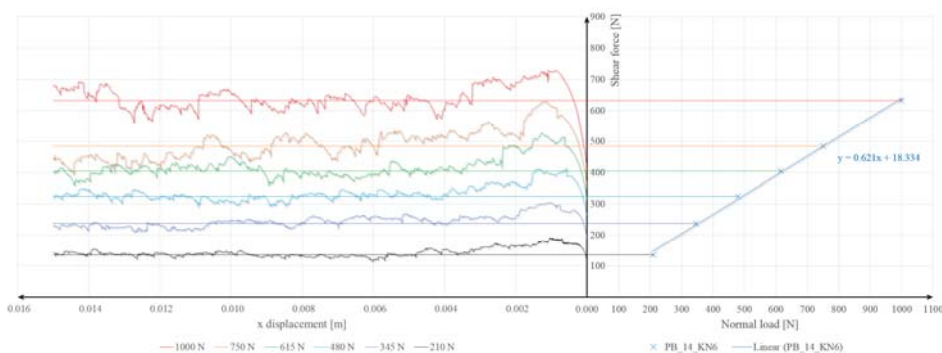


Figure 2. The results of the numerical direct shear tests in case of soil-type nr. 2.

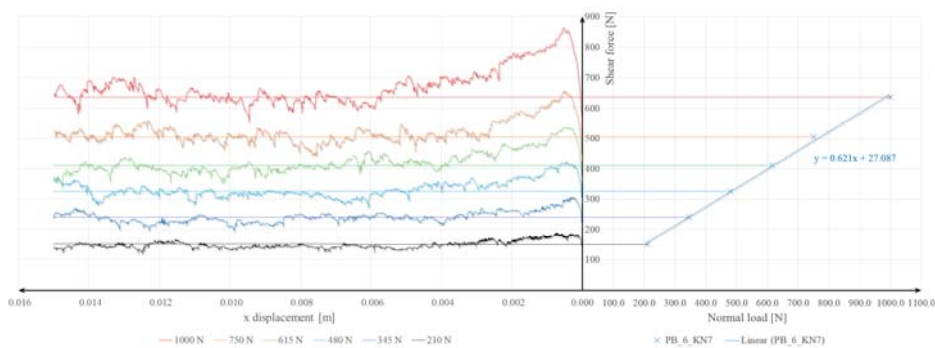


Figure 3. The results of the numerical direct shear tests in case of soil-type nr. 3.

On the right side of the above presented figures these average shear force was illustrated according to the normal load. Using the so-called Wald-method a line can be fitted to these points and the mechanical parameters of the soil can be calculated. The intersection of the line and the vertical axis defines the cohesion and the angle of the line and the horizontal axis defines the internal friction

angle of the soil-model. The results were summarised in Table 4 where the chosen values (see Table 1.) were represented in parentheses. In case of soil-type nr. 1 the cohesion and the internal friction angle is very close to the values in Table 1. So it is predictable to get results from the soil-wheel interaction calculations close to the theoretical values. In the other two cases the mechanical parameters were similar to the chosen values as well.

Table 4. The calculated mechanical parameters of the three soil-model.

Description	Unit	Soil-type nr. 1.	Soil-type nr. 2.	Soil-type nr. 3.
Cohesion (c)	kPa	1.78 (1.7)	5.09 (4.8)	7.52 (11.0)
Internal friction angle (φ)	°	32.70 (29.0)	31.84 (20.0)	31.84 (25.0)
Relative error of the cohesion	%	4.7	6.0	31.6
Relative error of the internal friction angle	%	12.8	59.2	27.4

Results of the soil-wheel interaction calculations

The rigid wheel was compacted to the soil-model with the loads of 5 N, 10 N, 15 N, 20 N, 25 N, 30 N, 50 N, 100 N, 150 N, 200 N, 250 N and 300 N, respectively. Then the sinkage was measured and represented according to the vertical load (see on Figure 4...6.). A trend-line can be fitted to the simulation’s results as well and that line have to be compared to the theoretical line which can be drawn using Formula 1.

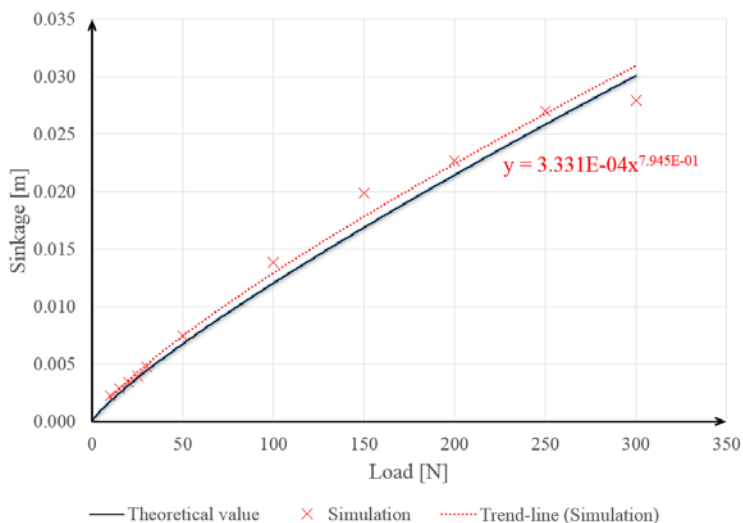


Figure 4. The results of the soil-wheel interaction calculations in case of soil-type nr. 1.

In case of soil-type nr. 1 we got the predicted results. The sinkage from the simulations are very close to the theoretical values and the tendency of the line is similar to the theoretical line as well. In the other two cases there were greater errors in the results which can be accounted for the errors of the mechanical parameters. However it can be seen that the vertical force in the range of 0...300 N cause approximately same sinkages to the ones that can be calculated with the Bekker-formula. Only the lines' tendency are not exactly the same to the theoretical lines because of the errors of the internal friction angles.

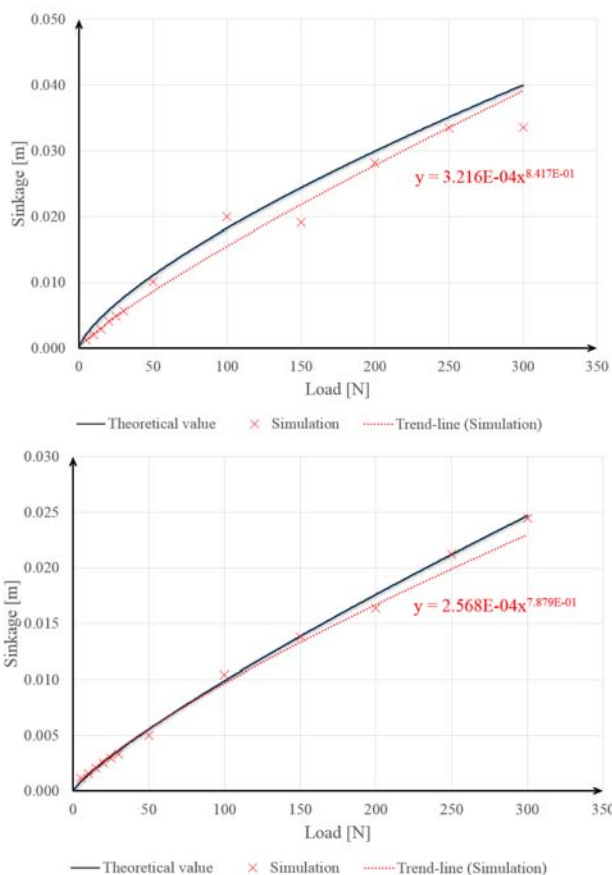


Figure 5. The results of the soil-wheel interaction calculations in case of soil-type nr. 3. (left) and in case of soil-type nr. 3. (right).

Conclusions

During our work the Discrete Element Method was used to model the soil-wheel interaction under different loads. Our goal was to prove that DEM is a permanently useful method in soil-mechanic simulations by comparing the rigid

wheel's sinkages to the theoretical values. These can be calculated by using the Bekker-formula.

First three types of soil-model was created using the PFC2D discrete element software. Simulating the cohesive behaviour of the soils the so-called Parallel Bond contact model was used. The mechanical attributes of the models (including cohesion and internal friction angle) were determined by performing numerical direct shear tests. Our goal was to set up these parameters close to the three values which were chosen from the Appendix 4 of McKyes (1985).

After that a rigid wheel with the given geometrical dimensions was compacted to the soil-models with different vertical loads. The results of these simulations show that the wheel's sinkage follows closely the theoretical values if the soil's mechanical attributes are corresponding. If they are not, the simulation results can be used only in the given range for further calculations.

Summarized the Discrete Element Method is an excellent numerical simulation method to model the soil's behaviour correctly.

Nomenclature

z	sinkage of the rigid wheel	m
b	width of the wheel	m
d	diameter of the wheel	m
N	vertical load of the wheel	N
n	soil-constant	-
k	soil stiffness constant	$\text{Pa}\cdot\text{m}^{-n}$
k_c	soil stiffness constant	$\text{Pa}\cdot\text{m}^{-(n-1)}$
k_φ	soil stiffness constant	$\text{Pa}\cdot\text{m}^{-n}$
c	cohesion of the soil	kPa
Greek letters		
φ	internal friction angle of the soil	$^\circ$

References

- [1] Bekker, M. G. (1960), Off the road locomotion: research and development in terramechanics, Univ. Of Michigan Press, Ann Arbor.
- [2] Cundall, P. A. and Strack, O. D. L. (1979), Discrete numerical model for granular assemblies, *Geotechnique*, 29(1), pp. 47-65.
- [3] MyKyes, E. (1985), *Soil Cutting and Tillage*, Elsevier, New York.
- [4] Potyondy, D. O. and Cundall, P. A. (2004), A bonded particle model for rock, *International Journal of Rock Mechanics & Mining Sciences*, 41, pp. 1329-1364.
- [5] Sitkei, Gy. Dr. (1967), *A mezőgazdasági gépek talajmechanikai problémái*, Akadémiai Kiadó, Budapest.

Developing a precise soil model by DEM

K. TAMÁS, J. RÁDICS, I. J. JÓRI

Department of Machine and Product Design,
Budapest University of Technology and Economics

Abstract

Using Discrete Element Method (DEM) have been carried out to investigate the effect of cohesion in the virtual soil. Virtual DEM models were developed in correspondence with the real tests. The conventional approach to explore the mechanical behaviour of soil mainly relies on experimental shearing tests under laboratory conditions. The implementation of DEM is carried out by a series of numerical triaxial tests on granular assemblies with varying confining pressures and bond conditions. The results demonstrate that the numerical simulations can produce correct responses of the soil behaviour in general, including the critical state response, as compared to experimental observations using the Mohr circles. The influence of cultivator sweep geometry was researched by DEM in 3D and were correlated with the soil bin tests results.

Keywords

DEM Model, Draught, Soil, Tillage, Force

1. Introduction

The mulch cultivators get more importance recently. Due to the high fuel prices and the need to preserve and improve the soil state are raising the importance of conservation tillage tools and practices. Development of cultivator tool geometry has a high importance because the expected working parameters like loosening and mixing can only be achieved by determining exactly the relations of tool geometry and work quality.

DEM is a discontinuous numerical method based on molecular dynamics. It was developed and applied for analyzing rock mechanics by Cundall in 1971. The soil which is cut or separated by soil engaging components is much more discrete, therefore DEM is an ideal method to analyze large discontinuous deformations of soil (Rubinstein and Shmulevich, 2006).

DEM appears to be a pertinent complementary tool for studying unsaturated soil mechanics (Bojtár and Bagi, 1989). The analysis of the dynamic mechanical behavior of cohesive soils subjected to external forces is very important in designing and optimizing the tillage tools. Cohesive soil contains water and the presence of water and other living components can produce cohesion between soil particles.

2. Materials and Methods

Experimental study of soil–tool interaction is expensive and may be limited to certain cutting speeds and depths. However, with increasing computational power and the development of more sophisticated material models, Discrete Element Models shows more promise in analyzing the factors of soil–sweep interaction. Aim of this research was to analyze the applicability of DEM (Discrete Element Method) to evaluate the soil mechanical properties and the tool draft force. The first study was to explore the use of DEM Method to deal with a specific particle bonding with the comparison of the soil bin test results (Tamás and Jóri, 2008).

Field experiments have shown that the β angle and cutting speed have significant effect on sweep tools work quality (Fenyvesi and Jóri, 2004), The influences of cultivator sweep geometry (mainly the β angle) were examined by DEM in 3D.

The Parallel-Bond

DEM is a numerical technique in which individual particles are represented as rigid bodies. Each particle can be in contact with neighboring particles or structure boundaries. The two particles are treated spheres (3D). These bonds establish an elastic interaction between particles that acts in parallel with the slip or contact-bond models. Thus the existence of a parallel bond does not preclude the possibility slipping. Thus parallel bonds may contribute to the resultant force and moment acting on the two bonded particles.

Shear Box Test Process

At first, the relevant behaviors of the intended physical material have to be determined (Terzaghi, 1943). Then the appropriate microproperties have to be chosen. During the calibration process in which the responses of the synthetic material are compared directly with the relevant measured responses of the intended physical material with the values of Parallal Bond model (normal and shear stiffness (stress/displacement); normal (σ_c) shear strength τ_c (stress) and bond radius (R.).

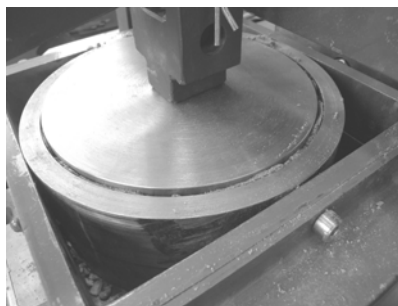


Figure 1. The Shear Box Test

The shear box was filled up with the sampled soil from the soil bin, and it was prepared by a compaction with a vertical force through a simple weight applied on the top plate. Because of this constant force, the sample could deform in vertical direction during the test. The measurement process was preceded by applying a vertical force on the upper half of the box at a constant (small) speed while the lower half was fixed (Fig 1.). This force gradually increases till the box moves, and value was measured by a strain gauge. After the horizontal force reaches its maximum it stays more or less constant, or it may slowly increase or decrease (McKyes, 1985).

The triaxial-test

Shear test simulations made with the discrete element method were used a three-dimensional tri-axial box, see, where the left and bottom walls are fixed. Stress- or strain controlled deformations were applied to the side- and top walls, respectively.

First step of the study was to generate the particle assembly of the soil sample to get a parallel bonded fine-resolution soil. The sample had a height of 63.4 mm and a width of 31.7 mm and particle size distributions bounded by R_{min} and R_{max} , with $R_{max} = 1.66 * R_{min}$ by defining the soil type with the particle distribution.

In the triaxial test simulations, the top wall was moved downwards with a constant speed, while the motion of the side walls were controlled by a constant stress attribute, resulted from the forces of the material in the box.

Comparing the test results of the real and the virtual samples, the parameters of the virtual model could be compared to the soil mechanical parameters: Young modulus, Poisson ratio, density, friction, cohesion and internal friction angle.

Results and Discussions

The material properties and the iteration process in DEM

To get such results, the basic Mohr–Coulomb criterion can be used to control shear behaviour at contacts between the discrete elements (Fig 2.). However, there is extensive work on the constitutive modelling used in DEM to study soils.

For codes such as PFC that synthesize macro-scale material behaviour from the interactions of microscale components, the input properties of the microscopic constituents are usually not known (Itasca, 1999).

In the following, only spherical particles were used. The recently developed micro–macro setting procedure was useful to understanding the macroscopic powder flow behaviour on microscopic foundations. Besides the experimental verification of the simulation results a DEM material model should allow to predict experimental results.

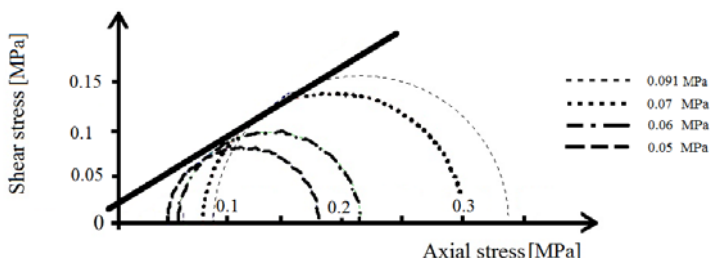


Figure 2. The Axial Stress-Strain and the resulted Shear Stress on confinements (0.05, 0.06, 0.07, 0.091 MPa).

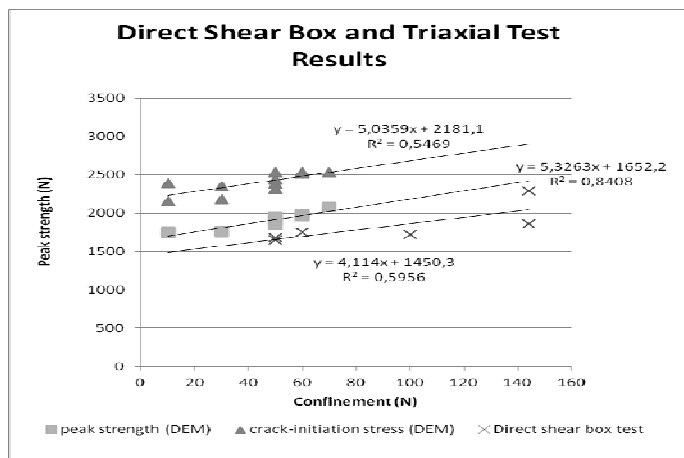


Figure 3. The results of the triaxial and direct shear box test.

The volume change of a typical simulation with cohesion, shows first compression, then dilatancy, where the side pressure is five times higher. At the same time, the stress response becomes more and more anisotropic. The vertical stress increases until it reaches a maximum, indicated by an arrow, while the horizontal stress remains constant (Fig 3.).

The peak stress value increases with the microscopic cohesion or adhesion force. From the macroscopic point of view, the flow behaviour of the system can be examined by plotting Mohr-circles for different confining pressures and for the maximum stress. The tangent to these circles can be seen as the flow function for the peak stress. The flow function is linear for the examined parameters with a slope slightly larger than expected from the microscopic friction at the contacts alone.

The results of each triaxial test stress and volumetric strain versus axial strain curves with different confinement. In the triaxial tests the compressive force that was act on the shear box contacted surface under the measurement process was: 24052,818 mm². We can see the similarity of the shear box test and the triaxial test Parameters and can use the most similar micro parameters in our test.

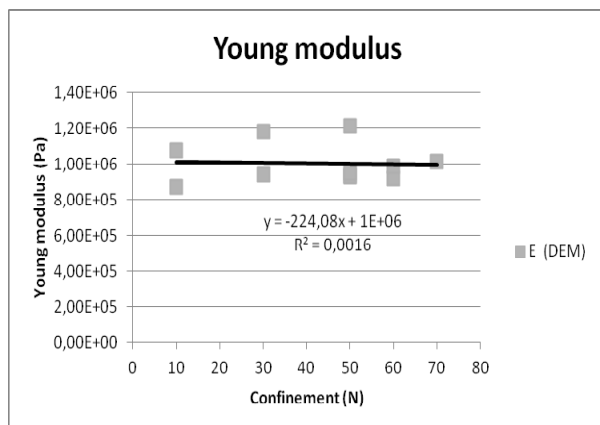


Figure 4. The resulted Young modulus in each confinement and the average value ($E=1e6$ Pa).

Using the results of the triaxial test (the peak strength and confining stress) the Mohr's circles were defined. Touching the circles the Coulomb line was draw. The angle of the line and the x axis defined the internal friction angle. The intersection of the Coulomb line and the y-axis defined the cohesion.

In the triaxial test by DEM can define the Young modulus (Fig 4.) and Poisson ratio (Fig 5.) beside the cohesion and the internal friction angle. The moor values defined the better DEM parameter set could be done.

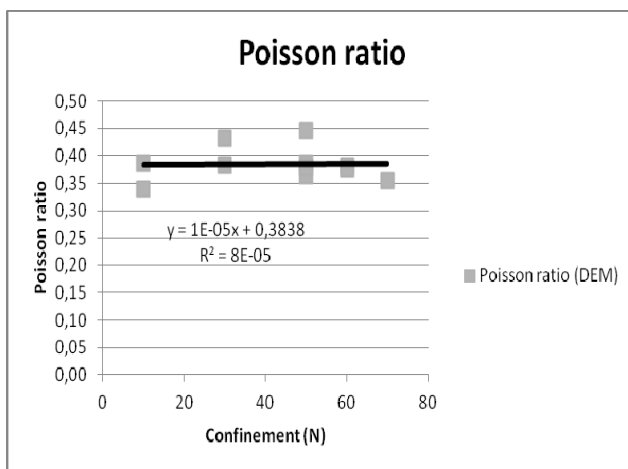


Figure 5. The resulted Poisson ratio in each confinement and the average value ($\nu=0,38$).

The cohesion is 12,3 kPa and the internal friction angle is 21° . This soil mechanics property following the real triaxial tests is a kind of loamy clay. In

the validation of these tests with the shear box test results was define the same material properties. With this process can be harmonize the real and the numerical methods.

Simulation of the loosening process by DEM

The main dimensions of the 3D model: the shank length was 256mm, the sweep width was 85mm, the γ angle was 63° , the β angle was 30° , the box of granular material length was 300mm and the height was 100mm, the cutting depth was 200mm. The box length is enough on this research, because give appropriate result to analyse the draft forces. A lot of Discrete Element Models were run. Most of the analyses were carried out through full length blade displacement in the horizontal plane along the X -axis direction. To verify the behaviour of the soil in front of the cutting blade, several analyses were run in different rake angles and speed.

Table 1. The 3D DEM Model parameters

Parameter in DEM	Value
Bulk density (kg/m^3)	1850
Particle shape	Ball
Normal spring coefficient (K_n) [N/m]	2,00E+07
Tangential spring constant (K_s) [N/m]	1,00E+07
Coulomb damping (μ_g)	0,3
Friction coefficient between particles (μ)	0,5
damp viscous normal [Ns/m]	0,7
damp viscous shear [Ns/m]	0,7
Particle radius distribution [mm]	23,44-39,07
Friction coefficient between particle and the sweep tool	0,6
	0,4595
Void ratio	
Parallel-Bond (Result of the synthesis)	
pb_rad	1
pb_kn (Pa/m)	2,00E+04
pb_ks (Pa/m)	1,00E+04
pb_nstren (Pa/m)	2,00E+03
pb_sstren (Pa/m)	1,00E+03
Time step of the calculation (Δt) (s)	4.0×10^{-5}

The calibrated micro-properties were used (Table 1.) in soil-tool DEM simulations and the results compared to experimental measurements and observations. With the CAD (Computer Aided Design) support function the tool geometry could imported from any CAD system. Under the measuring process a

programmed „routin” collecting the draft force x components of each triangle element that was used by STL format. With this method the Soil-Tool Interaction Model is well build to use other tool geometries.

The sweep initial depth was $h = 200$ mm and the rake angle $\beta = 30^\circ$. Snapshots were taken at displacement increments of full length. The predicted shape of the sweep that forms in front of the blade corresponds well to the experiment. Analytical methods do not allow predicting precisely the tool forces.

The DEM tests were repeated with different sweep speeds (2,3,4,5,6 m/s) and rake angles (5° , 10° , 15° , 20° , 30°). The draft forces were recorded and compared to the soil bin results. The force on the cultivator tool can be calculated using plasticity theory and the soil stresses in front of the sweep share.

There is a good agreement for measured draft forces but, there were different between the DEM and the measured forces. The reason for this might be the iteration process was not appropriate. To develop the micro- macro properties and its values, further tests need.

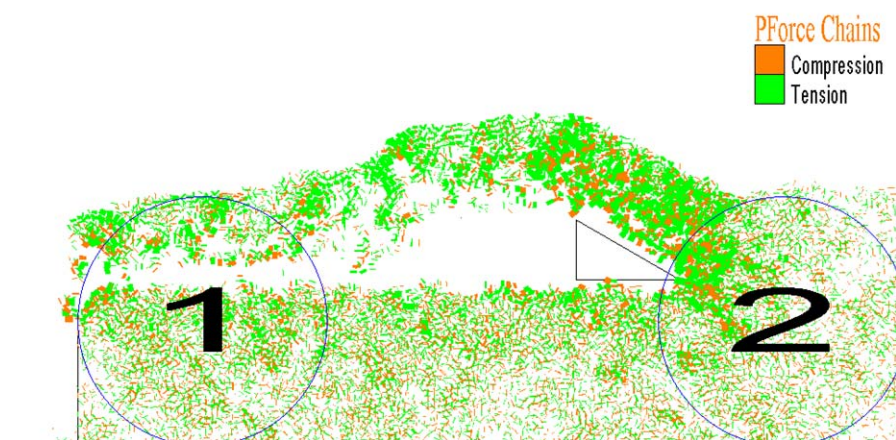


Figure 6. The von Mises stress created with the sweep tool of a rake angle β of 30° (a) and the lines of parallel bonds forces and the measure spheres (nr.1: before, nr.2: after the loosening)

The advantage of DEM simulation is that it provides information on the distribution of the horizontal and vertical forces along the soil-tool interface. Moreover, these results may help understand the mechanism that causes the distribution under the loosening process (Fig. 6.). The investigation of this tillage mechanism is so important because in the draft force prediction these forces were summarised. These total forces were record in this research. The DEM system seems to be a promising approach by the resulted datas and pictures to analyse the results in qualitative view.

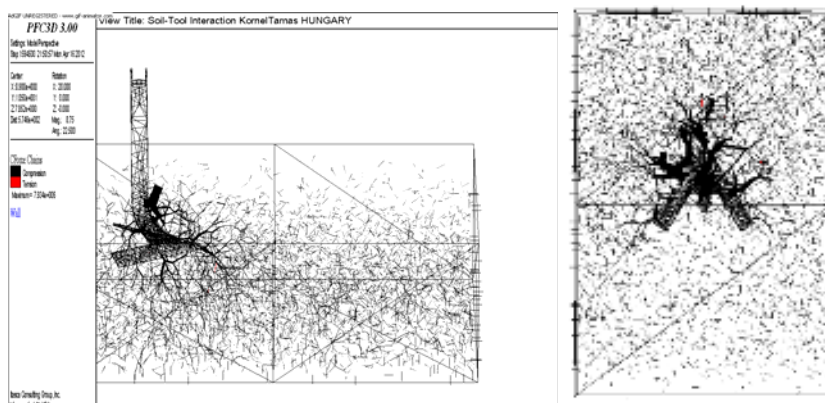


Figure 7. The force structure and its distribution under the soil surface a view in 3D and on the right the top views in different times (17,1s and 21,3s).

A series of models were analyzed with various soil properties, speed and rake angles using PFC3D Code. The results showed the significant effect (Fig.7.) of the tool rake angles and working speed on cutting forces in 20 cm depth. In this research between the two extremities (2,0-4,0 m/s and, 5°-30°) the results are parabolic. The parallel bonds produce cohesive forces between discrete particles, so parts of discrete particles are conglomerated and form particle aggregate clusters after the tillage process (Fig. 8.). The complete model is formed by bonding of elements in wide sizes.

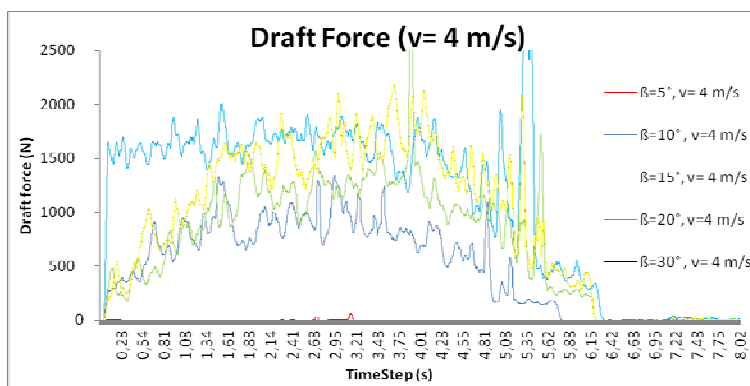


Figure 8. The influence of the speed (4,0 m/s) by DEM ($\beta=5^\circ, 10^\circ, 15^\circ, 20^\circ, 30^\circ$) in 20 cm depth.

When the maximum normal stress exceeds the normal bond strength, or the maximum shear stress exceeds the shear bond strength, the parallel bonds between the contact particles within the particles rupture. In the tillage process, the resulted clusters break and divide into smaller clusters or discrete particles.

That means, the clusters rupture and separate into more discrete particles with the tool tillage.

Conclusions

In the DEM numerical approach the parallel-bond contact was used to describe the behavior of the discontinuous, cohesive soil during soil-tool interface process. After the triaxial test method with which the micro to macro properties of the soil were validated. The simulations show that particle properties have a great effect on the soil stress-strain behaviour. Using the calibrated material parameters, a cultivator sweep moving through „soil” grains were modelled and the results compared to experimental results. In case the set of the appreciable parameters in DEM synthetic material with parallel- bonds between the particles, we can synchronizing the virtual triaxial test (micro properties) and could be compared directly with the measured response of the physical material.

Results show that during the initial stages of tool displacement, Discrete Element Method can predict the draft forces with irrelevant errors of 4-7%. Under the cutting process in 20 cm depth when the speed is increasing the draft force is increasing. If the β angle is increasing the draft force is increasing parabolic as well.

It can be concluded that the results of the discrete element method can accurately predict the tool forces in non-homogeneous soils and for the investigation of soil loosening and sweep performance. The model can be used in development procedures of soil loosening tools, reducing the number of soil bin and field test.

Acknowledgements

The authors wish to acknowledge for the Hungarian Institute of Agricultural Engineering Gödöllő and the grant from National Office for Research and Technology. These researches were partially supported by the Hungarian Research Fund, under grant no. OTKA 48906.

References

- [1] Asaf, D. Rubinstein, and I. Shmulevich (2006). Evaluation of link-track performances using DEM, *Journal of Terramechanics*. Vol. 43, pp 141–161.
- [2] Bojtár, I., and K. Bagi (1989). “Analysis of the Satake- and Cundall-Parameters of Granular Material sin Non-Linear State-Changing Processes,” in *Powders and Grains*, pp. 275-278. J. Biarez and R. Gourvés, Eds. Rotterdam: A. A. Balkema.

- [3] Fenyvesi, L.-Jóri J.I. (2004). Newest experiments with active soil tillage tools. cigr beijing. proceedings of session iv. of 2004 cigr international conference. china agricultural science and technology press. 102-106P. (Hungarian)
- [4] Itasca (1999). PFC2D theory and background manual Version 2.0. Available from: <http://www.itascacg.com>
- McKyes, E., (1985). Soil Cutting and Tillage. Elsevier, Amsterdam, Netherlands.
- [5] Mouazen, A.M., Nemenyi, M., (1999). Finite element analysis of subsoiler cutting in non-homogeneous sandy loam soil. Soil Till. Res. 51, 1–15.
- [6] Tamás K. Jóri J. István (2008). Measuring Cart Development for Soil Bin Test. Soil Tillage – New Perspectives – Book of Abstract, ISTRO – Branch – Czech Republic, 5th International Conference, Brno pp. 41
- [7] Terzaghi, K. (1943): Theoretical Soil Mechanics.

Energetic investigation of microwave treatment

P.V. R. KOVÁCS¹, S. BESZÉDES², L. LUDÁNYI²,
C. HODÚR², G. KESZTHELYI-SZABÓ²

¹Department of Engineering, Faculty of Engineering, University of Szeged,

²Department of Process Engineering, Faculty of Engineering, University of Szeged,

Abstract

Microwave (MW) irradiation as a method for sludge treatment has gained widespread popularity, mainly due to enhance biodegradability and increase yield of biogas. In this study energetic investigation of MW treatment was carried out using whey as test substance. Treatment was performed in a continuous flow treating system at different irradiation power levels, whey concentrations and flow rates. Experiments indicated that pre-treated whey gave higher yield of biogas compared to untreated whey. Moreover, the results of this study demonstrated that the flow rate and the duration of treating caused perceptible difference in yield of biogas. The most energy-efficient treatment was at low flow-rate, low power of magnetron, low treating time.

Keywords

microwave pre-treatment, biogas production (BP), anaerobic digestion

1. Introduction

Anaerobic digestion is an effective way of treating wastewater for yielding profitable biogas and alleviating environmental concerns. It consists of several processes in which the biodegradable materials are broken down in oxygen-free environment. The main features of AD process are mass reduction, biogas production and improved dewatering properties of the treated sludge.

Wastewater sludge has theoretically high biogas yield, but the degree and the rate of anaerobic digestion is limited by macromolecules and other chemical components. In order to access the energy potential of the materials, large organic polymers must firstly be broken down to their smaller components. Due to this fact however, anaerobic digestion has a great future amongst the biological technologies of sludge treatment, the low overall biodegradation efficiency of the sludge solids and long retention times result in only moderate efficiencies.

Most soluble organic materials which can be converted into biogas are produced during hydrolysis process, but it is identified as the rate-limiting step (Ghyoot and Verstrate, 1997). Consequently, the biogas production depends for the most part on the biodegradability and hydrolysis rate (El and H.E., 2003).

Pre-treatment of sludge to break down its complex structure can be used for enhancing anaerobic digestibility in order to lyse sludge cells further to facilitate hydrolysis. Thermal, chemical, biological and mechanical processes as well as different combinations of them have been studied as possible pre-treatments. Thermal treatments can be highlighted as no additional chemicals needed and they can be controlled easily. Microwave pre-treatment was found to be superior over the thermal treatment with respect to sludge solubilization and biogas production. (Beszédes et al, 2011)

2. Methods

Whey samples

Whey is a by-product of cheese production. It is one of the components that separates from milk after curdling. Cheese whey can be used in many ways; supplied as feed for animals is the most common practice because of its nutritional value. Lactose and whey protein can be recovered separately and be further used for other applications. High value-added products or nutrients that can be derived or recovered from cheese whey, there are certain disadvantages inhibiting these practices to be fully applied. The major disadvantages are its high content in water that must be removed and the high energy cost to process and dry and the competitive products already available in the market. However, markets are developing continuously, there is still a surplus of whey produced above and beyond the market for whey products. In this respect, the anaerobic digestion of cheese whey is a cost-effective configurations for the cheese producers who owe to dispose the wastewater safely and, at the same time, could benefit directly from the energy recovered in the form of biogas. (Antonopoulou G., et. al.)

Two concentrations of whey were examined. One of these is the original whey (whey) coming from a milk-processing factory (Szeged, Hungary), and the other is concentrated by membrane separation (concentrate). The ingredients of the samples can be found in Table 1.

Table 1. Ingredients of examined whey

	Protein [%]	Lactose [%]	Fat [%]	Total solids [%]
Whey	0.47±0.13	2.61±0.04	0.18±0.01	3.24±0.07
Concentrate	0.73±0.16	3.59±0.09	0.34±0.08	5.36±0.24

Microwave pre-treating system

Microwave pre-treating system contains a water-cooled, variable-power magnetron operating at 2450 MHz. High-voltage power supply feeding the

magnetron consists of two transformers, one of them produces cathode heating voltage and heating current, the other produces the anode voltage which can be controlled by the primary circuit of an external auto-transformer. With this device the power of the magnetron can be set as well. Electromagnetic energy of the magnetron spread over a resonant slot. Getting through this slot the energy gets in the toroidal resonator. (Kovács et al, 2012). During the operation of toroid resonator energy is given to the treated material. As a result of energy transmission the temperature of the material rises and the dielectric properties change continuously. The effect of the microwave energy intake, variable power, impedance and dielectric relationships are formed in the microwave resonator. Some of these can be measured (eg. power dissipation, reflected power), some of them can only be determined by calculation, knowledge of the other parameters (J. Zhu et al, 2007). Material is transferred in the continues-flow microwave treating system by a membrane pump with variable flow.

There is a dielectrometer attaching to the system. The material can flow through the waveguide of this measuring equipment in a Teflon tube. Electric signal of the dielectrometer, the inlet and outlet temperature of the material are received by the measurement data collector and recorded on-line by software and displayed in the computer screen. (Kovács et al, 2013)

Microwave pre-treatment

Treatments were carried out at different powers of magnetron, at different flows, and different treating numbers. Three levels from these parameters were used and combined (Table 2.).

Table 2. Microwave pretreatment conditions

Number of sample	Treated material	Flow [l/h]	Power of magnetron [W]	Number of treatings	MW irradiation time [s]	Energy demand [kJ]
1	Whey	6	350	1	300	105
2	Whey	6	600	1	300	180
3	Whey	6	850	1	300	255
4	Whey	15.5	350	1	120	42
5	Whey	15.5	600	3	702	421,2
6	Whey	15.5	850	1	120	102
7	Whey	25	350	5	1080	378
8	Whey	25	600	1	72	43,2
9	Whey	25	850	5	1080	918
10	Concentrate	6	350	5	4500	1575
11	Concentrate	6	850	1	300	255
12	Concentrate	25	350	1	72	25,2
13	Concentrate	25	850	5	1080	918

The energy demand of whey pretreatments was calculated from the power of the magnetron and the time of irradiation.

$$E = P_M \cdot t \quad (1)$$

Fermentation process, biogas measurement

Digestion was performed at mesophilic temperature range (35 °C). Whey samples were inoculated with anaerobic sludge, the whey: fire sludge volume ratio was 4:1.

BOD OxiTop PM manometric measuring system with 12 mini continuously stirred digesters was used for measuring biogas yield. (Fig.1.)



Figure 1. BOD OxiTop PM

3. Results and discussion

Biogas production

In our experiments the effect of intensity of microwave irradiation, volumetric flow and concentration on anaerobic digestion was investigated, which were characterized by cumulative biogas production.

Cumulative biogas production with pretreated and untreated whey is shown in Fig.2.

Biogas production rate was higher for all pretreatment conditions compared to the controls. Concentrates gave the highest biogas yield, but as we can see later, the specific energy demand was worse in these cases, not to mention the energy demand of membrane separation.

For having clearer picture effects of the parameters were investigated. Biogas yield wasn't particularly affected by the power of magnetron, although the higher level was more than double the lower level (Fig.3.).

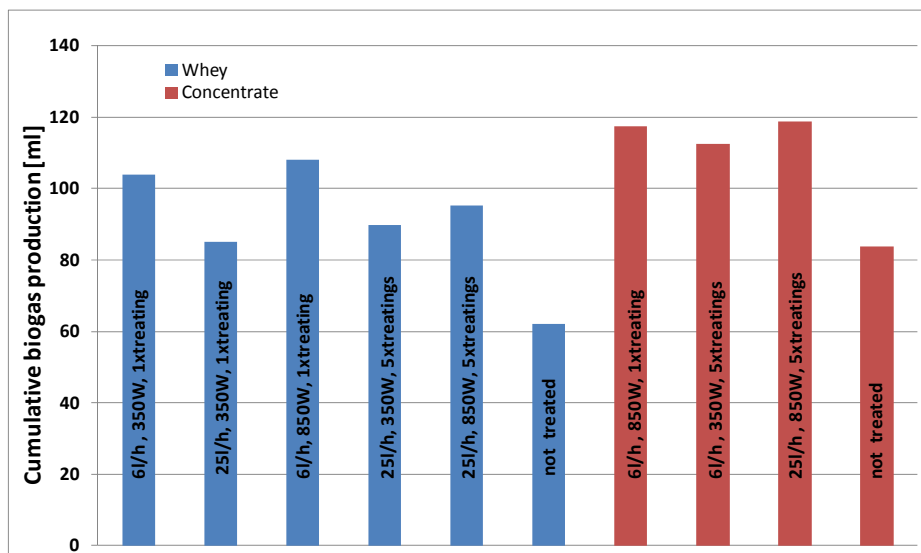
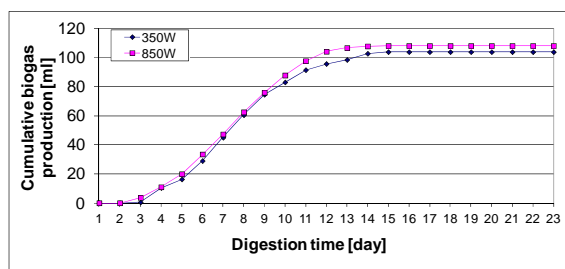


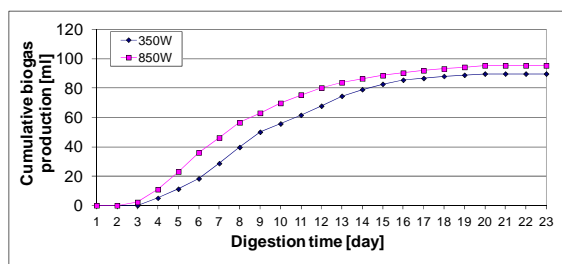
Figure 2. Cumulative biogas production under different conditions

In contrast, changing of flow rate caused perceptible difference in yield of biogas. (Fig.4.)

And as we could see in Fig.2. the difference in concentration also caused differences in the yield of biogas. (Fig.5.)



a)



b)

Figure 3. Biogas production of MW pretreated whey
a) 6 l/h, 1x treating, b) 25 l/h, 5x treatings

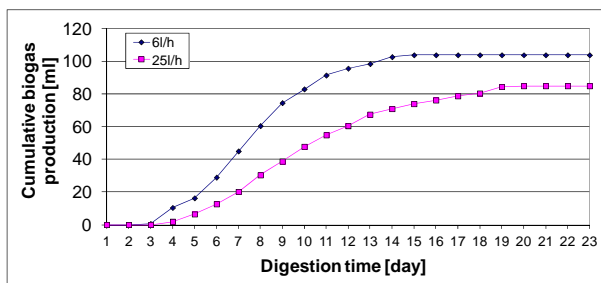
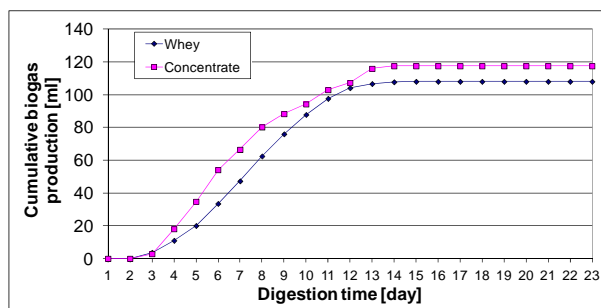
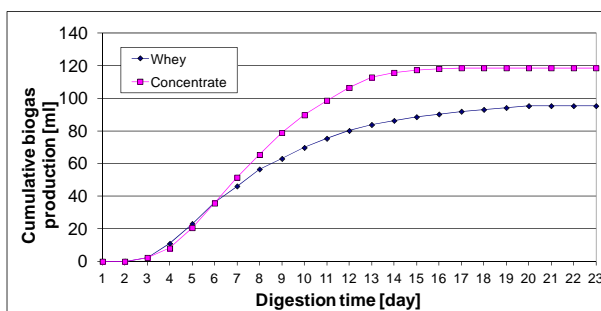


Figure 4. Biogas production of MW pretreated whey (350W, 1x treating)



a)



b)

Figure 5. Biogas production of MW pretreated whey and concentrate
a) 6l/h, 850W, 1x treating, b) 25l/h, 850W, 5x treatments

Specific energy consumption

In fact, previous investigations only provide information on effects of various parameters, however they are useless without energetic analyzes.

Pretreatment conditions and accordingly energy demand were very different, therefore specific energy demand was determined.

$$SED = \frac{E}{BP} \quad (2)$$

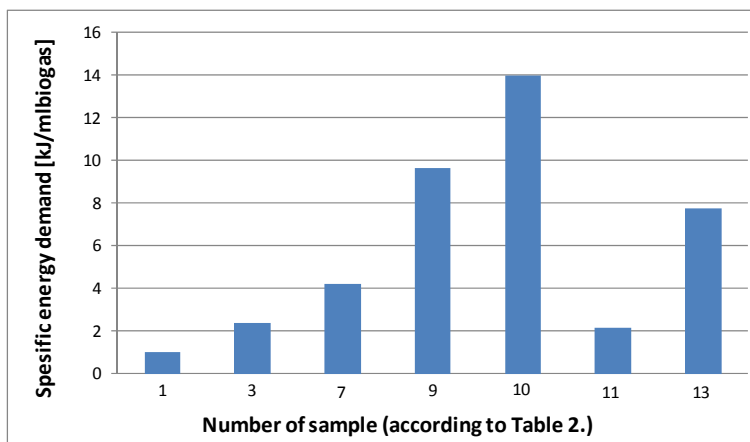


Figure 6. Specific energy demand at different conditions

From energetic investigation of the effect of MW pre-treatment we could identify that the effect of flow rate is the most significant. At sample 1., 3., 11. were the three lowest SEP and at these samples the flow rate was 6 l/h. At only one other sample was the flow rate 6 l/h (at sample 10), but the long treating time (5x treatings) resulted higher SED. This trend can be observed at the other three samples (Sample 7., 9., 13.) treated 5 times.

Thus conclude that the microwave treatment is most effective energetically when low flow rate, low power of magnetron and a small number of treatments are used.

Conclusions

Based on the measurement results we can determine that the biogas yield itself doesn't characterize a pretreatment process, amount of energy investment must be taken to consideration with the use of biogas quantity can be reached.

Nomenclature

E	energy demand of pretreatment	J
P	power	W
t	MW irradiation time	s

Subscripts

M magnetron

Acknowledgements

The authors are thankful for the financial support provided by the Hungarian Scientific Research Fund.(OTKA), under contract number K105021.

References

- [1] Antonopoulou G., Stamatelatou K., Venetsaneas N., Kornaros M. and Lyberatos G. (2008), Biohydrogen and methane production from cheese whey in a two-stage anaerobic process. *Ind Eng Chem Res* 47, 5227–5233
- [2] Beszédes S, László Z, Horváth Z H, Szabó G, Hodúr C (2011), Comparison of the effects of microwave irradiation with different intensities on the biodegradability of sludge from the dairy- and meat-industry *Bioresource Technology* 102:(2) pp. 814-821.
- [3] El-Mashad, H.E.-M.H. (2003). *Solar Thermophilic Anaerobic Reactor (STAR) for Renewable Energy Production Agrotechnology and Food Sciences*. Wageningen University, Wageningen. p. 238.
- [4] Ghyoot W, Verstraete W. (1997). Anaerobic digestion of primary sludge from chemical pre-precipitation. *Water Sci Technol*; 6-7:357-65.
- [5] Kovács P V R, Beszédes S, Ludányi L, Hodúr C, Szabó G (2012), Development of a continuous flow microwave toroidal cavity resonator 11th International Scientific Conference Mma 2012: Advanced Production Technologies, Novi Sad: University of Novi Sad, 2012. pp. 357-360.
- [6] Kovács Róbertné V P, Beszédes Sándor, Ludányi Lajos, Hodúr Cecilia, Keszthelyi-Szabó Gábor (2013) Folyamatosan áramló közeg dielektromos tulajdonságainak mérése *Műszaki Kémiai Napok 2013 Konferencia Kiadvány: Conference of Chemical Engineering Conference Proceeding Veszprém: Pannon Egyetem Műszaki Informatikai Kar Műszaki Kémiai Kutató Intézet*, p. 14.
- [7] J. Zhu, A.V. Kuznetsov, K.P. Sandeep (2007) „Mathematical modeling of continuous flow microwave heating of liquids”, *International Journal of Thermal Sciences*, Vol. 46, 328–341

Elastic behavior of sunflower (*Heliantus annuus*) seeds under constrained compression

I. M. DAL FABBRO, C. DE ALMEIDA,
J. GAZZOLA

Faculty of Agricultural Engineering,
Campinas State University

Abstract

This research work reports the application of the Generalized Hooke's Law to interpret the elastic behavior of sunflower seeds (*Helianthus annuus*) under constrained compression tests at several deformation rates. Results yielded the force and deformation curves from which the energy necessary to compress the constrained granular material was obtained. Compression tests were carried in an Emic DL mechanical press of 30000 N capacity, having the deformation ratios controlled from 15 to 80 mm/minute, with simultaneous force recording. Grain samples were placed into a rigid die of 20 cm height and 8,5 cm diameter to prevent samples to undergo through diametric deformation. Obtained force-deformation curve yielded the energy associated to deformation rate. Also the grain samples were kept under controlled moisture content. The paper conclusions resume the correlation between grain compaction density, compacting energy input and compacting deformation rate.

Keywords

linear elasticity, mechanical properties of vegetative materials, grain mechanical properties, compression energy.

1. Introduction

Adhesive The world production of agricultural grains in the year of 2013 reached the figure of 2,47 billion of tons including 32,391 million of tons of Sunflower. Brazil, in that same year, collaborated with the production of 180,411 million of tons including 92,7 mil of tons of Sunflower (see CONAB, 2013). Oil grain production reached the figure of 13,095 mil of tons of sunflower (see CONAB, 2013). A significant fraction of the oil grain production in Brazil is forward to human consumption, meanwhile a smaller percentage is devoted to industrial use. Handling of such an amount of grains turns to be a complex task, because it involves a diversity of factors as timing deterioration, mechanical damages, deterioration due to fungi and insects attaches, storage moisture and temperature control, storage and transport strategy, etc. Grain compressing

properties are considered important to extrusion, milling process, etc. This research work is particularly devoted in studying grain mechanical properties, emphasizing the linear elastic behavior, neglecting the time parameter influence which also takes part in the establishment of stress and strain relationships. In other words, a simple elastic model will be considered tested.

2. Theoretical background

The pertinent literature is consistent in considering vegetative tissue as to exhibit an ideal behavior i.e. continuous, isotropic and homogeneous, keeping a linear or non linear stress-strain relationship, being also time dependent or not. This is equivalent of saying that such a material exhibits linear or non-linear elastic or even linear or non-linear viscoelastic relationships. Generalized Hooke’s Law states that only four constants, E , ν , G and K are sufficient to determine the linear elastic behavior of a material which holds the above mentioned ideal conditions. It frequently happens to these constants to exhibit time dependence, in which case they are expressed as $E(t)$, $\nu(t)$, $G(t)$ and $K(t)$. These functions can yield, by means of the Laplace Transform, the expressions for $\Phi(t)$ and $\psi(t)$ known as relaxation and creep functions which are included in the analytical viscoelastic models expressed by means of hereditary integrals (see Dal Fabbro et al., 2003; Dal Fabbro et al., 2005 and by Dal Fabbro et al., 2002). The constitutive equation for a linear elastic solid, known as the Generalized Hooke’s Law establishes a linear relationship between the stress and strain tensors involving 81 independent elastic constants, as:

$$\sigma_j = C_{ijklm} \varepsilon_{klm} \quad (1)$$

However, if the above mentioned ideal conditions are maintained, that number is reduced to four constants, known as E (modulus of elasticity or Young’s modulus), ν (Poisson’s ratio), G (shear modulus) and K (bulk modulus). The above equation can be also expressed as:

$$\sigma_{ij} = \frac{E}{1+\nu} \left(\varepsilon_{ij} + \frac{\nu}{1-2\nu} \delta_{ij} \varepsilon_{kk} \right) \quad (2)$$

or

$$\varepsilon_{ij} = \frac{1+\nu}{E} \sigma_{ij} - \frac{\nu}{E} \delta_{ij} \sigma_{kk} \quad (3)$$

Where δ_{ij} is known as Kronecker’s delta which assumes the values of 1 when $i = j$ and 0 when $i \neq j$. It should also be emphasized that σ_{ij} , ε_{ij} and σ_{kk} will

assume the values designated by the indices i , and j ($i, j = 1, 2, 3$). The index k will also assume the values of (1,2,3), however the summation convention should be observed. These four constants keep the following relationship:

$$K = \frac{E}{3(1-2\nu)} \quad (4)$$

$$G = \frac{E}{2(1+\nu)} \quad (5)$$

$$K = \frac{\sigma_{kk}}{\varepsilon_{kk}} \quad (6)$$

$$\varepsilon_{kk} = \frac{\Delta\nu}{\nu} \quad (7)$$

The Generalized Hookes Law gives support to many particular loading cases directed to characterize elastic materials. In the uniaxial stress loading of a testing specimen the following conditions ($\sigma_{11} \neq 0$, $\sigma_{22} = 0$, $\sigma_{33} = 0$, $\varepsilon_{11} \neq 0$, $\varepsilon_{22} \neq 0$, $\varepsilon_{33} \neq 0$) are imposed, yielding the traditional equation known as:

$$\sigma_{11} = E \varepsilon_{11} \quad (8)$$

However, if the conditions ($\sigma_{11} \neq 0$, $\varepsilon_{11} \neq 0$, $\varepsilon_{22} = \varepsilon_{33} = 0$, $\sigma_{22} = \sigma_{33} \neq 0$) are imposed to the Generalized Hooke's Law, which is equivalent to prevent lateral deformations, the final equation will result as:

$$\sigma_{11} = \left(\frac{E}{(1+\nu)} \frac{1-\nu}{(1-2\nu)} \right) \varepsilon_{11} \quad (9)$$

$$M = \left(\frac{E}{(1+\nu)} \frac{1-\nu}{(1-2\nu)} \right) \quad (10)$$

$$\sigma_{11} = M \varepsilon_{11} \quad (11)$$

The rigid die tube test will generate stress in X_2 and X_3 directions but will not allow deformation at these same directions. If the modulus of elasticity E and M values are obtained respectively, from the uniaxial and rigid die tests, the value of ν can be obtained from the above equations (see Hughes & Segerlind, 1972), (see Dal Fabbro, 1979). These both tests, uniaxial and rigid die will generate an $\sigma_{11} \times \varepsilon_{11}$ curve, holding E and M as line coefficient, respectively (as illustrated on Figure 1) and (see Figure 2), respectively.

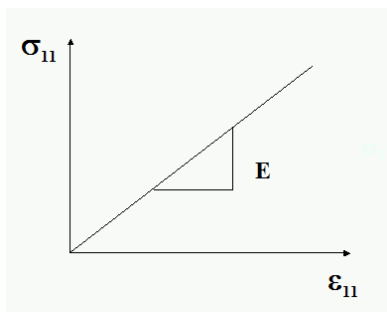


Figure 1. Uniaxial loading of a specimen as interpreted by Hooke's Law.

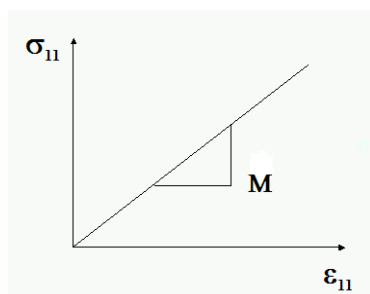


Figure 2. Constrained loading of a specimen as interpreted by Hooke's Law.

At this point in time, it should be observed that grains are loosen material, permitting only a constrained compression which does not generate the modulus of elasticity E , nor its time dependent counterpart $E(t)$. This way, this paper will not include the determination of Poisson's ratio ν , but only the constant M which includes both constants E and ν .

3. Materials and methods

A total mass of 7.5 kg of sun flower seeds was obtained from the local State Experimental Station and kept at 10% of moisture content. The testing device consisted of a 20 cm height and 8,5 cm diameter steel tube, similar to the rigid die employed in Poisson's ratio determination tests, which prevents the samples to deform at diametrical sense. A metal piston was introduced into the tube to compress the grains and following, the whole set was placed in a testing press and compressed at the deformation rates of 15 mm/min, 33 mm/min, 50 mm/min, 65 mm/min and 80 mm/min, meanwhile the axial force was being recorded. It was employed an Emic DL mechanical testing press of 30000 N capacity, which is coupled to a PC for recording. Obtained force deformation curves yielded the energy associated to grain density, both expressed as function of time. A testing time of 4.3 s was fixed for all the trials, i.e., the energy and

density are associated to a fixed compressing time. Figure 3 illustrates the experimental setup.

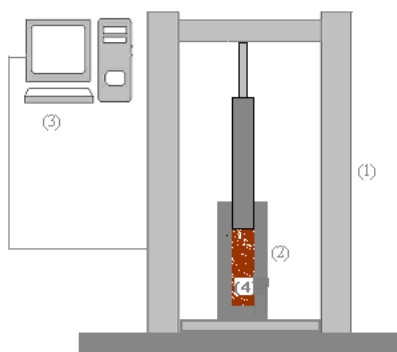


Figure 3. Experimental setup. (1) testing press, (2) rigid die, (3) data acquisition system and (4) grains.

4. Results and discussions

Experimental tests carried with five replications generated 5 plots of force versus deformation, for each one of the five applied deformation rates totalizing twenty five graphs. However only the graph corresponding to one replication for each deformation rate is presented here as exhibited from Figure 4 to Figure 8. By fixing a testing time from 0 to 4.3 seconds it was possible to calculate the compressing energy associated to each deformation rate, which results are shown on Table 1.

Table 1. Energy (N.m) in the period from 0 to 4.3 seconds for a given deformation.

Deformation rate (m/s)	Energy (N.m)				
	Replication				
	1	2	3	4	5
2.5×10^{-4}	41,50	39,50	37,17	44,08	43,61
5.5×10^{-4}	44,61	45,20	41,30	37,38	44,55
8.3×10^{-4}	40,61	44,94	38,92	49,05	46,59
10.8×10^{-4}	36,16	42,55	46,71	38,30	48,69
13.3×10^{-4}	40,46	42,19	39,07	46,54	50,83

Energy values were analyzed by means of a Standard Randomized Experiments through the software (see ASSITAT, 2008). Deformation rates stand for treatment in a number of replication equal to three. Table 2 shows the carried analysis of variance.

Table 2. Analysis of variance for the deformation rate treatment.

Source of variation	Degree of Freedom	Sum of Square	Mean Square	F
Treatments	4	26,0626	6,5157	0,386 NS
Residue	20	337,6207	16,8810	
Total	24	363,6833		

NS: no significant at 5% of probability ($p > .05$). Where: $F\text{-krit}(5\%) = 2,87$ and $F = 0,386$ ($F < F\text{-Krit}$). Coefficient of variation (CV) = 9,5%

Obtained data have for force-deformation for each replication for each deformation rate have been forward to the Excel software for best fitting, yielding the equations shown on Table 3.

Table 3. Polynomial fitting for force – deformation curves obtained from each replication.

Deformation Rate (m/s)	Polynomial square	R ²
2.5 x 10 ⁻⁴	$y = 2x10^7x^2 + 141,029x + 51.437$	0.9993
	$y = 2x10^7x^2 + 173,257x + 101.1$	0.9984
	$y = 1x10^7x^2 + 357,727x + 32.055$	0.9982
	$y = 2x10^7x^2 + 117,659x + 57.65$	0.9991
	$y = 2x10^7x^2 + 156,133x + 163.6$	0.9978
5.5 x 10 ⁻⁴	$y = 2x10^7x^2 + 239,166x + 252.81$	0.9954
	$y = 2x10^7x^2 + 97,283x + 91.634$	0.9981
	$y = 2x10^7x^2 + 94,119x + 104.42$	0.9984
	$y = 1x10^7x^2 + 384,981x + 89.39$	0.9972
	$y = 2x10^7x^2 + 99,128x + 107.41$	0.9986
8.3 x 10 ⁻⁴	$y = 2x10^7x^2 + 90,586x + 133.83$	0.9988
	$y = 3x10^7x^2 + 81,096x + 118.34$	0.9983
	$y = 1x10^7x^2 + 341,114x + 204.74$	0.9954
	$y = 3x10^7x^2 + 39,514x + 168.49$	0.9973
	$y = 3x10^7x^2 + 63,574x + 229.21$	0.9969
10.8 x 10 ⁻⁴	$y = 2x10^7x^2 + 360,152x + 208.87$	0.9959
	$y = 3x10^7x^2 + 72,187x + 139.15$	0.9977
	$y = 3x10^7x^2 + 79,944x + 206.68$	0.9978
	$y = 2x10^7x^2 + 499,996x + 114.82$	0.9963
	$y = 3x10^7x^2 + 137,406x + 213.09$	0.9980
13.3 x 10 ⁻⁴	$y = 3x10^7x^2 + 166,650x + 349.70$	0.9969
	$y = 2x10^7x^2 + 86,700x + 164.54$	0.9976
	$y = 2x10^7x^2 + 115,721x + 120.33$	0.9985
	$y = 2x10^7x^2 + 116,103x + 201.07$	0.9978
	$y = 2x10^7x^2 + 98,245x + 339.39$	0.9971

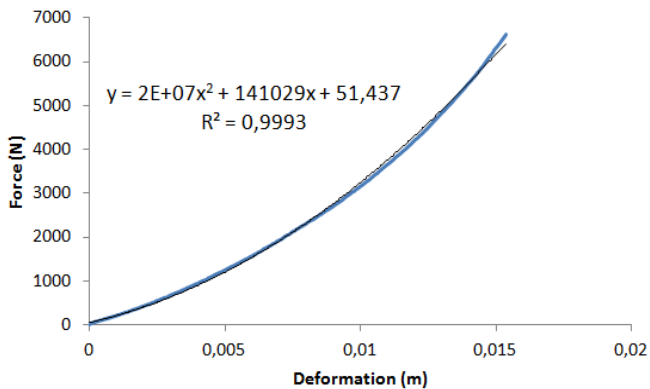


Figure 4. Plot of force versus deformation generated by the constrained compression of sunflower seeds at 15 mm/min of deformation rate.

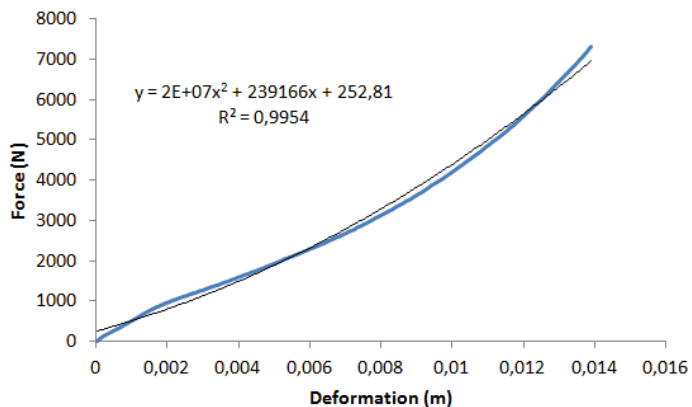


Figure 5. Plot of force versus deformation, compression of sunflower seeds at 33 mm/min deformation rate.

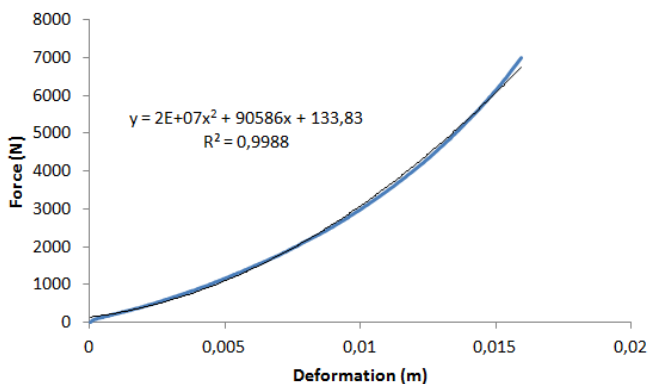


Figure 6. Plot of force versus deformation, compression of sunflower seeds at 50 mm/min of deformation rate.

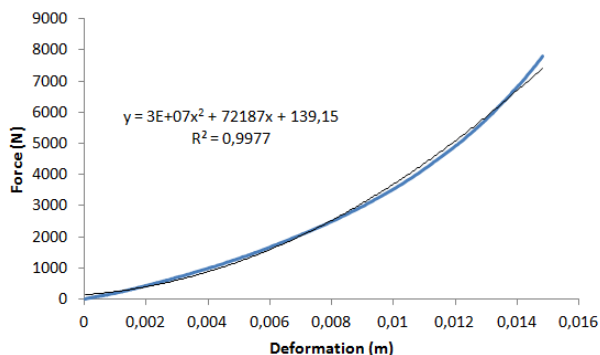


Figure 7. Plot of force versus deformation, compression of sunflower seeds at 65 mm/min of deformation rate.

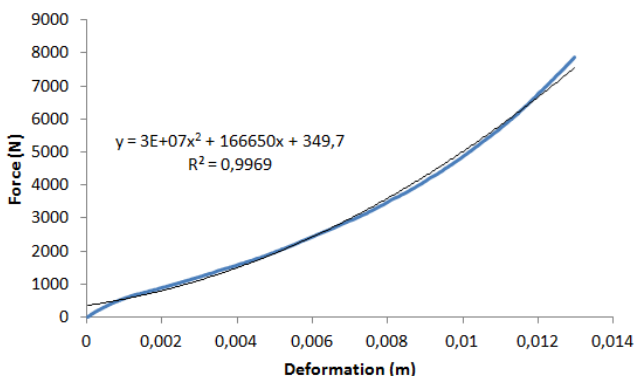


Figure 8. Plot of force versus deformation, compression of sunflower seeds at 80 mm/min of deformation rate.

The above results indicate no differences of energy requirement for sunflower seeds compaction for the tested deformation rates and at the adopted moisture content.

Conclucions

Based on what it has been exposed before, the following conclusions can be drawn. The results do not show significant differences for energy requirement for sunflower seeds compaction at the tested deformation rates.

Nomenclature

E	modulus of elasticity or Young's modulus	(MPa)
ν	Poisson's ratio	(dimensionless)
G	shear modulus	(MPa)
K	bulk modulus	(MPa)

δ	Kronecker's delta	(dimensionless)
σ	stress	(MPa)
ε	strain	(dimensionless)
M	constant (for constrained loading)	(dimensionless)

Subscripts

i,	1 or 2 or 3
j	1 or 2 or 3
k	1 or 2 or 3

References

- [1] ASSITAT Versão 7.5 beta, (2008) [HTTP://www.assistat.com](http://www.assistat.com). Registro INPI 0004051-2.
- [2] CONAB, Companhia Nacional de Abastecimento (2009). <http://www.conab.gov.br/>
- [3] Dal Fabbro, I.M., Cuccioli, E.A., Di Raimo, E., Bastos, M.A.A.. (2005) Time dependent modulus of elasticity of vegetative material. ITAFE 2005 - International Congress on Information Technology in Agriculture, Food and Environment. Çukurova, Turkey, october.
- [4] Dal Fabbro, Almeida,C.; I.M.; Di Raimo, E. (2005) Viscoelastic Properties of Compacted Sugarne (Sacharum officinarum,L) Bagasse. ITAFE 2005 - International Congress on Information Technology in Agriculture, Food and Environment. Çukurova, Turkey, october.
- [5] Finney, E.E. and C.W. Hall. (1967) Elastic Properties of Potatoes. Transactions of ASAE, 10(10):4-8.
- [6] Fridley, R.B.; R.A. Bradley, L.W. Rumsey, and P.A. Adrian. (1968). Some Aspects of Elastic Behavior of Selected Fruits. Transactions of the Asae, 11(1):46-49.
- [7] Ministério da Agricultura, Pecuária e Abastecimento (2009) <http://www.agricultura.gov.br/>
- [8] Malvern, L. E. (1969). Introduction to the Mechanics of Continuous Medium. Prenlice_Hall, inc., Englewood Cliffs, NJ.
- [9] Mase, G.E. (1970). Continuum Mechanics. Schaum's Outline Series. McGraw-Hill Company.
- [10] Mohsenin, N. N. (1971). Mechanical Properties of Fruits and Vegetables. Review of a Decade of Research, Applications and Future Needs. Asae paper n0 71-849.
- [11] Mohsenin, N. N. and H. Gohlich. (1962). Techniques for Determination of Mechanical Properties of Fruits and Vegetables Related to Design and Development of Harvesting and Processing Machinery. Journal of Agricultural Engineering Research, 7(4):300_315.
- [12] Segerlind L. and Dal Fabbro, I. (1980). A Failure Criterion for Apple Flesh. Asae paper 78-3556.

Physical properties of freeze dried vegetables by different thermal and chemical pre-treatments

T. ANTAL¹, B. KERÉKES¹, L. SIKOLYA²

¹Department of Vehicle and Agricultural Engineering, College of Nyíregyháza

²Department of Transportation and Infotechnology, College of Nyíregyháza

Abstract

In this study, the influences of the thermal and chemical pre-treatment methods on the physical properties and drying time of potato and carrot cubes were investigated. The vegetables cubes were dried in a freeze drier. The moisture content, water activity, hardness and rehydration capacity were determined.

Improvement of freeze dried food quality and drying rate (this value indirectly effect on drying cost) can be achieved by applying various pre-treatments before drying process. Four different pre-treatment (blanching in boiling water, dipping in hot water, alkaline-ionized water and NaCl solution) were considered in this studies. Pre-treatment using boiling water (5 min) and salt solution (10%, w/w) were found to be most suitable for increasing drying rate and product quality.

Keywords

freeze-drying, pre-treatment, drying time, hardness, rehydration.

1. Introduction

Consumers have a high wants for fruits and vegetables, which are an important dietary source of vitamins, carbohydrates, fibers and minerals. The intake of fruits and vegetables has been associated with a wide range of beneficial health effects. Potato (*Solanum tuberosum* L.) and carrot (*Daucus carota* L.) holds an important place in the nutrition of nations because of its high dietary value. Dehydrated carrots and potatoes are used as an ingredient in may prepared foods such as instant soups and are an excellent ingredient for developing healthy snack foods (Lin et al., 1998).

High quality products – high rehydration capacity, low bulk density, little shrinkage, high retention of color and bioactive substances, good appearance, soft texture – can be obtained using more expensive freeze drying methods. Freeze drying involves crystallization of water in ice crystals, which subsequently sublimate, thus leaving a porous dried product (Mujumdar and Law, 2010). Freeze drying is characterized by its poor heat supply conducted through a heated plate from the exterior to the interior of the material being dried. Reduction of the freeze drying time and optimization of the operating

parameters are usually regarded as effective methods to reduce the running cost by increasing the process efficiency, but the degree of quality reduction is very limited (Cui et al., 2008).

To improve the quality of a food product various pre-treatment methods have been suggested prior to drying. Many pre-treatments are found to help retain to improve various quality attributes of many food products. In terms of drying kinetics, thermal pre-treatments such as blanching and dipping in hot water change the physical properties of the sample cell structure, which in turn alter the rate of moisture removal (Pimpaporn et al., 2007). Hot water and blanching are a general pre-treatment methods applied before drying. The blanching avoids enzymes to be active at least during the drying process. Loosening of the cellular network and separation along the middle lamella has been observed in blanched materials which result in softening of the tissue. Blanching has been reported to lead to shorter drying time and increased drying rates of certain materials (Akissoe et al., 2003). Chemical pre-treatments, which involve immersion of food materials in chemical solutions such as NaCl solution and alkaline-ionized water have also been investigated and applied successfully to many food products including potatoes and apple (McMinn and Magee, 1999; Antal et al., 2011). The NaCl is often used as a pre-treatment of drying processes to reduce energy consumption and improve product quality (e.g., color, texture) (Lemus-Mondaca et al., 2009).

The objective of the present work is to compare the efficacy of selected pre-treatments such as blanching (3 and 5 min, 100°C), immersing in hot water (3 and 5 min, 85°C), alkaline ionized water solution (20 min, pH 9) and NaCl solution (20 min, 5 and 10%, w/w) on the drying time, water activity, hardness and rehydration of carrot and potato processed by freeze drying. Studies on pre-treatments of vegetables for freeze drying are rarely found in the literature.

2. Material and methods

Sample preparation

Fresh potatoes and carrots used in experiments were purchased from local supermarket. They were stored at a temperature of 5°C prior to the drying. Before freeze drying the samples were cleaned, peeled, and cut manually by using a vegetable slicer into 0,5 cm × 0,5 cm × 0,5 cm cubes. For the all pre-treatments, carrot and potato cubes samples of 200 g were placed in water/solutions. The mass ratio of the medium (solution) to the sample was 5:1 w/w. Sample was weighted on laboratory balance model JKH-500 (precision 0.1 g) produced by Jadever (Taiwan).

Then, the samples were blanched in boiling water (100°C) for 3 and 5 min, moreover immersed in hot water (85°C) for 3 and 5 min. After blanching and hot water treatments, the samples were cooled to room temperature under running cold water and then blotted with tissue paper to remove surface water. As for salt pre-treatments, two concentrations were employed (dipping time: 20

min, 5 and 10%, w/w). Potato and carrot cubes were dipped in alkaline-ionized water (pH 9) for 20 min. The pH of the water was then measured using a pH meter. After chemical pre-treatments, the samples were removed, and blotted with tissue paper to remove superficial water. For comparative purposes, a previously freeze dried samples were used as control (untreated).

Drying procedure

Experiments were performed in a laboratory-scale freeze dryer (Armfield FT33, Armfield LTD, Ringwood, England). The self-temperature was maintained at 20°C and the condenser temperature at -49°C, the vacuum was 40-48 Pa. Test samples were spread evenly covering tray in single layer. The tray was placed inside a working chamber. Each sample utilized in the experiment weighed 200 g. The change of the mass of the sample was detected continuously using a load cell (PAB-01, Emalog, Hungary) with a measurement range 1-5000 g and accuracy of ±1 g. During drying mass of samples was recorded at every 1 min interval. The samples were dried until a reaching the equilibrium moisture content (no mass change). After freeze drying, all products were packed in polyethylene bags to prevent water uptake and stored at 5°C.

Moisture content

The moisture content of potato and carrot were determined gravimetrically in triplicate by drying 3 g samples at 105°C until constant mass was achieved. The moisture content (M) of the samples in the drying process was calculated from (1):

$$M = \frac{W_t - W_k}{W_k} \quad (1)$$

The initial moisture content of raw potato and carrot were 3,608 kg/kg db and 7,547 kg/kg db, corresponding to 78,2% ($a_w=0,951$) and 88,3% ($a_w=0,984$) of water content (wb), respectively. The final moisture content of potato was 0,161 kg/kg db after 23 h of freeze drying time, while the final moisture content of carrot was 0,394 kg/kg db after 26 h of freeze drying time.

The dimensionless moisture content (MR) of the samples was calculated using the following equation (2):

$$MR = \frac{M - M_e}{M_0 - M_e} \quad (2)$$

Water activity

Water activity (a_w) of treated vegetables was determined at 22°C using a Novasina LabMaster-aw CH-8853 (Novasina AG, Switzerland) system previously calibrated with saturated solutions of different salts.

Rehydration

The rehydration ability was evaluated by immersing about 5 g potato and carrot cubes in 400 ml distilled water (temperature of water: 30°C); the rehydrated samples were withdrawn at 60 min, drained and weighed. After a specific time interval, the potato and carrot were removed and excess water gently blotted out with paper towel. The rehydration ratio (RR) of the sample was then calculated by (3):

$$RR = \frac{W_r}{W_d} \quad (3)$$

Hardness

Texture properties of the dried and pre-treated samples were measured using a texture analyzer (CT3-4500, Brookfield Engineering Laboratories, Middleboro, USA) with 4 mm diameter cylinder probe. A sample was placed on a planar base (diameter: 115 mm). The penetration distance was set to 20 mm, trigger force was 10 g and test speed was 1 mm/s. The compression test was carried out to generate a plot of force (N) vs. time (s). This plot was used to determine the value of hardness. The maximum force values were recorded in Newton (N).

Statistical analysis

Data were analyzed using the PASW Statistics 18 software (IBM, USA). Analyses of variance were performed by the ANOVA procedure. The Duncan's test was used to establish the multiple comparisons of mean values. Mean values were considered significantly different when $p \leq 0,05$. All experiments were performed in triplicate and the mean values were used for analysis.

Results and discussion

Effect of various pre-treatments on the drying time of freeze dried potato and carrot cubes

Drying time of two vegetables, potato and carrot, were studied in the freeze drying, under different pre-treatments: blanching, dipping in hot water, alkaline-ionized water and salt solution as shown in Table 1. It was observed that all of the pre-treatment exhibit shorter drying time in this case of vegetables than those of control samples. A significant difference in drying time was observed for all pre-treated samples compared to control samples. The Table 1. indicate that the drying time for the carrot was the longest (26 h) while the drying time of potato was the shortest (23 h) – along same conditions. There was no significant difference between treated with blanching and salt solution potato samples. The required drying times for blanched potato and carrot cubes (treatment time: 5 min) were 16 and 20 h, respectively. Drying time decreasing for blanched

(treatment time: 5 min) potato and carrot samples compared to freeze dried samples (control) was 30,43 and 23,07%, respectively. The drying rate increased with the increasing of immersing time and concentration, except of carrot samples dipping in hot water. It is concluded that blanching and salt solution is effective in improving freeze drying rate.

The faster drying time of blanched samples prior to freeze drying is because blanching in boiling water causes cell disruption, and increasing permeability of the cell, which allows moisture to be removed more easily (Aktas et al., 2006).

Table 1. Effect of pre-treatments on the average freeze drying time

Pre-treatment	Drying time, t (h)							
	Control (FD)	Blanching (3 min)	Blanching (5 min)	Hot water (3 min)	Hot water (5 min)	Alkaline water (20 min)	Salt 5%	Salt 10%
Potato cubes	23 ^c	17 ^{ab}	16 ^a	19 ^c	18 ^{bc}	21 ^d	18 ^{bc}	17 ^{ab}
Carrot cubes	26 ^d	22 ^b	20 ^a	21 ^a	21 ^a	24 ^c	23 ^b	21 ^a

^{abcde} Different letters the same rows indicate that values are significantly different ($p \leq 0,05$)

The final dimensionless moisture content (MR) of control potato, blanched potato samples (3 and 5 min), potato samples immersed in hot water (3 and 5 min), potato samples immersed in alkaline-ionized water and potato samples dipped in salt solution (5 and 10%, w/w) were found as 0.044, 0.050, 0.045, 0.030, 0.033, 0.036, 0.028, 0.026, respectively. The final dimensionless moisture content (MR) of control carrot, blanched carrot samples (3 and 5 min), carrot samples immersed in hot water (3 and 5 min), carrot samples immersed in alkaline-ionized water and carrot samples dipped in salt solution (5 and 10%, w/w) were found as 0.052, 0.048, 0.051, 0.045, 0.043, 0.039, 0.021, 0.020, respectively.

Water activity of vegetables with different thermal and chemical pre-treatments

Determination was made of a_w and the values obtained were within the interval from 0.506 to 0.360 (Table 2.). It was observed that the lowest value of a_w exhibited in this case of salt solution for 10% (w/w). The results showed that the value of a_w depends on the free water content in samples. As is known, foods with a_w values under 0,5 are stable against non-enzymatic browning, microorganism development and enzymatic activities during their adequate storage (Labuza, 1971).

Table 2. Water activity of the dried potato and carrot underwent different pre-treatments

Pre-treatment	Water activity, a_w (-)							
	Control (FD)	Blanching (3 min)	Blanching (5 min)	Hot water (3 min)	Hot water (5 min)	Alkaline water (20 min)	Salt 5%	Salt 10%
Potato cubes	0,476 ^c	0,506 ^g	0,488 ^f	0,421 ^b	0,435 ^c	0,459 ^d	0,365 ^a	0,360 ^a
Carrot cubes	0,489 ^g	0,471 ^f	0,477 ^f	0,432 ^d	0,446 ^c	0,408 ^c	0,397 ^b	0,385 ^a

^{abcde} Different letters the same rows indicate that values are significantly different ($p \leq 0,05$)

Effect of different pre-treatments on the physical properties of potato and carrot cubes

Texture is considered one of the most important criteria concerning consumer acceptance of finished product. Fig 1. gives results of texture tests. The hardness of potato and carrot samples were 8,11 and 11,022 N for freeze drying (control), respectively. The blanched (5 min) potato and carrot samples had significantly less hardness values: 4,106 and 5,144 Newtons, respectively. The blanching treatment (5 min) resulted in a 1,97 and 2,14-fold decrease in hardness of potato and carrot compared to control samples. There was no significant difference in hardness between blanching (3 min) and blanching (5 min) except for the blanched carrot (3 min) which is worse than that of the pre-treated in boiling water. Potato and carrot hardness decreased with an increase in immersion time and concentration from 3 to 5 min and from 5 to 10% (w/w), except of potato dipping in hot water (5 min). These results clearly indicated that the pre-treatment of blanching for 5 min gave the best product in terms of texture.

According to Leeratanarak et al. (2006), this phenomenon is probably due to the fact that blanching can cause starch gelatinization, softening of structure and led to less hardness of dried starchy product (e.g. potato).

Rehydration capacity is an important criterion for evaluating the quality of a drying method. It is a complex process indicating the chemical and physical changes caused by drying. The rehydration capacities of vegetable samples treated by different methods were calculated by Eq. (3) and presented in Fig. 2. The rehydration ratio (RR) of potato cubes was greater than that of RR of carrots. RR for unblanched (control) carrot and potato cubes were 3,12 and 5,42, after blanching for 5 min these values were 8,81 and 10,31, respectively. On the other hand, thermally pre-treated carrot and potato samples showed a 2,83-fold and 1,9-fold improvement in RR. Blanched (5 min) samples exhibited the significantly highest rehydration capacity than the other three pre-treatment methods. Pre-treated potato and carrot cubes with higher concentrations (from 3 to 5 min and from 5 to 10% [w/w]) resulted in a significant increase in rehydration ($p \leq 0,05$). Pre-treatment with salt solution in a small compass increased the rehydration ability of vegetables, probably due to salt crystals accumulating on the product surface. This can inhibit the movement of water into intercellular spaces of sample (Wang et al., 2010).

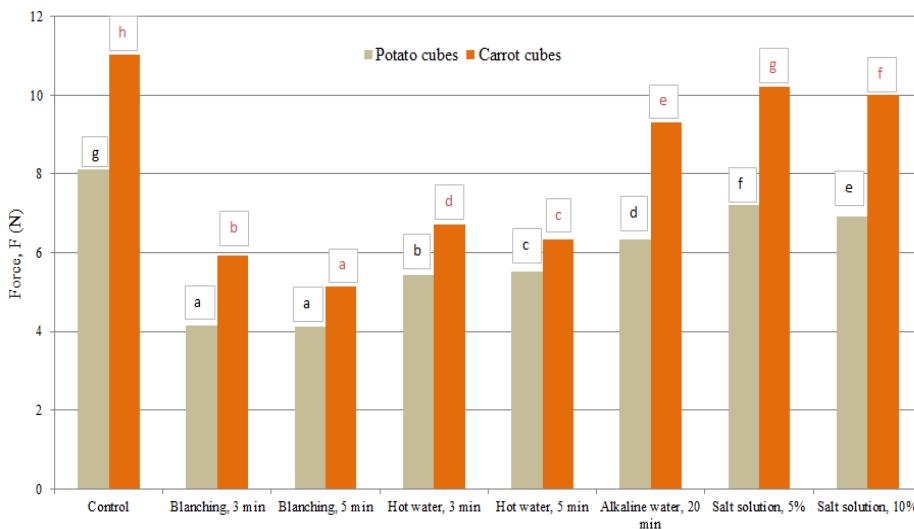


Figure 1. Hardness value of potato and carrot cubes treated by various pre-treatments (Different superscripts in the same column mean that the values are significantly different, $p \leq 0,05$)

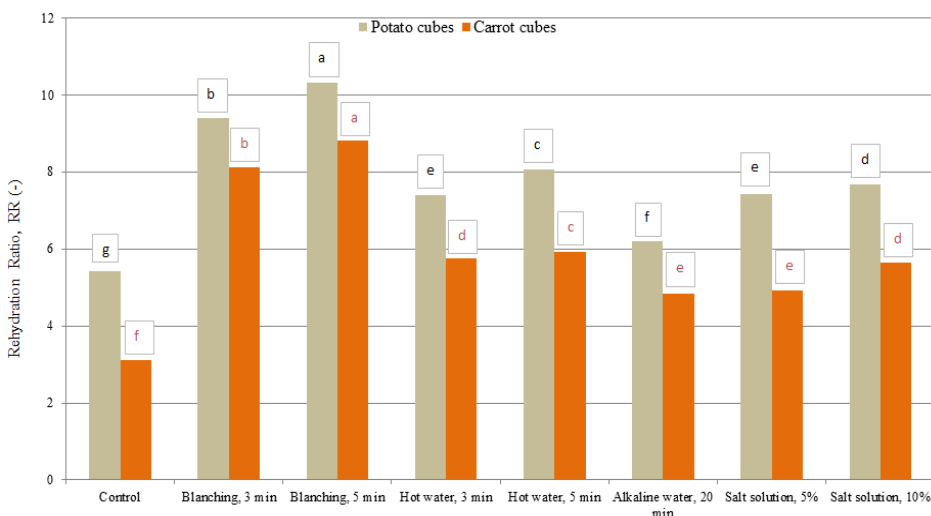


Figure 2. Rehydration ratio of dried vegetables associated with different pre-treatments (Different superscripts in the same column mean that the values are significantly different, $p \leq 0,05$)

According to microstructural observations, Sanjuán et al. (2005) indicated that blanching of carrots at 95°C for 1 min tends to cause separation along their cell walls, forming voids among the phloem parenchyma cells. These voids would be filled with water during rehydration, thus showing the higher rehydration

properties. In addition, as it can be seen in Fig. 1-2., freeze dried vegetables are less hard and increased ability to rehydrate more easily (Rother et al., 2011). Freeze dried potato and carrot have a soft and fragile texture.

Conclusions

The present study examines the effect of thermal and chemical pre-treatments on drying time, water activity, texture and rehydration capacity of horticultural products. The drying rate for blanched (treatment time: 5 min) potato and carrot were relatively faster than another pre-treated samples, and about 30,43 and 23,07% of the total drying time could be reduced by blanching in comparison with the control. The results indicate that the blanching in boiling water for 5 min can significantly enhance the hardness and rehydration of potato and carrot cubes. Concentration and immersing time of pre-treatments also affected the measured physical properties of potato and carrot. The blanching and salt solution (10%, w/w) could prove to be a very useful tool in maintaining the quality of vegetables and decreasing the drying time during preserving. However, more work is needed for confirmation. Further research is needed regarding the best pre-treatments, on quality factors such as texture, color, rehydration, microstructure and chemical component of the dried products.

Nomenclature

a, b, c, n	function parameters	
a_w	water activity	
db	dry basis	
m	mass	g
M	moisture content	kg/kg db
MR	moisture ratio	
M_e	equilibrium moisture content	kg/kg db
M_0	initial moisture content	kg/kg db
N	Newton	
P	pressure	Pa
p	significance level	
RR	rehydration ratio	
t	time	h
T	temperature	°C
wb	wet basis	%
W_r	weight of the rehydrated sample	g
W_d	weight of the dried sample	g
W_t	sample weight at a specific time	kg
W_k	sample dry weight	kg

Acknowledgements

This research was supported by the European Union and the State of Hungary, co-financed by the European Social Fund in the framework of TÁMOP 4.2.4. A/2-11-1-2012-0001 ‘National Excellence Program’.

References

- [1] Akissoe, N., J. Hounhouigan, C. Mestres and M. Nago (2003), How blanching and drying affect the colour and functional characteristics of yam flour, *Food Chemistry*, Vol. 82, pp. 257-264.
- [2] Aktas, T., S. Fujii, Y. Kwano and S. Yamamoto (2006), Effects of some osmotic pre-drying treatments on drying kinetics, desorption isotherms and quality of vegetables, *CD-ROM Proceedings, 15th International Drying Symposium*, Budapest, Hungary, August 20-23, 2006, pp. 877-883.
- [3] Antal, T., B. Kerekes, L. Sikolya and I. Szöllősi (2011), Effect of pre-treatment on the quality of dried apples using alkaline water, *CD-ROM Proceedings, II. Synergy in the Technical Development of Agriculture and Food Industry*, Gödöllő, Hungary, October 9-15, 2011.
- [4] Cui, Z-W., C-Y. Li, C-F. Song and Y. Song (2008), Combined microwave-vacuum and freeze drying of carrot and apple chips, *Drying Technology*, Vol. 26, pp. 1517-1523.
- [5] Labuza, T.P. (1971), Kinetics of lipid oxidation in foods, *Critical Reviews in Food Science and Technology*, Vol. 2, pp. 355-405.
- [6] Leeratanarak, N., S. Devahastin and N. Chiewchan (2006), Drying kinetics and quality of potato chips undergoing different drying techniques, *Journal of Food Engineering*, Vol. 77, pp. 635-643.
- [7] Lemus-Mondaca, R., M. Miranda, A. Andres Grau and V. Briones (2009), Effect of osmotic pretreatment on hot air drying kinetics and quality of chilean papaya (*Carica pubescens*), *Drying Technology*, Vol. 27(10), pp. 1105-1115.
- [8] Lin, T.M., T.D. Durance and C.H. Scaman (1998), Characterization of vacuum microwave, air and freeze dried carrot slices, *Food Research International*, Vol. 31, pp. 111-117.
- [9] McMinn, W.A.M. and T.R.A. Magee (1999), Studies on the effect of surfactant, blanching and osmotic pretreatments on the convective drying of potatoes, *Journal of Food Process Engineering*, Vol. 22, pp. 419-433.
- [10] Mujumdar, A.S. and C.L. Law (2010), *Drying Technology: Trends and applications in postharvest processing*, *Food and Bioprocess Technology*, Vol. 3(6), pp. 843-852.
- [11] Pimpaporn, P., S. Devahastin and N. Chiewchan (2007), Effects of combined pretreatments on drying kinetics and quality of potato chips undergoing low-pressure superheated steam drying, *Journal of Food Engineering*, Vol. 81, pp. 318-329.

- [12] Rother, M., P. Steimle, V. Gaukel and H.P. Schuchmann (2011), How to meet the freeze drying standard in combined drying processes: Pre and finish drying of carrot dice, *Drying Technology*, Vol. 29, pp. 266-277.
- [13] Sanjuán, N., I. Hernando, M.A. Lluch and A. Mulet (2005), Effects of low temperature blanching on texture, microstructure and rehydration capacity of carrots, *Journal of the Science of Food and Agriculture*, Vol. 85, pp. 2071-2076.
- [14] Wang, R., M. Zhang and A.S. Mujumdar (2010), Effect of osmotic dehydration on microwave freeze-drying characteristics and quality of potato chips, *Drying Technology*, Vol. 28, pp. 798-806.

Effect of measure settings on creep-recovery test results of candy gums

Gy. CSIMA, E. VOZÁRY

Department of Physics and Control, Corvinus University of Budapest

Abstract

The Creep-Recovery Test (CRT) of candy gums can be used in creating the rheology model of it. The effect of setting parameters (loading force, speed of deformation, creeping-recovering time) on CR curves characteristics was investigated with a 2^3 type full factorial experiment design. CRT curves were recorded with a TA.XT-2 precision texture analyzer (Stable Micro System) on commercial candy gums samples loaded with a cylinder probe of 75 mm diameter. The loading force had the most effect, the deformation speed and creeping-recovering time had less effect on CRT result parameters.

Keywords

candy gum, texture analyzer, creep recovery test, parameter effects

1. Introduction

The candy gums are one of popular confectionery products. Describing quality properties, know and able to manage the changes in candy material, caused by produce technological parameters or component changing, has primary importance from aspect of producer. The material of candy gum has a complex gel structure, the gelation process during the production is occurred by decrease of temperature and pH of hot raw mass after melting into pressed starch powder form. The quality and quantity of applied gelatin determines the main quality and sensory properties of candy gums (Mohos, 1993).

Lots of research describes properties of different gelatins. Most of them use rotation and/or oscillation viscometry, which give very precise and accurate describe of gelation properties. Montero et al (2002) analyzed gelatins with different origin and found that gel structure stability depends on producing technology. Nevertheless these methods are not appropriate for modeling consumption (biting, chewing). The Creep Recovery Test (CRT) can give a better describe of elastic properties. Dolz et al (2006) characterized the rheological behavior of food emulsions like gels with creep test and give a good model description for these materials. Vozáry et al (2012) investigated the rheological behavior of candy material by different stress strain and deformation speed values, simulating biting. They found, that at higher stress strain and by

higher deformation speed the range of elastic parameter of candy gum changes significantly because of cracking of gel structure (Foegeding, 2007).

So the aim of our work presented here was to evaluate the influence of measuring parameters of CRT (loading force, creeping-recovering time, deformation speed) on CRT quality parameters. Further goal was to optimize measuring parameters of CRT in case of candy gums. With an appropriate measuring setting the CRT could be suitable for follow up the changes of candy gum quality (caused by e.g. storage condition).

2. Materials and methods

Materials

For the experiments candy gums purchased from local market were used. The candy gums originate from the same production. The candies contained order in decreasing weight: glucose syrup, sugar, gelatin, dextrose, citric acid, fruit juices from concentrate (as taste components), extracts from fruits and vegetables, aromas (as color and smell components), bee waxes and invert sugar syrup (as polish components). The candy gums had the same complex, three dimension shape with smooth surface. The overall size of the samples was 2 cm x 1 cm x 1 cm with a weight of about 2.40 g. The candies were packed in semi permeable film. One package contained about 80-84 candies with a weight of 200 g.

The samples were stored in original packaging in a fridge at temperature of 5°C till the time of the measurements. The packages were taken out from fridge and opened just before the measurements. The unopened packages were stored in a thermos during the experiments to avoid possible changes in candy properties caused by drying or by temperature changing.

Methods

The Creep-Recovery Tests (CRT) (Figure 1-3.) is a complex rheological measuring method, which contains 3 period. At first the sample is compressed with a definite deformation speed until the determined loading force (F) is reached (in this point the measured deformation is D_1). After that the definite loading force is held for a definite time. During this time period the deformation increases by constant loading force, it's creeping. At the end of the creeping period the measured deformation is the maximal one (D_{max}). At the beginning of the third period, called recovering, the loading force is fallen to zero and the relaxation of deformation is measured for the same time as the creeping was endured. At the end of the recovering period the measured deformation is the irreversible plastic deformation (P). The difference of maximal deformation (D_{max}) and plastic deformation (P) is the elastic deformation (E).

The experiments were featured with a TA.XT-2 type precision texture analyzer (Stable Micro System, UK) in July 2013. The texture analyzer was operated in 'Measure force in compression' mode with 'relaxation test' method. For the measurements a cylinder metal plate of 75 mm diameter was used with.

The data acquisition rate was 25 points pro seconds, the trigger force was 0.05 N. On the samples CRT were recorded with loading force (F , N) of 1 N, 5.5 N and 10 N, with deformation speed (dD/dt , mm/s) of 0.1 mm/s, 0.3 mm/s and 0.5 mm/s and creeping-recovering time (t , s) of 30 s, 60 s and 90 s (in every setting the measurement of CRT curve was repeated three times).

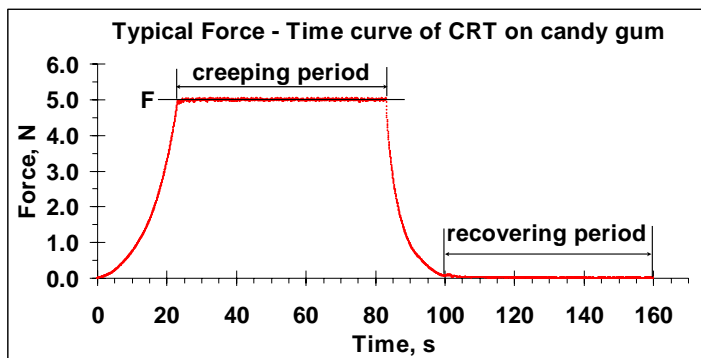


Figure 1. Typical Force – Time curve of CRT featured on candy gum

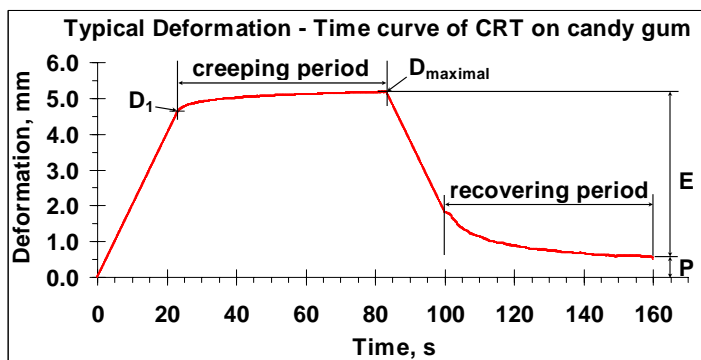


Figure 2. Typical Deformation – Time curve of CRT featured on candy gum

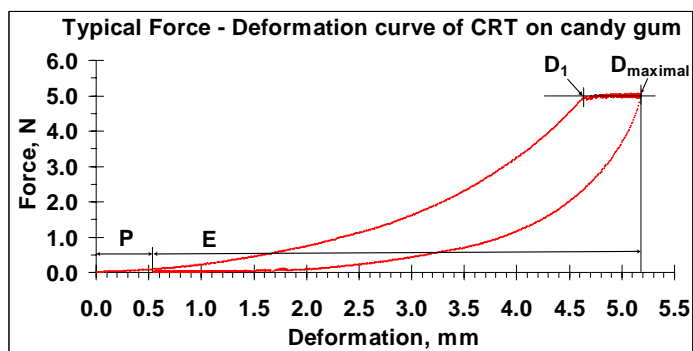


Figure 3. Typical Force – Deformation curve of CRT featured on candy gum

The measured CRT curves were saved and evaluated on computer with Texture Exponent 1.21. and MS Office® Excel 2003 SP3 software. Several parameters were calculated from curve data:

- ratio of loading force (F) to deformation before creeping (D_1)
- ratio of loading force (F) to deformation after creeping (D_{max})
- creeping deformation (the difference of deformation before and after creeping; $D_{max} - D_1$)
- ratio of creeping deformation ($D_{max} - D_1$) to original sample size (h)
- ratio of elastic deformation (E) to maximal one (D_{max})
- ratio of plastic deformation (P) to maximal one (D_{max})
- ratio of elastic work ($W_{elastic}$) to deformation work (W_{def}). These two work values were calculated from area under force – deformation curve: from start point to D_1 was deformation work (first period of CRT), from D_{max} to last point was elastic work (third period of CRT).

Table 1. Factors of creep recovery test

factor	Loading force	Deformation speed	Creeping-recovering time
	F	dD/dt	t
	z_1	z_2	z_3
z_{j0}	5.5	0.3	60
Δz_j	4.5	0.2	30
$z_{j,max}$	10	0.5	90
$z_{j,min}$	1	0.1	30

Table 2. Factors of creep recovery test

i	F	dD/dt	t	transformed factors							
	z_1	z_2	z_3	x_0	x_1	x_2	x_3	x_{12}	x_{13}	x_{23}	x_{123}
1	1	0.1	30	1	-1	-1	-1	1	1	1	-1
2	10	0.1	30	1	1	-1	-1	-1	-1	1	1
3	1	0.5	30	1	-1	1	-1	-1	1	-1	1
4	10	0.5	30	1	1	1	-1	1	-1	-1	-1
5	1	0.1	90	1	-1	-1	1	1	-1	-1	1
6	10	0.1	90	1	1	-1	1	-1	1	-1	-1
7	1	0.5	90	1	-1	1	1	-1	-1	1	-1
8	10	0.5	90	1	1	1	1	1	1	1	1

The experiments were designed with 2^3 type full factorial experiment design (Kemény and Deák, 1993), which is suitable for characterizing main effects of measuring parameter on CRT result parameters. The three factors were the loading force, the creeping-recovering time and the deformation speed. For the

measured data - obtained with the maximal and minimal values of set parameters - adequate linear model was fitted. The factors and the experimental parameter settings are shown in Table 1 and 2. The measured CRT parameters in center of experiment design are used for estimate of deviation of measured parameters.

3. Results and discussion

The results of full factorial experiment design are presented in Table 3. in which the red numbers show the significant effect on result CRT parameters, while the italic numbers show the non-significant effects on CRT result parameters. From Table 3 it is obvious that the force had the main effect on CRT result parameters, it was expected. The creeping-recovering time was the second important measuring parameter, while the deformation speed proved to third important one. The secondary cross effects had no significant effect on CRT result parameters. In case of every parameter the fitted linear model was adequate on confidence level of $\alpha=0.05$.

Table 3. Result of full factorial experiment design in case of CRT – transformed parameters

parameters		F/D _{max}	D _{max} -D ₁	(D _{max} -D ₁)/h	E	E/D	P/D	W _{elast} /W _{def}
b ₀	---	1.048	0.546	0.044	3.936	0.913	0.087	0.312
b ₁	F	0.669	<i>0.017</i>	0.000	1.545	0.021	-0.021	-0.036
b ₂	dD/dt	0.000	0.158	0.000	0.000	0.000	0.000	-0.124
b ₃	t	<i>-0.017</i>	0.059	0.000	0.109	0.011	-0.011	-0.040
b ₁₂	F*(dD/dt)	<i>0.007</i>	0.000	0.000	0.000	-0.009	0.009	-0.021
b ₁₃	F*t	<i>-0.004</i>	<i>0.015</i>	0.000	0.000	0.000	0.000	-0.020
b ₂₃	(dD/dt)*t	<i>-0.005</i>	0.000	0.000	0.000	0.000	0.000	0.036
b ₁₂₃	F*(dD/dt)*t	<i>-0.008</i>	0.000	0.000	0.000	0.000	0.000	0.000

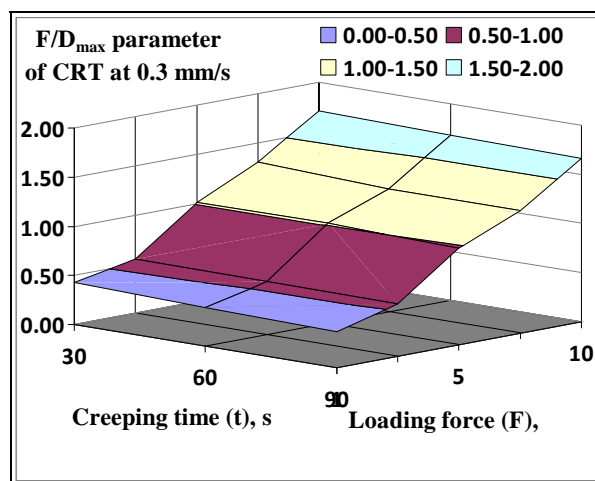


Figure 4. Effect of loading force on F/D_{max} parameter of CRT at 0.3 mm/s deformation speed

The effect of measuring parameter on CRT result parameters are shown on Figure 4-7.

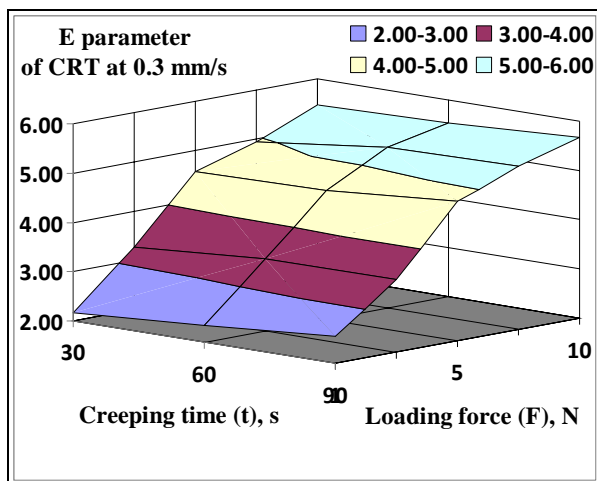


Figure 5. Effect of loading force on E parameter of CRT at 0.3 mm/s deformation speed

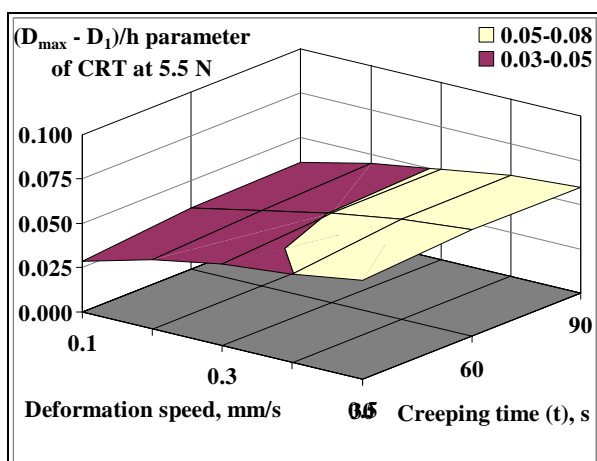


Figure 6. Effect of deformation speed and creeping time on $(D_{\max}-D_1)/h$ parameter of CRT at 5.5 N loading force

As it was mentioned above, the loading force had the main effect on CRT result parameters, while the creeping time and deformation speed had effect just in case the half of result parameters (E , E/D_{\max} , P/D_{\max} , and $W_{\text{elast}}/W_{\text{def}}$ respectively). The close connection between E and P , and between E/D_{\max} and P/D_{\max} was proved with the factor analysis as well.

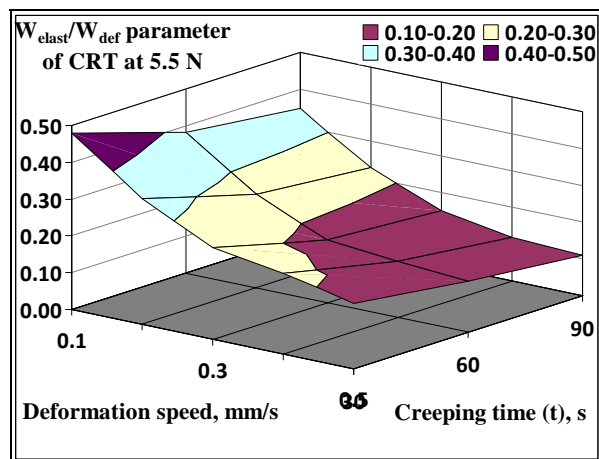


Figure 7. Effect of deformation speed and creeping time on F/D_{max} parameter of CRT at 5.5 N loading force

From the experimental comes that the careful measure parameter choosing is very important from measure technique aspect. At lower loading force the measurable deformation could be too small. At higher loading force the applied deformation could occur cracking in the material of candy sample. The setting of creeping-recovering time is important from view of creeping investigation. The chosen creeping-recovering time must be twofold-threefold bigger than the retardation time of candy material. Applying too long creeping-recovering time is unnecessary. By higher deformation speed bigger overshoots and other measuring errors could be occurred. It is suggested to choose such a slow one, by which the measuring errors are minimal.

4. Conclusions and proposals

Conclusions

Based on experimental results the loading force has the most effect on CRT result parameters. Nevertheless it is suggested to choose an appropriate loading force for CRT, e.g. 5 N.

Applying a suitable creeping-recovering time the time need for realize one CRT is smaller, 60 s could be enough for the total realization of creeping and recovering period.

Deformation speed has no significant effect on result parameters, but it has importance from measure technique aspect. Choosing a medium range one, e.g. 0.2 mm/s, the errors in deformation measurement could be avoid.

Proposal

Further experiments are suggested to refine and CRT measure parameters. An optimized CRT method could be very useful in investigation of changes in

candy gum material or other combined gel structures. As mastication simulate test method, CRT is suitable for follow up changes in gel structure under storage.

Nomenclature

b_j	estimated value of effect of transformed j. factor	---
dD/dt	in CRT: deformation speed (set parameter)	mms^{-1}
D_1	in CRT: measured deformation at the end of the first test period	
		mm
D_{\max}	in CRT: measured maximal deformation at the end of the second test period	mm
E	in CRT: elastic deformation, $E = D_{\max} - P$	mm
F	in CRT: loading force (set parameter)	N
h	in CRT: original sample size (high) before measurement	mm
P	in CRT: plastic deformation at the end of the third test period	mm
t	in CRT: creeping-recovering time (set parameter)	mm
W_{def}	in CRT: area under F – D curve from start to D_1 point (test period 1)	Nmm^{-1}
W_{elast}	in CRT: area under F – D curve from D_{\max} to last point (test period 3)	Nmm^{-1}
x_j	transformed j. factor; $x_j = (z_j \pm z_{j0}) / \Delta z_j = \pm 1$	(according to factor)
z_i	j. factor of full factorial experimental design	(according to factor)
z_{j0}	basic level of j. factor, $z_{j0} = (z_{j,\max} - z_{j,\min}) / 2$	(according to factor)
Δz_j	variation interval of j. factor, $\Delta z_j = z_{j,\max} - z_{j,\min}$	(according to factor)
$z_{j,\max}$	maximal value of j. factor	(according to factor)
$z_{j,\min}$	minimal value of j. factor	(according to factor)

Subscripts

i	number of experimental design point
j	number of factor, $j = 0 \dots 3$ (0 - constant; 1 – F; 2 – $-dD/dt$; 3 – t; 12, 13, 23, 123 – cross effects)

Acknowledgements

This project was supported by TÁMOP – 4.2.1/B-09/1/KMR-2010-0005.

References

- [1] Dolz M., M.J. Hernández, D. Delegido (2008), Creep and recovery experimental investigation of low oil content food emulsions, Food Hydrocolloids, Vol. 22, pp. 421-427.

- [2] Foegeding, E.A. (2007), Rheology and sensory texture of biopolymer gels, *Current Opinion In Colloid and Interface*, Vol. 12, pp. 242-250.
- [3] Kemény S and A. Deák (1993), *Kísérlettervezés*, Chapter No 13 in *Mérések tervezése és eredményeik értékelése*, 2nd edition, Műszaki Könyvkiadó, Budapest, pp. 249-277.
- [4] Mohos, F. (1993), *Szakágazati édesipar II*, 8th edition, Mezőgazdasági Szaktudás Kiadó, Budapest, pp. 127-135.
- [5] Montero P., M.D. Fernández-Díaz and M.C. Gómez-Guillén (2002), Characterization of gelatin gels induced by high pressure, *Food Hydrocolloids*, Vol. 16, pp. 197-205.
- [6] Sitkei, Gy. (1981): *A mezőgazdasági anyagok mechanikája*, Akadémiai Kiadó, Budapest, pp. 108-132.
- [7] Vozáry E., Á. Krisán and Gy. Csima (2011), *Rheological Properties of Gummy Confections*, PRAE Conference, Nitra, Slovakia, October 10-11., 2011.

Development of a compensator element for the ITER core CXRS diagnostics

T. BAROSS¹, L. JÁNOSI², Á. KREJCZINGER¹

¹WIGNER RCP, RMKI

²Department of Mechatronics,

Institute for Mechanical Engineering Technology,

Szent István University

Abstract

ITER Charge exchange recombination spectroscopy (CXRS) is going to be an important diagnostic of ITER with the main goals of measuring the ion temperature, impurity concentrations, toroidal rotation and effective ion charge. This optical diagnostics consists many vulnerable components to fulfil the measuring requirements and protect optics in a harsh ITER environment. According to the earlier reference design a replaceable tube holds one or more of these components which has expectable short lifetimes. This article deals with a flexible ring as a compensator and support element at the vacuum boundary of this tube structure. It has to compensate thermal expansion of the tube while it shall support the tube weight and additional loads by electromagnetic forces during plasma disruptions. A flexible compensator element was developed and proved with special lamellar form to optimize the stress distribution and increase its flexibility.

Keywords

ITER core CXRS, retractable tube, flexible ring

1. Introduction

The optical system inside the Upper Port Plug #3 in ITER vacuum vessel have highlighted challenge with specific components as first mirror, shutter, cleaning system as introduced in [3]. According to the earlier “reference” design these components were held by a retractable tube that could be replaced in time. Significant engineering problem is the proper cooling layout and the adequate support system of the tube. This article focuses on a compensator-support element. The same problems are concerned in T. Baross et al. (2013) and J.F. Koning et al. (2011). Later on a testing equipment driven pneumatically looks preferable as detailed in Földi L. at al.(2011). The Hungarian contribution to the ITER CXRS system design was summarized in G. Pokol et al. (2010).

Fig. 1. shows the alternative cCXRS port plug main components including the tube, where the Diagnostic Shield Module serves as the first basement of the tube, and the intermediate PP flange as a second support at the vacuum boundary.

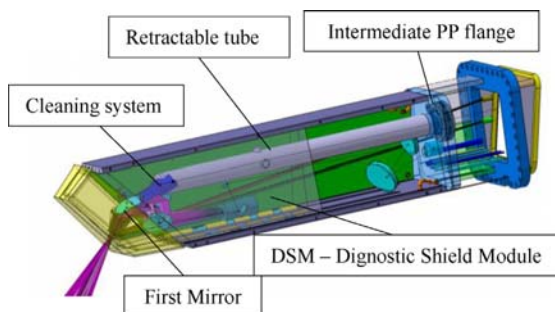


Figure 1. „Alternative” cCXRS port plug option [1]

2. Retractable tube size limitations

According to T. Baross et al. (2013) says the size of the tube is determined by the cleaning device with diameter of 150 [mm], that has to be fitted into a reserved envelope of 250 [mm]-diameter. In this way the tube diameter is also assumed to be 250 [mm], the tube length is around 3.5[m], filled with water and steel inside. Further limitations of the flange can be the remote handling tools size that has to reach the tube flange and fit through the port plug seal flange.

3. Support system

The tube support scheme is shown on Figure 2., where there are two suspension points, marked “A” and “B” inside the port plug. The “B” suspension point is the point of interest in this article.

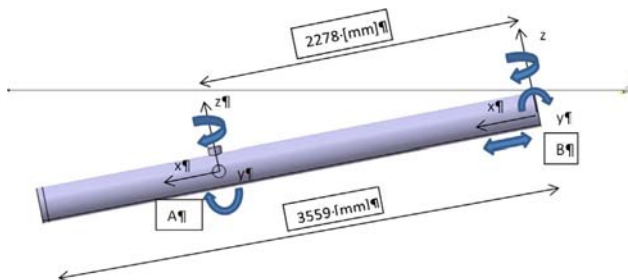


Figure 2. Tube supporting scheme showing degrees of freedom. [Ref.1].

- At “A” support the tube can rotate around y , z , other movements are fixed.
- At “B” support the tube can rotate around z and y and can move in x direction.

4. Thermal expansion of the tube

The tube handing and support concept are introduced in J.F. Koning (2011) where at the vacuum boundary a floating flange concept layout is

considered for compensation of the thermal expansion. The major thermal expansion/elongation of the tube comes from the tube cooling, where the water temperature in normal operation assumed to be 150 °C. During ITER bake-out campaigns it shall reach the 250 [°C]. Although we suspect a small temperature difference between the environmental components and tube, we have assumed 50 [K] as worst case. On the 2.28 [m] long section between A and B point elongates 1.9 [mm] in x direction at B point. For safety reasons the target value was chosen to 3 mm.

Another distortion can be resulted by the intensive neutron loads, where the maximum heated value is ~ 2.4 [W/cm³]. Figure 3 shows the heat generation function along the tube length.

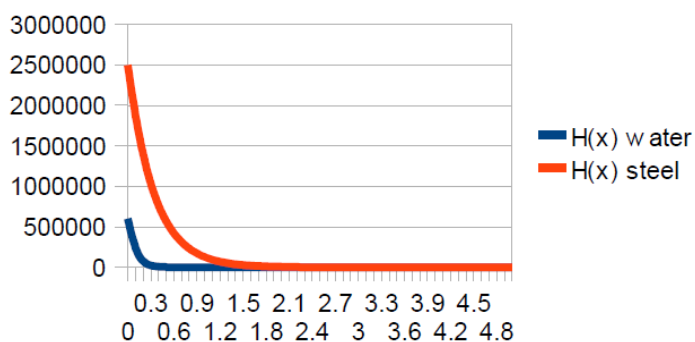


Figure 3. Heat generation functions in W/m³ in steel [316 L(N)-IG] and water along the tube calculated with in [3]

5. Development of the flexible ring

To solve the abovementioned problems at vacuum boundary a compensator-support element was designed to ensure the free motion of the tube structure. It shall compensate the axial differential thermal expansion and carries the radial loads from weight and electromagnetic forces. A floating flange concept was introduced in Yu. Krasikov et al (2011).

The second vacuum flange, called floating flange, fixed to cassette, provides the vacuum boundary. It is connected to the RT via double bellows. The cooling water and gas pipes, going into the tube back and other elements around the flange limit the minimum and maximum radius of this support element.

The concept was to find a geometry that can be manufactured from a cylindrical solid with slots similar to a widely used flexible beam coupling. Its material is 316L(N)-IG, that is a widely used in ITER environment. It could avoid frictional elements, and in normal conditions it shall not need maintenance. Table 1. summarizes the applied loads on the ring. The major loads are the force in z direction coming from the weight and electromagnetic events introduced in [1]. The thermal expansion of the tube were taken to 2 and 3 mm.

Table 1. Applied loads/displacement of flexible ring according to [1]

$M_{E-M,x}$ (Nm)	$F_{E-M,z}$ (N)	$F_{B,z}$ (N)	x (mm)
250	750	2141	3 and 2

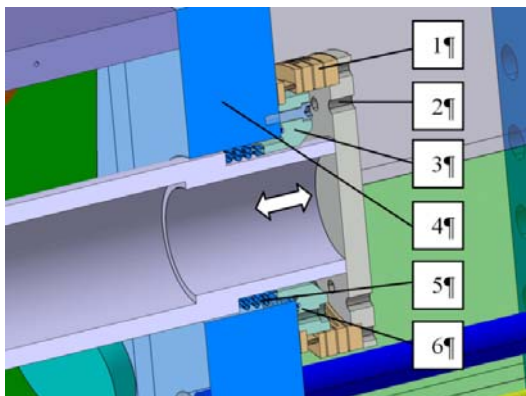


Figure 4. Tube support with a flexible ring [1]

Denominations: (1) flexible ring; (2) structural flange; (3) floating flange; (4) PP intermediate plate; (5) double bellow (schematic view); and (6) vacuum gasket

After some design iterations a ring with eight segments in parallel with four springs (lamellar) were formed. This construction is proven to have strength against radial loads, while in axial direction has enough flexibility. See figure 5 and 6.

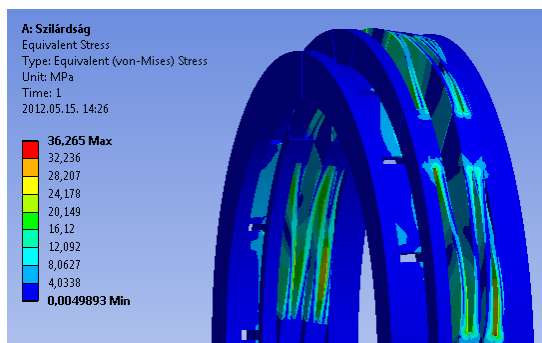


Figure 5. Stress distribution under the tube weight and E-m loads

The analysis showed that the peak stresses are concentrated in a small area, i.e. in the corner of a flexible plate, where there is no radius. After refining the

mesh this value was increased, because of this shape. Further idea was a weakened lamellar to optimize the stress distribution along its length.

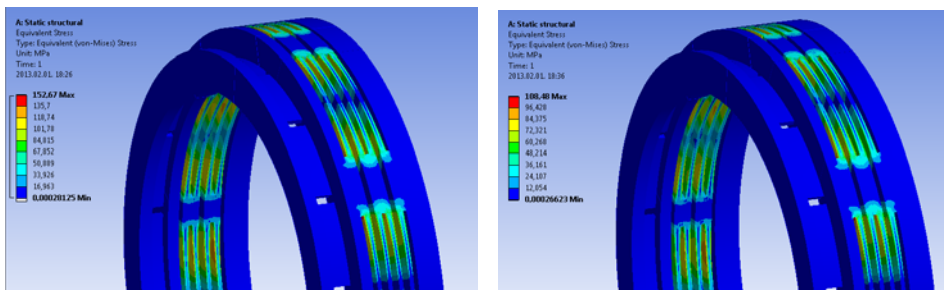


Figure 6. Stress distribution at combined load with 3 and 2 [mm] displacement [1]

6. Weakened lamellar concept

The lamellar shape was designed to approximate beam with homogenous stress along its length. With the following equations we could define an exact shape of a beam with homogenous stress distribution:

$$\sigma = const. = \frac{M_h(x)}{I(x)} \cdot \frac{h(x)}{2} \text{ and } I(x) = \frac{h(x)^3 b}{12} \rightarrow h(x) = \sqrt{\frac{|M_h(x)|}{b} \cdot \frac{6}{\sigma}}$$

Since the middle point of this function is zero, on a 3d model the function of the thickness was approximated by a polynomial, shown in Figure 7. Figure 5 and 4 refers to the case with 4...6 case.

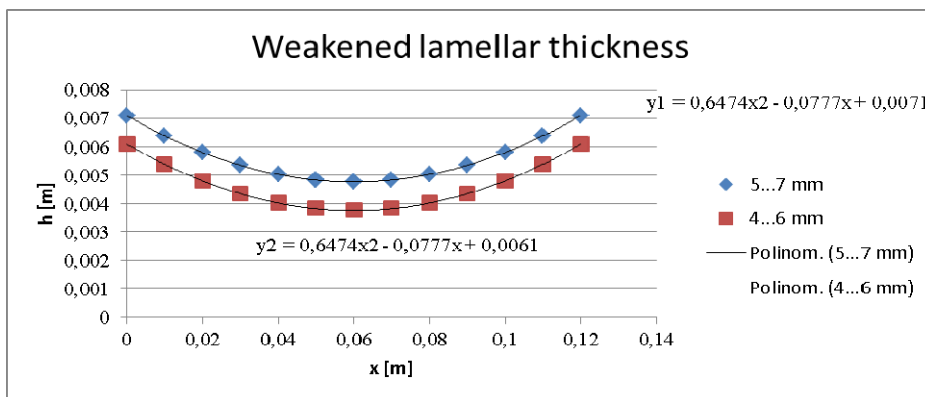


Figure 7. Weakened lamellar shape functions, where the 4...6 mm was used

The system is divided in two separate system: a cantilevered beam with a concentrate load at the end, and a cantilevered beam with a concentrated moment at the end.

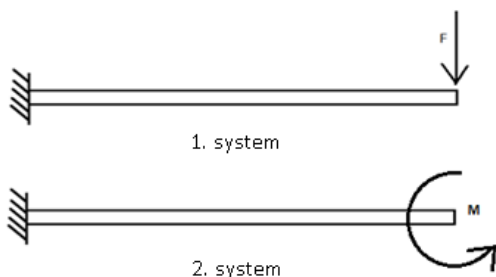


Figure 8. Two separate system for beam calculations

The two cantilevered systems are solvable separately with the differential equation of the elastic curve. The functions of moment are determined as following:

$$M_1 = F(l - x)$$

$$M_2(x) = M_0$$

The deflection functions and its derivatives can be calculated by integrations:

$$w_i'(x) = \int \frac{M_{hi}(x)}{I(x)E} dx + A_i$$

$$w_i(x) = \iint \frac{M_{hi}(x)}{I(x)E} dx + A_i x + B_i$$

The i is the number of the system. Since this integration with a non-constant second moment of inertia $I(x)$ is a difficult calculation, in this way it were calculated by Maple program. After integration four equations were derived, which have five parameters: A_1 , A_2 , B_1 , B_2 és M_0 . To determine the parameters the boundary conditions shall be calculated:

$w_1(0) = 0$: the 1. system deflection is 0

$w_1'(0) = 0$: the 1. system rotation is 0

$w_2(0) = 0$: the 2. system deflection is 0

$w_2'(0) = 0$: the 2. system rotation is 0

$w_1'(l) + w_2'(l) = 0$: with superposition the rotation at the end of the beam is 0.

For verification a FEM analysis of a one lamellar was performed with same parameters as in analytical case. The analytical and FEM calculations were compared in Table 2.

Table 2. ANSYS and Maple results on one lamellar of flexible ring with 8 segments

Geometry: height= 4...6 [mm]; width= 39 [mm]; length= 0,12 [m]						
	Nr. of lamellar	Max. stress [MPa]	Deflection /lam. [mm]	Required force/ lam. [N]	Sum of force [N]	Sum of deflection [mm]
Maple	4	103	0,75	385	3080	3
Ansys	4	122	0,75	383	3064	3
Maple	5	83	0,6	310	2480	3
Ansys	5	98	0,6	307	2456	3

It can be seen, that the peak stresses are under 100 [MPa] and there are no large deviations between the FEM and analytical solutions. On Figure 9. an example is given for the FEM and analytical results. The applied stainless steel [316 L(N)-IG] properties are summarized in Appendix 1.

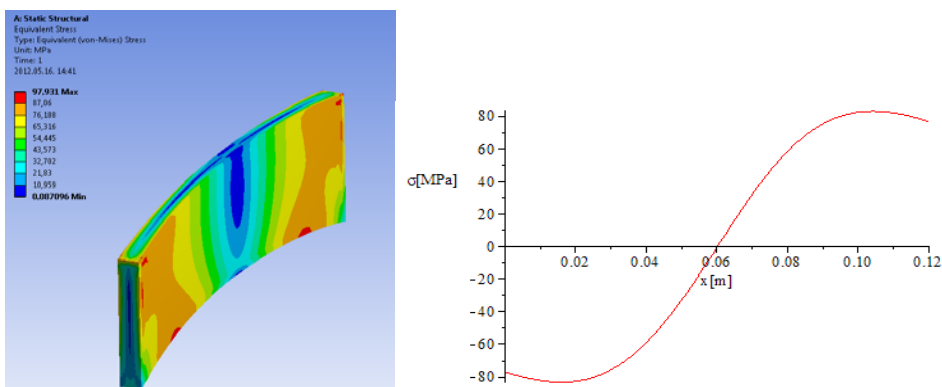


Figure 9. Comparison of the FEM and analytical calculations

Results and conclusions

A concept of a flexible ring element to compensate the axial tube expansion was developed for a retractable tube in ITER CXRS upper port plug. The results

show that this concept is feasible in view of axial expansion and the main load on the tube support. Further investigation is needed to decrease the peak stresses regions with fillets and find the optimum between the number of lamellar, thicknesses, inner and outer radius of the flexible ring.

An additional challenge can be the manufacturing problems of a similar ring.

References

- [1] T. Baross, W. Biel, A. Krejczinger, Yu. Krasikov, A. Panin, Retractable tube design issues in ITER CXRS UPP #3, Fusion Engineering and Design 88 (2013) 1352– 1356
- [2] J.F. Koning, Feasibility of upper port plug tube handling, Fusion Engineering and Design 86 (2011) 2060–2063.
- [3] Yu. Krasikov, T. Baross, W. Biel, A. Litnovsky, N. Hawkes, G. Kiss, et al., Development of design options for the port plug components of the ITER core CXRS diagnostic, Fusion Engineering and Design 86 (2011) 2055–2059.
- [4] Földi.L. et al. Novel cylinder positioning system realized by using solenoid valves, SUSTAINABLE CONSTRUCTION & DESIGN 3:(1) pp. 142-151. (2011)
- [5] G. Pokol, et al., The development of the ITER core CXRS diagnostics, Nukleon (2010), article 59 (in Hungarian).

Appendix

Austenitic Stainless Steel		316L(N)-IG			
Property	Temp range, °C	Evaluation formula	for T = 240 °C		
Density	20 - 1400	$\rho = 7968.2 - 0.37632 * T - 7.28724 \cdot 10^{-5} * T^2$	$\rho =$	7873,7	kg/m ³
Young's Modulus	20 - 700	$E = 194 - 0.0814 * T$	$E =$	174,5	GPa
Poisson's Ratio	20 - 500	0,3	$\nu =$	0,3	-
Mean Thermal Expansion	20 - 1000	$\alpha_m = 15.815 + 0.0060742 * T - 2.0796 \cdot 10^{-6} * T^2$	$\alpha_m =$	17,3	10 ⁻⁶ K ⁻¹
Thermal Conductivity	20 - 1400	$k = 0.01434 * T + 13.651$	$k =$	17,1	W/mK
Specific Heat	20 - 1400	$C_p = 465.49 + 0.21045 * T + 8.6641 \cdot 10^{-7} * T^2$	$C_p =$	516,0	J/kgK
Tensile strength	75 < T ≤ 500	$S_u = 1.112 * (530 - 0.95 * T + 0.0026 * T^2 - \dots)$	S_u	463	MPa
Yield strength	20 < T ≤ 650	$S_y = 226 - 0.74 * T + 0.0025 * T^2 - \dots)$	S_y	137	MPa
Design stress intensity	125 < T ≤ 675	$S_m = 0.9 * (226 - 0.74 * T + 0.0025 * T^2 - \dots)$	S_m	117,2	MPa

Development of process control for small scale biodiesel production plant

L. JÁNOSI, V. ERDÉLYI, E. SÁRKÖZY

Department of Mechatronics, Institute for Mechanical Engineering Technology,
Szent István University

Abstract

Biodiesel is gaining more and more importance as an attractive fuel due to the depleting nature of fossil fuel resources. The transesterification is the process of removing the glycerides and combining oil esters of vegetable oil with alcohol.

This paper is about the development of a novel process control of the small scale biodiesel production. The method shown in this article is a feasible solution to eliminate the drawback of unequal quality produced by the small scale production technology.

Keywords

renewable energy, small scale biodiesel production, process control, transesterification

1. Introduction

Biodiesel is a fatty acid alkyl ester derived from the transesterification of vegetable oil and is considered as a renewable fuel that can be substituted for traditional diesel. Nearly all diesel-powered equipment can use up to 20 % biodiesel and many engines can use blends or even pure biodiesel with little or no modification. Moreover, emissions of greenhouse gases, carbon, monoxide and particulates can all be significantly reduced.

Researchers and scientists had developed different methods for biodiesel production from different bio fuels. Most of the researchers/ scientists reported that the production of biodiesel was more when the process was used a catalyst.

Ahn et al. (1995) followed a two-step reaction process to produce biodiesel. Using this method canola methyl ester (CME), rapeseed methyl ester (RME), linseed methyl ester (LME), beef tallow ester (BTE) and sunflower methyl ester (SME), synthesized in a batch reactor using sodium hydroxide, potassium hydroxide and sodium methoxide as catalysts. Cvengro and Povaz (1996) described biodiesel production by using two-stage low-temperature transesterification of cold pressed rapeseed oil with methanol at temperatures up to 70 °C. A new enzymatic method of synthesizing methyl esters from plant oil and methanol in a solvent-free reaction system was developed by Masaru et al. (1999). In the same year, Uosukainen et al. (1999) presented statistical and experimental

design to evaluate interdependence of process variables in enzymatic transesterification. The authors also studied the alcoholysis of rapeseed oil methyl ester (biodiesel). Fangrui and Hanna (1999) had reviewed the biodiesel production. Samukawa et al. (2000) investigated the effects of the pretreatment of immobilized *Candida antarctica* lipase enzyme (Novozym 435) on methanolysis for biodiesel fuel production from soybean. Ikwuagwu et al. (2000) discussed the production of biodiesel using rubber seed oil. The effect of three principal variables namely molar ratio of methanol to oil, amount of catalyst and reaction temperature on the yield of acid-catalyzed production of methyl ester (biodiesel) from crude palm oil had been studied by Crabbe et al. (2001).

Waste frying oils transesterification was studied by Felizardo et al. (2006) with the purpose of achieving the best conditions for biodiesel production. In the same year, Miao and Wu (2006) introduced an integrated method for the production of biodiesel from microalgal oil. Zhu et al. (2006) produced biodiesel from *Jatropha curcas* oil using a heterogeneous solid super base catalyst (calcium oxide). Meher et al. (2006) reviewed the technical aspects of biodiesel production by transesterification. Al-Zuhair et al. (2006) discussed the effect of fatty acid concentration and water content on the production of biodiesel. Xue et al. (2006) had developed a new method for preparing raw material for biodiesel. Production of fatty acid methyl esters from crude tobacco seed oil (TSO) having high free fatty acids (FFA) was investigated by Veljkovic' et al. (2006). Royon et al. (2007) studied the enzymatic production of biodiesel by methanolysis of cottonseed oil. A two-phase membrane reactor had developed to produce biodiesel from canola oil by Dube' et al. (2007). Exergy Flow Analysis (ExFA) is applied to the process of biodiesel production by Talens et al. (2007). Production of fatty acid methyl ester from palm fatty acid distillate (PFAD) having high free fatty acids was investigated by Chongkhong et al. (2007). Response surface methodology (RSM) based on central composite rotatable design (CCRD) was used to optimize the three important reaction variables namely methanol quantity, acid concentration and reaction time for reduction of free fatty acid content of the oil to around 1% by Tiwari et al. (2007). Rathore and Giridhar (2007) investigated synthesis of biodiesel from edible oils like palm oil and groundnut oil and from crude non-edible oils like *Pongamia pinnata* and *Jatropha curcas* in supercritical methanol and ethanol without using any catalyst from 200 oC to 400 oC at 200 bar. Demirbas (2008) studied a non-catalytic biodiesel production with supercritical methanol, which allows a simple process and high yield because of the simultaneous transesterification of triglycerides and methyl esterification of fatty acids. Non-catalytic biodiesel production technologies from oils/fats in plants and animals developed by Imahara et al. (2008) employing supercritical methanol.

2. Objectives of the study

The overall objective of this study is to identify the technology properly applies in a small scale biodiesel production plant and results a uniform quality end

product as a result of the production. The biodiesel produced should be in conformity with the EU standards EN 14214.

3. Biodiesel production

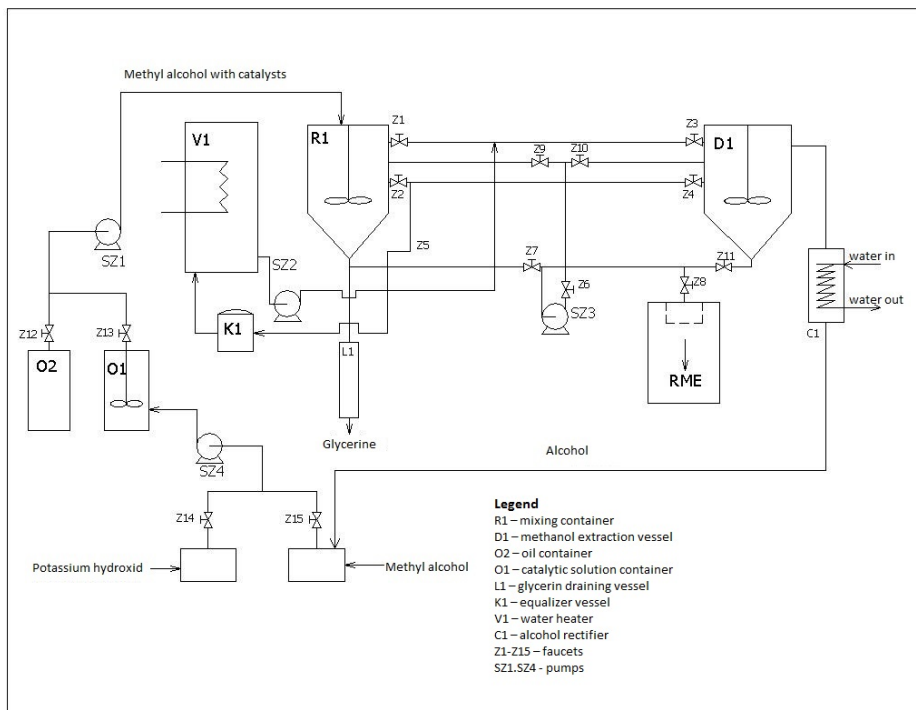


Figure 1. Small scale production technology design



Figure 2. Small scale biodiesel production model

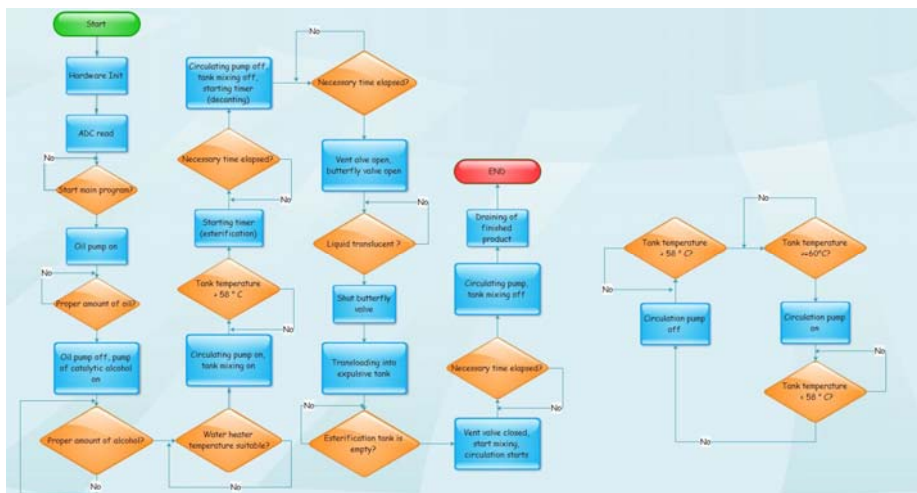


Figure 3. Logical operation of biodiesel technology

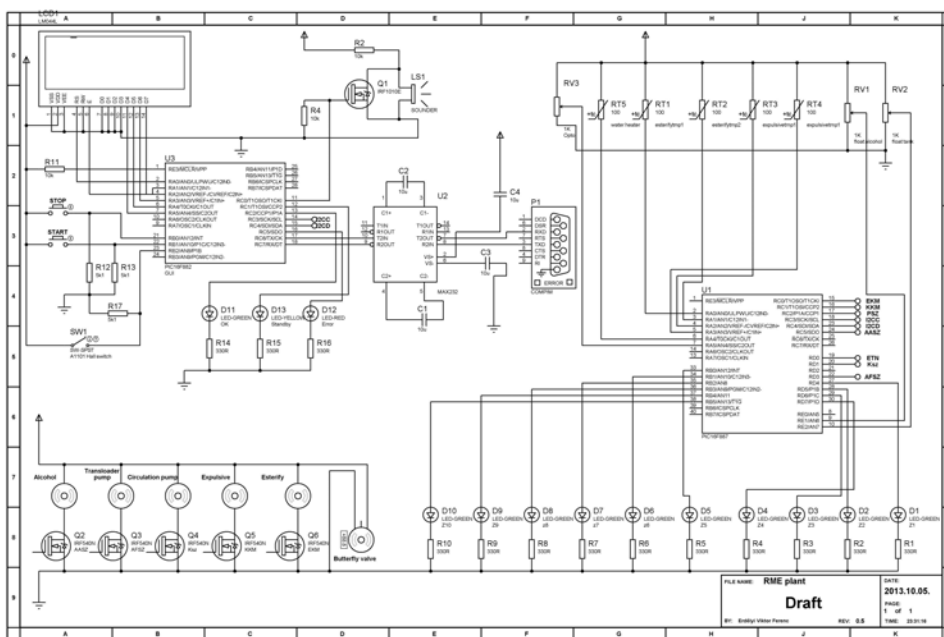


Figure 4. Digital circuit of automatic control of biodiesel production technology model

Biodiesel production is based on trans-esterification of vegetable oils and fats through the addition of methanol (or other alcohols) and a catalyst, giving glycerol as a co-product. Feedstock includes rapeseeds, sunflower seeds, soy seeds and palm oil seeds from which the oil is extracted chemically or mechanically. Advanced processes include the replacement of methanol of fossil

origin, by bioethanol to produce fatty acid ethyl ester instead of fatty acid in order to expand the relatively small resource base of biodiesel, new processes have been developed to use recycled cooking oils and animal fats though these are limited in volume. Hydrogenation of oils and fats is a new process that is entering the market. It can produce a biodiesel that can be blended with fossil diesel up to 50% without any engine modifications. Synthetic biofuel production via biomass gasification and catalytic conversion to liquid using Fischer-Tropsch process (biomass conversion to liquids BTL) offers a variety of potential biofuel production processes that may be suited to current and future engine technologies. The largest biodiesel producer is Germany, which accounts for 50% of global production. Biodiesel is currently most often used in 5%-20% blends (B5, B20) with conventional diesel, or even in pure B100 form.

Results and conclusions

Many previous projects were conducted before this automation setup. These days the small scale biodiesel production technology is already clear and well known. The experts have a lot of experiences on the details of the technology. At the same time many different raw materials are suitable for producing biodiesel fuel. The different inputs have different chemical and physical features while we need levelly the same fuel quality because the fossil diesel fuel could be substituted only this way.

To produce a well balanced and constant quality of biodiesel fuel the ability of controlling every step of the production technology is highly required. In case the technology is controllable independently of the quality of the input material the standardized quality of output is insurable. This goal is fulfilled by the control system shown in this paper.

Acknowledgements

This paper was produced by the back of TÁMOP-4.2.1.B-11/2/KMR-2011-0003 program “Levelling the research and education up at the Szent Istvan University”

References

- [1] Ahn E, Koncar M, Mittelbach M, Man R. (1995), A low-waste process for the production of biodiesel. *Separation Science and Technology* 1995;30:2021–33.
- [2] Cvengro J, Povaz AF. (1996), Production and treatment of rapeseed oilmethyl esters as alternative fuels for diesel engines. *Bioresource Technology* 1996;55: 145–50.

- [3] Kaieda Masaru, Samukawa Taichi, Matsumoto Takeshi, Ban Kazuhiro, Kondo Akihiko, Shimada Yuji, et al. (1999), Biodiesel fuel production from plant oil catalyzed by *Rhizopus oryzae* lipase in a water-containing system without an organic solvent. *Journal of Bioscience and Bioengineering* 1999;88:627–31.
- [4] Uosukainen E, Lamsa M, Linko Y, Linko P, Leisola M. (1999), Optimization of enzymatic transesterification of rapeseed oil ester using response surface and principal component methodology. *Enzyme and Microbial Technology* 1999; 25:236–43.
- [5] Ma Fangrui, Hanna Milford A. (1999), Biodiesel production: a review. *Bioresource Technology* 1999;70:1–15.
- [6] Samukawa Taichi, Kaieda Masaru, Matsumoto Takeshi, Ban Kazuhiro, Kondo Akihiko, Shimada Yuji, et al. (2000), Pretreatment of immobilized *Candida antarctica* lipase for biodiesel fuel production from plant oil. *Journal of Bioscience and Bioengineering* 2000;90:180–3.
- [7] Ikwaugwu OE, Ononogbu IC, Njoku OU. (2000), Production of biodiesel using rubber [*Hevea brasiliensis* (Kunth Muell.)] seed oil. *Industrial Crops and Products* 2000;12:57–62.
- [8] Crabbe Edward, Nolasco-Hipolito Cirilo, Kobayashi Genta, Sonomoto Kenji, Ishizaki Ayaaki. (2001), Biodiesel production from crude palm oil and evaluation of butanol extraction and fuel properties. *Process Biochemistry* 2001;37:65–71.
- [9] Felizardo Pedro, Joana Neiva Correia M, Raposo Idalina, Mendes Joaõ F, Berkemeier Rui, Bordado Joaõ Moura. (2006), Production of biodiesel from waste frying oils. *Waste Management* 2006;26:487–94.
- [10] Miao Xiaoling, Wu Qingyu. (2006), Biodiesel production from heterotrophic microalgal oil. *Bioresource Technology* 2006;97:841–6.
- [11] Zhu Huaping, Wu Zongbin, Chen Yuanxiong, Zhang Ping, Duan Shijie, Liu Xiaohua, et al. (2006), Preparation of biodiesel catalyzed by solid super base of calcium oxide and its refining process. *Chinese Journal of Catalysis* 2006; 27:391–6.
- [12] Meher LC, Vidya Sagar D, Naik SN. (2006), Technical aspects of biodiesel production by transesterification—a review. *Renewable and Sustainable Energy Reviews* 2006;10:248–68.
- [13] Al-Zuhair Sulaiman, Jayaraman Kishnu Vaarma, Krishnan Smita, Chan Wai-Hoong. (2006), A new method for preparing raw material for biodiesel production. *Biochemical Engineering Journal* 2006;30:212–7.
- [14] Xue Feiyan, Zhang Xu, Luo Hui, Tan Tianwei. (2006), A new method for preparing raw material for biodiesel production. *Process Biochemistry* 2006;41:1699–702.
- [15] Veljkovic' VB, Lacic'evic' SH, Stamenkovic' OS, Todorovic' ZB, Lazic' ML. (2006), Biodiesel production from tobacco seed oil with a high content of free fatty acids. *Fuel* 2006;85:2671–5.

- [16] Royon D, Daz M, Ellenrieder G, Locatelli S. (2007), Enzymatic production of biodiesel from cotton seed oil using t-butanol as a solvent. *Bioresource Technology* 2007;98:648–53.
- [17] Dube MA, Tremblay AY, Liu J. (2007), Biodiesel production using a membrane reactor. *Bioresource Technology* 2007;98:639–47.
- [18] Talens Laura, Villalba Gara, Gabarrell Xavier. (2007), Exergy analysis applied to biodiesel production. *Resources Conservation and Recycling* 2007;51:397–407.
- [19] Chongkhong S, Tongurai C, Chetpattananondh P, Bunyakan C. (2007), Biodiesel production by esterification of palm fatty acid distillate. *Biomass and Bioenergy* 2007;31:563–8.
- [20] Tiwari Alok Kumar, Kumar S Akhilesh, Raheman Hifjur. (2007), Biodiesel production from jatropha oil (*Jatropha curcas*) with high free fatty acids: An optimized process. *Biomass and Bioenergy* 2007;31:569–75.
- [21] Rathore Vivek, Madras Giridhar. (2007), Synthesis of biodiesel from edible and nonedible oils in supercritical alcohols and enzymatic synthesis in supercritical carbon dioxide. *Fuel* 2007;86:2650–9.
- [22] Demirbas Yhan. (2008), Comparison of transesterification methods for production of biodiesel from vegetable oils and fats. *Energy Conversion and Management* 2008;49:125–30.
- [23] Imahara Hiroaki, Minami Eiji, Hari Shusaku, Saka Shiro. (2008), Thermal stability of biodiesel in supercritical methanol. *Fuel* 2008;87:1–6.
- [24] Eszter Sárközi - László Jánosi (2009): The comparison of various rapeseed sorts' oil by their heating values in the viewpoint of technical utilization, *Synergy & Technical Development International Conferences in Agricultural Engineering*, 30. August-3. September 2009. Gödöllő, CD
- [25] F. Lujaji, G. Kafuku, E. Sárközi, L. Janosi, A. Bereczky, M. Mbarawa (2009): Technical aspects of production of methyl esters from non-edible oils feedstock, *Synergy & Technical Development International Conferences in Agricultural Engineering*, 30. August-3. September 2009. Gödöllő, CD
- [26] Eszter Sárközi – László Jánosi (2008): Ranking of various rapeseed sorts' oils by their fatty acid compositions according to the expectable physical properties, 7th Youth Symposium on Experimental Solid Mechanics, 14.05.-17.05.2008., Wojcieszycze, Poland; CD
- [27] F. Lujaji, A. Bereczky, L. Janosi, Cs. Novak and M. Mbarawa (2010), Cetane number and thermal properties of vegetable oil, biodiesel, 1-butanol and diesel blends, *Journal of Thermal Analysis and Calorimetry*, Online First™, 12 March 2010